SECURITY CLASSIFICATION OF THIS PAGE *(When Data Entered)*

REPORT DOCUMENTATION PAGE

READ INSTRUCTIONS BEFORE COMPLETING FORM

1. REPORT NUMBER: NRL Report 7838	2. GOVT ACCESSION NO.
3. RECIPIENT'S CATALOG NUMBER	
4. TITLE *(and Subtitle)*: LASER-FUSION STUDIES AT NRL — A Report to AEC for the Period July 1973 to June 1974	5. TYPE OF REPORT & PERIOD COVERED
	6. PERFORMING ORG. REPORT NUMBER
7. AUTHOR(s): Edited by J.A. Stamper and L.S. Levine	8. CONTRACT OR GRANT NUMBER(s)
9. PERFORMING ORGANIZATION NAME AND ADDRESS: Naval Research Laboratory, Washington, D.C. 20375	10. PROGRAM ELEMENT, PROJECT, TASK AREA & WORK UNIT NUMBERS: 77 H02-34
11. CONTROLLING OFFICE NAME AND ADDRESS: Atomic Energy Commission	12. REPORT DATE: October 1974
	13. NUMBER OF PAGES: 191
14. MONITORING AGENCY NAME & ADDRESS*(if different from Controlling Office)*	15. SECURITY CLASS. *(of this report)*: Unclassified
	15a. DECLASSIFICATION/DOWNGRADING SCHEDULE

16. DISTRIBUTION STATEMENT *(of this Report)*

Approved for public release; distribution unlimited.

17. DISTRIBUTION STATEMENT *(of the abstract entered in Block 20, if different from Report)*

18. SUPPLEMENTARY NOTES

19. KEY WORDS *(Continue on reverse side if necessary and identify by block number)*

Lasers
Plasmas
Fusion
Diagnostics
Laser plasma interaction

20. ABSTRACT *(Continue on reverse side if necessary and identify by block number)*

This report summarizes work done at NRL on laser fusion related problems during FY 1974. Included are sections related to laser development, and to experimental and theoretical studies of laser plasma interaction.

DD FORM 1 JAN 73 1473 EDITION OF 1 NOV 65 IS OBSOLETE
S/N 0102-014-6601

SECURITY CLASSIFICATION OF THIS PAGE *(When Data Entered)*

CONTENTS

INTRODUCTION AND OVERVIEW iv
L.S. Levine and J.A. Stamper

I. LASER FACILITY OPERATION 1
J.M. McMahon and O.C. Barr

II. LASER RESEARCH AND DEVELOPMENT 9
J.M. McMahon, O.C. Barr, and R. Lehmberg

III. TARGET INTERACTION FACILITY AND DIAGNOSTICS 43
B.H. Ripin, J.A. Stamper, E.A. McLean, and F.C. Young

IV. EXPERIMENTAL LASER-PLASMA BACKSCATTER STUDIES 54
B.H. Ripin, E.A. McLean, J.M. McMahon, W.M. Manheimer, and J.A. Stamper

V. SOFT X-RAY EMISSION FROM LASER-PRODUCED PLASMAS 65
*D.J. Nagel, P.G. Burkhalter, G.A. Doschek, C.M. Dozier, U. Feldman, B.M. Klein, and R.R. Whitlock**

VI. HARD X-RAY STUDIES 120
F.C. Young

VII. THEORETICAL PLASMA STUDIES 126
W.M. Manheimer

VIII. TWO DIMENSIONAL COMPUTER MODELLING OF LASER HEATED PLASMAS 135
D. Colombant, K. Whitney*, N.K. Winsor, J. Davis, and D.A. Tidman**

IX. MODEL STUDIES 159
*J. Davis and K. Whitney**

X. LASER RADIATION FORCE 179
J.A. Stamper

XI. PUBLICATIONS AND REPORTS 183

*Science Applications, Incorporated, Arlington, Virginia.

INTRODUCTION AND OVERVIEW

This Report covers recent NRL research and development related to the AEC laser-pellet fusion program. The work covered in this report was primarily carried out under AEC Contract No. AT(04-3)-878 between July, 1973 and June, 1974. In some cases, for the sake of clarity, work not performed during this period has been included. In addition, the report discusses the large complementary program supported by the Defense Nuclear Agency at NRL on the study of laser produced plasmas in high atomic number materials. A significant part of the soft x-ray experimental studies (Chapter V) and all of the numerical modelling studies (Chapter VIII and Chapter IX) were supported by the DNA program. This work has been included in the present report for the sake of completeness and since many of the results obtained are of direct benefit to the AEC laser-fusion effort.

There is some overlap in time, with the period covered by the last NRL report, which was presented to the Laser-Fusion Coordinating Committee in November, 1973. However, it was felt useful to establish the precedent of fiscal year reporting starting with this Annual Report. In the future, a report on the AEC supported laser-fusion studies at NRL will appear on a semi-annual basis.

Studies of laser produced plasmas began at NRL in 1968. Development of a large Q-switched glass laser facility was carried out under ARPA sponsorship. Additional support for laser development was received as part of a DNA-supported program to study the interactions between an expanding laser-produced plasma and an ambient magnetized plasma background. The DNA program also provided NRL with the genesis of its expertise in the study of laser plasma generation and interactions. The glass laser system was developed under joint ARPA and DNA sponsorship to the point where, by FY 72, it represented the state-of-the-art in high power short pulse lasers. The system included an NRL designed mode-locked YAG oscillator system and a disc amplifier which became a prototype for those now in use and under development in the laser-fusion program.

When a large AEC supported laser-fusion effort began in FY 72, NRL was a logical place to turn to for support in building up the programs of the AEC laboratories. Shortly after the start of AEC-supported work at NRL, a DNA program at NRL was initiated to study laser produced high atomic number plasmas. The aim of this program was to develop a new source of soft x-rays for weapons effect simulation. The combined AEC and DNA supported programs have been known within NRL as the Laser-Matter Interaction (LMI) Program and Dr. John Stamper has served as Program Manager since its inception. The LMI Program has included contributions from a number of divisions at NRL and has involved both experimental and theoretical studies. The funding of the program during FY 74 consisted of $500,000 from the AEC for laser-fusion studies as well as additional funding from DNA for x-ray source investigations.

One of the unique features of the NRL laser-fusion program has been the availability of a reliable Nd:glass laser system which produces exceptionally clean pulses (i.e., spatially, temporally and spectrally pure) at sufficient power levels ($\lesssim$ 0.5 TW) for many studies of interest to laser fusion. Over 1500 laser shots were put on target in FY 74 for our AEC

and DNA programs. In addition to routine laser operation, there was considerable advancement in glass laser technology made during the same period. An improved disc laser was developed, which showed 20% improvement in gain over the prototype system in use. There was also improvement in component lifetimes and in the mechanical and electrical design of the laser. The introduction of liquid rod cladding has reduced rod damage to less than half the level of the previous year. Theoretical predictions of laser self-defocusing in cesium vapor were followed by an experimental demonstration. This effect offers the potential for correcting the nonlinear wavefront distortion found in glass lasers.

Additional work has been done on characterizing the incident and focused laser pulse. The temporal character of the laser pulses were checked with a picosecond streak camera. Characterization of the focal region was achieved by observing the burn patterns on thin films placed in the focal region. Techniques were developed for positioning small targets with the accuracy ($\sim$ 25 μm) required for targets as small as 100 μm in diameter. Some new diagnostics were introduced including interferometry, PIN detectors (for soft x-rays) and ion detectors.

One particularly interesting and significant research effort during the past year was the series of time-resolved and time-integrated studies that were made of the backscattered and specularly reflected laser light. A saturation of the backscattered power (at about 0.5 GW) was observed with increasing laser power. The experimental data can be explained by assuming that stimulated Brillouin backscatter is responsible for most of the energy which is directly backscattered. The specularly reflected light was observed to be greatly reduced in intensity from that of the backscattered light. However, due to its larger solid angle, specularly reflected light can account for 5-10% of the incident energy.

Soft x-ray emission has continued to be a useful diagnostic of plasma conditions. Analysis of spectra has yielded time and space-averaged electron temperatures in the 0.5-1 keV range and densities in the 10^{19}-10^{20} cm^{-3} range. Evidence for non-equilibrium effects was observed, emphasizing the need for rate equation calculations of laser-plasma x-ray emission. As part of our DNA-supported research, targets from polyethylene through uranium were used for spectral and intensity studies. These studies show a high conversion efficiency from laser light to x-rays and help to provide the basis for understanding the role of x-rays in composite fusion targets.

Hard x-ray emissions (i.e., photon energies above about 15 keV) were studied in order to determine the role of superthermal electrons in laser target interactions. These x-rays were emitted from a source localized in the focal region and had an approximately isotropic distribution. Unlike the soft x-rays, their emission was not sensitive to target atomic number. There is some suggestion that the electrons producing these x-rays were generated in the plasma volume with the spontaneous magnetic fields playing a role.

The theoretical work during the past year was concerned mainly with anomalous electron heating. Non-thermal tails on the distribution function, formed in the anomalous absorption and scattering of laser light, have been given particular attention. Absorption at the critical density was shown to be reasonably and simply modelled by a large amplitude plasma wave, launched at the critical density and propagating toward lower densities. As the wave propagates, it Landau-damps and converts its energy into energetic electrons. Studies also were made of energetic electron production by Raman backscatter, and electron heating by stimulated Compton scatter.

Finally, sophisticated computational models were developed under DNA sponsorship to study laser plasma production and soft x-ray emission. A two-dimensional computer code was developed with fully time-dependent atomic physics, magnetohydrodynamics and radiation transport. It has shown significant conversion efficiencies of absorbed laser energy into x-rays should be possible. Spectra and "pinhole photographs" as well as plasma parameter profiles are generated by the computer model. Also, a one-dimensional non-hydrodynamic "hot-spot" model was developed to study x-ray emission on a subnanosecond time scale. The model is first correlated with experiment and then used to study the conversion efficiency of laser energy to *K*-line x-rays in carbon, fluorine and aluminum plasmas. The conversion efficiencies were found to peak at well defined values of input energy density for laser pulse widths smaller than the pumping times for *K*-line emissions.

The above overview can only touch upon some of the work done at NRL during the past year. The research is discussed in much more detail in the chapters that follow in this Report. It is clear that significant contributions have been made by the NRL group to the nation's laser-fusion effort. For example, the achievements in glass laser development will bear significant fruit in the large new glass laser systems being built over the next few years. The observation of saturation in the backscattered laser light from a target is also of importance, not only because of the insight it has provided to the nature of the coupling process but because it demonstrates that backscattering is not nearly as severe a problem as some had thought. These are the sort of critical contributions which we would hope that the relatively small group at NRL can make to the national laser-fusion effort in forthcoming years. The combination of good experimental and diagnostic capabilities with equally high quality theoretical and computational programs, has led to a fruitful research program. The work during FY 75 and beyond should continue to build upon these strengths and couple them ever closer to the key scientific and technical problem areas in the AEC laser-fusion program.

We are grateful for the contributions to x-ray studies from L. S. Birks, R. D. Bleach, D. B. Brown, J. W. Criss, R. D. Cowan (LASL), and W. E. Behring (NASA). Technical assistance in the laser facility operation were provided by R. Burns, T. DeRieux, J. Roddy, and L. Scott. Technical assistance at the target facility was provided by E. Turbyfill.

I. LASER FACILITY OPERATION

A. INTRODUCTION

The Naval Research Laboratory (NRL) glass laser capability has evolved over the past six years from the original purchased 2 GW (30 nsec) system operated in 1968 to the present subnanosecond pulse system which has operated extensively at 100-200 GW on target over the past two years. This evolution has been gradual with major emphasis on *reliable and economical operation* rather than on generating a few shots of very high peak power at the expense of reliability. It thus reflects the viewpoint that extensive, well diagnosed target interaction experiments must be carried out to master the physics of the laser matter interaction to an extent sufficient for the design of optimum laser-fusion targets. The NRL laser has had to operate frequently and dependably in order to calibrate and check out all the experimental packages needed to characterize the laser-target coupling on both the AEC (Atomic Energy Commission) and DNA (Defense Nuclear Agency) programs. The operational characteristics and usage of the laser are described more fully in section B.

During this evolution several significant achievements stand out. These were critical, not only in reaching our present status, but also in terms of advancing the state of solid state laser technology to the point where the base now exists for the design of 10^3-10^4 joule systems such as the one presently under construction at Lawrence Livermore Laboratory. These milestones include

- recognition that narrow linewidth, high gain, crystalline neodymium host-materials have the potential for generating 20 psec to 1 nanosecond pulses without the nonlinear effects which plague glass oscillators, the calculation of expected oscillator performance; and the operation of an optimized, prototype Nd:YAG oscillator (1969-1970);

- operation of the first transmission-line KD*P Pockels cells which allowed 30-33 dB background suppression per stage (1971);

- design, construction, and operation of the first high gain, high efficiency disc amplifier. This amplifier was the first disc laser to offer significant advantages over rod amplifiers (1971);

- computer modeling of xenon flashlamp pumping of Nd glass (GENEFF CODE) and optical transfer (ZAP CODE) as well as modeling of the parasitic oscillation problem in laser discs and solution of this problem in the NRL system (1971-1972);

- experimental observation that Fresnel diffraction was triggering self-focusing well below the whole beam self-focusing threshold and the first use of apodization techniques to suppress Fresnel diffraction, thereby allowing stable, routine operation of a high power glass laser system (1972);

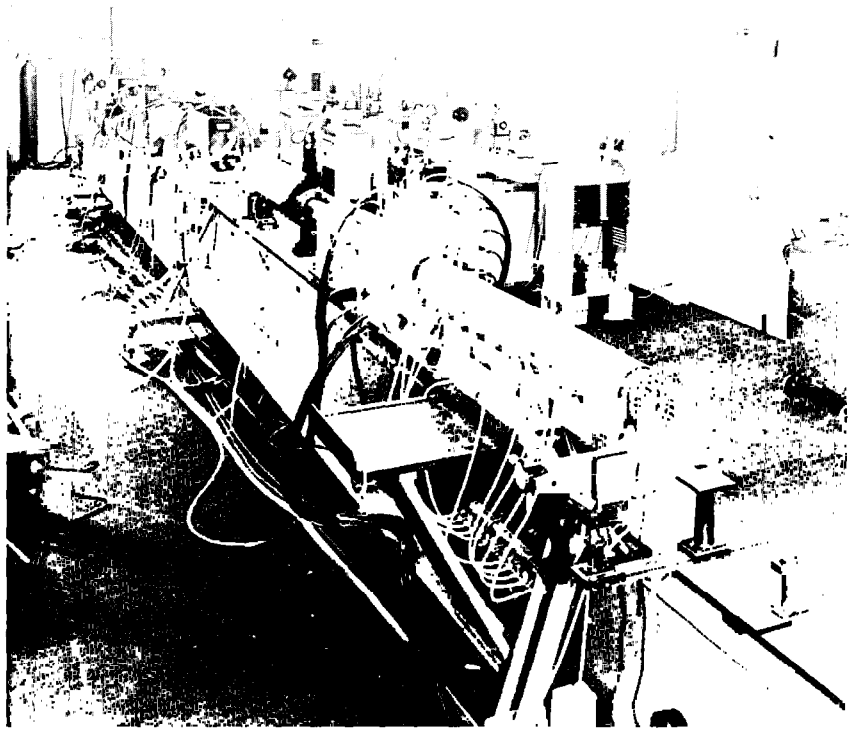

Fig. 1 — Present configuration of NRL disc laser. The mode locked oscillator and preamplifiers are on the optical bench on the far side of the room while the CGE rod amplifiers, 44 and 66 mm disc amplifiers and optical isolators are on the Steel I beam nearer the camera.

- design, construction and installation of the first total back reflection isolation system using optimized Faraday rotators and Pockels cells to suppress any prepulse or prelase as well as to offer total laser protection from back reflection; and carrying out of experiments characterizing the observed backscatter (1973).

B. GLASS LASER SYSTEM — PRESENT STATUS

The overall configuration of the NRL laser system at present is similar to that previously reported. The mode locked Nd:YAG oscillator, Pockels cell pulse switch and Nd:YAG preamplifiers are housed on one granite optical bench while the Nd:glass rod and disc amplifiers are mounted on a parallel steel I beam. Two mirrors are used to turn the pulse from the output of the preamplifier section to the input of the power amplifier section. This configuration decouples the alignment of the two subsystems so that changes in the oscillator section such as the insertion (or deletion) of an etalon (to change the pulsewidth) will not necessitate realignment of the whole system but at most will involve realignment of the preamplifiers and turning mirrors. Figure 1 shows the system as it is now used.

LASER FACILITY OPERATION

There have been significant changes since last year in the 44 mm disc amplifier and in the staging of the rod amplifiers. The present 44 mm disc amplifier is a retrofit to the CGE 64 mm amplifier head and was designed as a sealed amplifier in order to minimize dirt and dust problems. It functions as an intermediate stage between the rod amplifiers and the 66 mm disc amplifier and has a small signal gain of 3.5. Figure 2 shows the construction of this amplifier.

The staging of the outputs from the rod amplifiers has been modified as a result of the successful use of liquid claddings to suppress parasitic oscillations. The output intensity from the 45 mm amplifier is unchanged at a maximum value of 1.3×10^{10} W/cm^2 but the output of the 32 mm amplifier has been decreased to $\sim 2.5 \times 10^9$ W/cm^2 (from 5×10^9 W/cm^2) and the output of the 23 mm amplifier to 2×10^8 W/cm^2 (from 10^9 W/cm^2). This staging should further improve component lifetime and should minimize the gain for small scale self-focusing in the rod section of the system.

The beam spatial profile evolves through the system in a reasonable fashion. The oscillator TEM_{oo} mode is truncated at the e^{-4} point before the YAG preamplifiers and is then retruncated at the first zero of the Airy pattern in the far field of the first aperture. This procedure is used rather than an aperture with radially graduated transmission for several reasons:

- There does not appear to be any significant penalty. The spatial noise generated by the second truncation appears to be weaker than that generated by index inhomogeneities in the laser components; the damage patterns which accumulate over 500-1000 shots do not appear to be caused by the self-focusing of Fresnel fringes but are rather randomly distributed with the highest density of filaments in the center of the rod where the intensity is highest.

- This type of truncation aperture is easy to align.

- When radially graduated transmission apertures become commercially available it will be worthwhile to install a soft aperture in our system; until that point it seems dangerous to make system operation depend on a component for which spares may not be readily available.

The rod amplifiers have a strong radial variation of gain coefficient which results in an enhancement of the wings of the pulse as it diverges through them. Additionally, the 25 mm aperture Pockels cell isolator has a higher transmission at the edge than at the center. The approximately Gaussian character of the input profile is modified by these effects such that the beam profile out of the 45 mm amplifier most closely fits a shape function

$$F(r) = F(o) \exp - [(r/r_o)^5] .$$

Figure 3 shows the results of measurements on the beam profile together with the best fits obtained for various shape functions. As was noted in the last LLL Semi-Annual Report this function has about the fastest radial roll off which can be tolerated without severe spatial "ringing" on further amplification [1] due to the nonlinear index of refraction. At the output of the disc amplifier this profile is flattened more but does not have

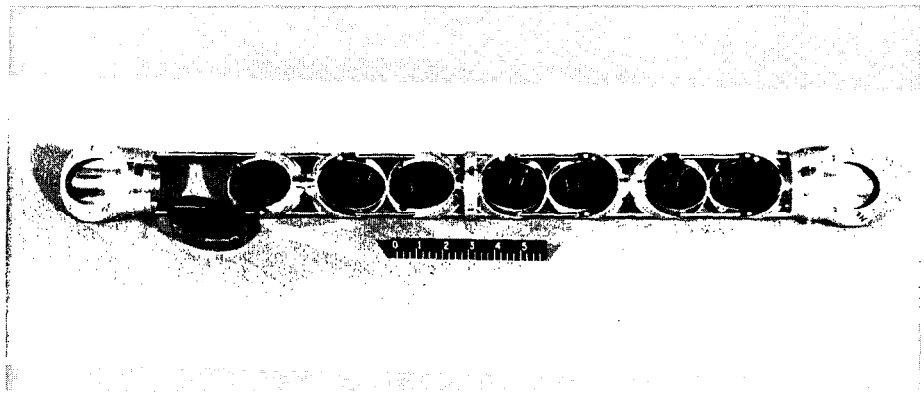

Fig. 2a — 44 mm aperture disc laser structure which was retrofitted into the CGE 64 mm laser head

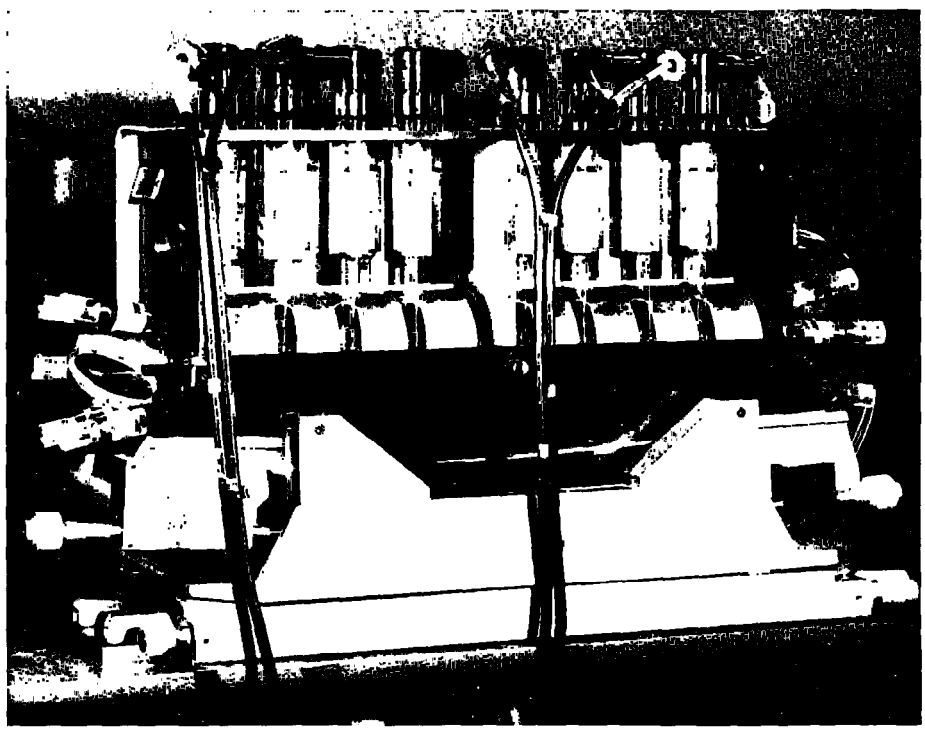

Fig. 2b — View of CGE V64A8 amplifier head with disc laser assembly installed. The assembly is sealed and has achieved a gain of 7%/cm.

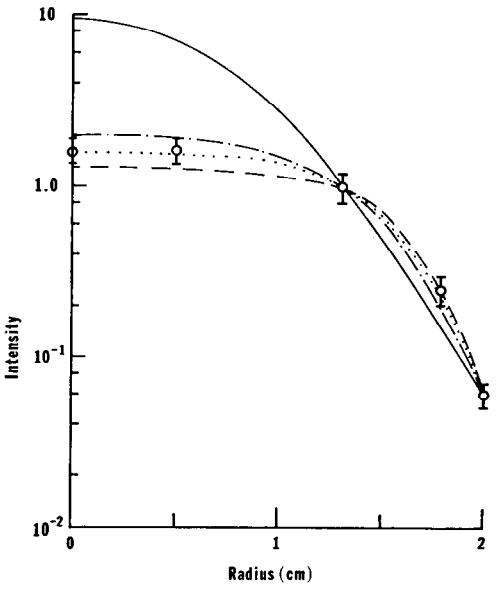

Fig. 3 — Measured beam profile out of the 45 mm rod amplifier at 7 joules in a 250 psec pulse. Fits are shown for various shape functions $F = F(o)\exp -[r/r_o]^n$ for n — 2(-); 4(---); 5(····); 6(-·-).

to propagate through any significant path of high n_2 material before the target (2 windows, 1 beam splitter, 1 lens) so that good energy extraction is obtained without beam breakup.

The wavefront shape is reasonable. Through the 45 mm rod the beam is a spherical wave to a very good approximation and can be collimated to a parallel wavefront with less than $\lambda/2$ departure from perfection. Figure 4 shows a shearing interferogram obtained at this point.

The disc amplifier and stacked plate polarizer introduce slight astigmatism into the beam because of cumulative polishing errors. At present the astigmatism limits the best focal spot with the F/14 lens to ~100 μm and ~30 μm with the F/1.9 aspheric lenses. Efforts are underway to reduce or eliminate this astigmatism by several means: the Fecker Division of Owens—Illinois has repolished laser discs to have a better surface finish with a more random residual than was shown in the initial discs; the new amplifier has a smaller number of discs (6 vs. 11) operating at a higher gain and should show less distortion; for 100 psec or shorter operation the stacked plate polarizer can be replaced by available dielectric polarizers without damage problems; and a small residual astigmatism can be compensated by tilting the focusing lens.

Dynamic effects have been examined to determine their effect on focusing on target. The major effect noted was a dynamic shift of focus due to the rod amplifiers. At typical operating levels these were determined, by shearing interferometry, to be equivalent to long focal length diverging lenses. The 23 and 32 mm amplifiers appeared to be ~16 meter lenses while the 45 mm amplifier appeared to be equivalent to a 35 meter lens. Also, the Pockels cell was equivalent to a 15 meter divergent lens. Thus it is necessary to carefully collimate the laser and change the position of the collimating lens if the pump energy is changed.

Fig. 4 — Shearing interferogram of the laser wavefront out of the system with a 20 J, 250 psec pulse

No nonlinear shift of focus was noted with well behaved beams (although the dynamic testing of collimation would also result in setting for the best compensation of the nonlinear shift). Nonlinear effects were noticeable when the disc amplifier was operated with severely degraded disc surfaces. In this case less than 50% of the energy reached the target lens and the beam would not focus to less than 200-300 μm spots with the F/14 lens.

C. LASER OPERATION ON TARGETS

In FY-74 the NRL glass laser system was used for a wide variety of experiments in support of both the AEC and DNA interaction programs. Additionally, the laser system was run for a number of laser experiments and a number of shots were consumed by trouble shooting and realignment following changes in pulsewidth. Table 1 gives a month by month summary of the number of shots and the pulsewidth (full width, half maximum). The chronological distribution of pulsewidth reflects the early receipt of DNA funds and the considerably later receipt of AEC funds. Median energies on targets at the different pulse widths were:

900 psec — 50 joules
250 psec — 20 joules
40 psec — 7 joules.

Table 1
Laser Operation Summary (FY-74)

Month/ Type	All Purposes	Target Experiments			Laser Physics Experiments	Alignment and Maint.
		40 psec	250 psec	900 psec		
July[1]	108	—	—	12	84	12
August	331			118	120	93
September	103	—	—	90	—	13
October	322	—	—	312	—	10
November	135	—	100	32	—	3
December	217	59	148	—	—	10
January	259	—	—	212	—	47
February	205	—	—	187	—	18
March[2]	116	—	—	—	58	58
April	165	139	—	—	—	26
May[3]	332	—	77	—	177	78
June[3]	300	128	38	—	—	134
Total	2583	326	363	963	439	502

Note: 1. A/C system failure.
2. New master control system installed and debugged.
3. Construction of adjacent building (vibration plus A/C mod).

The most intense shots were about twice these values. The intensities out of the laser were 30-40% higher with the pulse diagnostics and transmission losses accounting for the balance. The medium energies achieved in FY-74 are about twice those for FY-73 and reflect the degree of success achieved toward the program goal of increasing system output without sacrificing reliability.

There were several planned (as well as unplanned) interruptions with the shooting schedule as noted in the Table but, by and large, the laser operated reliably enough that it was not the sole pacing item. The fairly low totals in August and September are tracible to the nature of the experiments in progress. The target chamber vacuum had to be broken and x-ray films changed between shots; in October a multiple film holder was installed and calorimeter measurements were undertaken and the number of shots on target tripled.

With the evolutionary modifications planned for FY-75 (sealed ILC disc laser in routine use and high gain 64 mm rod amplifier or 44 mm disc amplifier) it appears reasonable to plan for the same number of shots on target at median energies on target twice those achieved this year, i.e.:

15-20 J in 40-50 psec pulses
30-50 J in 100 psec pulses
100-150 J in 250 psec pulses.

There are at present no specific plans for experiments at longer pulse duration, but at a nominal nanosecond (900 psec) the system should be capable of routinely irradiating targets with more than 200 joules.

Experience with component damage in the past year has been relatively benign. The one exception has been the prototype NRL disc amplifier, in which disc surface damage has been a problem. Careful filtration of the N_2 purge gas and careful assembly has reduced, but not eliminated, the damage due to dust or foreign matter settling on disc surfaces and being exploded by the flashlamps.* ZAP calculations performed at LLL on the cerium absorption of pump light in ED-2 [2] laser glass make it appear plausible that the surface of the discs are highly strained and that any cerium oxide polishing compound imbedded in the surfaces can cause localized failures. A set of cerium doped fused silica flashlamps is being procured to reduce the ultraviolet loading on the discs.

NRL experience with Pyrex shatter shields in the 44 mm disc amplifier was similar to that noted by LLL.[3] With careful annealing and cleaning there were no problems for 50-100 shots but, as the flashlamps damaged the outside surface the inner surface began to ablate material; therefore fused silica tubing was substituted. There appeared to be some long term advantage in mounting the discs vertically to reduce the settling of dust and dirt on the disc surfaces. The ILC amplifier will be installed in this configuration.

The effect of disc surface damage on laser performance has been less dramatic than might be anticipated. Typically, for the first hundred shots the beam coherence was quite reasonable. Over the next 400-500 shots there was a gradual deterioration in the level at which a high quality beam could be generated. At the end of this period, the output level for a beam with a reasonable wavefront is decreased by a factor of 2-2.5 and the discs must be repolished to regain the initial output levels. This relatively benign situation is tracible to the abrupt staging of the amplifier (high gain per unit length) which only allows a short path length for buildup of small scale self focusing as well as the relatively long average air path between discs (13 cm). The new ILC amplifier should perform even more respectably because the gain is higher, the path length is shorter and more advanced sealing techniques are employed.

Rod amplifier damage rates have not been a serious problem ($\sim$ 1 final rod per 500 shots) and the index matching liquids should improve the situation since the 40% higher gain coefficient of the final amplifier will allow operation with a reduced input. Indications to date are that the rate is increased but at this point the degree of improvement is not available. Earlier experience in damage vs intensity would lead to an expected improvement greater than a factor of two. Replacement of other components is required at a rate of once a year or less and can be as well correlated with operator error as with the statistical damage probabilities for the components.

REFERENCES

1. LLL Laser Fusion Semi-Annual Report, UCRL-50021-73-2, p. 135.
2. Ibid, p. 40.
3. Ibid, p. 13.

*Additionally, flashlamp induced damage in the surfaces was noted.

II. LASER RESEARCH AND DEVELOPMENT

During the past year two research efforts have achieved significant progress and have demonstrated the potential for further advances in the state of the art of generating high intensity pulses from solid state lasers. These efforts are concerned with parasitic oscillations and de-focusing in cesium vapor.

Parasitic oscillation has been demonstrated to limit the achievable gain in laser rod amplifiers to approximately half of what is expected with optimized optical pumping. In the past year we have found liquid solutions which suppress this parasitic depletion in rods while not absorbing flashlamp pump light. Thus it now appears possible to achieve $\alpha D \sim 0.65\text{-}0.70$ with these solutions whereas $\alpha D \sim 0.35$ was the highest gain previously attained. The result is a potential factor of 3 to 4 increase in the safe output intensity which can be generated by a rod system; this is sufficient to allow the use of economical and simpler rod amplifiers up through a 6-7 cm aperture rather than much more expensive and complex disc amplifiers. For larger apertures, surface area to volume ratio constraints still demand disc amplifiers, but it now appears that a cheap, simple and reliable front end for a large system is practical.

The major obstacle to the successful realization of very high peak power lasers has proven to be self-focusing of the laser beam at the high intensities necessary for efficient operation with subnanosecond pulses. Research has been underway at NRL for some time on ways to ease this restriction and a recent accomplishment offers the hope of minimizing or eliminating this effect. Self-defocusing was demonstrated in cesium vapor at 1.064 μm and was of sufficient magnitude to offer the possibility of correcting nonlinear wavefront distortion (due to whole beam self-focusing) and self phase modulation in very high intensity laser beams. This effect will allow separate correction of linear and nonlinear wavefront distortion in systems for laser fusion experiments; also allows fundamental checks on self-focusing theory; and may be very useful in satisfying longer-term needs for shaped, laser pulses.

These efforts are described in more detail in Sections B and C respectively. In addition results are presented in Section A, on the new NRL-ILC disc amplifier which is 20% more efficient than the NRL prototype (1971). Finally an evaluation of the potential of pulse compression and multiple pulse techniques to improve the overall efficiency and/or energy output of lasers for fusion applications appears in Section D, and some considerations of safe output levels from solid state lasers are presented in Section E.

A. NRL-ILC DISC AMPLIFIER DEVELOPMENT

As reported last year, the original NRL prototype disc amplifier had a satisfactory high gain/unit length but also demonstrated several problems in routine operation which were severe enough to warrant a redesign of the equipment to attain more reliable operation while retaining the high gain shown by the prototype:

(a) the open structure allowed unacceptably high rates of surface degradation because of airborne dirt and dust;

(b) the magnetic forces between adjacent lamps caused unacceptably high rates of lamp breakage above 80% of bank energy. There were also non-negligible ground currents present which caused sputtering of metal from sharp edges in the laser head and consequently surface degradation of the discs;

(c) the gold plating on the aluminum disc holders tended to flake off causing degradation problems.

The program chosen to achieve this goal consisted of several tasks performed both at NRL and under contract at ILC, Inc., Sunnyvale, California.

The ILC contract called for first testing representative disc laser flashlamps to ensure that the explosion and lifetime characteristics of large xenon flashlamps scaled from the earlier results on smaller lamps; then evaluation of the magnetic forces in the prototype laser head; the design of a new laser head geometry, incorporating the results learned from the first increments of the program, and finally, testing of a new lamp module to ensure adequate life. The conclusions of this contract were that the explosion and lifetime characteristics did scale, that magnetic forces were a serious problem in the prototype but could be minimized by reversing currents in adjacent lamps, and that a new lamp module was tested for 500 shots at full power with no failures.

At the same time, testing was underway at NRL on the prototype to determine whether polished aluminum disc holders would offer advantages over the original gold plated aluminum holders. This was found to be the case. Also the N_2 purge supply was filtered and this reduced the surface damage rate.

At this point a complete disc laser head was designed in collaboration between NRL and ILC, was fabricated by ILC and was delivered to NRL in October 1973. The number of flashlamps received was not sufficient to begin initial testing at NRL until late November 1973.

During these initial tests and subsequent tests in April 1974, when more lamps were delivered, several problems were encountered which had not occurred in the testing of the lamp module.

(1) In the initial lamp testing the flashlamp module case was ungrounded; in the initial disc-laser testing the case was grounded for personnel safety. Several of the new lamps were delivered with the tip off at the anode end rather than the (specified) cathode end. This is not apparent on a visual inspection because the end region of the lamp is potted. During testing the high voltage apparently arced through the envelope in this region to the case and caused massive destruction in the head.

A change has been made in the grounding system to prevent a recurrence of this problem. The head was floated off ground by a 1 megohm resistor. This still is adequate for personnel safety since the case will be at ground before anyone can reach the head from the control room after a shot; it will however limit current flow after a fault to a value low enough that the spark gap switch on the module will shut off. In lamp testing with this floating case configuration there has been no triggering problem over the expected working range of the device (15-20 kV).

(2) An autopsy on failed lamps revealed deviations in the end system as constructed from that specified and tested in the prototype. Strong representations have been made to the manufacturer that this is unacceptable, and it is hoped that this production problem will be resolved in the very near future. In the interim, all new lamps are being subjected to twice the usual number of acceptance testing shots in the high voltage (anode — 20 kV, cathode — 10 kV) and low voltage (anode — 10 kV, cathode — 0 kv) positions in the two lamp circuit. A careful investigation was also made to determine whether the lamp mounting in the laser head stressed the lamp envelopes and this did not appear to be a factor.

In the limited active testing which has been accomplished to date, the new amplifier geometry has been found to be significantly more efficient than the original pump geometry. Figure 1 shows several views of the equipment and Fig. 2 shows a comparison of the new and old disc amplifiers. The ~20% increase in efficiency is in reasonable agreement with ZAP predictions of the results expected by removing internal flashlamp supports and by extending the arc length by 10% to operate with a lower peak current density.

The sealing of the device has been substantially modified from the original design to improve the isolation from room air; the option has been retained to run with or without a shatter shield but the shatter shield is no longer a necessary part of the sealing system.

Present plans are to incorporate the amplifier into the laser system in late August 1974 and to retire the prototype. Several refinements will be tested over the next year and retained if they offer significant advantages.

- ED-8 (originally ED-H) laser discs are on order from Owens-Illinois. According to the testing at LLL [1] these should raise the gain coefficient to 11-12%/cm.

- A set of flashlamps with cesium-doped fused silica envelopes is on order from ILC. These may reduce or eliminate the surface damage problem.

- A crenelated reflector retrofit is being designed because the LLL results would indicate that in combination with the ED-8 discs gain coefficients of 14-15%/cm may be attained with the present capacitor banks. This implies an overall improvement of 66%-80% over the NRL prototype.

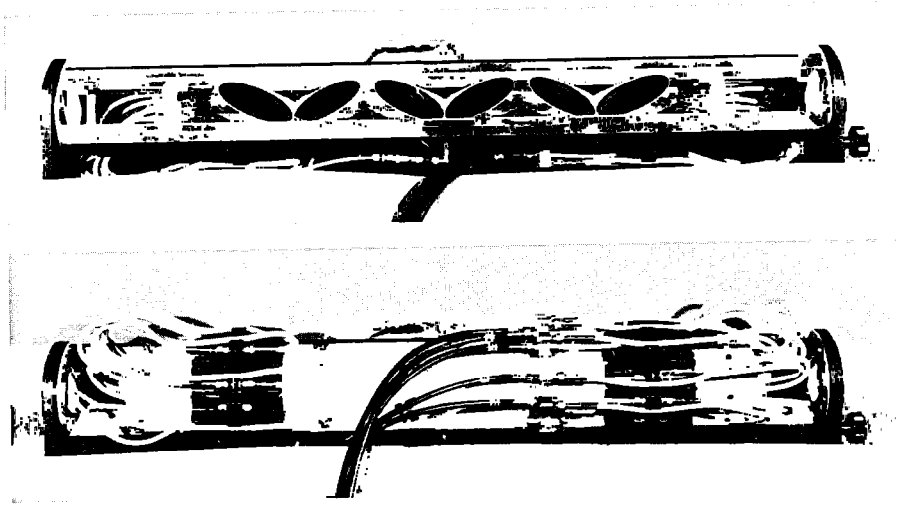

Fig. 1 — NRL-ILC disc amplifier with top reflector shell removed (top) and in place (bottom). The device can be rotated about its centerline for any desired orientation. The fixtures for sealing the beam from the atmosphere are not shown.

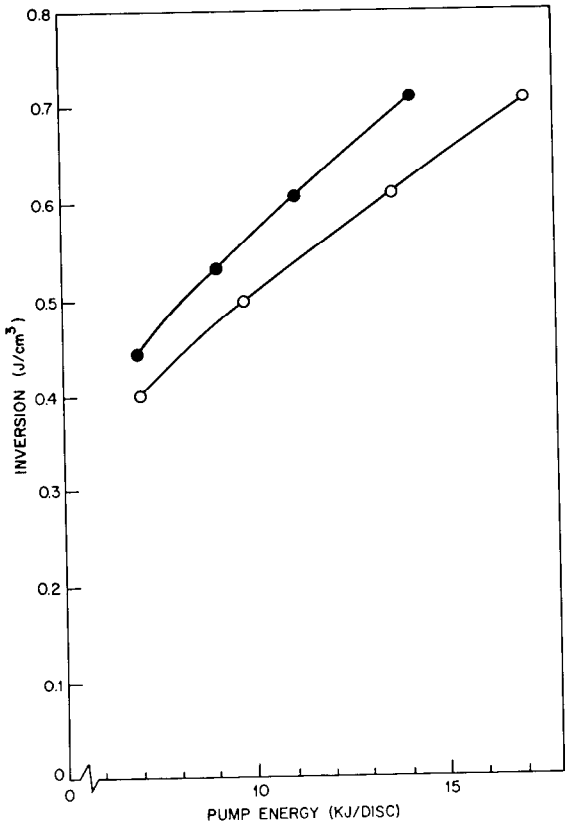

Fig. 2 — Energy storage vs pump energy for the new disc amplifier (●) and the prototype (○)

B. PARASITIC SUPPRESSION IN LASER ROD AMPLIFIERS

Introduction

The generation of intense subnanosecond laser pulses is required for laser fusion and related applications. Total energies in the kilojoule range and subnanosecond pulse require laser systems capable of operating routinely at intensities above 10^{10} W/cm^2. For neodymium glass laser systems nonlinear effects severely impact the ability to generate the necessary peak powers with high system reliability and efficiency. The breakup of the laser beam into filamentary regions with consequent damage to laser components has been studied extensively in recent years because this represents the major limitation for high peak power laser design. Marberger has pointed out that the dominant effect is not beam collapse (self focusing of the entire beam) but the self focusing of intensity fluctuations on the beam; the latter effect can have a much lower threshold than that for whole beam self-focusing [2]. Suydam has extended this analysis to laser amplifiers and finds that the gain coefficient for the growth of intensity fluctuations at the most unstable ripple frequency will be ~0.73 of that given by Marberger's analysis for passive propagation because the intensity varies in the amplifier [3]. More importantly, he found that the safe operating level will vary directly as the gain coefficient α (for amplifiers where saturation is not present). Experiments at NRL and LLL have yielded data which are in reasonable agreement with these results.

Apodization techniques have resulted in improved laser performances by minimizing the spatial frequency "noise" (ripple) on the pulse but these cannot totally eliminate the problem since index inhomogeneities will always be present to some degree and will constitute a spatial noise source [4,5,6]. It is more appropriate to attempt to suppress beam breakup by increasing the gain coefficient per unit length because this will tradeoff directly with safe intensity.

Disc amplifiers offer distinct advantages over rod amplifiers at large aperture diameters, because there is no surface area to volume ratio constraint on the optical pumping [7]. Parasitic oscillation problems have been extensively investigated and adequate solutions appear to be in hand for practical systems [7,8,9,10]. On the other hand, the many surfaces in a disc amplifier present a maintenance problem and some indications of flashlamp induced damage to disc surfaces have been observed at NRL.

However, rod amplifiers also offer a number of significant advantages where they can be used. Relative to discs, there is no surface problem, the pumping efficiency is much higher and it is a much cheaper geometry to construct. There have, however, been reports in the literature of transient losses under very hard pumping [11,12], as well as results showing a very fast roll off in the gain coefficient as the pump energy is increased [13]. Because of the possibly large benefit in high gain, large aperture rods over moderate aperture disc amplifiers we decided to investigate the reasons for the reported behavior of rod amplifiers.

The CGE rod amplifiers provide a convenient test vehicle for this investigation because all the flashlamp pumping modules are identical and successive amplifiers have twice the beam area while the radius-neodymium doping product is held constant. This allows

intercomparison of optical pumping efficiencies as well as giving different radial and axial gain aspect ratios (αD vs αL). A further experiment was to retrofit the 64 mm laser head with a 44 mm aperture disc laser structure. This allowed a direct measure of the variation of gain with pump energy in a case where parasitics were stabilized and also allowed a direct intercomparison of the relative coupling efficiency to disc and rod structures. It was found that, contrary to the published result, there was no fast roll off in the gain coefficient of the rod but rather that the coefficient increased as was expected from earlier results from the ZAP optical pumping code [10,11]. It was further found that the pump geometry coupled three times more efficiently to the 64 mm rod than to the disc structure [14].

The disc laser results allowed a prediction of the relative gain coefficient vs. pump energy for the 45, 32 and 23 mm amplifier rods. All three amplifiers were found to depart from the predicted values above $\alpha D = 0.19$. This factor strongly argued against a flashlamp induced loss coefficient as the cause of the rollover. The gain dependence indicated that it was a parasitic oscillation dependence and the fact that αD and not αL was the relevant parameter indicated that it was a radial parasitic rather than a longitudinal parasitic mode.

The pump geometry for the three CGE amplifiers offers several possible parasitic paths. One radial mode, has a ray path in which the ray bounces around the rod at the critical angle. For the indices of refraction of ED-2 and water this ray can only run in the outer periphery of the amplifier ($R_m > (\sqrt{3/2})R$); however scattering of some of the energy off the roughened sidewall into the center of the rod would deplete the gain. A second radial mode consists of light which is reflected at the critical angle from the interface between the water jacket and air. There are two analogous longitudinal modes.

Suppression of the Lowest Order Parasitic Mode

The approach attempted to suppress the lowest order parasitic mode was to dope the water with samarium salts to increase the index of refraction. The high 1.06 μm absorption of the solutions employed would suppress modes involving long parasitic ray paths in the water jacket.

A threshold condition for the radial mode internal to the rod can be calculated by noting that the mode corresponds to m sidewall bounces at the critical angle per transit with some scattering loss at each bounce, hence

$$S\alpha_T = m \ln R. \tag{1}$$

Where S is the path around the rod ($\sim \pi D$) and α_T is the gain value where the mode exceeds threshold (the gain at the periphery is 1.2 the central gain in these amplifiers). We can also calculate the number of bounces as a function of index mismatch as

$$m = \left[1 + \frac{180}{90 - \arcsin(1 - \epsilon)}\right] \tag{2}$$

where $\epsilon = \Delta n/no$.

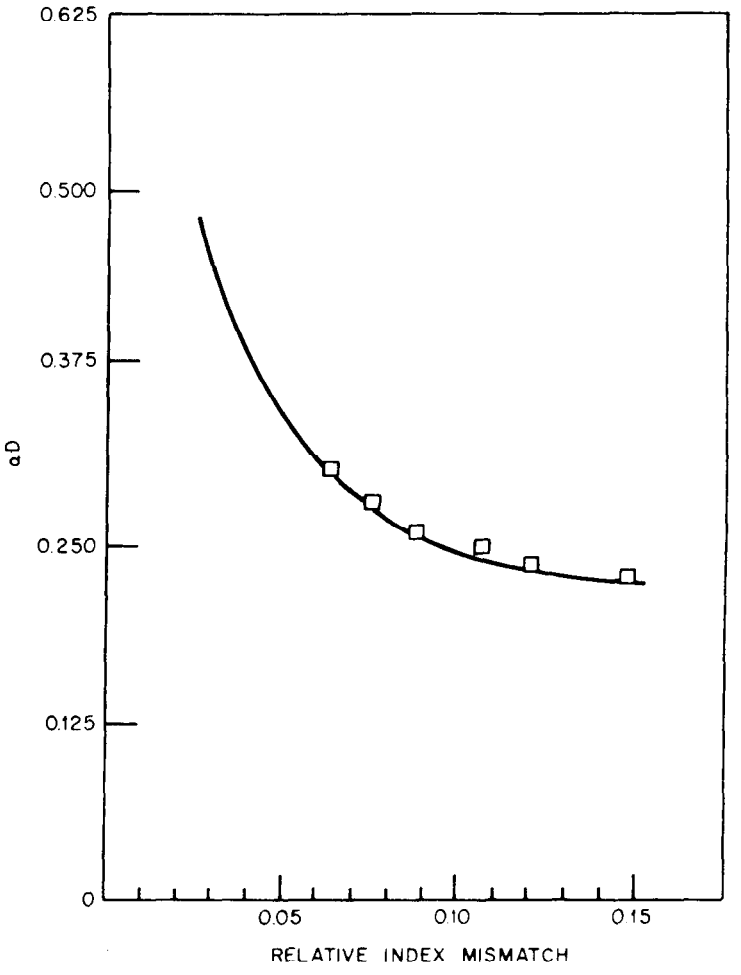

Fig. 3 — Threshold for radial mode. The data points are experimental, the curve is calculated from Eqs. (1) and (2).

For water in the jacket, Eqs. (1) and (2) and the experimental results gave R = 91% which implies R_s = 9%. The samarium solutions were then used to raise the index to n = 1.46 in several steps. The pumping efficiency was not affected by the samarium solution. Figure 3 shows the variation in threshold vs. index mismatch. The fit to the calculation is quite good and implies that it is indeed this mode which first exceeds threshold. Figure 4 shows the improvement in the 45 mm amplifier. Further, it can be inferred that with a solution with an index of 1.50 the CGE amplifiers would be stabilized ($\alpha D \leqslant 0.37$).

Results with High Index Solutions

The index of the samarium solutions could not be increased above n = 1.46 before the samarium began to precipitate out at 20°C. Therefore, solutions of zinc chloride and zinc bromide were investigated [15]. Figure 5 shows the index of refraction vs.

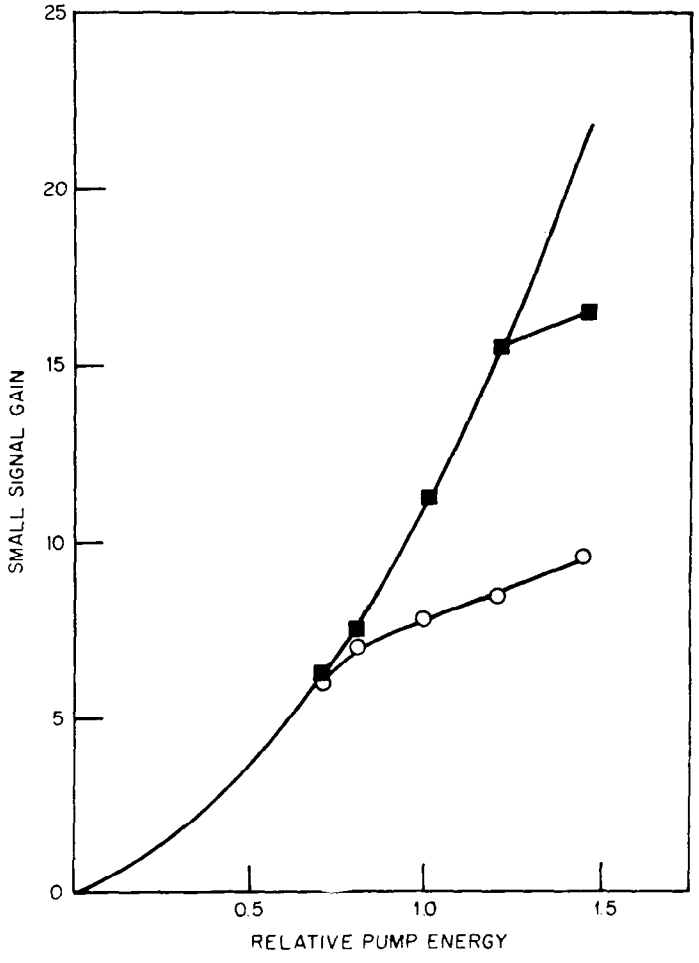

Fig. 4 — Gain vs pump energy for V45A4 amplifier with water (○) and with a samarium chloride solution with an index of 1.46 (■)

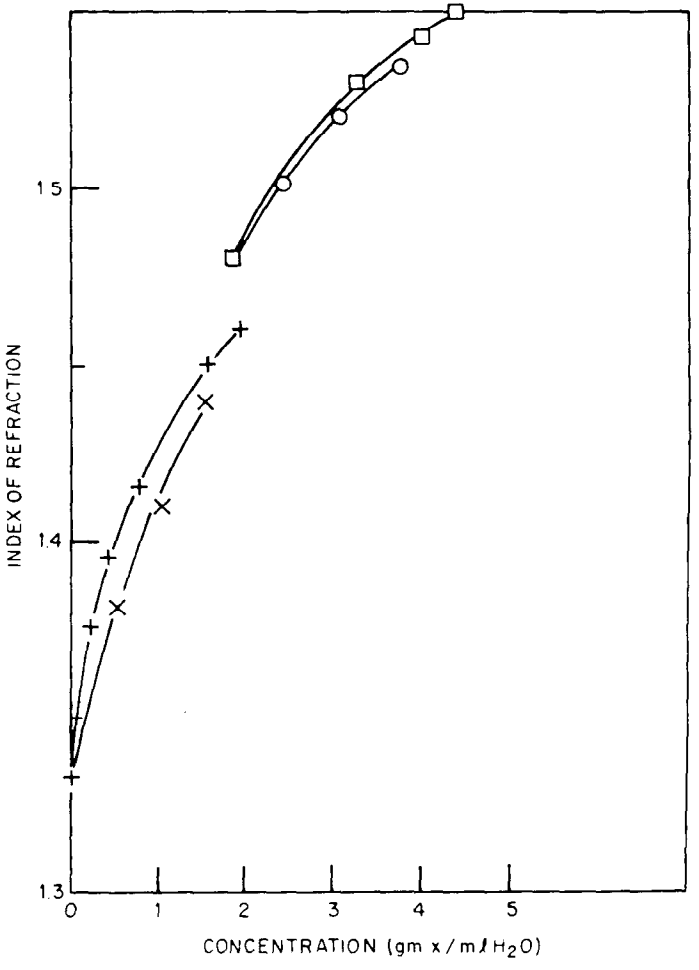

Fig. 5 — Index of refraction vs concentration for solutions used. X — samarium nitrate; + — samarium chloride; ○ — zinc chloride; □ — zinc bromate.

concentration for both the zinc and samarium solutions. $ZnCl_2$ solutions could be stably obtained with an index of 1.53 as determined by a minimum deviation prism technique [15,16]. Although the $ZnBr_2$ solutions had the higher indices of refraction, they were highly absorbing in the laser pump bands. The zinc chloride solutions were measured on a Cary 14 and found to be quite transparent in the neodymium pump bands. Experiments in the laser heads with zinc chloride solutions showed that optical pumping produced an undesirable chemical change. $Zn(OH)_2$, which is a white insoluble compound, was formed in a few shots. This reaction was prevented by adding 3-5% HCl to the solution.

Initially a $ZnCl_2$ solution with an index of 1.50 was tried in the 32 mm amplifier. It was found to perform almost as poorly as the same amplifier with water alone in the jacket. Some samarium chloride was added to the solution and there was a dramatic improvement. Figure 6 shows the results with the 32 mm amplifier with the various solutions.

Factor of two improvements in the gain (23% increase in α) were found with the best solutions compared to water cladding. However, it was clear that a parasitic oscillation involving paths in the water jacket was also present. The increase in gain when samarium was added to the water jacket corresponded to stabilization of the radial water jacket mode.

The only remaining possible parasitic mode corresponds to a longitudinal oscillation involving the rod faces, sidewalls and water jacket. To test for this mode, one end of the 23 mm rod was anti-reflection (AR) coated ($R \simeq 0.01$). As shown in Fig. 7, the gain curve followed the predicted curve almost all the way to peak energy. The roll off was due to the single AR coating being insufficient to avoid oscillation at the highest gains. With better AR coating(s) this mode would have been completely suppressed. The fact that the curve exceeds the predicted values is due to improved coupling between rod and lamps and indicates an area where large increases in the gain coefficient may be possible. With the solution with an index of 1.52 and anti-reflection coatings the gain coefficients of the 23 and 32 mm CGE amplifiers can be increased by 47% and 55% respectively. The gain of the 45 mm amplifier is pump-energy limited but it has been increased by 40% by use of the index matching solution.

Pumping Efficiency of CGE Rod Amplifiers

It was found that while the achieved gain coefficient α varied as R^{-1} the pumping efficiency improved a great deal for the larger amplifiers. This fact was found to have a geometrical interpretation in the coupling of pump light to the water jacket. In this geometry the water jacket should be 1.33 times the rod diameter to image the rod at the full jacket diameter. This is, in fact, not quite the case with the CGE amplifiers as is shown in Table 1. The optimum diameter is listed as D^*. D_L is the center line diameter of the helical flashlamps.

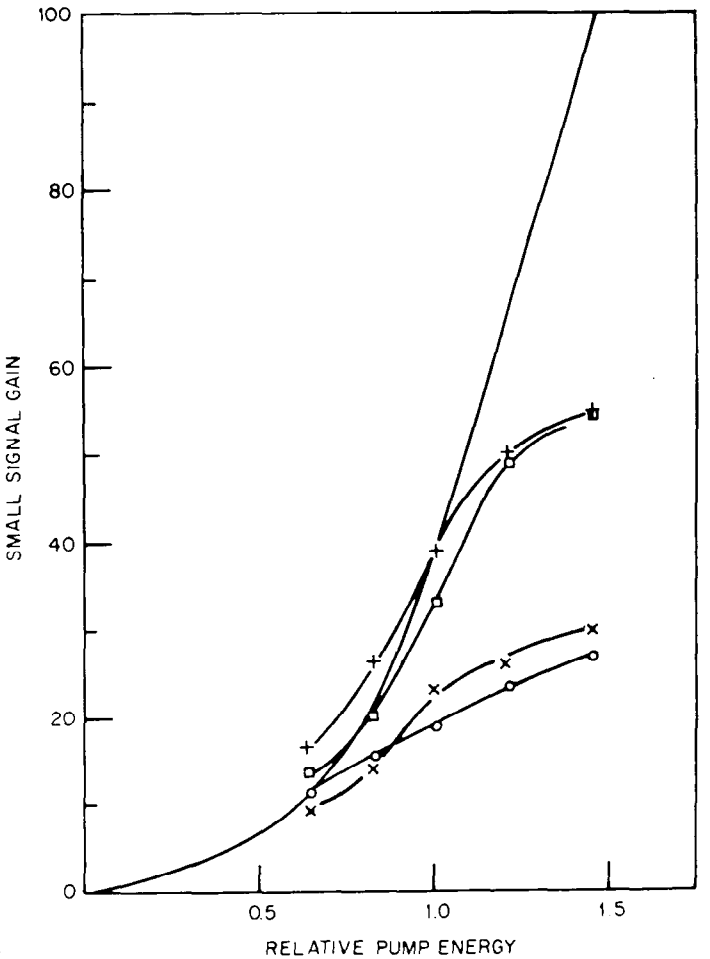

Fig. 6 — Gain vs pump energy for V32A4 amplifier with various solutions. ○ — H_2O; □ — samarium chloride (n-1.44); X — zinc chloride (n-1.50); + — zinc chloride and samarium chloride (n-1.50).

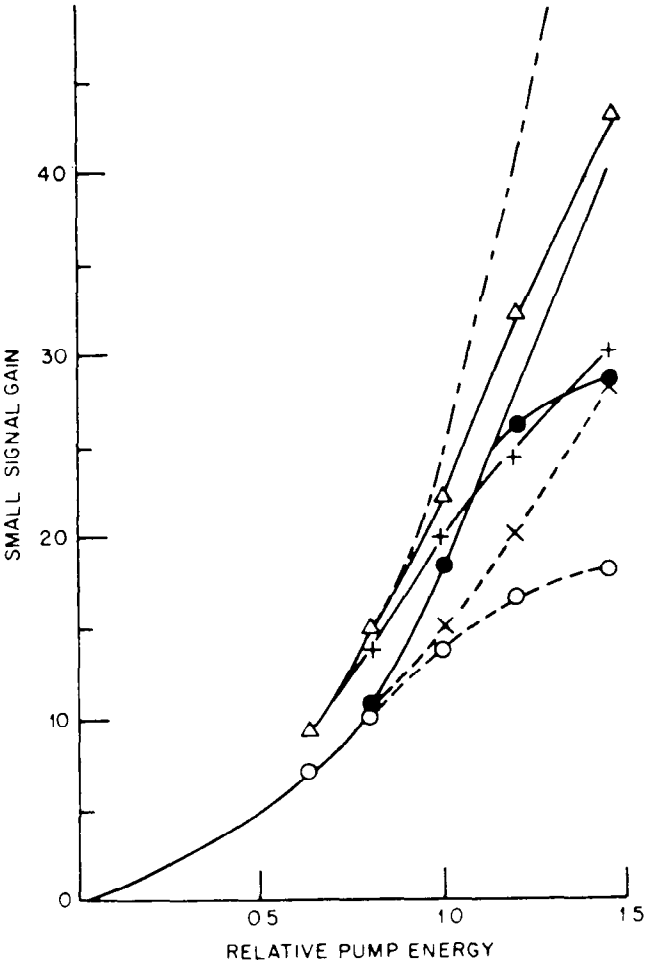

Fig. 7 — Gain vs pump energy for V23A2 amplifiers with various solutions. ○ — H_2O; ● — samarium chloride (n-1.46); + — zinc chloride and Sm chloride (n-1.52); △ — same as + but with laser rod end anti-reflection coated.

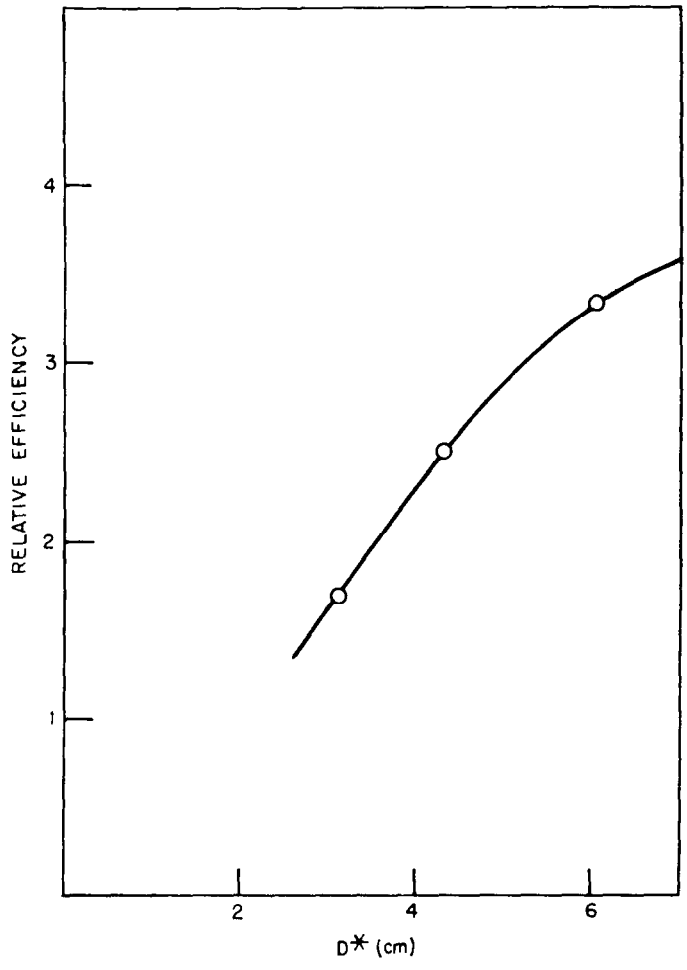

Fig. 8 — Relative pumping efficiency of 23, 32 and 45 mm laser heads. Curve is $(D^*/D_L)^2$ vs D normalized to the 23 mm data.

Table 1
Physical Parameters of CGE Amplifiers

Amplifier	Rod Dia.	Jacket Dia.	D^*	Lamp Dia. (D_L)
V23A2	23 mm	36 mm	30.6 mm	53 mm
V32A4	32 mm	46.5 mm	42.6 mm	62 mm
V45A4	45 mm	58 mm	60 mm	75 mm

A comparison of the relative transfer efficiencies of the amplifiers shows that it scales as $(D^*/D_L)^2$ (Fig. 8). With the higher index solutions D^* increases and a geometrical improvement in pumping efficiency of 23% for the 23 mm head and 19% for the 32 mm head would be expected if there were no additional absorption by the dopants in the water. With the samarium solutions, the efficiency stayed the same as samarium was added, indicating that the blue absorption of the samarium was sufficient to offset the geometrical improvement. The amount of samarium chloride in the high index zinc

Table 2
On-Axis Gain Coefficients for
Three CGE Amplifiers

Amplifier	$(\alpha\ell)_o$	$(\alpha\ell)_F$
V23A2	2.9	4.25
V32A4	3.3	5.1
V45A4	2.25	3.10

solutions was decreased to 6 gm/100 ml (which was still sufficient to stabilize the second parasitic mode) and both the 23 and 32 mm amplifiers showed ~12% increases in pumping efficiency. This indicates that there was an 8-10% loss due to the solution which was more than counter-balanced by improvements in the geometrical coupling. Table 2 lists the initial and final results for the on-axis gain coefficient for the three CGE amplifiers.

With helical pumping in the CGE heads and parasitic suppression, values of $\alpha D \sim$ 0.36-0.38 can be attained. This does not represent the ultimate which can be achieved. With a zinc solution with an index of 1.53; an $\alpha D = 0.6$ could be attained without parasitic oscillation problems.

With close coupled linear flashlamp arrays, values of αD in this range can be attained. Use of a pump geometry similar to the linearly pumped NRL disc amplifier would allow pumping to a value of $0.65 < \alpha D < 0.7$. The results achieved at Rochester on a 9 cm amplifier are consistent with a pump limited $\alpha D \leqslant 0.7$ if it is noted that the water jacket parasitic is evident in their data beginning at $\alpha D \sim 0.19$ (Fig. 9). With state of the art pumping geometries energy storage efficiencies of $\simeq 2\%$ (at $\alpha D = 0.6$) appear realistic.

Summary

The dominant gain limitation in glass rod amplifiers is parasitic oscillation. By use of available index matching solutions the lowest threshold mode can be stabilized for $\alpha D \leqslant$ 0.6. The next lowest threshold mode involves reflection from the rod ends and can be suppressed in any one of a number of ways, such as anti-reflection coating the rod ends.

With helically pumped CGE amplifiers it has proven possible to increase the gain coefficient by 30-50% by using solutions which are stable in the laser head. With optimized linear pumping geometries it should be possible to achieve $\alpha D = 0.6$. From small scale self focusing theory and experiments this should result in a safe output power density from 64 mm rod amplifiers which is 3 times higher than that from the standard CGE amplifier.

If disc amplifiers and rod amplifiers are equally susceptible to small scale self focusing, the tradeoff point in terms of equivalent gains (9-10%/cm) will occur at 6-7 cm aperture diameters but the approximately three-fold efficiency factor in favor of rods may make the economic tradeoff point occur at a 10-11 cm aperture. For a system with exponential gain throughout, measurements indicate a safe level of $I_o < 3 \times 10^{11} \alpha$ W/cm^2 for stable beams with less than $\lambda/2$ wavefront distortion and no beam breakup. For an amplifier

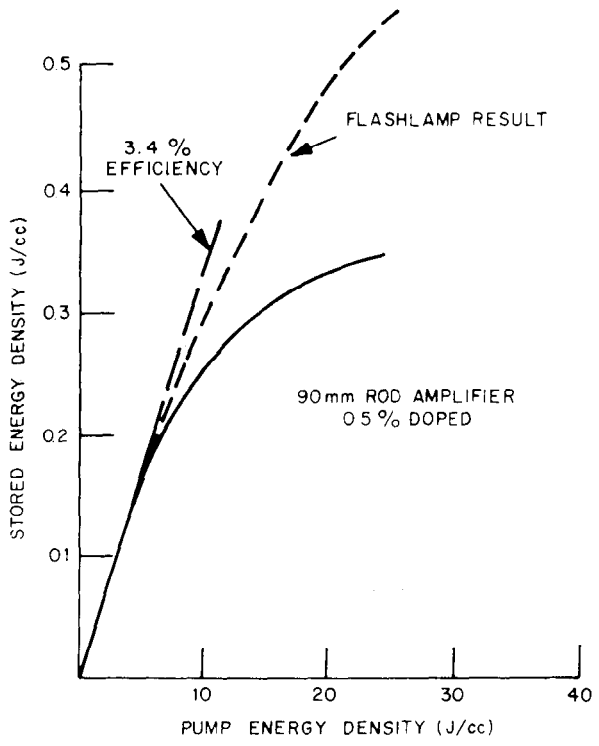

Fig. 9 — University of Rochester result for a linearly pumped 90 mm rod amplifier. — Rochester data; ---- expected result from flashlamp transfer.

with $\alpha D = 0.6$, this implies that the safe level is $1.8 \times 10^{11} D^{-1}$ W/cm^2. For nanosecond pulses and $D < 10$ cm, surface damage will be the problem and not small scale self-focusing.

No pump induced loss was found in this study. If any such loss was present it could not have been greater than 1%/cm. The authors of the earlier reports which appeared to show this effect (present company included) were probably misled by using the rod fluorescence as an energy storage diagnostic when this parasitic without an abrupt apparent threshold was present.

C. TWO-PHOTON RESONANTLY ENHANCED SELF-DEFOCUSING IN Cs VAPOR AT 1.06 μ

The useful output power which can be generated in many pulsed solid state lasers is limited by the occurrence of self-focusing and self phase modulation due to the positive, nonlinear refractive index n_2 of the amplifying material. It would appear to be possible to raise the useful output power from such lasers by compensating for the self action effects of the laser amplifier by means of complementary self action effects in a material with a negative nonlinear refractive index. Compensation is anticipated to be effective under conditions where the spatial and temporal distortions of the beam due to the positive n_2 are small.

The negative nonlinear refractive indices which have been observed previously have arisen either from two-level resonance effects which occur in restricted wavelength ranges attainable only by the use of tunable lasers [17], or from thermal effects [18] which are too slow to be of use in compensating for the self focusing of pulses in the nanosecond range or shorter. It has recently been noted that Cs vapor should exhibit a negative value of n_2 at the Nd:YAG wavelength [18]. Therefore cesium vapor might offer the potential for compensation of the self focusing and self phase modulation in high power glass lasers, and the potential was felt worthy of investigation.

The negative nonlinear refractive index of Cs at 1.06 μ arises from two distinct contributions: one from a two photon resonance, and the other from population redistributions. The energy level diagram of Cs is shown in Fig. 14. The nonlinear susceptibility at 1.06 μ is determined primarily by interactions between the $|6s>$ ($\equiv |0>$) and the $|6p>$ ($\equiv |1>$) and $|7s>$ ($\equiv |2>$) levels because of two-photon resonances respectively. In the slowly varying envelope approximation, it can be shown that the nonlinear refractive index has two distinct contributions:

$$\delta n^{NL} = n - n_o = \delta n_A + \delta n_B \tag{3}$$

where n_o is the linear refractive index.

The first term is given by

$$\delta n_A \equiv n_2^{02} \langle E^2(t) \rangle = \frac{\pi N \mu_{01}^2 \mu_{12}^2}{h^3(\omega_{20} - 2\omega)(\omega_{10} - \omega)} \left[\frac{1}{\omega_{10} - \omega} + \frac{1}{\omega - \omega_{21}} \right] \langle E^2(t) \rangle, \tag{4}$$

where $E(t)$ is the optical field of frequency $\omega = 2\pi c/\lambda$, N is the atomic density, μ_{ij} the atomic dipole matrix elements between levels $|i>$ and $|j>$ and ω_{ij} the atomic frequency splitting between $|i>$ and $|j>$. The $<>$ denotes an average over an optical cycle. In the case of 1.06 μ radiation in Cs, $\omega_{10} - \omega$, $|\omega_{20} - 2\omega| << \omega$, and we are justified in ignoring anti-resonant contributions to the above expression. In deriving this result, we have also assumed that the atomic and laser line widths are small compared to the detuning frequencies $\omega_{10} - \omega$ and $|\omega_{20} - 2\omega|$.

Expression (4) arises from a two photon interaction between the $|6s>$ and $|7s>$ levels. In solids such terms are usually positive, and are generally accepted as being responsible for the self focusing observed in materials such as laser glass [20]. For 1.06 μ radiation in Cs vapor, however, $\omega_{20} - 2\omega < 0$, while both $\omega_{10} - \omega$ and $\omega - \omega_{21} > 0$; $n_2^{02} < 0$, and one obtains self defocusing and negative frequency chirping for laser pulses. The effect is resonantly enhanced by the two photon denominator ($\omega_{20} - 2\omega \simeq -260$ cm^{-1}), and n_2^{02} can be comparable in magnitude to the n_2 of laser glass at modest vapor densities ($N \sim 10^{+17}$ cm^{-3}).

The second contribution to δn^{NL} arises from intensity-dependent population redistribution between the $|6s>$ and $|6p>$ levels, and is given by:

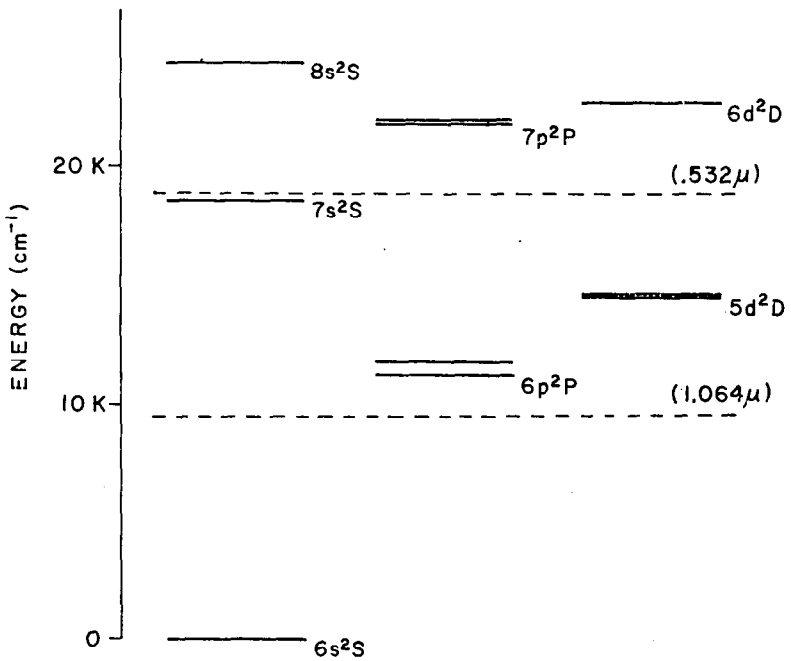

Fig. 10 — Energy level diagram of Cs. With reference to the text the $6s$ level is referred to as level $|0>$, the $6p$ levels as $|1>$ and the $7s$ level as $|2>$. The dotted lines show the position of the laser fundamental at 1.06 μ and its two photon level at 0.532 μ.

$$\delta n_B = -\frac{\pi N}{h}\left[\frac{2\mu_{01}^2}{\omega_{10}-\omega}+\frac{\mu_{12}^2}{\omega-\omega_{21}}\right]\frac{\mu_{01}^2}{2h^2}\left[\int_{-\infty}^{t}\exp-(t-t')/T_1\;\epsilon^*(t')\right.$$
$$\left.\times\int_{-\infty}^{t}dt''\exp\left[i(\omega_{10}-\omega+i/\tau)(t'-t'')\right]\epsilon(t'')+c\cdot c\cdot\right] \tag{5}$$

where ϵ is the complex amplitude of the optical field defined by $E(t) = 1/2\;\epsilon(t)\,e^{i\omega t} + c\cdot c\cdot$, T_1 is the lifetime of the $|6p>$ level, and τ is the atomic dephasing time. The actual form of δn_B depends on the magnitude of the laser pulse duration t_p relative to τ and T_1. For short pulse durations $t_p << \tau,\ T_1$,

$$\delta n_B = n_2^{01}\;\langle E^2(t)\rangle = -\frac{\pi N}{h^3(\omega_{10}-\omega)^2}\left[\frac{2\mu_{01}^4}{\omega_{10}-\omega}+\frac{\mu_{01}^2\,\mu_{12}^2}{\omega-\omega_{21}}\right]\langle E^2(t)\rangle\ . \tag{6}$$

This term is analogous to the expression derived by Grischowsky in the adiabatic following approximation of the two level system [17]. It has the same form of intensity dependence as δn_A, and is also negative, since $\omega_{10}-\omega,\ \omega-\omega_{21} > 0$.

When $\tau << t_p << T_1$, Eq. (5) reduces to

$$\delta n_B = \frac{2}{\tau} n_2^{01} \int_{-\infty}^{t} dt' \langle E^2(t') \rangle \tag{7}$$

where n_2^{01} is defined in Eq. (6). The term leads to a form of thermal self defocusing.

In order to verify these results, the self defocusing of radiation from a mode locked Nd:YAG laser in a cell of Cs vapor was studied. The input beam consisted of a single pulse with a duration of 30 psec and an energy which was varied between 0.2 and 8 mJ. The beam had a spatial profile in the form of a collimated Airy disc with a diameter D_o = 3.5 mm between minima. The Cs cell was 1 m long with an atomic density of 0.5 $\times$ 10^{+17} cm^{-3}. The temperature of the Cs reservoir was maintained at 330°C while the temperature of the cell was held at 600°C in order to reduce linear absorption from Cs dimers. The output beam profile was measured by imaging the beam emerging from the vapor cell onto an image converter camera with a minimum resolution of 6 p/mm. The change in beam size was observed as the input energy was varied over a factor 40.

Figure 11 shows typical results from three different measurements. In part A, the output beam is shown for a low power (0.2 mJ) linearly polarized input beam, with the cell filled with Cs. The beam diameter here was essentially the same as that which was observed without Cs in the cell. Part B shows the results of the same measurement when the input beam power was increased by a factor of 40 to about 8 mJ (I_{in} = 1.1 $\times$ 10^{10} W/cm^2). The beam diameter increased by a factor of about five over that observed in part A. Measurements at intermediate intensities showed that the output beam diameter increased monotonically with increasing input power, indicating that the change in beam size was actually due to self defocusing, rather than self focusing. Part C shows the result obtained when nearly circularly polarized light was used instead of linearly polarized light. With the same input energy of 8 mJ, the increase in beam diameter was only a factor of 3.7.

The expected change in beam size can be estimated by using the paraxial ray approximation [18] and the expressions for n_2 given earlier. If we approximate the Airy profile of the input beam by a Gaussian profile with an $1/e$ diameter of the intensity distribution equal to $d_o = D_o/2$, the ratio of output to input beam diameters is given by

$$\frac{D_{out}}{D_o} = \frac{d_{out}}{d_o} = \left[1 + \frac{P_o}{P_c} \left(\frac{4\ell}{k d_o^2}\right)^2\right]^{1/2} \tag{8}$$

where P_o is the input power, ℓ the cell length, $k = 2\pi/\lambda$, and $P_c = \lambda^2 c/32\pi^2 n_2$.

For the experiments described above, the high level input power is 270 MW. For a density of 0.5 $\times$ 10^{17} cm^{-3}, we find that $n_2^{02} = -0.9 \times 10^{-13}$ esu from Eq. (4) and $n_2^{01} = -0.25 \times 10^{-13}$ esu from Eq. (6). Under these experimental conditions, the atomic dephasing time is 40 psec, so Eq. (6) is not precisely valid for calculation n_2^{01}; however, it can be used to give a lower estimate of its magnitude. The nonlinear index then results mainly from the two photon resonance term, and its response is expected to

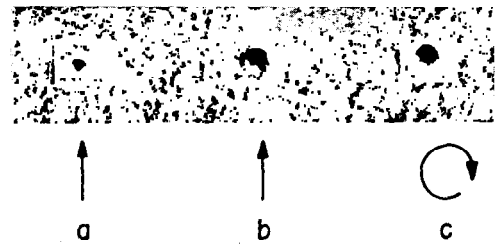

Fig. 11 — Photographs of the output beam profile after propagating through a 1 m cell of Cs vapor, (a) input beam linearly polarized at 0.2 mJ (2.8 X 10^8 W/cm^2); (b) input beam linearly polarized at 8 mJ (1.1 X 10^{10} W/cm^2); (c) input beam nearly circularly polarized at 8 mJ (1.1 X 10^{10} W/cm^2)

be instantaneous on the time scale of the laser pulse. One expects the largest effect for linearly polarized light, because both the δn_A and δn_B terms contribute to the nonlinear index, and both are negative. In this case, the expected increase in beam size given by Eq. (8) is a factor of 4.4, in fair agreement with the observed increase of a factor of five.

If circular polarization is used, the defocusing is expected to be smaller, because in this case the two photon resonance term does not contribute. The theory predicts an increase in beam size of a factor of two. The increase in beam size in Fig. 11(c) is observed to be smaller than that in Fig. 11(b) in qualitative agreement with the theory, although the observed difference is not as large as predicted. The discrepancy could be due to the use of Eq. (6) in predicting the value of δn_B, rather than the most exact expression in Eq. (5). It could also result from a deviation of the input beam from true circular polarization, possibly caused by birefringence in the sapphire cell windows. The observations are, however, in qualitative agreement with the theory.

In summary, the electronic nonlinear refractive index in Cs vapor has been shown to have two distinct contributions: one contribution arises from a two photon resonance, and the other from population changes between the ground and first excited state. For radiation at 1.06 μ, both terms are negative, and can be made conparable in magnitude to the n_2 of laser glass at modest vapor densities. Self defocusing in Cs vapor of a single pulse from a Nd:YAG mode locked laser has been observed experimentally under conditions in which the two photon resonance term makes the major contribution to the nonlinear index. The increase in beam size for linear polarization is in reasonable agreement with the theory. The increase in size of a nearly circularly polarized beam is in good qualitative agreement and fair qualitative agreement. This effort is continuing and more quantitative values will be measured. In addition an assessment of the direct impact of this technique on lasers for fusion applications will be made once the quantitative aspects are determined.

D. OPTICAL PULSE COMPRESSION

Optical pulse compression [21,22] has been proposed as a technique for increasing glass laser efficiency without the increase in peak intensity that leads to self focusing or beam distortion [23,24]. The idea is to amplify a long pulse with a variable carrier frequency (i.e. a chirp). If this propagates through a dispersive delay line beyond the final amplifier, it will be compressed in time if the delay is longer for the carrier frequency in the earlier portions of the pulse. We have studied two compression proposals based on the use of self phase modulation to generate the chirp. The NRL proposal [23] would be most suitable for generating 1-10 psec pulses, whereas the Fisher-Bischel proposal [24]. is tailored to the 100 psec regime suitable for CTR experiments.

NRL Short Pulse Proposal

In this system, a large, effectively monotonic chirp is provided by the Kerr liquid [25]. and saturable absorber combination shown in Fig. 12. A pulse from the preamplifier is propagated through a path length ℓ of CS_2, which is distributed over 5-10 well spaced cells $K_1, K_2, \ldots K_n$ in order to avoid beam breakup due to small scale self focusing [26]. For an on-axis intensity $I(t, x)$, the resulting self phase modulation (SPM) produces a chirp

$$\omega_c(t) = -(8\pi^2 n_2/n_o \lambda\, c)\, dD(t)/dt \tag{9}$$

where

$$D(t) = \int_o^{\ell} I(t, x)\, dx \tag{10}$$

is the so-called distortion parameter, and n_o and n_2 are, respectively, the linear and nonlinear refractive indices defined by $n = n_o + n_2 \langle E^2 \rangle$. The integral, of course, extends only over the CS_2 cells.

For a Gaussian pulse of FWHM width Δt, $I(t, x) = I_o(x) \exp[-(4\ell n\ 2)t^2/\Delta t^2]$, and $\omega_c(t)$ has the form shown in Fig. 13. The extremes of $\omega_c(t)$ occur at times $\pm t_m = \pm (1/8\ \ell n\ 2)^{1/2}\ \Delta t$, and the total chirp bandwidth is

$$\begin{aligned} \Delta\omega_c &= \omega_c(t_m) - \omega_c(-t_m) \\ &= 2(8\pi^2 n_2/n_o \lambda c)(8\ell n 2/e)^{1/2}\ D(0)/\Delta t. \end{aligned} \tag{11}$$

For $\lambda = 1.06\ \mu$, $\Delta\omega_c \Delta t = 5.7\ D(0)$ is expressed in units of GW/cm.

If the amplified version of $I(t, x)$ were propagated through a grating pair [22] or other suitable dispersive delay line, the center portion $|t| < t_m$ could be optimally compressed; however, the falloff of $\omega_c(t)$ for $|t| > t_m$ would result in long leading and trailing edges on the output pulse [25]. An increase in the dispersion would not solve this problem, but would result only in the creation of large humps on the leading and trailing edges. All such effects are highly undesirable for most short-pulse laser-plasma experiments. One could eliminate them by a saturable absorber located beyond the grating pair, but this would also attenuate the center portion, especially if the output pulse width Δt_1 is comparable to the relaxation time of the absorber dye. A better solution is to place the saturable absorber SA as shown in Fig. 12. With this arrangement, the noncompressible outer portions of the pulse are eliminated, as shown in Fig. 13, prior to the main amplifiers. The net energy attenuation is about 8 dB, but the loss can be easily recouped at this low signal level.

The output of SA can be written as

$$I'(t) = T_o\, e^{S(t)}\, I(t), \tag{12}$$

where $I(t)$ is the input intensity, T_o is the low-signal transmission, and $S(t)$ is a saturation parameter. $S(t)$ is a solution of the equation

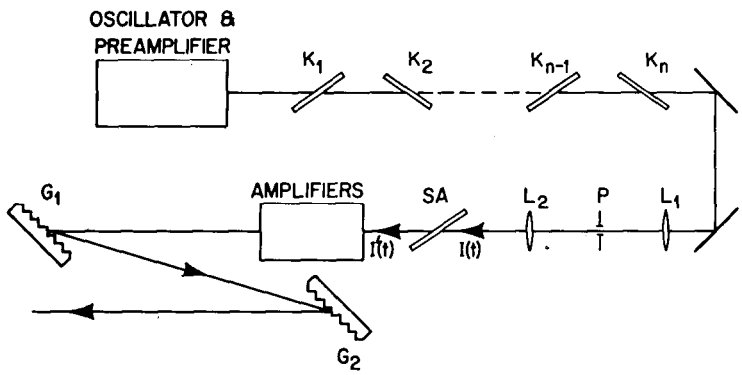

Fig. 12 — Proposed NRL optical pulse compression system

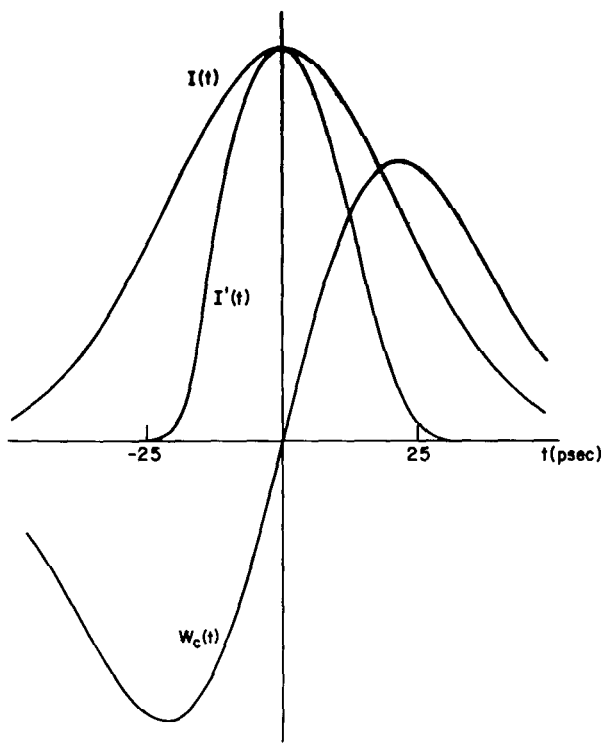

Fig. 13 — Action of the saturable absorber SA (Fig. 12) on a 50 psec chirped pulse, showing normalized input and output intensities $I(t)$ and $I'(t)$, respectively, and instantaneous chirp frequency $\omega_c(t)$. The relevant parameters are $I(0) = 1$ GW/cm^2, $I_s = 0.05$ GW/cm^2, $T_o = 10^{-6}$, and $T_1 = 6$ psec. Net energy loss is 8 dB.

$$\dot{S}(t) = [1 - T_o e^{S(t)}]\ I(t)/I_s - S(t)/T_1 \tag{13}$$

(subject to the condition $S \to 0$ as $t \to -\infty$), where I_s is the saturation intensity, and T_1 is the dye relaxation time. For Kodak 9860, $I_s \simeq 50$ MW/cm^2, and $T_1 \simeq 6$ psec.

From the saturable absorber, the pulse, of width $\Delta t' \simeq \Delta t/2$, proceeds through the main amplifiers to the compressor gratings $G_1 G_2$. Under favorable operating conditions, the additional bandwidth due to self phase modulation in the amplifiers would be small in comparison to $\Delta\omega_c$, so that $\omega_c(t)$ remains monotonically increasing in time.

The minimum attainable pulsewidth from $G_1 G_2$ is

$$\Delta t_1(\min) \simeq 4\ell n\ 2/\Delta\omega_c, \tag{14}$$

and since $\Delta t' \simeq \Delta t/2$, the maximum compression ratio (using CS_2) is

$$\Delta t'/\Delta t_1\ (\min) \simeq \Delta\omega_c \Delta t'/4\ell n 2 \simeq 1.0\ D(0). \tag{15}$$

With the lens-pinhole system of Fig. 12, we expect values of $D(0)$ up to 20 GW/cm without severe beam distortion or breakup.

Although this type of system is, in principle, applicable to any time regime, it appears to be most suitable for times $10 < \Delta t' < 50$ psec. For $\Delta t' < 10$ psec, the 6 psec relaxation time of the saturable dye significantly reduces the net transmission of SA. For $\Delta t' > 50$ psec, the required temporal dispersion (hence, the spacing) of the gratings becomes too large. The required spacing for gratings of blaze angle Θ is

$$L \simeq \frac{4\pi c^2}{5.7} \frac{\Delta t'^2}{D(0)\lambda \tan^2\Theta}. \tag{16}$$

For example, if $\Theta = 45°$, $\lambda = 1.06\ \mu$, $D(0) = 20$ GW/cm, and $\Delta t' = 50$ psec, then $L \simeq 24$ meters.

One could compress longer pulses with a multistage Gires-Tournois interferometer [27], but the large time-bandwidth product would necessitate an inordinate number of stages in order to obtain enough dispersion. For example, for $D(0) = 20$ GW/cm and $\Delta\omega_c \Delta t' = 57$, one would require about 30 stages. An additional consideration is the fact that longer pulses can be amplified to higher energies; hence, more stages of amplification are required. This results in a larger SPM contribution from the amplifier material, and the total chirp may again become triple valued.

The pulse compression experiment outlined above will be set up in the near future, and preliminary experimental results should be available by late 1974. Eventually, it will be incorporated into the short-pulse x-ray generation experiments of the NRL Interaction Physics Group.

Fisher-Bischel Proposal

In the system proposed by Fisher and Bischel [24], the nonlinear chirp is provided by the self phase modulation inherent in the amplifier glass. The chirped pulse would then be compressed in a multi-stage Gires-Tournois interferometer (GTI) at the output. Fisher and Bischel model their "amplifiers" by a single passive glass rod 2 m long, carrying a pulse of peak intensity 2 GW/cm^2; hence, $D(0)$ = 400 GW/cm. Since only the center portion of this pulse could be adequately compressed, the effective compression efficiency at the output is about 76% for a Gaussian temporal shape and a compression ratio of 8. The remainder of the output pulse would consist of the long leading and trailing edges discussed above, and some means would have to be devised to eliminate at least the leading edge without further attenuating the center portion. In a real system where amplification is present, this problem becomes even more serious on account of saturation.

The raison d'etre for pulse compression is that it allows more efficient amplification of short pulses; i.e., it allows higher energy fluxes in the amplifier stages, without the high peak intensities that would cause self focusing. At present, Nd:glass amplifiers appear to be capable of handling 100 psec pulses at fluxes of 1-2 J/cm^2 (about 30-60% saturation flux for ED-2) without pulse compression [28]. To obtain appreciably higher efficiency, one must therefore operate some of the amplifiers near or even above the saturation flux. This lowers the gain per stage, and hence requires more stages and a longer glass path than a linear system. It also tends to shift the chirp characteristic $\omega_c(t)$ backward in time, so that the minimum value of ω_c occurs near the peak output intensity, as illustrated in Fig. 18. As a result, only the trailing edge of the pulse can be effectively compressed, while the leading edge may actually be expanded slightly. The usable compression ratio is therefore limited to a value on the order of two.

Assuming a fixed input energy of 0.5 joule, we have calculated the output energies, distortion parameters, and chirp bandwidths for various combinations of the amplifier modules developed by Lawrence Livermore Laboratories (LLL) [28]. All of the combinations chosen here would give a higher efficiency than the present LLL design if longer pulsewidths were allowed. A Gaussian form $\exp[(-4\ell n2)t^2/\Delta t^2]$ has arbitrarily been chosen for the output intensity of the final amplifier in order to compare the results for each case. With these results, one can select the combinations most suitable (or least objectionable) for use with pulse compression.

The main disc amplifier chain in the initial LLL design consists of four pairs of amplifier modules A, B, C, and D of apertures 3, 10, 20, and 30 cm, respectively [28]. This particular combination will be designated by the notation 2A2B2C2D. Each module consists of an amplifier, which is made up of six discs, followed by an isolation system consisting of a Faraday rotator and polarizer. For simplicity, we assume that all losses in module M can be lumped into an isolator transmission $T_m < 1$.

Let $I_M(t)$ and $I'_M(t)$ be the respective on-axis input and output intensities of the Mth amplifier, and define the corresponding fractional energy fluxes

$$F_M(t) \equiv E^{-1} \int_{-\infty}^{t} I_M(t_o)dt_1, \qquad F'_M(t) \equiv E^{-1} \int_{-\infty}^{t} I'_M(t_1)dt_1, \tag{17}$$

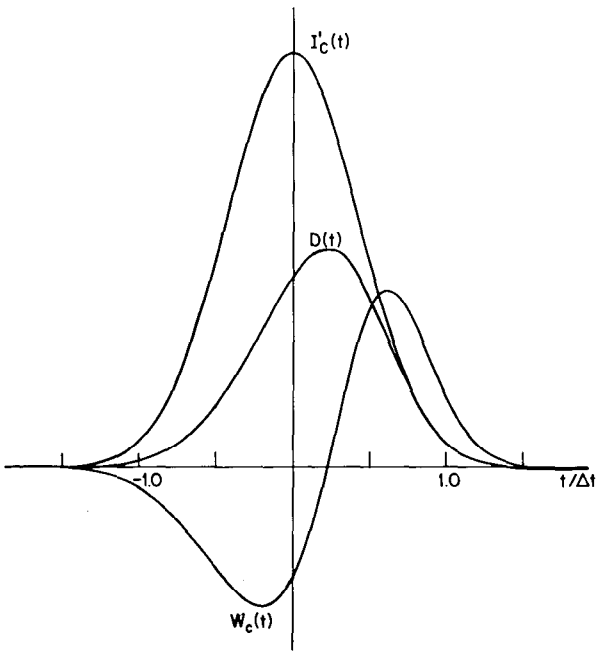

Fig. 14 — Distortion parameter $D(t)$, chirp frequency $\omega_c(t) \sim -D(t)$, and amplifier output intensity for the 4A2B3C configuration. The vertical scale is linear, but the units are arbitrary.

where $E = h\omega/2\sigma$ is the saturation flux. ($E \simeq 3.2$ J/cm^2 for ED-2 glass.) From the usual rate equation analysis [29], one obtains the relationship

$$\exp\left[F'_M(t)\right] - 1 = \left\{\exp\left[F_M(t)\right] - 1\right\} G_M, \tag{18}$$

where $G_M = \exp(\alpha_M \ell_M)$ is the small-signal gain of the Mth amplifier whose glass path length is ℓ_M. The output energy of module M is

$$0_M = \frac{\pi d_M^2}{4} n_o \frac{T_M E F'_M(\infty)}{Q_M}, \tag{19}$$

where d_M is the beam diameter, n_o is the refractive index (1.56 for ED-2), and $Q_M \geqslant 1$ is a shape factor that allows for the small decrease in beam intensity with radius for $r < d_M/2$. The fluxes in adjacent modules are related by the expression

$$F_{M+1}(t) = T_M F'_M(t)\, d_M^2/d_{M+1}^2. \tag{20}$$

In Table 3, we have listed the values of G_M, d_M, and other parameters used in the calculations.

The total distortion parameter of the amplifier system is

$$D(t) = \sum_M D_M(t) = \sum_M \int_o^{\ell_M} I_M(t, x)dx, \tag{21}$$

Table 3
Parameters of Disc Amplifier Modules

Module (M)	G_M	$\alpha_M(\text{cm}^{-1})$	$d_M(\text{cm})$	Q_M
A	3.8	0.12	2.6	1.5
B	3.7	0.078	8.1	1.5
C	2.7	0.056	18	1.5
D	2.6	0.038	26	1.5

where $I_M(t, x)$ is the on-axis intensity at a point x centimeters of glass from the input of the Mth amplifier. From an expression similar to (18), one can show that

$$D_M(t) = \frac{I'_M(t) \exp [F'_M(t)]}{\alpha_M \{\exp [F'_M(t)] - 1\}} [F'_M(t) - F_M(t)]. \tag{22}$$

The instantaneous chirp frequency is related to $D(t)$ by Eq. (9), and the chirp bandwidth is $\Delta\omega_c = \omega_c(t_{\text{MAX}}) - \omega_c(t_{\text{MIN}})$, where t_{MAX} and t_{MIN} correspond to the extremum points of $\omega_c(t)$.

In the first part of this section, it was shown that without saturation, the peak value of $D(t)$ occurs at time $t = 0$, the extremum points of $\omega_c(t)$ at $t = \pm t_M = \pm (1/8 \ln 2)^{1/2} \Delta t$, and $\Delta\omega_c$ was related to $D(0)$ by Eq. (11). Saturation distorts $D(t)$, and retards them in relation to the final amplifier output pulse; i.e., $D(t)$ now peaks at time $t = t_p > 0$. However, the relative positions of t_{MAX}, t_p and t_{MIN}, and the relationship between $\Delta\omega_c$ and $D(t_p)$ remain nearly unchanged. In all of the cases considered here, Eq. (11) with $D(0) \to D(t_p)$ remains accurate to within 3%, and the relationship

$$t_{\text{MAX}} - t_p = t_p - t_{\text{MIN}} = t_M \simeq 0.42\ \Delta t \tag{23}$$

remains accurate to within 5%. One can therefore estimate the position and size of $\omega_c(t)$ knowing only t_p and $D(t_p)$.

In Table 4, the performance of various amplifier combinations has been evaluated in comparison to that of the LLL configuration 2A2B2C2D. For 2A2B2C2D, the pulsewidth is $\Delta t_{\text{LLL}} = 100$ psec, and the peak distortion parameter is $D_{\text{LLL}} \simeq 27E/\Delta t_{\text{LLL}}$; hence, if $E = 3.2$ J/cm^2, one obtains $D_{\text{LLL}} \simeq 860$ GW/cm and $\Delta\omega_{c\text{LLL}} \Delta t_{\text{LLL}} \simeq 64$. We have listed for each combination the minimum compression ratio $\Delta t/\Delta t_{\text{LLL}}$ that would be required to satisfy the condition $D(t_p) \leqslant D_{\text{LLL}}$, assuming that the desired pulsewidth Δt_{LLL} could be obtained at the output of a compressor. Since $D(t_p) \sim 1/\Delta t$ in all cases, $\Delta t/\Delta t_{\text{LLL}}$ is identical to the ratio $D(t_p)/D_{\text{LLL}}$ that would be found if $\Delta t \to \Delta t_{\text{LLL}}$. Table 4 also lists the chirp displacement $t_p/\Delta t$, the energy from each set of modules, the estimated amplifier output per amplifier cost (relative to 2A2B2C2D), and the estimated number of Gires Tournois stages N that would be required to compress the pulse *if* its chirp were symmetric.

The energy/cost was estimated simply by assuming that the cost of each module is directly proportional to the area of its aperture. The number of Gires Tournois stages is estimated by noting that for a symmetric chirp, the dispersive time delay $\tau(\omega_c)$ will have maximum and minimum values that satisfy

Table 4
Performance and Pulse Compression Requirements
of Selected Amplifier Module Combinations

Configuration	0_A (J)	0_B (J)	0_C (J)	0_D (J)	Amplifier Energy/Cost	$\Delta t/\Delta t_{LLL}$	$t_p/\Delta t$	N
2A2B2C2D	5	48	240	1000	1	1	0.06	0
2A2B2C3D	5	48	240	1740	1.3	1.7	0.10	14
3A2B3C1D	13	102	825	1490	1.8	2.1	0.15	18
4A2B2C1D	26	170	665	1245	1.8	2.4	0.22	19
4A2B3C	26	170	1100		2.2	2.6	0.22	21
3A3B3C	13	215	1260		2.3	2.8	0.20	22
2A2B2C4D	5	48	240	2680	1.6	3.0	0.13	23
3A2B3C2D	13	102	825	2370	2.1	3.1	0.17	23
4A3B2C	26	300	1000		2.5	3.2	0.26	23
4A2B2C2D	26	170	665	2060	2.0	3.3	0.22	24
3A3B3C1D	13	215	1260	2080	2.4	3.7	0.22	25

$$\tau_{MAX} - \tau_{MIN} \simeq (t - t_{LLL})_{MAX} - (t - t_{LLL})_{MIN} \simeq (1/2\ell n2)^{1/2}(\Delta t - \Delta t_{LLL}). \quad (24)$$

Using the same operating range as Ref. 1, we obtain $\tau_{MAX} - \tau_{MIN} \simeq 1.6\ N/\Delta\omega_c$. When this is combined with Eq. (24) and the condition $\Delta\omega_c\Delta t = \Delta\omega_{cLLL}\Delta t_{LLL} \simeq 64$, the result is

$$N \simeq \frac{\Delta\omega_c\Delta t}{1.6(2\ell n2)^{1/2}}\left(1 - \frac{\Delta t}{\Delta t_{LLL}}\right) \simeq 34\left(1 - \frac{\Delta t}{\Delta t_{LLL}}\right). \quad (25)$$

Table 4 shows a significant increase in amplifier energy output/cost with increasing compression ratios up to about 2.8. In comparing these numbers, however, one must bear in mind the following two points: (a) the costs calculated here do not include the N stage Gires Tournois interferometer, (b) excepting for the 2A2B2C2D case, the output energy should be multiplied by an effective compression efficiency ϵ to account for waste due to uncompressible portions of the pulse. For the modest compression ratios and chirp displacements of interest here, $\epsilon \approx 0.84$. From these considerations and the fact that N increases with $\Delta t/\Delta t_{LLL}$, it is evident that the usable energy/total cost will be smaller and will increase somewhat more slowly than indicated by the numbers in Table 4.

The third configuration (3A2B3C1D) appears to be the closest thing to a practical choice because it offers high output energy and requires a compression ratio of only 2.1:1. It has the additional advantage that the chirp characteristic remains relatively symmetric, as seen in Fig. 15. This means that part of the pulse's leading edge may be compressed. It also suggests the possibility of increasing $\Delta t/\Delta t_{LLL}$ beyond 2.1:1 in order to reduce $D(t_p)$ below the 860 GW/cm "standard" selected here. If we can assume $\epsilon = 0.84$, then the

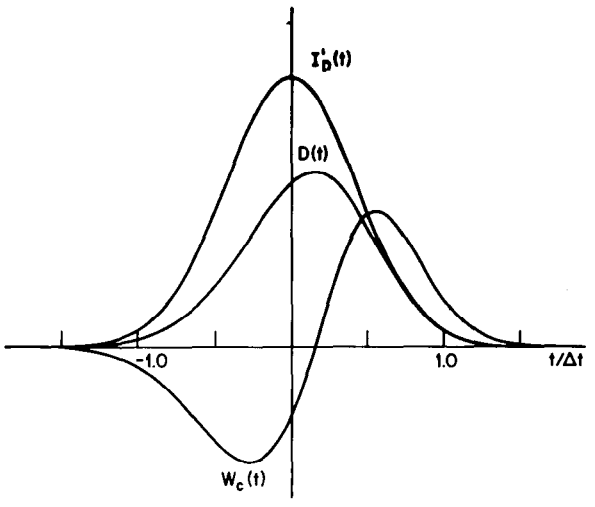

Fig. 15 — Same as Fig. 14 for 3A2B3C1D configuration

energy/amplifier cost $\simeq$ 1·5 that of 2A2B2C2D; however, when the cost of the interferometer is included, this margin of advantage may be reduced significantly.

The two combinations 4A2B3C and 3A3B3C are interesting because they eliminate the large D module. Because of the sizeable chirp asymmetry, however, it remains doubtful whether the necessary compression ratios could actually be achieved (Fig. 14). Another factor to consider is that for these combinations, the cost of the interferometer is more lifely to be an appreciable fraction of the total cost.

In a more accurate calculation, the pulse from the amplifiers would be traced through a Gires-Tournois interferometer whose operating parameters could be systematically varied to select the best output shape and width. Such a calculation would be worthwhile for the 3A2B3C1D, 4A2B3C, and 3A3B3C configurations, especially to examine the possibility of pulse shaping. It is unlikely that the other combinations requiring appreciably higher compression could actually be compressed in a real system.

Discussion

The results presented here indicate that the Fisher-Bischel proposal may offer some improvement of laser efficiency, but it is likely to be marginal. In practice, the size of this margin will depend upon the cost of the N stage interferometer. One naturally wonders whether there exist other more manageable techniques for efficiency enhancement that could provide at least as large an improvement as pulse compression. Aside from the straightforward approach of improving module gain and using glasses of lower n_2, there are two other techniques that appear promising. The first, which is discussed elsewhere in this report, would use the negative n_2 found recently in cesium vapor [30] to compensate the self focusing in the glass. The second technique would amplify two or more

separate pulses in the same amplifier, then delay them by different amounts so that they combine at the target [31,32]. Prior to the large aperture amplifiers, each pulse would be deflected (either electro-optically or by a set of beam splitters) along different directions that are slightly off-axis. At a sufficient distance beyond the output stage, the pulses would then be separated by an amount greater than their aperture; hence, they could be channeled along different delay paths by mirrors. This technique would be especially efficient if the pulses were temporally spaced by about 5-10 nsec, in order to take advantage of the decay of the Nd terminal level $^4I_{11/2}$.

E. SAFE OUTPUT LEVELS FROM SOLID STATE LASERS

Analysis of Self Focusing in Laser Systems

Considerations related to small scale self-focusing have dominated solid state laser design recently because of the dramatic nature of the effect; an initially high quality laser beam may emerge from the amplifier with the coherence degraded to the extent that it cannot be focused to a small spot and may additionally have very complex temporal and spectral characteristics.

While it is not totally clear that such pulses are useless for laser fusion; at the very least they increase the complexity of any interaction experiment enormously because of the much greater ambiguity in the laser intensity distribution. In the light of the desire to avoid such effects we will examine the present state of the technology in designing laser systems to avoid small scale self focusing.

The problem is that high spatial frequency intensity ripples can self-focus in a distance short compared to that for the whole beam to collapse. It must also be noted that in any real system spatial noise will exist because of diffraction or optical inhomogeneities in components.

Marberger's analysis for propagation of a beam through a passive medium with a nonlinear index of refraction n_2 suggests that such ripples will be exponentially amplified and there will be a spatial frequency K_{max} with the highest gain coefficient [2]

$$g = \frac{2\pi n_2 I \ell}{\lambda n_o} . \tag{26}$$

Suydam has analyzed the buildup of intensity ripples in amplifying media also and finds for this case that the growth rate at the most unstable spatial frequency is [3]

$$g = 2\pi(0.73)\frac{n_2 I}{\lambda \alpha n_o} \tag{27}$$

where α is the gain coefficient of the amplifier. The major difference in the two cases is that in the active case the gain is suppressed somewhat because the most unstable spatial frequency varies with position in the amplifier.

Quantitative application of this theoretical analysis is of dubious value given the restrictions under which it was derived, but if we assume it correctly predicts the sequence of events, we can attempt to define safe operating regimes. Several questions must be experimentally answered before it is possible to use this analysis in laser systems design.

- Is the growth cumulative through the entire system, or can intervening air spaces be used to damp out the ripples?

- What value of the growth rate can in practice be tolerated?

In order to answer these questions, we can analyze several experiments at NRL which have been performed at various times in tuning up the NRL glass laser system with rod and disc amplifiers. In all cases, the oscillator pulse was apodized to suppress Fresnel diffraction.* Also in the three particular experiments we will analyze, the system was optimally aligned, and a range of output levels run such that an operating point was picked 15-20% below the experimentally measured level at which noticeable beam degradation occurred. For analysis purposes the on axis value of $\int IdZ$ for passive components was increased by a factor of 1.4 relative to active components as suggested by a comparison of Eqs. (26) and (27). Amplifier saturation was included in the analysis.

- In the first experiment the system was run through the 45 mm rod amplifier with 250 psec pulses. High quality beams were obtained at 25 Joules while at 30 Joules small scale self focusing was evident. Through the system $\int IdZ = 4.3 \pm 0.2 \times 10^{11}$ W/cm while for the 45 mm rod alone $\int IdZ = 3.2 \times 10^{11}$ W/cm.

- In the second experiment the 64 mm rod amplifier was added and run at maximum gain with the input reduced to the point where a high quality beam was obtained (50 J in 250 psec). Once again at 20% higher levels small scale self focusing was evident. Through the system $\int IdZ = 4.5 \pm 0.2 \times 10^{11}$ W/cm while for the final amplifier alone $\int IdZ = 3.9 \times 10^{11}$ W/cm.

- In another experiment the laser was tuned up at 40 psec with the disc amplifier in operation and optical isolators in place. High quality beams were obtained at levels up to 16 Joules in this particular case. Through the system $\int IdZ = 4.6 \pm 0.2 \times 10^{11}$ W/cm while through the final amplifier $\int IdZ = 1.9 \times 10^{11}$ W/cm.

From these three experiments several conclusions can be drawn about the phenomena of small scale self-focusing;

- The growth factor for the entire system is the important factor, not simply the growth through the final stage. It appears that net values of $\int IdZ$ less than 4.5×10^{11} W/cm yield stable beams while values greater than 5×10^{11} W/cm yield beams where small scale self-focusing is evident.

- This would imply that the most unstable frequency corresponds to a frequency which is over the threshold at $\sim 10^9$ W/cm^2 ($K < 130$ cm^{-1}). For such frequencies the growth factors are in the range of e^5-e^7.

*The mode was truncated at the e^{-4} points and then re-truncated at the first dark ring of the far-field pattern.

• This sort of growth factor appears to be reasonably consistent with the spatial amplitude noise spectrum expected from the dual aperture truncation procedure. It further suggests that there may be some merit in pursuing further apodization in the amplifier chain to decouple growth in the early part of the system from growth further downstream.

Systems Design

At this point it is worth reiterating the major conclusions reached in the preceding section. First, Suydam's analysis of small scale self-focusing in laser amplifiers is at least operationally correct; the gain for small scale self focusing appears to scale as I_o/α. Second, it is a cumulative process involving the total path through the amplifiers and a safe value (for the NRL system at least) appears to be $\int IdZ \leqslant 4.5 \times 10^{11}$ W/cm.

The message for the systems designer is unmistakable. The premium is very large for designing amplifiers with the highest possible gain coefficient consistent with overall reliability as the safe power output is directly proportional to the gain coefficient. We will next discuss the present state of the art in design and construction of high gain disc amplifiers and then examine several systems to see what appears practical.

Table 5 shows a comparison of the prototype and latest NRL 66 mm amplifiers with the Livermore A & B modules under near identical conditions. The first four rows compare the values of the parameters which determine the pumping efficiency relative to the NRL prototype. The last two rows compare the measured and computed overall efficiencies and gain coefficients.

The first parameter which influences the efficiency is the flashlamp operation. In order to maximize lamp life in their very complex final system the LLL designers used longer than optimal pumping pulses. Similarly to equalize the threshold for the two lowest threshold parasitic modes the LLL choice was to use discs with about 70% of the doping of those in the NRL machines. The filling factor is basically a normalization factor for the pump energy density in the laser head. It can be seen that there is generally quite good agreement between the product of these factors and the measured relative efficiencies. The low efficiency of the LLL A module is tracible in large part to the poor filling factor caused by the relatively large size of the flashlamps relative to the discs. As noted by the LLL group it is possible to achieve considerably higher gain coefficients (and efficiencies) with some further improvements. The use of a crenelated reflector significantly improved the situation in both these cases and the use of ED-H (ED-8) laser glass also resulted in significant increase in gain (15%).

Table 6 lists a number of the options and the efficiency increase expected from each of them. The 20 cm aperture LLL C module is included for comparison in Table 6. Based on the LLL and NRL results, gains of ~ 14%/cm for 10 cm or smaller apertures are largely a matter of parasitic suppression. The exact levels at which feasible solutions exist is not clear, but for present techniques it is apparently at $\alpha D \geqslant 3.0$ [33]. This would imply that the D module (30 cm aperture) under construction at LLL would limit at ~ 5%/cm.

Table 5
Comparison of NRL and LLL Disc Amplifiers
with Cylindrical Gold Reflectors

Parameter		NRL Proto.	NRL-ILC	LLL A Module	LLL B Module
η_{FL} (Flashlamp Efficiency)	1	1.0	1.0	0.75	0.75
$\eta_{\alpha o}$ (Disc Doping)	2	1.0	1.0	0.90	0.90
η_G (Geometrical)	3	1.0	1.2	1.1	1.1
η_I (Filling Factor)	4	1.0	1.0	0.60	1.2
$\Pi\eta_{(EST)}$		1.0	1.20	0.44	0.88
η_{MEAS}	5	1.0	1.20	0.40	0.93
α (%/cm)		8.4	10	8.7	8.0

NOTES:
1. η_{FL} calculated from Ref.1, p. 42; the ratio is also in agreement with NRL results on 350 vs 800 μsec capacitor banks pumping ED-2 discs in $D(44)$ amplifier.
2. Scaled from Reference 1, Fig. 45, p. 40.
3. Known for NRL from ZAP code; est. to be same (and constant) for LLL systems with a 10% correction for the shatter shields.
4. Estimated for LLL systems by assuming 1 mm interlamp spacing and $\pi D_L = N(d_L + 1 \text{ mm})$ and $\eta_F = (D_o)/(D_L)^2$.
5. Measured LLL values taken from Reference 1, pp. 14-19.

Table 6
Disc Laser Improvement

Amp / Parameter	NRL		LLL		
	Proto.	New	A	B	C
α_o (Table 6)	8.4%	10%	8.7%	8%	5%
(1) ED-H Substitution	9.6%	11.5%	10%	9.2%	5.8%
(2) Crenel. Reflector	11%	13-13.5%	11.7%	9.8%	6.1%
(3) Cren. Refl. w (1)	12.5%	15-15.5%	13.5%	11.1%	7.1%
(4) 15 mm Lamps + (1) & (2)	N.C.	N.C.	N.C.	12.2%*	7.9%*
(5) Re-opt Doping	N.A.	N.A.	14.8%	N.A.	N.A.
(6) Re-opt Lamps 1, 2, 4	N.A.	N.A.	N.A.	16%*	10%*
Energy Storage Eff (6) (%)	0.98	1.01	0.36	1.02	1.5%

*Real value will depend on parasitic limit — probably ~ 14% for B Module 7% for C Module.

Staging

Given some (hopefully) realistic values of what gains can be achieved in disc amplifiers and some idea of the tolerable growth for small scale self focusing we can now proceed to attempt to determine the optimum system we can construct given these boundary conditions. Suydam's analysis would predict for an amplifier chain which was not staged (i.e., all amplifiers were the same diameter) the safe output intensity would be $4.5 \times 10^9 \alpha$ W/cm (where α is in %/cm). The inclusion of isolators decreases this value by $\sim$ 15-20% to $(3.6\text{-}3.8) \times 10^9 \alpha$ W/cm^2. If small scale self focusing were not a problem the optimum staging for energy extraction would be to have successively larger modules all operated at the same output level. Unfortunately self focusing is a problem and if there are m different modules all of the same gain the safe intensity will be $\sim 3.8 \times 10^9 \alpha/m$ (which is a disappointingly small value for $m > 1$).

The optimum approach appears to be a compromise between these two extremes. Figure 16 shows the results of this type of analysis applied to the NRL system. The early system without isolators is shown as is the initial system with isolators (which were also test cases for the $\int IdZ$ value). As can be seen, by use of the small (44 mm) disc amplifier and higher gain rods the present system with isolation is capable of 20% higher outputs than the original system without isolation. The other two systems shown use two new disc amplifiers and correspond to a reasonable expectation of the achievable performance at 100 psec (including saturation in the final stage). With the expected increase in gain with the ILC modules the output level should increase from 50-60 Joules to 80-90 Joules in a 100 psec pulse. This would correspond to 35 GW/cm^2 at the output and raises the question as to whether this is a reasonable projection. Figure 17 lends some plausibility to this notion. Plotted are achieved (experimental) and projected (computational) output levels vs final stage gain coefficient. The experimental points are the present NRL system (22 GW/cm^2) and a result achieved at LLL in testing the A modules of 30 GW/cm^2 [33]. From the figure it appears that reasonable staging leads to a safe output level. The safe output varies as $I_o \sim 2.5 \times 10^9 \alpha$ (α in %/cm) which is $\sim$ 2/3 of what an unstaged system would yield (but with higher overall efficiency).

Comparison computations have also been carried out for the 1 KJ laser under construction at LLL. For a 1000 J output and a 100 psec pulsewidth the value of $\int IdZ$ obtained was 9.1×10^{11} W/cm which appears high by about a factor of two. Most of the instability gain was in the D modules (5.3×10^{11} W/cm). This suggests that the pulsewidth will have to be increased to $\simeq$ 200 psec to meet the design output. Although the D modules will be limited by parasitic oscillation to a gain value between 3%/cm and 5%/cm some relief can be obtained increasing the gain of B and C moduels to the parasitic limit and perhaps by spatially filtering high spatial frequency ripples between the amplifiers.

The identified alternative system with amplifier chains terminated by C modules has much more flexibility. As originally designed this chain should be capable of 320-340 Joules in 100 psec. If parasitic suppression which allows a gain of 7%/cm in the C's and 12-14% in the B's proves possible, the higher gain plus the reduced flux in the early stages should allow outputs of 450-500 Joules in 100 psec to be obtained from this option.

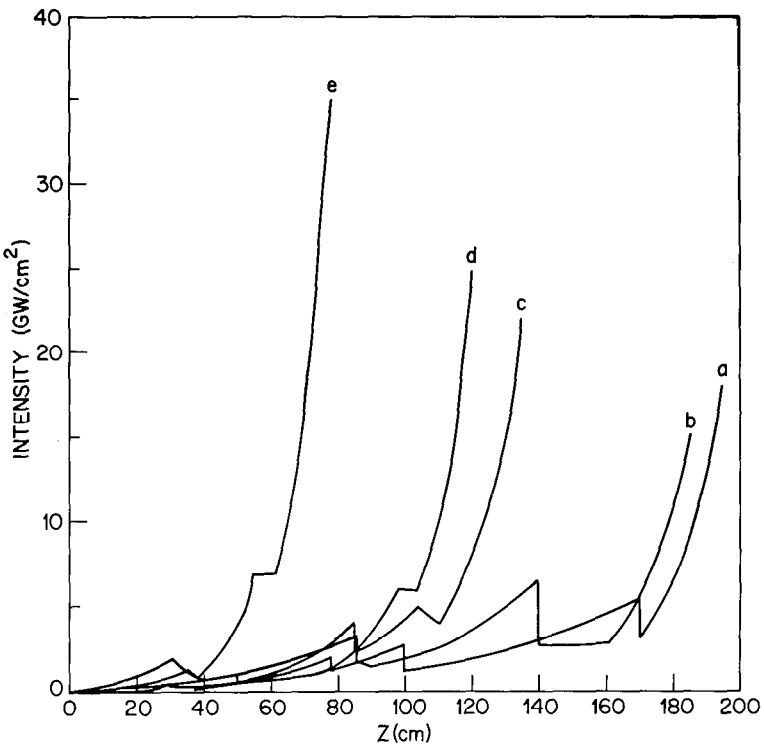

Fig. 16 — Staging diagrams for various iterations of NRL systems
(a) original (1971) system
(b) isolated system (1973)
(c) present system with small disc amplifier
(d) with new ILC-NRL disc amplifiers
(e) with high gain (14%/cm) disc amplifiers

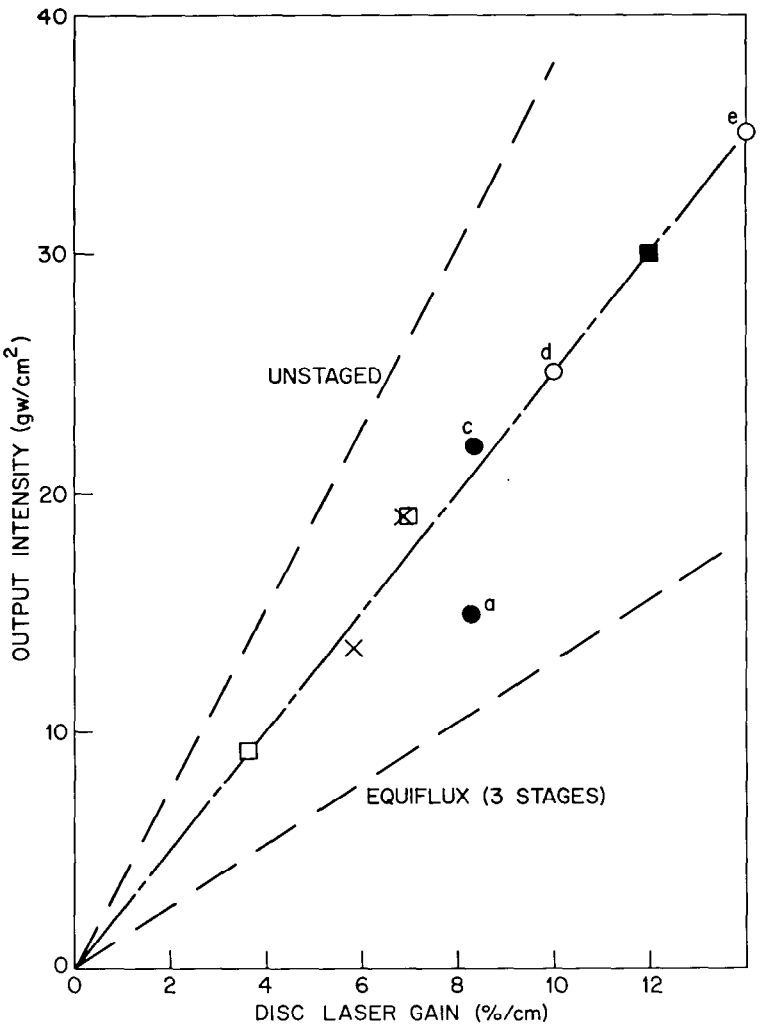

Fig. 17 — Comparison of systems calculations with experiments ● — systems a and c (Fig. 20) exps.; ■ — LLL exps.; ○ — calculations for systems d and e (Fig. 20); □ — CALC for LLL system terminated with "D" module; X — CALC for LLL chain terminated with "C" module; ⊠ — parasitic limited C module chain

REFERENCES

1. LLL Laser Fusion Semi-Annual Report, UCRL-50021-73-2, p. 34.
2. J. Marburger, NBS Spec. Publication 356, 51, (1971).
3. B.R. Suydam, Los Alamos Scientific Laboratory Report LA-UR-73-671 (1973).
4. J. Marburger, R. Jokipii, A. Glass, J. Trenholme, Laser Fusion Program Semi-Annual Report Jan.-June 1973, UCRL-50021-73-1, 145 (1973).
5. J.F. Holtzrichter, et al., "Laser Target Interaction Exps. at NRL," APS Plasma Physics Division Meeting, Monterey, California (Nov. 1972).
6. R. Speck, E. Bliss, IEEE Conf. on Laser Engineering and Applications, Washington, D.C., May 1973.
7. J.L. Emmett, et al., "High Peak Power Lasers," IEEE International Quantum Electronics Conference, Montreal, Canada, May 1972.
8. S.W. Mead, R.E. Kidder, J.E. Swain, F. Rainer and J. Petruzzi, Appl. Optics 11, 345 (1972).
9. J.B. Trenholme, NRL Memorandum Report 2480 (July 1972).
10. J.M. McMahon, J.L. Emmett, J.R. Holzrichter and J.B. Trenholme, IEEE J. Quant. Elect. QE-9, 992 (1973).
11. J.M. McMahon, ASTM Spec. Technical Publication 469, 117 (1969).
12. C.R. Jones, P.V. Avizones, P. Sivgals, NBS Special Publication 341, 28, (1970).
13. J. Soures, S. Kumpan and J. Hoose, Laboratory for Laser Energetics, U. of Rochester, Report No. 20, 24 (1973).
14. J.M. McMahon, O.C. Barr and R.P. Burns, IEEE Proc. & Int'l. Electron Devices Meeting (1973).
15. G. Dubé and N.L. Boling, Applied Optics, 13, 4, 699 (1974).
16. J. Strong, *Concepts of Classical Optics*, W.H. Freeman and Co., San Francisco (1958), p. 214.
17. D. Grischkowsky and J.A. Armstrong, Phys. Rev. A 6, 1566 (1972).
18. S.A. Akhmanov, R.V. Khokhlov, and A.P. Sukhorukov, *Laser Handbook*, Vol. 2, edited by F.T. Arecchi and E.O. Schulz-Dubois (North Holland Publishing Company, Amsterdam, 1972).
19. R.B. Miles and S.E. Harris, IEEE J. Quant. Electron. QE-9, 470 (1973).
20. J.T. Fournier and E. Snitzer, IEEE J. Quant. Electron. QE-10, 473 (1974).
21. J.A. Giordmaine, M.A. Duguay, and J.W. Hansen, IEEE J. Quantum Electron. QE-4, 252 (1968).
22. E.B. Treacy, IEE J. Quantum Electron. QE-5, 454 (1969).
23. R.H. Lehmberg, IEDM Digest, 565 (Dec. 1973).

24. R.A. Fisher and W.K. Bischel, Bull. Am. Phys. Soc. 18, 1586 (1973); Appl. Phys. Lett. 24, 468 (1974).

25. R.A. Fisher, P.L. Kelley and T.K. Gustafson, Appl. Phys. Lett. 14, 140 (1969).

26. A. Laubereau, Phys. Lett. 29A, 539 (1969).

27. F. Gires and P. Tournois, C.R. Acad. Sci. 258, 6112 (1964).

28. *Laser-Fusion Program Semiannual Report*, Lawrence Livermore Laboratory, UCRL-50021-73-1 (Jan.-June 1973) and UCRL-50021-73-2 (June-Dec. 1973).

29. P.G. Kriukov and V.S. Letokhov, *Laser Handbook*, Vol. 1 (North Holland Publishing Co., Amsterdam, 1972) p. 565.

30. R.H. Lehmberg, J.F. Reintjes, and R.C. Eckardt, Appl. Phys. Lett. 25 (1 October 1974).

31. NRL 1973 Annual Review, p. 134.

32. P.J. Mallozzi, et al., post-deadline paper, VIII International Conference on Quantum Electronics (June 1974).

33. J. Emmett (LLL), private communication.

34. J. Holzrichter (LLL), private communication.

III. TARGET INTERACTION FACILITY AND DIAGNOSTICS

This chapter discusses the target interaction facility and its associated diagnostics. Some detail is provided concerning some new plasma and neutron diagnostics. Later chapters will consider x-ray diagnostics and results in more detail. The target interaction facility is essentially unchanged from previous reports. However, new diagnostics have been added and the capability of irradiating small targets has been developed by concentrating on the problems of focusing and target positioning. The target room, designed for laser-fusion studies, is in a separate building from the laser. The laser beam propagates between the two buildings in an evacuated, 50 foot long tube. A 26 port vacuum chamber is used for the target interaction studies. This chamber with accompanying instrumentation is shown in Fig. 1.

A. FACILITY INSTRUMENTATION

The instrumentation includes monitors of the laser beam and focusing. Laser energy incident and back-reflected power and hard x-ray yield are monitored on a shot-by-shot basis. Hard x-rays have proven to be a good monitor of focal position. Some of the more important operational diagnostics are listed below. Studies utilizing these diagnostics are discussed in some detail later in the report.

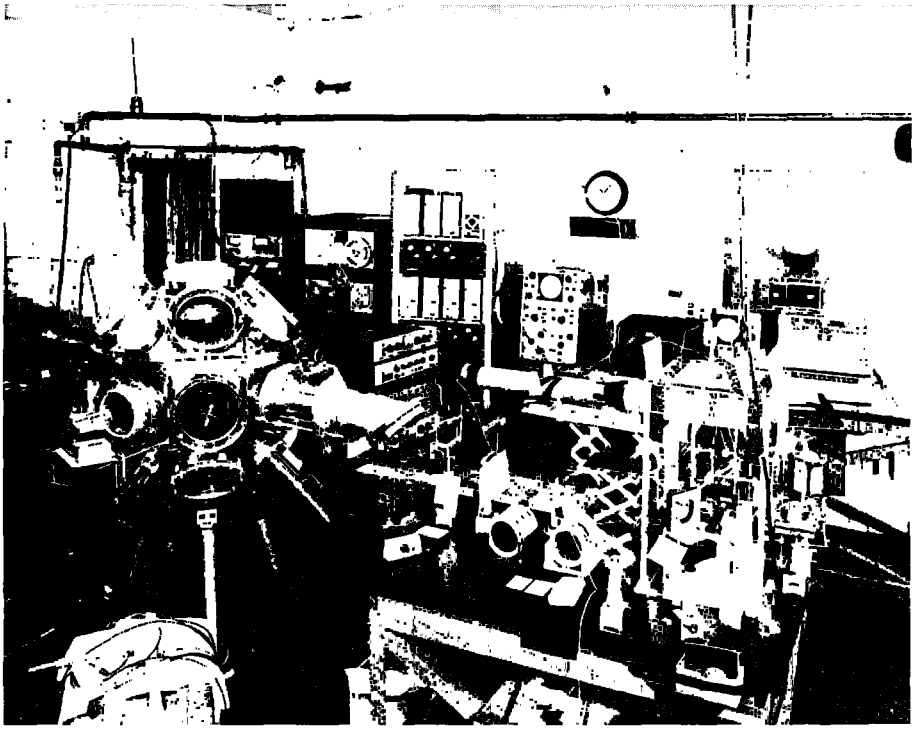

Fig. 1 — Target interaction chamber and associated instrumentation. Laser beam enters from the right through the 45° flat.

(i) *Incident Laser Pulse*: calorimeter (energy); photodiodes (timing); picosecond streak camera (pulse shape).

(ii) *Soft X-Ray Diagnostics*: calorimetry, pin-hole photography, crystal-film and grazing incidence grating spectroscopy with active detectors yield information about spectral, spatial and temporal properties of x-rays.

(iii) *Hard X-Ray Detectors*: an array of NaI detectors behind absorbers yields angular distribution with some spectral information.

(iv) *Back-Reflected Laser Radiation*: calorimeter, polarizer, spectrograph and picosecond streak camera are used to characterize energy, polarization and spectral content.

(v) *Interferometry*: a Jamin interferometer, utilizing the frequency doubled light of a split-off portion of the laser beam, gives information on plasma density.

(vi) *Ion Detectors*: Faraday cups determine the isotropy of plasma expansion and provide a measure of the plasma temperature by time-of-flight.

(vii) *Neutron Diagnostics*: BF_3 array, Li^6-glass scintillator and Rh-foil activation counter systems have been checked out and calibrated and are ready to use.

B. FOCUSING THE LASER BEAM

It is convenient to use the low energy pulses from the oscillators for focusing. However, one must take into account any differences in the collimation angles for the oscillator and amplified pulses. It is useful to set up a He-Ne alignment laser to have the same overall beam character as the amplified laser beam. This is done by firing through a mask, consisting of a pattern of holes, in the laser building. The pattern, recorded on burn papers at the target end, is a diagnostic of the beam character and can be used to set the collimation angle of the alignment laser (see the Appendix).

The He-Ne alignment beam, having been set to the collimation angle of the amplified laser beam, can be used to place the target in the focal plane. This is illustrated in Fig. 2.

A mirror, M_1, is supported at a distance d in front of the target plane T. A shearing plate P is placed in the incident beam so that the incident shearing pattern appears on the screen S. A mirror M_2 is used to position the reflected shearing pattern on the screen. Focusing is accomplished by matching the shearing patterns. They can be matched at two positions. If the incident beam is converging (diverging) the focus is that position toward (away from) the laser. If d is set up to be the difference between the focal lengths at 6328 Å and 10,600 Å then the target plane is at the focus for 10,600 Å when M_1 is at the focus for He-Ne beam.

The character of the focal region is determined by placing coated glass slides at the lens focus. The most useful coating used to date has been a 2000 Å vacuum deposited layer of indium. The burn pattern on these thin films due to irradiation may then be microphotographed or densitometered. The spatial resolution using this method appears to be less than 5 μm. As the slide is translated through focus one could see an elliptical

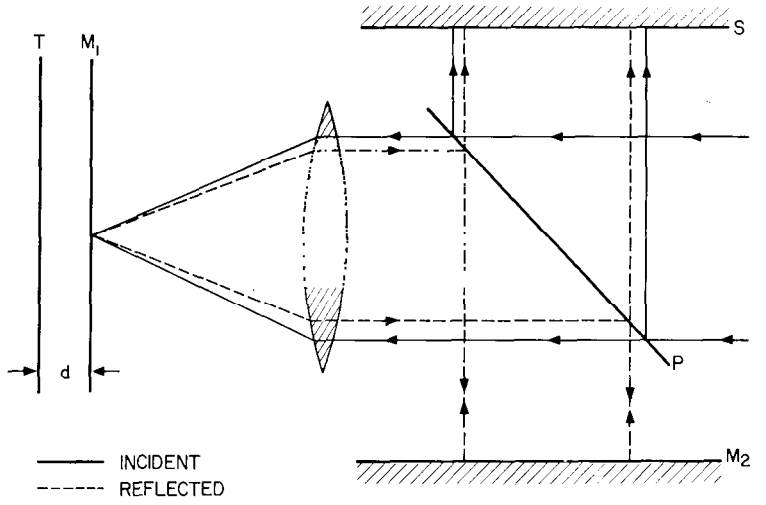

Fig. 2 — Arrangement for determining laser focus with shearing interferometry

burn that is rotated by 90°, i.e., astigmatism. This astigmatism was carried primarily by the laser beam (as opposed to being caused by the focusing lens) and has subsequently been localized and eliminated. The focal positions obtained by the shearing plate method described previously agree with that deduced from the minimum spot size on a coated slide.

The intensity distribution within the focal region is explored, using the coated slide method, by successively placing larger and larger attenuation in front of the focusing lens and then examining the burn pattern on the coated slide. Figure 3 shows a representative example of the irradiated slides by this method for an f/14 lens. By making the assumption that the deposited energy required to burn away the indium coating at the perimeter of each burn pattern is constant, one may draw a set of iso energy contours, shown in Fig. 3 for the focal region of our f/14 lens. One sees from the graph of these data, Fig. 3, that the full width half maximum (FWHM) mean diameter for intensity in the focal region is $\simeq 40$ μm. This is consistent with the manufacturer's (Itek) specifications. The corresponding mean radius for total energy (FWHM) is then $\simeq$ 110 μm. The focal region is therefore much more compact than that measured elsewhere [1]. It is noted that the focal region astigmatism is intensity dependent.

C. POSITIONING LIMITED MASS TARGETS

In addition to focusing upon a target longitudinally, one must position the desired target within the lateral extent of the focal region. In the case of slab targets this is no problem. However, for limited mass targets (spheres, lollipops, μ-dots, etc.) with dimensions the order of the focal spot size this is of concern.

To accomplish this positioning in our experiment a cw He-Ne beam which has been set collinear with the main laser's optic axis is centered on the focusing lens. The target is translated and centered in the He-Ne beam's focal region. The diffraction pattern

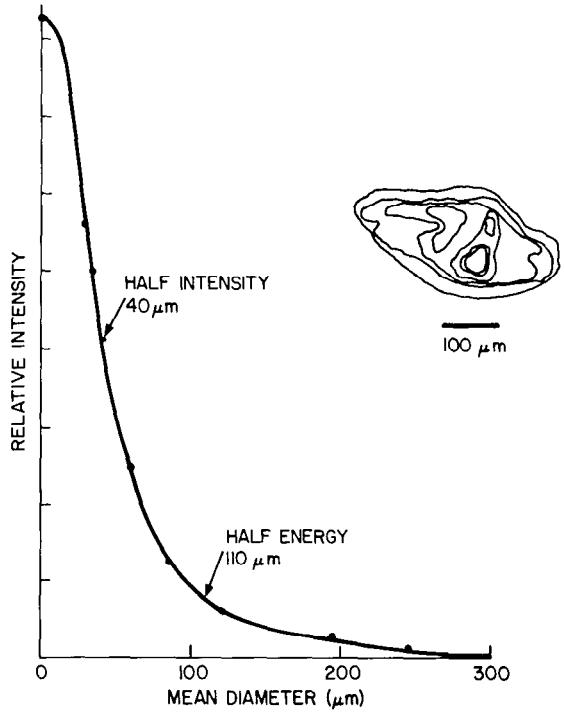

Fig. 3 — Intensity versus mean diameter and a set of iso-intensity contours (3 dB levels) in the focal region

caused by the target becomes symmetric when this has been accomplished. The target is then translated by a known distance into the 1.06 μm beam's focus. The separation between the He-Ne and the 1.06 μm focal spots is caused by the slightly different refraction in the optical wedges in the system at the two wavelengths plus any misalignment of the reference and 1.06 μm beams. This displacement is determined experimentally before each run. To appreciate the magnitude of the problem one notes that a deviation of the laser beam by 33 μ radians causes a 25 μm displacement at the focus of a 74 cm, f/14 lens. This displacement varies as the lens f-number and is hence reduced to 2.5 μm for an f/1.4 lens. To date we are able to focus upon a point with an accuracy of ±25 μm (one standard deviation). This is accurate enough to assure hitting limited mass targets of size $\simeq$ 100 μm reasonably squarely.

To determine how symmetrically an actual power shot hit a limited mass target we use three diagnostic methods. First, burn paper placed behind the target indicates a symmetry (or lack of it), second, ion charge detectors measure the symmetry of the late time plasma blowoff, and third, an optical interferometer measures the symmetry of the plasma density shortly after irradiation. These methods indicate that we reliably are able to hit small targets symmetrically.

D. OPTICAL INTERFEROMETRY

A wealth of information about the plasma properties may be obtained by either interferometry or shadowgraphy. These methods are most useful to obtain the electron density profile of the plasma because of the insensitivity of the method to neutrals, plasma temperature variations and other plasma properties. This information is essential to characterize the plasma's density gradient, shock formation, plasma expansion speeds, etc..

An inexpensive commercial Jamin interferometer is arranged as shown in Fig. 1 of Section IV. A portion of the laser oscillator output is frequency doubled to 5320 Å and used as a probe beam for the interferometer. Using this beam and an achromatic lens to focus the laser produced plasma on the filmplane we obtain an interferogram magnified by 3-4 times. The Fresnel diffraction pattern of the target edge (slightly out of focus) shows that the system has a resolution better than 15 μm. The advantage of this system over more complex arrangements is its simplicity and the convenience of having all components outside of the vacuum vessel.

Examples of interferograms obtained with this setup are shown in Fig. 4. Here the incident laser pulse width is 50 psec FWHM and the interferometry beam is approximately 35 psec FWHM* in duration. Figure 4a was taken approximately 1 nsec after the main pulse hit the target and Fig. 4b is a double exposure of this plasma at 1 nsec and 9 nsec after formation. Interferograms like these are Abel inverted to obtain radial profiles as a function of time before and after the arrival of the main laser pulse.

The major limitation to the usage of the interferometer, other than refraction effects when the plasma density approaches the critical density, is the time smearing of fringes caused by motion of the density profile during the probe beam's duration. A simple estimate of this restriction is given by

$$\Delta x = \Delta\tau \, c_s, \tag{1}$$

where Δx is the spatial resolution due to time smearing, $\Delta\tau$ is the probe beam duration, and c_s is the ion acoustic sound speed. Typical values of $\Delta\tau$ = 35 psec, $c_s \simeq 3 \times 10^7$ cm/sec yields a resolution limitation of approximately 10 μm. Another limitation arises due to the finite correlation length of the probe beam. A time-bandwidth limited probe beam pulse,

$$\Delta\omega\Delta\tau \approx \pi, \tag{2}$$

has a correlation length $\Delta\ell$ FWHM given by,

$$\Delta\ell \approx \lambda^2/2\Delta\lambda, \tag{3}$$

*The pulse width is reduced in the frequency doubling process.

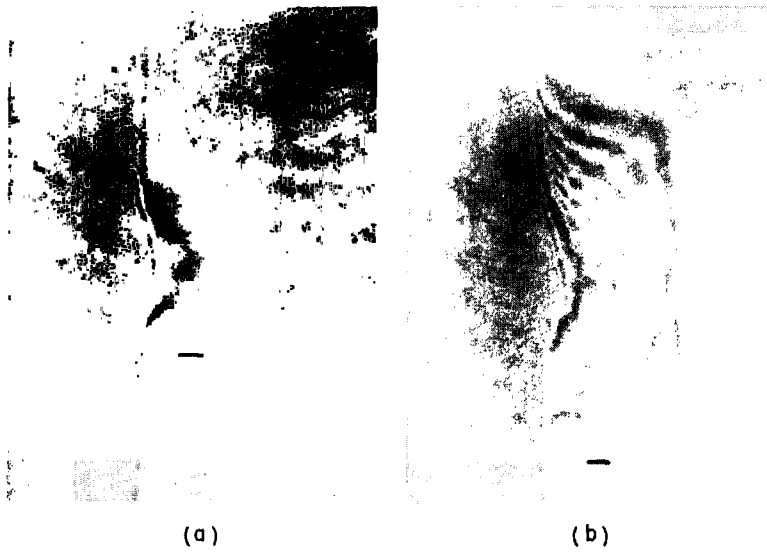

Fig. 4 — Interferograms of laser produced plasma (a) approximately 1 nsec after irradiation with a 50 psec, 7.5 J laser pulse, and (b) double exposure 1 nsec and 9 nsec after irradiation with a 50 nsec, 9.5 J laser pulse on a (CH_2) slab target. Markers are 100 μm long.

where $\lambda = 0.532$ μm, is the probe beam's wavelength and $\Delta\lambda$ is its FWHM spectral width. Typically, $\Delta\lambda \simeq 4$ Å yields $\Delta\ell \simeq 350$ μm. This specifies the precision by which the probe and reference beam's path lengths must be equalized.

E. ION ANALYSIS

Monitoring the ion efflux from the laser-plasma provides several useful pieces of information concerning the characteristics of the plasma. The symmetry of the plasma ablation is found by the angular distribution of the ion efflux, the total energy in the plasma particles is contained in the ion streaming energy, and an estimate of the plasma temperature may be deduced from the ion energy distribution.

Six to ten ion current detectors with the design shown in Fig. 5 are placed at various angles about, and at a distance $d \approx 30$ cm from the laser-plasma region. The ion current $I(t)$ in each of these is monitored such as shown in Fig. 6a. The total charge collected by each detector is just the area under each curve, i.e.,

$$Q = \int_o^\infty I(t)\, dt, \tag{4}$$

the total ion energy collected by each analyzer is,

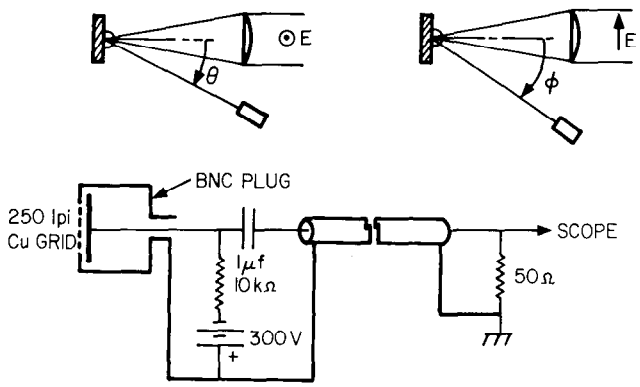

Fig. 5 — Schematic diagram of ion charge collectors and their placement around the target

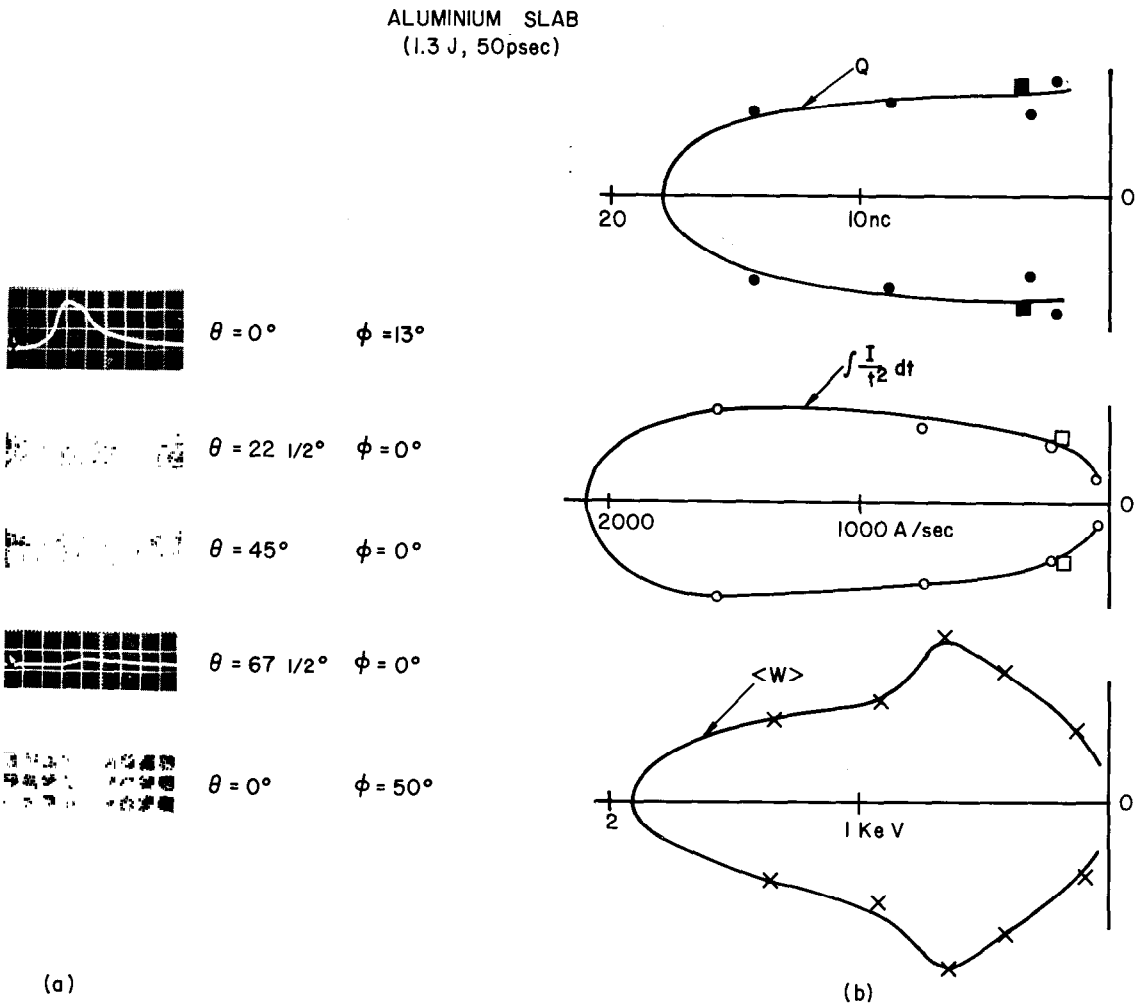

Fig. 6 — (a) Sample charge collector currents for a 50 psec, 1.3 J shot on an aluminum slab target aligned normal to the laser beam, and (b) polar plots of the total charge, total plasma energy and mean energy for current traces shown in (a)

$$E_{\text{ion}} = \frac{1}{2}\frac{M_i d^2}{Z_i e}\int_o^\infty \frac{I(t)}{t^2}\,dt \tag{5}$$

and, the average energy per ion collected is

$$\langle W\rangle = \frac{1}{2}\frac{M_i d^2}{Q}\int_o^\infty \frac{I(t)}{t^2}\,dt. \tag{6}$$

Here the ion mass is denoted by M_i and its charge Z_i. The knowledge of the ion mass and charge states, however, must come from other sources. Figure 6b shows polar plots of these quantities for the current traces of Fig. 6a.

F. NEUTRON DIAGNOSTICS

The detection of neutrons from hot plasmas containing deuterium and/or tritium can be used to indicate that fusion reactions have been produced. A package of neutron diagnostics for this purpose appropriate to laser-produced plasmas had been developed in FY-73 and has been tested on pulsed plasma sources in FY-74. Both the total neutron yield per laser pulse and the neutron energy are measured using three different detectors.

Neutron yields of 10^2 to 10^6 per pulse have been observed for laser-produced plasmas [2,3] and larger yields may be expected as higher power lasers become available. To cover the range from 10^2 to 10^{12} total neutron yield, two different types of detectors are used. The more sensitive system uses a ^{6}Li-glass scintillator. For sources of greater than 10^5 neutrons a Rh-foil activation counter is used. Both detectors employ neutron moderation to optimize sensitivity. Detailed characteristics of these detectors have been reported [4]. During FY-74 both detection systems have been used to detect neutrons from pulsed plasma sources. The ^{6}Li-glass detector has been used to detect neutrons from laser-produced plasmas [3] and from vacuum-spark plasmas [5]. The Rh-foil counter has been used to measure neutrons resulting from electron-beam generated plasmas [6] and exploded wires [7].

A large area neutron time-of-flight detector has been developed and tested for neutron energy measurements. This detector consists of a 30-cm diameter by 10-cm thick plastic scintillator (Pilot B) coupled by a lucite light pipe to a fast rise time photomultiplier (58 AVP). The thickness of the scintillator is optimized for the detection of 2.5-MeV neutrons. With such a large area detector one can measure neutron energies at flight paths of several meters from sources as small as 10^4 total neutrons. During FY-74 this detector was used successfully on measurements of 2.5-MeV neutrons from vacuum-spark plasmas of 10^3 to 10^4 total neutrons for flight paths of up to 4.2 meters.

A complete package of neutron diagnostics for laser-produced plasmas has been developed and tested on pulsed plasma sources. The small neutron yields observed to date on laser-produced plasmas at NRL preclude the use of neutrons as a very significant diagnostic of the laser-matter interaction process. When the laser facility is developed to the stage where increased neutron yields may be expected, appropriate neutron diagnostics for laser-fusion experiments are available.

REFERENCES

1. P.J. Brannon, G.L. Cano, J.F. Cuderman, K.M. Gilbert, J.J. Hohlfelder, E.D. Jones, M.A. Palmer and J.E. Powell, VIII International Quantum Electronics Conference, June 10-13, 1974, San Francisco.

2. S.W. Mead et al., App. Opt. 11, 345 (1972); C. Hamanaka et al., Phys. Rev. 6A, 2335 (1972); F. Floux et al., Phys. Rev. A1, 821 (1970); O.N. Krokhin, IEEE J. of Quantum Electron. QE-8, 565 (1972).

3. J.A. Stamper et al., "Laser-Matter Interaction Studies at NRL," Third Workshop on Laser Interactions and Related Plasma Phenomena, Troy, N.Y., Aug. 13-17 (1973).

4. F.C. Young, "Neutron Diagnostics for Laser-Induced Fusion," Report of NRL Progress, Naval Research Laboratory, Washington, D.C., May, 1973, p. 37.

5. T.N. Lee and F.C. Young, Bull. Am. Phys. Soc. Ser. II 19, 944 (1974).

6. M. Friedman, F.C. Young and I.M. Vitkovitsky, Bull. Am. Phys. Soc. Ser. II 19, 534 (1974).

7. S.J. Stephanakis, L.S. Levine, D. Mosher, I.M. Vitkovitsky and F.C. Young, Bull. Am. Phys. Soc. Ser. II 18, 1332 (1973).

Appendix

FOCUSING CONSIDERATIONS

The beam coming into the lens is characterized by an angle ϕ_c, describing the overall beam collimation or sphericity of the wave front and an angle ϕ_b (Fig. A1), describing the angular spread of rays passing through a point in the beam. The angle ϕ_c will be referred to as the collimation angle and ϕ_b will be referred to as the beam divergence. For an uncollimated beam ($\phi_c \neq 0$), the beam divergence varies with axial position along the beam so that the product of ϕ_b and beam diameter is constant. This is due to conservation, along a beam ray, of the specific intensity or photon angular distribution function. Beam divergence is determined by the source of the beam and is a measure of the spatial coherence of the beam. It can thus be quite small (typically 10^{-4}) for a beam coming from a laser.

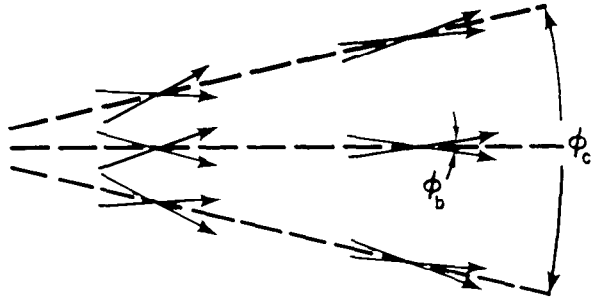

Fig. A1 — Angles characterizing a laser beam: collimation angle ϕ_c and beam divergence ϕ_b

There are several conditions which determine the effective angular beam spread ϕ_s for focusing. Beam divergence and lens aberrations make a contribution. Diffraction effects can also be important for laser beams. The full diffraction angle (between first minima) is $\phi_d = 1.22\ \lambda/r$ where r is the beam radius. The effective beam spread for focusing due to beam divergence, diffraction and spherical aberration in the lens is given by $\phi_s^2 = \phi_a^2 + \phi_b^2 + \phi_d^2$ when the contributing effects are weakly correlated. An effective focal spot diameter is given by $d_o = f\phi_s$.

The beam waist near the focus can be approximated by a hyperbola. The diameter $d(x)$ at a position x from the beam waist or focus is given by

$$d(x) = d_o\sqrt{1 + \frac{x^2}{F^2\ d_o^2}} \tag{A1}$$

where $d_o = f\phi_s$ is the focal diameter and F is the f-number (focal length over diameter) of the incoming beam. A halving in irradiance ($\pi d^2(x) = 2\pi d_o^2$) is obtained at $x = Fd_o$.

Spherical aberration in a quartz lens (n = 1.45) produces an effective focal spot diameter of 1.1 r/F^2 and an effective beam spread $\phi_a = 0.55/F^3$. For f-numbers less than about 15, spherical aberration must be taken into account.

For highest irradiance, the target must be placed accurately at the position of the focal point for the beam used in the experiment. This position depends on the lens, beam collimation and the wave length. Beam collimation is particularly important. A small collimation angle ϕ_c for the incident beam will cause a small deviation $\Delta\theta = (n - 1)$ ϕ_c from the collimation angle θ for the focused beam. The corresponding change Δf in focal position is given approximately by $\Delta f/f = \Delta\theta/\theta$ for a weak lens. Thus,

$$\frac{\Delta f}{f} \cong 2F(n - 1)\ \phi_c. \tag{A2}$$

For an f-number of 15, a quartz lens (n = 1.45) and a 1 milliradian collimation angle the fractional change in focal position is 0.0135. This would give a shift in focal position of 1 centimeter for the 74 cm focal length lenses used in many of our experiments.

A larger shift occurs at smaller radius in the beam (bigger F), but, by Eq. (A1), this is compensated for by less sensitivity of the focal diameter to focal position. It is useful to derive a collimation condition which is independent of beam radius or f-numbers. One could ignore collimation effects on focal position if the shift Δf in Eq. (A2) were small compared to the distance Fd_o from focus which produces a 100% change in intensity. This can be expressed as $\phi_c << \phi_s/2(n - 1) \sim \phi_s$. Thus, beam collimation is at least as important as the angular beam spread in focusing. In practice, this means that focusing should be done with a beam having the same collimation as the beam used in the experiment.

IV. EXPERIMENTAL LASER-PLASMA BACKSCATTER STUDIES

A. INTRODUCTION

Considerable effort has been expended toward understanding the physics and the scaling of the scattered laser light resulting from laser-plasma interactions. This is primarily because the reflection of laser light by the irradiated target may represent an important energy loss to the target system, in addition to possibly damaging the laser itself. One would hope that an understanding of the details of the reflection mechanism would lead to methods of either avoiding a strong reflection or using it to advantage. Both of these possibilities will be discussed below.

A number of experimental [1-8] and theoretical [9-12] studies of backscatter at NRL and elsewhere indicate that an appreciable amount of energy is backreflected from the target with an energy and modified spectrum in excess of that expected by simple specular reflection. We describe below recent experiments at NRL on laser backscatter from slab targets which indicate the following major results:

1. Two major sources of scattered laser radiation have been found and distinguished. The first is stimulated Brillouin backscatter with a wavelength near that of the incident laser (λ_o = 1.064 μm) and directly backscattered toward the laser. The second is specular reflection off the plasma critical surface whose intensity peaks at the specular reflection angle.

2. The directly backscattered power tends to saturate at a relatively low level ($\sim$ 0.5 GW) when an f/14 focal length lens was used to focus the laser energy on the target and when the incident irradiance on target was above $\sim 10^{14}$ W/cm^2.

3. Dependence was found for the direct backscatter saturation level on the f-number of the focusing lens.

4. Second harmonic backscatter does not play a significant role in the energy balance.

B. EXPERIMENTAL ARRANGEMENT

The experimental setup used in these studies consisted of the neodymium glass laser beam (λ_o = 1.064 μm), described in Section I of this report, focused with either an f/14 or an f/1.9 lens onto a slab target in the evacuated target chamber [4]. The pulse duration used was either 900, 250, 100, or 50 psec full width half maximum (FWHM) with energy $\leqslant$ 100 J. A prepulse identical in shape to the main pulse with approximately 5% of the pulse energy was usually applied 720 psec ahead of the main pulse. For the main pulse the irradiance at the focal spot was in the range $I \leqslant 5 \times 10^{15}$ W/cm^2. Calorimeters independently monitored the incident energy and the energy reflected back through the lens. Figure 1 schematically shows the arrangement for most of the backscatter measurements. To perform spectral measurements on the directly backscattered radiation, the light reflected from the target directly back through the lens was intercepted by a pellicle

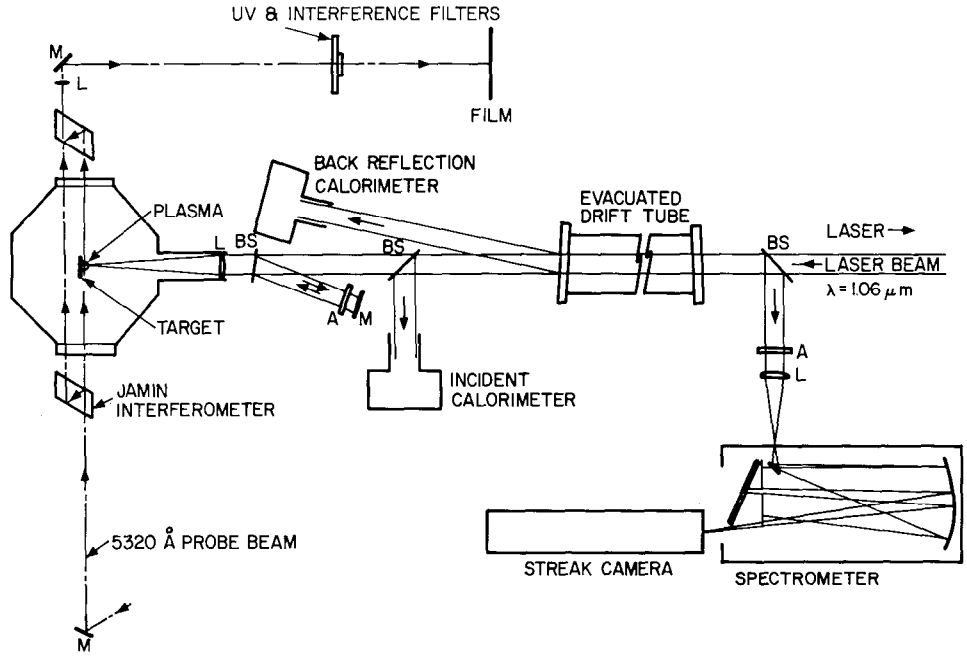

Fig. 1 — Diagram of experimental apparatus. Included are schematics of the Jamin interferometer apparatus, incident and backreflection calorimeters, backscatter spectrometer and streak camera arrangement.

placed near the laser. A portion of this light was focused with a cylindrical lens onto the slits of a 2-m Ebert spectrograph, where time-integrated spectra were taken using hypersensitized, Kodak I-Z plates. There was sufficient light so that a spectrum could be taken with a single exposure. Alternately, for time-resolved studies an Electro-Photonics, Ltd. fast streak camera with an S-1 photo cathode was used in place of the film. This camera has an inherent time resolution of $\lesssim 5$ psec. For the time resolved measurements the spectrometer was modified to reduce the temporal dispersion caused by differing optical path lengths within the spectrometer. An instrumental risetime of the spectrometer of ~ 20 psec was achieved by aperturing the dispersive grating. In this configuration the spectrometer is almost time-bandwidth limited with a wavelength resolution of ~ 0.8 Å. Typically, the back reflected signal required attenuation of the order of 10 dB to 20 dB when used with the streak camera.

C. SPECULAR REFLECTION AND REFRACTION

A semiquantitative measurement of the angular distribution of the scattered 1.06 μm laser radiation at solid angles other than back through the focusing lens was performed using an arrangement shown in Fig. 2. Here the target (slab, foil, fiber or sphere) was surrounded by Hadron footprint paper wrapped around a 1-in. diameter pyrex cylinder (to shield the emulsion from possible UV exposure) with entrance and exit holes for the focused laser beam. Tests were performed using IR transmitting visible and UV blocking filters to insure that exposures were indeed caused by IR radiation. With the f/14 focusing

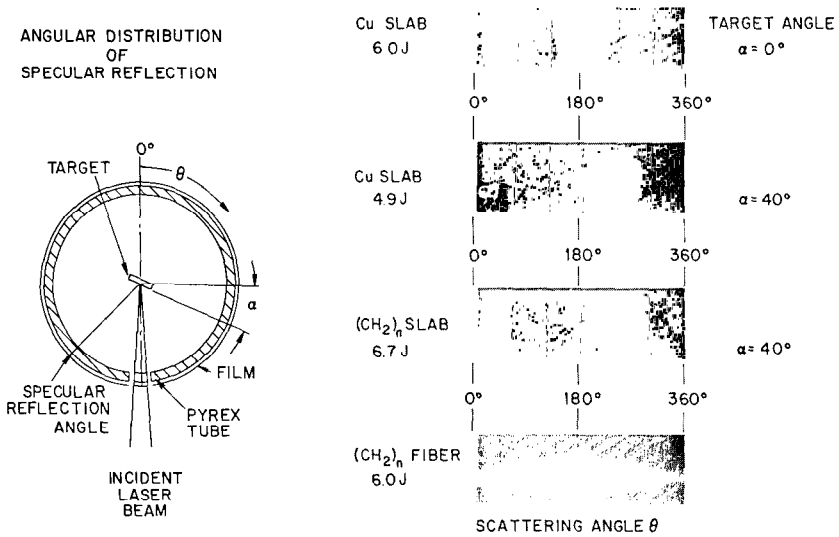

Fig. 2 — Apparatus to measure the isotropy of the scattered laser radiation plus examples of typical results. As the target is rotated with respect to the laser beam a large scattering contribution occurs at the specular reflection angle.

lens approximately 90% of the available solid angle was monitored. The laser-plasma IR emittance was estimated by calibrating the exposure on the Hadron paper.

Figure 2 also illustrates typical results by this method. By rotating a slab target, it was determined that the intensity of this scattered radiation peaks at the specular reflection angle for both metallic and nonmetallic target materials. The scattered radiation has an angular extent ($\pm 40°$) much greater than that of the incident beam ($\pm 2°$), and possess a total energy content of 5-10% of the incident laser energy. Notice that the angular extent and energy content of the specular reflection (Cu) metallic versus nonmetallic ($(CH_2)_n$) target were the same within the experimental uncertainty. The specular reflection energy per solid angle was typically small compared with that of direct backscatter (i.e., the reflection which was within the focusing lens' solid angle). However, the total energies scattered outside and inside the solid angle subtended by the f/14 lens were comparable. Figure 3 shows a typical intensity polar plot including specular reflection and direct backscatter. The reasons why the angular extent of the specular reflection is so broad compared to perfect mirror reflection is not yet determined. Possible explanations include refraction of the specular reflection, a smooth but curved critical surface, a "rough" critical surface, a photon-plasma wave scattering process or, most likely, a combination of the above. Experiments are underway to narrow down the possible explanations.

Specular reflection off of nonplanar targets, such as fibers (Fig. 2) cylindrical sections or spheres have angular distributions more consistent with their geometry. This is reasonable since ion analyzer measurements indicates that plasma ablation tends to peak normal to the target surface.

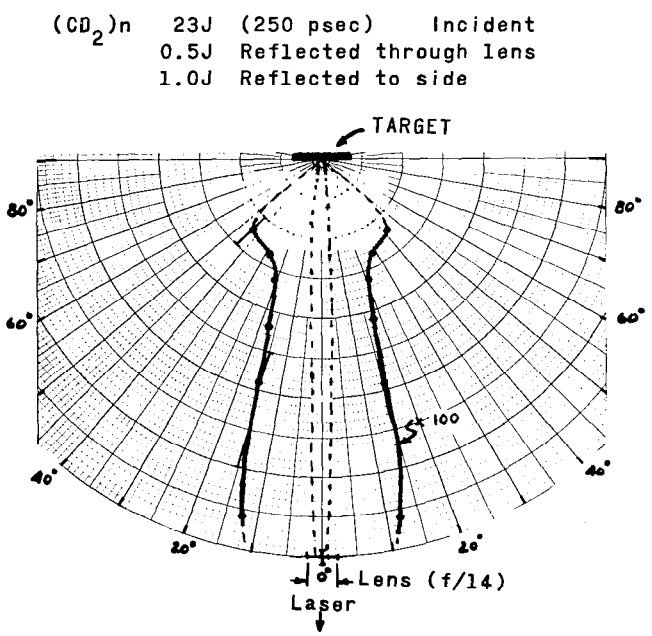

Fig. 3 — Scattered laser intensity versus polar angle for a slab target. Note the specular reflection intensity is more than an order of magnitude below that of direct backscatter.

Preliminary experiments are underway to use this burn paper technique and calorimetry to study the refraction of the incident beam in the laser-produced plasma from limited mass targets and foils. Numerical raytracing calculations will be used to model absorption, reflection and refraction for comparison with experiment.

The feasibility of using the specularly reflected laser light as a diagnostic probe is presently being investigated. It is radiation which has sampled the critical surface vicinity where a good portion of the "action" occurs. Preliminary experiments indicate that specular reflection is highly polarized but rotated from the direction of the incident radiation. The possibility is intriguing that a rotation or spreading of the angle of polarization by the Faraday effect is due to intense magnetic fields generated by the laser produced plasma.

D. DIRECT BACKSCATTER — A STUDY OF THE STIMULATED BRILLOUIN INSTABILITY [8]

The fact that we independently detect specular reflection allows us to conclude that the much more intense light which is directly backscattered through the lens is the result of some anomalous process. Henceforth we will discuss only the 1.06 μm radiation backscattered through the lens solid angle.

A number of characteristics of the backscatter radiation were discussed in the 1973 NRL Annual Report to the AEC. For completeness we reiterate them here. It was found

that the backscattered light is almost completely polarized in the same plane as the incident laser beam. Further, the optic rays of the scattered radiation retraced the optic rays of the incident beam to a very high degree [3].

The total hard x-ray energy ($\gtrsim$ 20 keV) emitted in the laser-matter interaction and the backscattered energy both increase with the incident energy [13] — a correlation which could reflect a common physical process [14].

Another quite remarkable property of the integrated backscattered radiation at 1.06 μm is that its total energy increases exponentially with incident laser energy up to a "saturation level" as shown in Fig. 4a. A saturation occurs in the case of an f/14 lens at approximately 10 J incident energy, 900 psec pulse length, ($\sim 10^{14}$ W/cm^2) at which point $\sim$ 5% of the energy is directly backscattered. The large scatter in the data is shot-to-shot reproducibility, not diagnostic uncertainty. There does not seem to be a target material dependence. The "saturation" of the energy backscattered through the lens may *not* imply a saturation of the *total* scattered radiation since considerable energy is scattered outside the sampled solid angle. The backscattered *energy* above saturation decreases with decreasing pulse width. This is shown in Fig. 4c for pulse widths from 50 psec to 900 psec. This result indicates that the direct backscatter *power* tends to saturate at approximately 0.5 GW when an f/14 lens is used. Since the backscatter *power* tends to saturate at incident irradiances of $\gtrsim 10^{14}$ W/cm^2 then the backscattered *energy* decreases with decreasing pulse width. This appears to be good news for the fusion effort. The saturation mechanism has not been determined at this time and is the subject of theoretical investigation at NRL.

An almost exponential dependence of the backscattered laser light upon incident energy is also found with the f/1.9 lens. If the specular reflection portion through the lens (1% of the incident energy) is subtracted from each shot obtained with the f/1.9 lens then the exponential dependence is reasonable as is seen in Fig. 4b. Once again the energy behavior of the back-reflected energy has little sensitivity to the target material. However, no saturation is observed within the energy range covered with the f/1.9 lens. The explanation for the different behavior of the f/1.9 and f/14 lenses has not been uniquely determined as yet, although the f/1.9 aspheric lens produces a smaller focal spot diameter ($\sim$ 30 μm) than the f/14 plano convex lens ($\sim$ 100 μm) and causes a more convergent optical path. This point is under study now.

The exponential increase of reflected energy with incident power is characteristic of the linear behavior of stimulated Brillouin backscatter if the power is such that the system is above the inhomogeneous threshold. This instability is consistent with the polarization and ray retracing measurements. The amplification factor for power of this instability [10] is

$$P_r \propto \exp(2\pi\gamma^2 L^2/cv_s), \tag{1}$$

where γ is the instability growth rate near threshold given by $\gamma^2 = (\omega_{pe}^2/8)(v_{os}/v_{te})^2\ (v_s/c)$, L is the spatial extent for phase coherence, c, v_s, v_{te}, and v_{os} are the speed of light, ion acoustic speed, electron thermal speed and peak electron quiver speed in the laser field, respectively. Assuming the underdense plasma to be isothermal, the phase coherence length L is given by

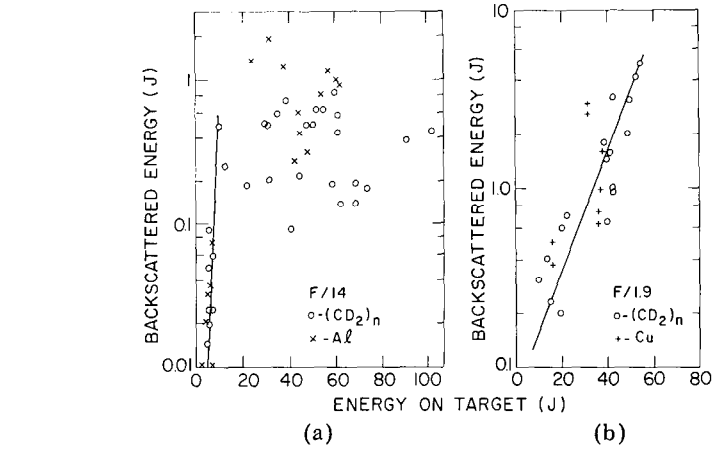

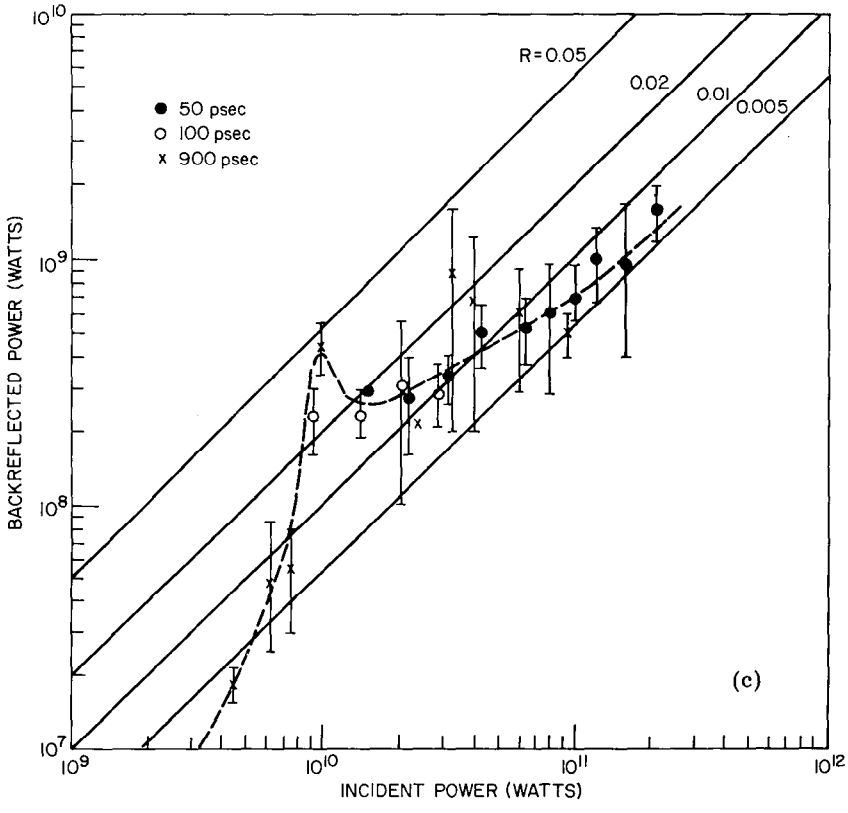

Fig. 4 — Laser energy backscattered through the focusing lens near 1.06 μm versus incident energy for (a) deuterated polyethylene and aluminum slab targets using an f/14 focusing lens and 900 psec FWHM laser pulses, and, (b) deuterated polyethylene and copper slab targets using an f/1.9 focusing lens and 900 psec FWHM laser pulses. In this plot the specular reflection contribution (1% of the incident energy) is subtracted from the backreflected energy. (c) The backscattered power vs incident laser power tends to saturate near ~ 0.5 GW for pulse widths between 50 psec and 900 psec.

$$L^{-2} = k_i \left[\frac{2v_f}{(v_f - v_s)L_v} - \frac{\omega_{pe}^2}{(\omega^2 - \omega_{pe}^2)L_n} \right], \tag{2}$$

where k_i is the incident laser wave number, L_n and L_v are, respectively, the plasma density and flow velocity gradient scale lengths, and v_f is the plasma flow velocity. For a typical temperature of 700 eV [4], and assuming interaction near one-fourth the critical density, we find that Eq. (1) gives a good fit to the exponential portion of Fig. 4a if we take L = 4 μm. A density gradient scale length of 30 μm, a velocity gradient scale length of 200 μm, and an initial fluid velocity of one-fourth the sound speed gives approximately this value. The comparable number obtained for the f/1.9 data, adjusted for specular reflection and laser irradiance at the interaction region, is $L \simeq 2.7$ μm.

Spectra of the backscattered light, time-integrated over the laser shot showed many characteristics similar to those obtained by other groups [2,3,5]. Briefly, the spectra were broadened by 10-50 Å with centroids shifted from the incident wavelength (often to the blue) by up to 10 Å. It was found in our experiment, however, that as the target is rotated away from normal incidence to the laser beam the spectrum shifts toward the red. This is shown in Fig. 5. The magnitude of these spectral shifts with target angle are numerically consistent with a superimposed doppler blue shift, due to plasma motion normal to the target surface, ($\langle v_f \rangle \simeq 4 \times 10^7$ cm/sec), and a red shift due to ion acoustic waves propagating into the target ($\Delta f \simeq 7 \times 10^{11}$ Hz). The time-integrated spectra often shows a line-like structure.

The time-resolved spectra of the backscatter, such as those shown in Fig. 6, show that the spectrum may evolve considerably during the laser pulse and, therefore, correct conclusions based solely upon time-integrated spectra appear fortuitous. The slab geometry target is normal to the incident beam in each case. A small portion of the incident beam spectrum is monitored and it is usually found to be roughly Gaussian in time and monochromatic to within 1 Å. The backscatter spectra have varying characteristics; however, they share an initial red shift, a time dependent spread in wavelength, a very fast risetime, and complex structure in time and wavelength. After onset the reflected energy appears distributed for the duration of the laser pulse. A question arises as to why there is not cutoff threshold for instability. Both the velocity and density scale lengths increase with time in the laser produced plasma and, therefore, the threshold for Brillouin backscatter would be reduced at the end of the pulse. When the incident beam is time modulated (caused by, for example, self-phase modulation) the backreflected spectrum is similarly modulated. Thus, in cases where backreflected flight exhibits temporal modulation it is essential to monitor the incident beams to determine its cause.

There is also a tendency for the centroid of the spectra to increasingly blue shift with time. This is especially evident in Fig. 6a which exhibits a blue shift linear in time. This blue shift could occur due to a constant *acceleration* of the interaction region toward the laser for the duration of the shot. This is consistent with the effect of target rotation upon time-integrated spectra noted earlier. It is likely that the initial spectral red shift is due to a stimulated process such as Brillouin scattering rather than a doppler shift since the interaction region would not have an initial net velocity away from the laser. The magnitude of the initial red shifts from the incident laser line (2-10 Å) correspond to ion acoustic wave frequencies, i.e., from 2% to 10% of the ion acoustic frequency at the

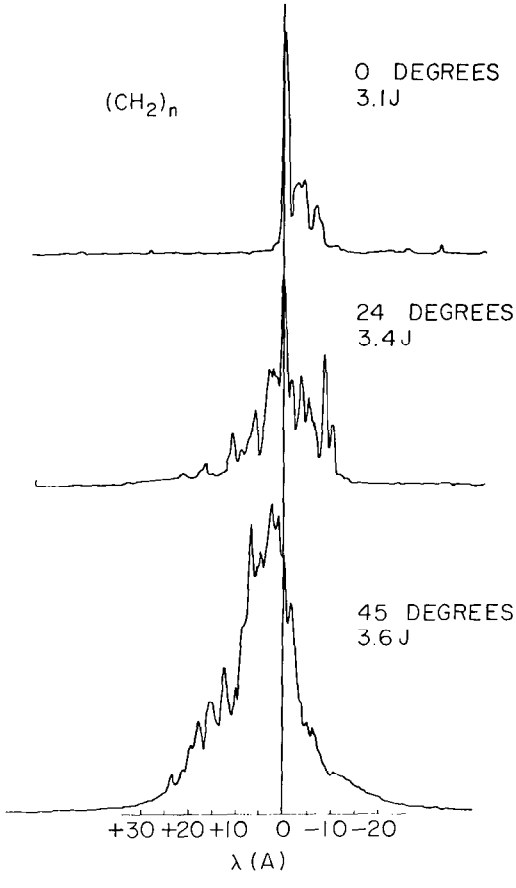

Fig. 5 — Shift of backscatter time-integrated spectra towards the red for an increasing angle θ between the target normal and laser direction

critical surface. Assuming the usual dispersion relations for the incident and reflected electromagnetic waves ($\omega_{i,r}^2 = \omega_{pe}^2 + k_{i,r}^2 c^2$) and ion acoustic waves ($\omega_{ia} = (v_s - v_f)k_{ia}$) and that the backscatter matching relations $k_r = -k_i = -1/2\, k_{ia}$, $\omega_i = \omega_r + \omega_{ia}$ hold in the interaction region, the spectral measurements lead to estimates that the interaction region is between 0.1 and 0.9 of the critical density and is typically near 0.25 of the critical density [15].

The rapid risetime of the backscatter and the existence of an intensity threshold is demonstrated in Fig. 6c. Figure 6c is a densitometer tracing along the time axis through the center at the spectrum of Fig. 6b which shows that the risetime of the backscatter onset, due to both the laser prepulse and main pulse, is less than the resolution of the spectrometer ($\sim$ 20 psec). When the backscatter is streaked directly without going through the spectrometer the risetime still appears instrument limited ($\sim$ 6 psec). The broad spectrum at the onset of the backscatter spectrum in Fig. 6b, if a result of a time-bandwidth limited effect ($\Delta\omega\Delta\tau \simeq (\pi/2)$ HWHM), would correspond to a risetime of about 1 psec. This 1 psec risetime is consistent with the calculated growth rate for Brillouin backscatter of $\gamma \simeq 10^{12}$ sec^{-1} near the threshold power observed of approximately 10^{13} W/cm^2. This threshold value is that predicted by the theory [10] within experimental error. The threshold and intensity of backscatter appears insensitive to the

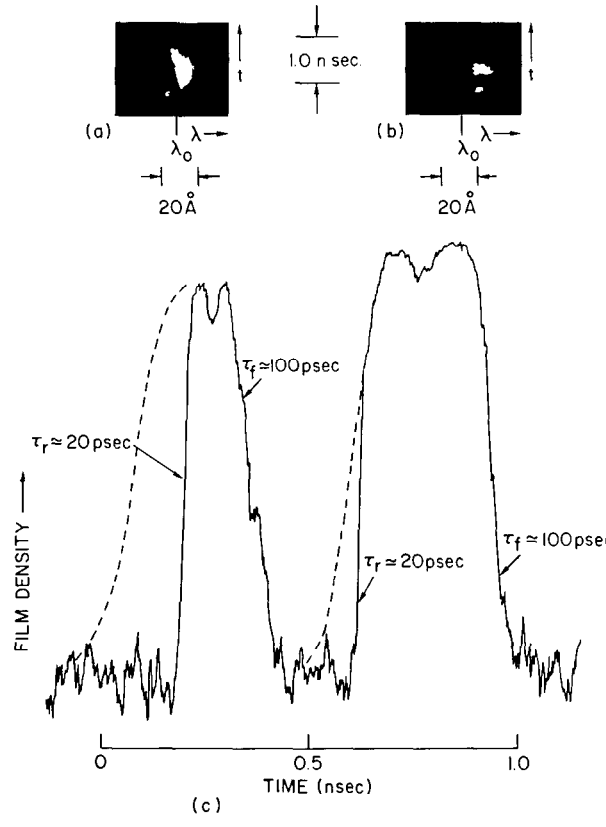

Fig. 6 — Time-resolved backscatter spectra for: (a) a copper target, f/14 lens, 8.6 J, 900 psec laser pulse with 100 psec temporal resolution (b) a deuterated polyethylene target, f/14 lens, 16 J, 250 psec laser pulse with 20 psec temporal resolution, and (c) densitometer tracing of (b) along the time axis through the center of the spectrum. Traces have not been corrected for film exposure vs density curve and are saturated at the peaks. Structure in front of the main pulse is due to a prepulse which carries about 5% of the total incident energy.

presence of a prepulse for all laser pulse durations used. Subsequent to onset, the backscatter intensity qualitatively follows that of the laser pulse and even exhibits the laser pulse fall time.

Another aspect of the backscatter spectra that is intriguing, but not yet satisfactorily explained, is the occasional appearance of line structure as in Fig. 6a. These lines are rather closely spaced ($\sim$ 2 Å) and may represent multiple Brillouin backscatter. However, it is difficult to satisfy all the matching conditions except very close to the critical surface ($\sim$ 0.96-0.98 n_c).

The bulk of our experimental evidence supports the hypothesis that stimulated Brillouin backscatter is responsible for most of the energy *directly* backscattered. Saturation occurs at a fairly low level backscatter power ($\sim$ 0.5 GW) when an f/14 focusing lens is used, and at approximately 15% to 20% when an f/1.9 lens is used. Specular reflection accounts for 5-10% of the incident energy but is reduced in intensity with respect to the direct backscatter by a large factor.

REFERENCES

1. N.G. Basov, et al., Kvantovana Elektronika **5**, 63 (1972) [Sov. J. Quantum Elec. **2**, 439 (1973)].
2. J.L. Bobin, M. Decroisette, B. Meyer and V. Yitel, Phys. Rev. Lett. **30**, 594 (1973).
3. J.F. Holzrichter, et al., Bull. Am. Phys. Soc. **17**, 972 (1972). K. Eidmann and R. Sigel, to be published in *Laser Interaction and Related Plasma Phenomena, Vol. 3*, (H. Schwarz and H. Hora, Eds.) Plenum, New York 1974.
4. J.A. Stamper, et al., to be published in *Laser Interaction and Related Plasma Phenomena, Vol. 3*, (H. Schwarz and H. Hora, Eds.) Plenum, New York 1974.
5. L.M. Goldman, J. Soures and M.J. Lubin, Phys. Rev. Lett. **31**, 1184 (1973).
6. P. Lee, D.V. Giovanielli, R.P. Godwin and G.H. McCall, Appl. Phys. Lett. **24**, 406 (1974).
7. J.E. Swain, Bull. Am. Phys. Soc. **18**, 1256 (1973).
8. B.H. Ripin, J.M. McMahon, E.A. McLean, J.A. Stamper and W.M. Manheimer, Phys. Rev. Lett. **33**, 634 (1974).
9. D.W. Forslund, J.M. Kindel and E.L. Lindmann, Phys. Rev. Lett. **30**, 739 (1973).
10. M.N. Rosenbluth, R.B. White and C.S. Liu, Phys. Rev. Lett. **31**, 1190 (1973).
11. H.H. Klein, W.M. Manheimer and E. Ott, Phys. Rev. Lett. **31**, 1187 (1973).
12. W.L. Kruer, K.G. Estabrook and K.H. Sinz, Nucl. Fusion **13**, 952 (1973).
13. F. Young, private communication.
14. See for example: B.H. Quon, A.Y. Wong, and B.H. Ripin, Phys. Rev. Lett. **32**, 406 (1974).
15. Interpretation of red shifts from time-integrated spectra as ion acoustic waves might underestimate the ion acoustic wave frequency because of the superimposed blue doppler shift and place the calculated interaction region closer to the critical surface that is actually the case.

V. SOFT X-RAY EMISSION FROM LASER-PRODUCED PLASMAS

A. INTRODUCTION

The goals of x-ray diagnostics of laser-produced plasmas are the same as for those for the other diagnostics. Emphasis in the x-ray work is naturally given to two major laser-fusion problem areas.

(a) Energy coupling: Analysis of soft x-ray data yields average plasma conditions (temperatures, densities, etc.) near the time of peak emission. From these the thermal energy of the plasma (nkT) can be computed as an estimate of how much of the laser energy went into heating the plasma. Hard x-ray data (discussed in the next chapter) indicate the extent of non-thermal processes such as energetic electron production which occur during laser-light absorption.

(b) Energy redistribution: A substantial fraction of the absorbed energy can be radiated in the x-ray region. Hence, soft x-ray integrated intensity measurements provide an important part of the answer concerning the ultimate fate of the laser pulse energy. Average radiative cooling rates are also obtained from intensity, angular distribution, time history and source-size x-ray data.

Furthermore, high-resolution soft x-ray spectra indicate whether or not a plasma is in ionization equilibrium. Such information is an important guide to theoretical work because it shows that rate-equation calculations are required. X-ray spectra also have shown which ionization stages and levels had to be included in numerical calculations. Of course, both soft and hard x-ray data provide tests of the calculation results as well as guide in setting up the computation.

X-ray diagnostics have important strengths. The main advantage derives from the fact that x-rays originate primarily in the dense (10^{19}-10^{20} cm^{-3}) part of the plasma at the time when major processes of interest are occurring. This region of the plasma has not yet proven accessible to other diagnostics (except measurements of neutrons when thermonuclear conditions are achieved). Early-time laser-light measurements (of under- and critically-dense regions) and late-time probe and other plasma measurements (of the under-dense plasma) can be compared with x-ray measurements which sample the dense parts of the plasma around the time of peak temperature. The major disadvantage of x-ray data is shared by other diagnostic techniques, namely it is difficult to obtain multiply-resolved data (e.g., spectral and spatial resolution, or spectral and time resolution). We would like to measure the x-ray intensity $I(E, \bar{x}, \bar{r}, t)$ as a function of photon energy (E), position ($\bar{x}$) within the plasma, direction ($\bar{r}$) of emission, and time (t). However, experimental realities limit what can be obtained to certain integrals of this function over several of its variables.

The present chapter concerns measurements of soft x-rays in the 50 eV to 5 keV range from the thermal part of laser-produced plasmas. The equipment used to obtain spectra, absolute intensities, the angular distribution, emission time limits and the x-ray

source size is described next. Then the equipment, parameters and calculations necessary to manipulate and reduce the data to a useful form for empirical studies or for comparison with theory are reviewed. Next, the results are summarized for CH_2 and heavier targets. Brief discussions of soft x-ray compression diagnostics and of the relation of the reported work to production of soft x-ray lasers and to other x-ray plasma diagnostics are included.

This chapter includes results obtained in work sponsored by the Defense Nuclear Agency. The material is included because much of the data, especially for low-atomic-number targets, is directly applicable to the laser fusion problem. All of the results, even those from heavy targets, are relevant to possible applications of the high-power lasers being developed for fusion research.

B. DATA ACQUISITION

It is convenient to classify the apparatus used to obtain information on laser plasmas from soft x-ray measurements according to the x-ray characteristic measured.

X-Ray Characteristic	Hardware
Spectra	Grating and Crystal Spectrographs
Intensities	Integrating Detectors
Angular Distributions	X-Ray Film Cassettes
Emission Times	Fast Detectors
Source Sizes	Imaging Devices

We will outline in this section the equipment used at NRL for these areas and for combination measurements. A schematic of most of the apparatus is given in Fig. 1.

Spectra (Grating and Crystal Spectrographs)

Spectra not only provide the most useful x-ray diagnostic data, but they are also a necessary prelude to other x-ray measurements. That is, proper interpretation of other x-ray data frequently requires knowledge of the spectrum. Figure 2 shows schematically the x-ray spectrum from a laser-produced plasma. A wide variety of instruments can be used to obtain photon energy resolution, as indicated in Fig. 2 for various energy ranges. High resolution ($\Delta E/E < 10^{-3}$) measurements of line spectra at the lower photon energies are obtained with dispersive instruments using photographic recording. Low resolution ($\Delta E/E > 10^{-2}$) measurements of continuous spectra at the higher energies are made either with dispersive instruments having discrete readouts or with non-dispersive (absorption) instruments. Here we consider high-resolution dispersive spectrographs useful in the region of greatest x-ray intensity.

Grazing-incidence grating spectrographs are used to disperse spectra from less than 50 eV to 1 keV. They include fine entrance slits which permit very high resolution work including line-profile analysis. However, they are very inefficient and difficult to align because of the fine slit. Also, it is notoriously difficult to calibrate the efficiency of grating instruments on an absolute scale.

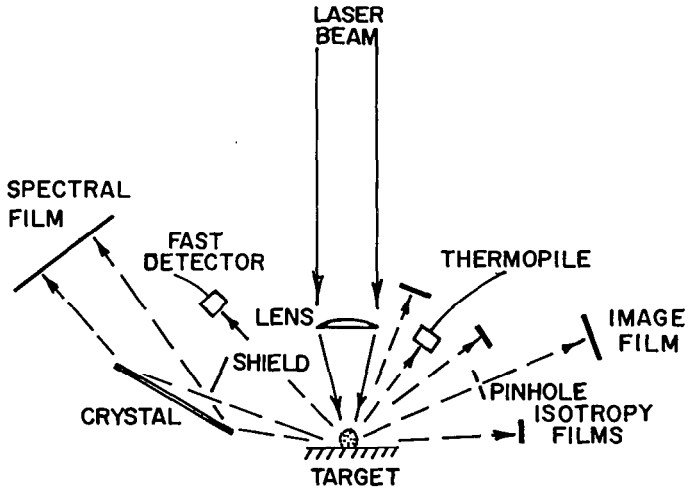

Fig. 1 — Schematic of soft x-ray apparatus used in the polyhedral target chamber

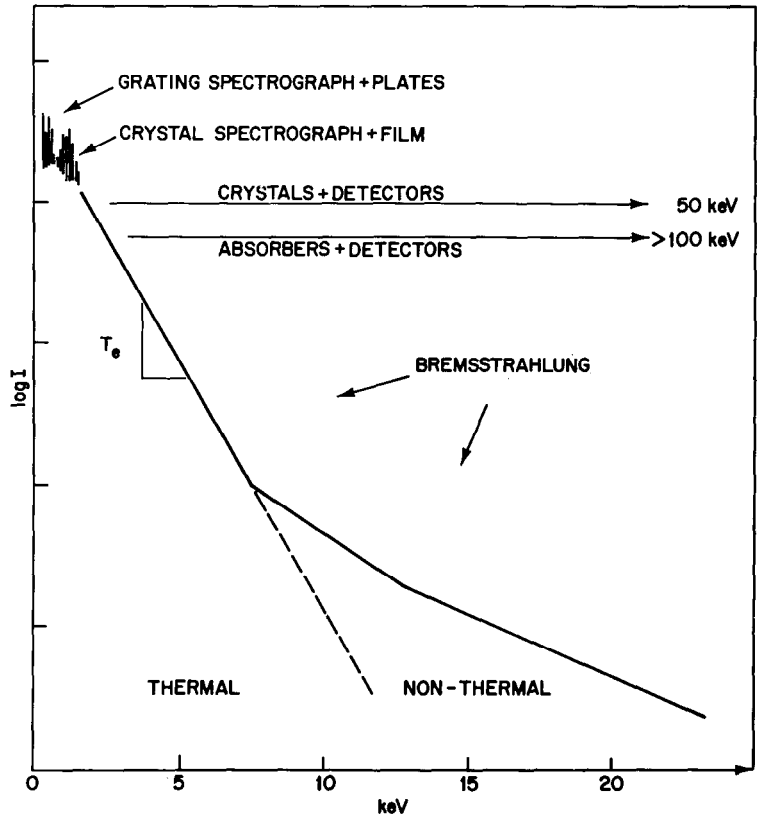

Fig. 2 — Schematic x-ray spectrum from a laser-produced plasma. Various spectrally-sensitive equipment can be used in the energy regions indicated.

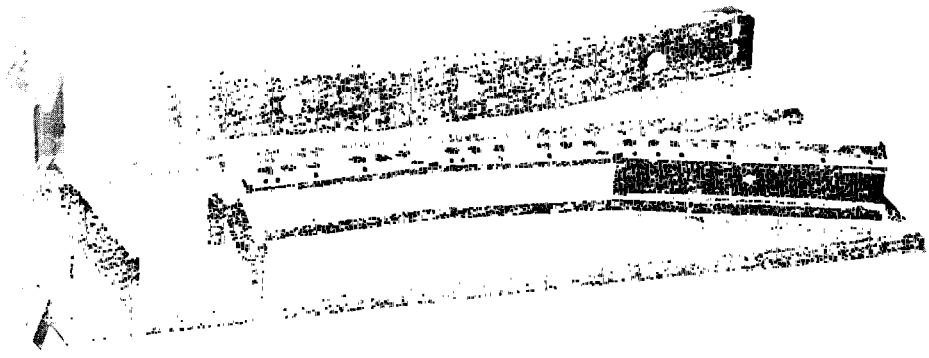

Fig. 3 — A view of the NASA 3m grating spectrograph and its reflection in its light-tight cover. The radiation passes through the slit on the left to strike the grating, which is partially hidden by the baffle. Two photographic plates are in place.

A high-quality 3-meter grating instrument with a 3 μm entrance slit borrowed from the NASA Goddard Space Flight Center [1] is shown in Fig. 3. Rather than mate it to the main target chamber, pulses were brought to a small target box at the spectrograph entrance. Spectra with 0.015 A resolution (0.015% at 100 A) were obtained with a 1200 line per mm grating and Kodak 101-05 plates in a few shots with a distance of about 20 cm between the laser focus and the entrance slit. The NASA grating instrument was returned for a solar rocket-flight experiment. A 2.2 meter grating-incidence spectrograph with interchangeable 5 and 10 μm slits is available but has not yet been used to measure laser-produced spectra. This instrument is shown in Fig. 4.

Crystal spectrographs are used to disperse spectra above about 500 eV, a limit set by the opaque windows used to protect the recording film. Line spectra up to almost 5 keV have been obtained to date. Slitless instruments with a resolution of better than 0.2% are generally used to measure laser-plasma spectra. They image the source and do not permit line-shape analysis. However, they are quite efficient and easy to align.

Two generations of flat-crystal spectrographs have been used in the LMI program. The earlier instruments were used in the initial target chamber. They have been replaced with spectrographs such as the one shown in Fig. 5 [2]. The diffraction angle and energy range of these new instruments can be varied without breaking vacuum. A variety of crystals have been used, including ethylenediamine-d-tartrate ($2d$ = 8.808A), ammonium dihydrogen phosphate ($2d$ = 10.642A) and potassium and rubidium acid phthalates ($2d$ = 26.632 and 26.12 for KAP and RAP, respectively). The film (10 cm square) can be translated behind the 25μm Be window (1% transmissive at 800 eV) so that 10 spectra can be recorded before the film has to be replaced (see Fig. 12). Kodak No-Screen x-ray film was commonly used, although a film with a single, large-grain (sensitive) emulsion would have been adequate. That is, little radiation less than 5 keV penetrates to the second emulsion in the two-sided No-Screen film.

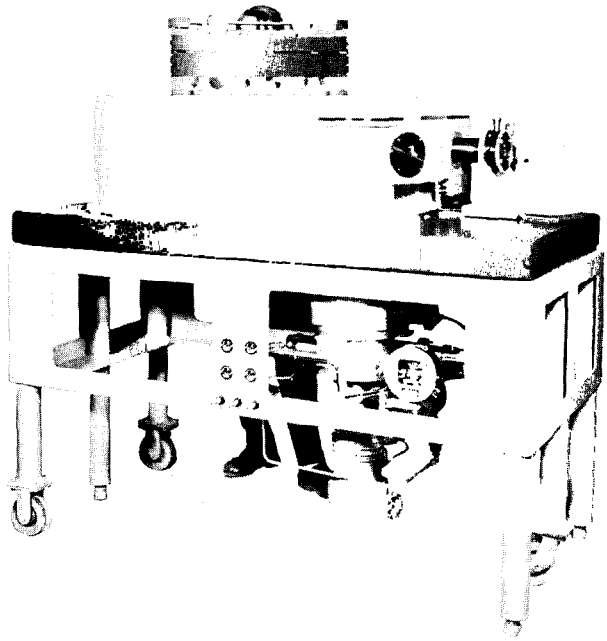

Fig. 4 — The commercial 2.2m grating spectrograph presently available for use in the LMI program. The daylight-loading camera is shown being lowered into position inside the vacuum housing.

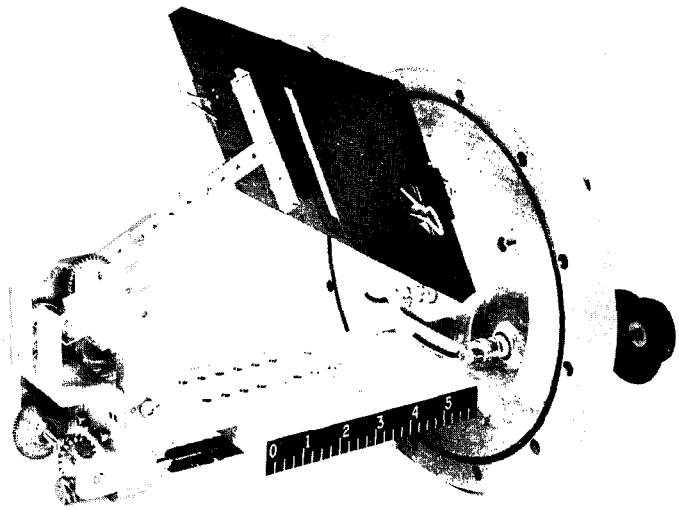

Fig. 5 — A crystal spectrograph for use on the large ports of the polyhedral target chamber. The Bragg angle can be set manually and the x-ray film advanced electrically from outside the vacuum. Shielding used to keep direct radiation out of the film pack was removed for this photograph.

Although flat-crystal spectrographs have proven highly satisfactory, the use of curved-crystal spectrographs is sometimes desirable. For low intensity spectra, a crystal curved at right angles to the dispersion direction permits more radiation to be diffracted to one position on the film. If ample intensity is available, then a convex-curved-crystal spectrograph [3] can be used to broaden the spectral range.

Absorber-foil measurements of continuum spectra are widely used to obtain the slope of such emission and thence the effective peak plasma temperature. The absorbers must be thick enough to stop all line radiation. This is easily accomplished for CH_2 targets for which the carbon lines are below about 500 eV. Filters of Be and Al with thicknesses near 25 μm are useful in the 1-2 keV region. The transmitted x-ray intensity is enough so that detectors with no internal amplification can be used. Silicon p-i-n detectors are convenient for this application. One of these detectors with its filter, is shown in Fig. 6, along with two Si surface barrier detectors. Above a few keV, there is not enough intensity (for few-joule, 100 psec pulses on CH_2) to use p-i-n detectors. Heavier absorbers must be employed with scintillator, photomultiplier (PM) readout. Relatively small (1/8-1/4 in. diameter) plastic and NaI scintillators with 125 μm Be or 25 μm Al sealed windows are used. Filters of heavier metals (e.g. Ni) about 25 μm thick are used with this system. It is convenient to put light pipes between the scintillators and the PM tubes in order to be able to vary the plasma-scintillator distance and angle while keeping the PM tubes outside the vacuum system. The experimental arrangement is shown in Fig. 7. Still heavier absorbers with large NaI crystals and re-entrant ports for the PM tubes are used above 15 keV, as described in the chapter on hard x-ray measurements.

Intensities (Integrating Detectors)

Intensities integrated over part or all of the spectrum are important for testing radiation codes and for computing part of the energy budget. Numerical integration of high-resolution spectra obtained on an absolute basis has been used to obtain the energy in x-ray lines. However, it is laborious to calibrate spectrographs and to integrate spectra. Usually it is better to use a wide band x-ray detector to integrate the x-ray intensity physically. Each detector has an energy-dependent response function, that is, a curve giving the detector efficiency as a function of x-ray energy. In general, the low energy response is limited by entrance window absorption. The high-energy response falls off as the active material in the detector becomes increasingly transparent. The measured signal (usually one number) is the integral of the product of the response function and the spectrum.

Detectors can be classified as passive (stored signal) or active (time-decaying signal which must be promptly recorded). Film and the thermal-luminescent (TL) detectors are the most common passive recording devices although several other techniques are available. Several Kodak x-ray films of varying sensitivity have been used as indicators of overall x-ray intensity. They (and their approximate relative sensitivities) are No-Screen (100), Type T (10), Fine Grain Positive (1) and Special Order Film Number 343 (0.1) [4]. Two types of TLD's (LiF and CaF:Mn) have been used. The latter is the more suitable for photon energies of a few keV or greater.

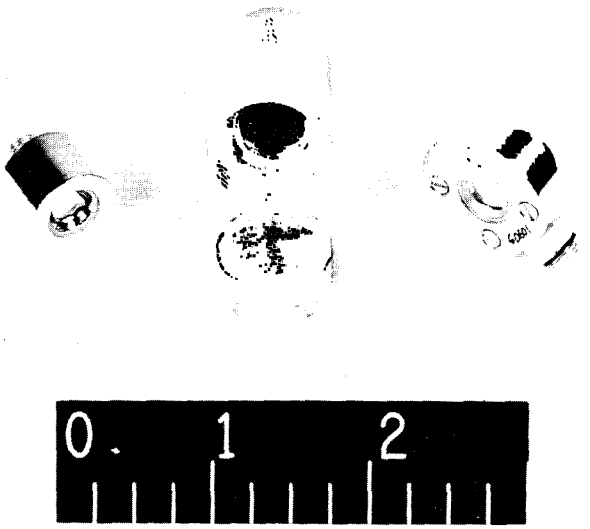

Fig. 6 — Commercial silicon-diode detectors. A p-i-n detector rests on the holder for its light-tight window in the center. Surface barrier detectors without their windows are on the left and right.

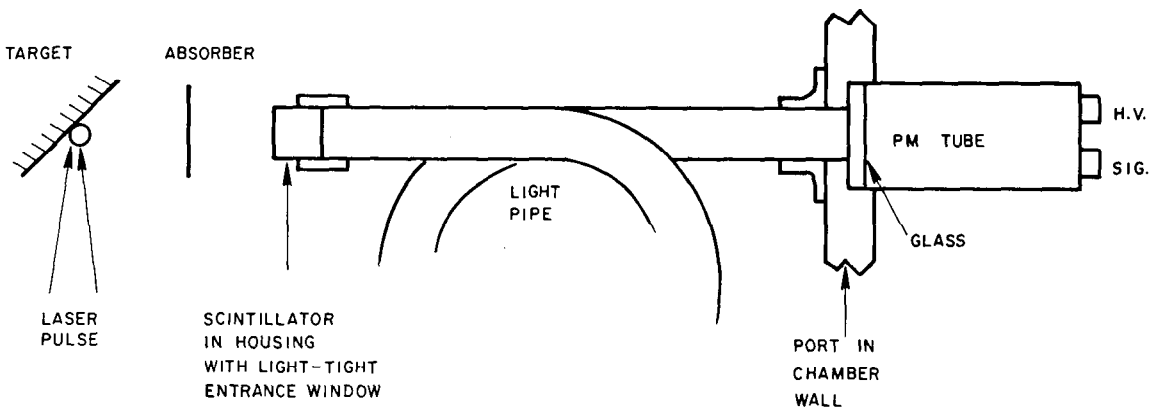

Fig. 7 — Schematic of the absorber-scintillator-light-pipe-photomultiplier arrangement. The use of light pipes permits the position (distance and angle) of the scintillator relative to the plasma to be varied easily.

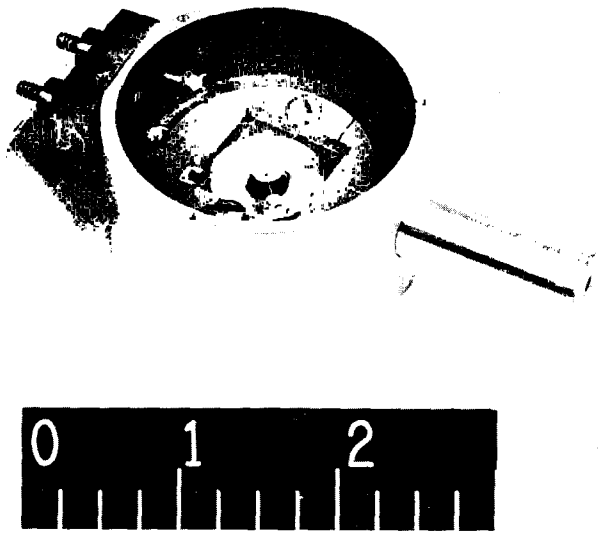

Fig. 8 — Back view of the 62 μm thick, 5.6 mm diameter Ag disk with attached thermocouples inside of a commercial thermopile

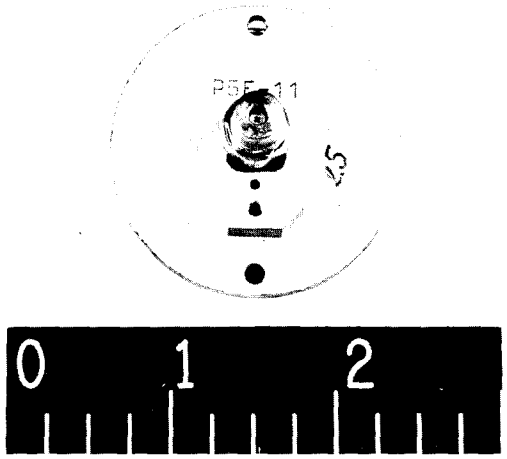

Fig. 9 — Pyroelectric detector, showing 1 mm diameter active element inside its housing

Active detectors can be grouped by the sequence of processes between x-ray absorption and recording. Photoelectrons are generated and produce an electrical signal directly in vacuum x-ray diodes (which are not light sensitive and can be used below 100 eV). X-rays produce electron-ion pairs which are subsequently collected in ionization chambers. In some solid state detectors, x-rays produce electron-hole pairs, as in Si p-i-n and surface barrier diodes. In others, such as pyroelectric, calorimeter and thermopile detectors, heat generated by x-ray absorption produces the electrical signal. Signals from active detectors must be integrated electrically or numerically to obtain the x-ray intensity.

A variety of active detectors have been built, or purchased, and tested for use at NRL. They include: (a) x-ray diodes with stretched polypropylene windows ahead of the biased anode consisting of a high transmission screen and the aluminum photocathode, (b) center-wire, sealed ionization chambers with 125 μm Be entrance windows and argon fill gas, (c) the silicon p-i-n diodes shown in Fig. 6, (d) silicon surface barrier detectors, also shown in Fig. 6, which operate like p-i-n devices but have a voltage-dependent active region, (e) the scintillator/photomultiplier detector systems sketched in Fig. 7, (f) a thermopile detector which has a silver element and is shown in Fig. 8, and (g) a lithium tantalate pyroelectric detector, shown in Fig. 9. All of these detectors can be used for absolute x-ray intensity measurements, but not all of them have been adequately calibrated to date. The silicon p-i-n and NaI detectors and the Ag thermopile have been used for quantitative intensity-level measurements. Operational tests on most of these detectors are performed using x-rays (near 1.4 keV) produced at the focus of a commercial 0.5 GW ruby laser [5].

Angular Distributions (X-Ray Film Cassettes)

Intensities integrated over photon energy are obtained with instruments which intercept a relatively small part of the total solid angle. In order to compute the total x-ray emission by integrating over solid angle, it is necessary to know the angular distribution of x-ray emission with respect to the laser beam and target. A non-uniform x-ray intensity distribution could result from a non-spherical plasma which is not optically thin. X-ray films (in separate packs behind 25 μm Be windows) placed at equal distances from the laser-plasma have been used to search for variations in the x-ray intensity with emission direction as indicated in Fig. 1. Filters were used for some exposures to provide crude energy discrimination as indicated in the center of Fig. 10. Cassettes which provide continuous angular resolution have also been used, as shown in Fig. 10.

Emission Times (Fast Detectors)

Measurement of variations in the rate of x-ray emission is important for two reasons. Firstly, time history data are useful for checking the results of rate-equation output calculations. Secondly, it can be combined with total x-ray intensity data (integrated over spectrum and solid angle) to yield the average radiative cooling rate (expressed as watts of x-ray emission above some photon energy limit).

X-ray rate measurements with subnanosecond time resolution were not done prior to the advent of short-pulse lasers. Some solid-state devices such as p-i-n detectors were known to have response times of about 1 nsec. Recently the pyroelectric IR detector shown in Fig. 9 was found to be x-ray sensitive [6]. But its risetime of 0.7 nsec cannot be fully utilized because the response times of cables and oscilloscopes are comparable. X-ray diodes have faster rise times ($<$ 100 ps) but a sampling system must be used to record the signals to realize such time resolution [7]. The rise times of fast scintillators have also been sampled in a new type of fast x-ray detection system [8]. Calculations show that coupling a scintillator to an optical streak camera might yield time resolutions of around 10 nsec [9]. But the best x-ray time response demonstrated to date was that of a streak camera with a special x-ray photocathode. It is presently limited to 50 psec

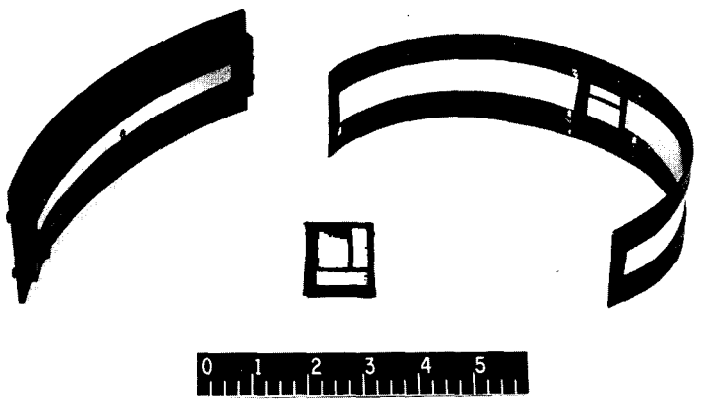

Fig. 10 — Be-window x-ray film pack (with absorbers) in the center, and two Be-window film cassettes with different radii of curvature used for angular distribution measurements

resolution by the relatively wide electron energy distribution from the photocathode [10]. It was suggested that including an electron spectrometer within the streak tube would improve the resolution. However, quantum-yield calculations indicated that the electron intensity is not sufficient to permit such an improvement. We note that x-ray detectors with subnanosecond time resolution might find use on synchrotron x-ray sources, at least one of which has a 100 psec pulse length.

In the absence of an x-ray streak camera in the LMI program, p-i-n (Fig. 6) and pyroelectric (Fig. 9) detectors were used to place a limit on the x-ray emission time produced by subnanosecond laser pulses. For the pyroelectric detector shown in Fig. 9, a combined time response of the detector-cable-scope system of approximately 1 nsec was realized.

Source Sizes (Imaging Devices)

The size of the region in the laser plasma from which x-rays arise is also doubly important, that is, to test codes and to compute the x-ray power density. An example of a calculated source size picture is given in the numerical simulation chapter. The power density (watts of x-rays per cm^3 of the plasma) is computed from the measured x-ray power and measured source size.

The extent of the plasma volume emitting x-ray can be determined in a variety of ways [11]. The first class of devices, which depends on the wave nature of x-rays, includes Fresnel lenses (up to 1.5 keV) and glancing-incidence reflection devices (up to a few keV). The second grouping uses x-ray absorption in collimator, pinhole, or knife-edge devices to yield an x-ray image.

Early measurements [12] of x-ray source size were done using a mesh and filter as shown in Fig. 11. The resolution was limited by the mesh-wire size (53 μm). Simple

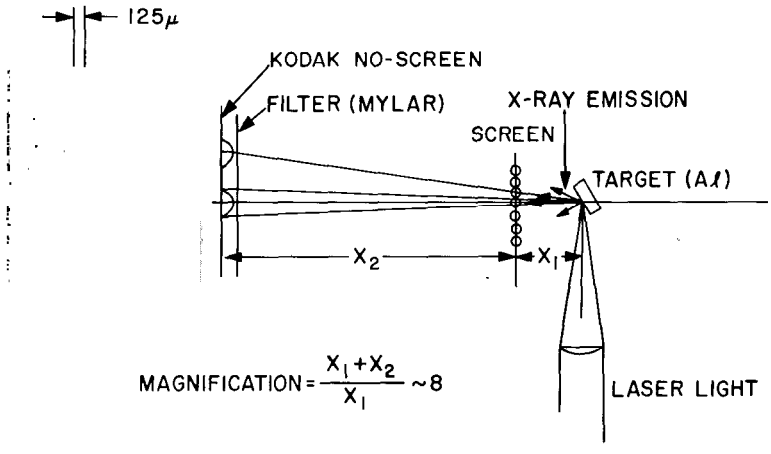

Fig. 11 — Shadowgraph arrangement and resulting film for a laser-produced Al plasma

cameras with pinholes as small as 25 μm have been used with No-Screen film recording. As shown in Fig. 12, the same film pack as is used for crystal spectrographs is used for the pinhole camera. No image intensification was used to date. A collimator device consisting of bundles of small tubes 1 mm in diameter and 3 cm long, also shown in Fig. 12, was used to measure the extent of the large but weak x-ray emitting region in the plasma plume. Such an instrument is sensitive but offers only crude (~ 1 mm) spatial resolution.

Combination Measurements

Simultaneous measurement of several of the x-ray characteristics discussed above is useful and has frequently been done with individual instruments. However, by the use of single instruments specially designed to yield more than one type of data, additional information can be obtained. For example, combination of an entrance slit (in the diffraction plane) with the crystal spectrograph shown in Fig. 5 gave both spectral and spatial resolution. The resulting information could not be gotten from an x-ray spectrum and an x-ray image obtained with separate instruments. A spectrometer for use ahead of an x-ray streak camera has been designed as a step towards combined spectral and temporal resolution. The instrument will increase the intensity in a single x-ray line available at the entrance window of a streak tube by two orders of magnitude over that from the simple spectrometers presently in use.

C. DATA ANALYSIS

The equipment and techniques used to acquire various types of x-ray information from laser-generated plasmas were discussed in the last section. Now attention is given to the other equipment, calibration procedures, parameters, calculations, and methods required for handling and analysis of the data in order to extract useful information. Reduction of spectra from grating and crystal instruments has much in common. However,

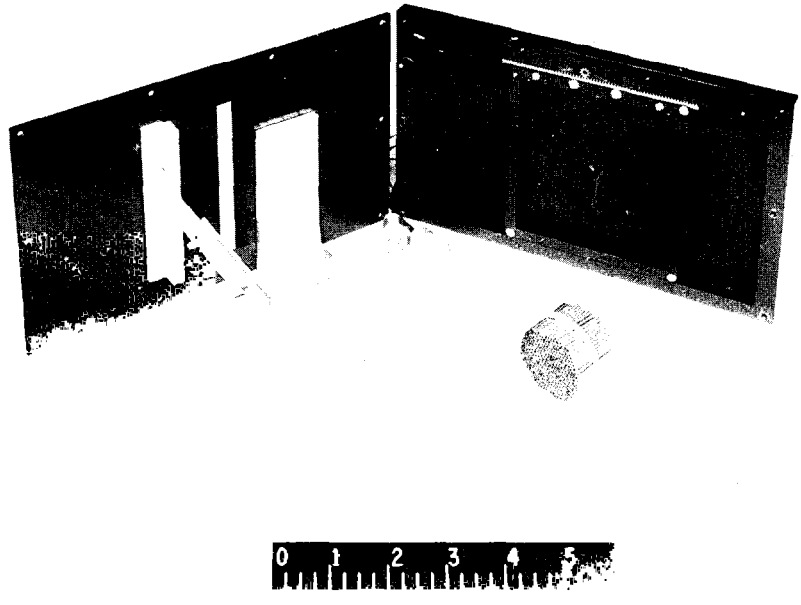

Fig. 12 — Pinhole camera and tube-collimator devices used to obtain x-ray images. Three pinholes are mounted on the arm attached to the camera front. Radiation passes through the Be window to a film mounted on the motor-driven rack inside the camera back. The film pack is also used with the crystal spectrograph (Fig. 5). A film pack similar to that shown in the center of Fig. 10 is used with the collimator which is made up of 1 mm ID, 3 cm long Ni tubes.

efficiencies for the grating and plates used in recording spectra at lower photon energies were not determined. Hence, only line spectra obtained with crystal spectrographs (as well as continuum spectra measured with active detectors) were put on an absolute basis. Calculations of intensity ratios and line profiles, discussed in this section, were performed assuming an isothermal plasma. They do not embrace the full time-dependent hydrodynamic, emission and radiation transport problem described in the section on numerical simulation. Hence, the emission calculations used for analysis of the x-ray data provide only average and "effective" plasma parameters near the time of peak temperature. They are useful characteristic values for the plasma conditions (temperatures and densities). Of course, the optimum approach involves numerical calculation of observables such as spectra, intensities, time histories or pinhole images. If the computed x-ray characteristics compare well with experiment, the codes can be used with additional confidence to compute plasma conditions in detail, i.e., as a function of space and time. In short, the "products" of the x-ray data analysis are (a) empirical, averaged values for plasma conditions, which are useful when studying how plasma characteristics change as a function of the laser-pulse, focusing and target conditions, and (b) information, such as spectra on an absolute basis, which can be compared with calculations.

Linear Densitometry

The first step in analysis of spectra from both grating and crystal instruments is to "read" the plates or films. Four scanning densitometers are used for this work. One, which is used primarily to read plates, has an oscilloscope line-determination system for accurate location of lines. It yields a deck of computer cards, one for the position and peak density of each line, or a continuous chart record for line profile scans. The second unit is computer-controlled, with magnetic tape as well as chart paper outputs. It is used primarily to read x-ray films when the film sensitivity correction is to be done by (a separate) computer. The third densitometer yields accurate densities on chart paper, although with less resolution than the first two machines. The resolution is adequate for many tasks and the machine is readily available. The fourth densitometer is not used for quantitative work, but it does produce the best appearing scans for use in reports.

Energy (Wavelength) Calibration

The distance along a plate or film, as recorded on cards, magnetic tape, or paper, must be converted to photon energy or wavelength. This is done by the use of lines in the spectrum being analyzed, the energies of which are known. Sometimes, several lines of the element of interest are sufficiently well-known to serve as standards. However, most often lines from another element are used. These may be introduced into a spectrum by coating the target with powder or an evaporated layer, or by using compound targets. Or else, they may occur naturally, as in the case of carbon and oxygen which are on the surface of most targets. The use of "internal" wavelength standards in spectra obviates the need for highly accurate geometrical measurements of a spectrograph and its distance to the plasma. A least-squares computer program based on the grating equation is used to accurately determine wavelengths of lines measured on glass plates. Another program incorporating the Bragg equation, or else graphical means, is used to obtain line energies of spectra on x-ray films measured with a crystal spectrograph.

Crystal Spectrograph Efficiency Calibration

The record of photographic density as a function of photon energy has to have three corrections applied to it to yield a spectrum on an absolute basis: (a) the film response, (b) the crystal diffraction efficiency, and (c) the source-spectrograph geometry. Taken together, the three factors give the spectrograph efficiency. The first two of these require experimental parameters which are interpolated by use of theory and the third is computed on the basis of measured distances and angles.

Absolute calibration of crystals and x-ray films is a complex, on-going project. It requires a monochromatic x-ray beam of known intensity, usually obtained from elements fluoresced by an x-ray tube. Descriptions of earlier calibration experiments at energies above 5 keV are available [13]. Similar work at energies down to 1 keV has been performed recently for potassium acid phthalate crystals [14]. Figure 13 shows the measured and computed first order reflections of KAP. Figure 14 gives the relative H + D curve for Kodak No-Screen film at 1.34 keV as measured with x-rays from laser-produced

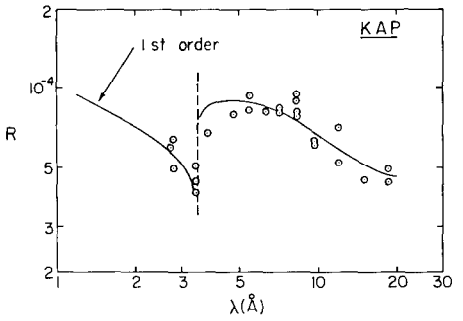

Fig. 13 — The integral reflection coefficient vs wavelength for (001) KAP crystals. The potassium K edge is at the position of the dashed line.

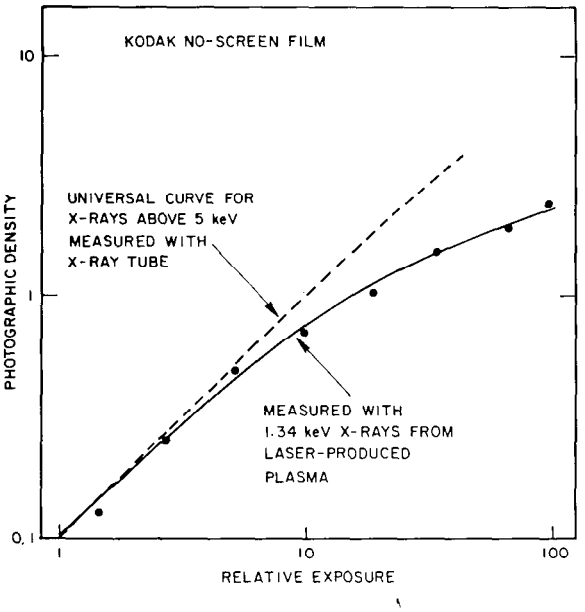

Fig. 14 — Relative density-exposure curve for Kodak No-Screen x-ray film at 1.34 keV

plasmas [15]. The absence of reciprocity loss in x-rays was checked down to 9 keV earlier [16]. Theoretical considerations and limited other data indicate that reciprocity loss will not affect quantitative x-ray spectroscopy at photon energies in the range above 800 eV used in this work.

Atomic Structure Calculations

The energies of observed lines, obtained as described above, and their intensities, gotten from use of crystal, film and geometrical factors are of relatively little use by themselves. The integrated intensities do give the overall x-ray output. However, much more information is available if the ionization stages and transitions can be identified for each line. Then it is possible to determine plasma conditions such as temperature and density. The most probable transitions for candidate ionization stages can be anticipated by consideration of collision and emission cross sections. The computation of x-ray line

energies for particular elements, ionization stages and transitions serves to pin down the origin of each line. Such calculations can be done in the frozen-orbital, transition-stage, or relaxed-orbital approximations using a variety of programs of increasing sophistication:

a. Screening Constant (Veigele) Program [17]
b. Hartree-Fock-Slater (Herman-Skillman) Program [18]
c. Hartree-Fock (Froese) Program [19]
d. Relativistic (Liberman) Program [20]
e. Multiplet (Cowan) Program (21,22].

The computation of x-ray energies is still a subject for further research due to questions concerning, for example, the statistical exchange parameters to use in few-electron ions. However, generally the most intense lines can be identified by use of theoretical x-ray energies. The construction of isoelectronic sequences from empirical energies for neighboring elements is also useful in analysis of spectra.

Line Intensity Ratio Calculations

Once the origin of the major lines in a spectrum is determined, the intensity ratio for similar transitions in different ionization stages can be used to estimate the effective plasma temperature. Such estimates are commonly made for spectra from high temperature plasmas such as solar flares [23].

We have made extensive use of integrated line intensity ratios in resonance spectra ($1s$-np, n = 2,3 .... transitions). In particular, the ratio of $1s$-$2p$ intensities for one- and two-electron ions is usefully sensitive to temperature in the range around 1 keV (10^7 K) for elements in the range $10 < Z < 20$. Under the assumption of Coronal equilibrium (collisional excitation equals radiation recombination), the $1s$-$2p$ intensity ratio is a unique function of temperature, as shown in Fig. 15 for Al [24]. Such a curve can be used with measured intensity ratios to determine empirical temperatures. Inclusion of three-body recombination makes the ratio sensitive to density also. This produces a range of temperatures, corresponding to densities in the emitting region, for a given observed intensity ratio.

Other line ratios are useful in determining plasma temperatures. These include, in particular, ratios of satellite lines from three-electron ions which accompany the $1s$-$2p$ lines in two-electron ions. Some of the satellite lines are produced in ions formed from two-electron species by dielectronic recombination, the inverse process of autoionization [25]. Hence, their ratio is independent of the density (of the two-electron species) since it appears in the numerator and denominator of the ratio and cancels. But, the ratio is temperature sensitive because the rates for dielectronic recombination and collisional excitation of two-electron ions have different temperature dependencies.

Ratios of particular three-electron satellite lines can be used to determine whether or not a plasma is in ionization equilibrium, that is, if the state of ionization correctly corresponds to the plasma electron temperature. The theory of such analysis is still under

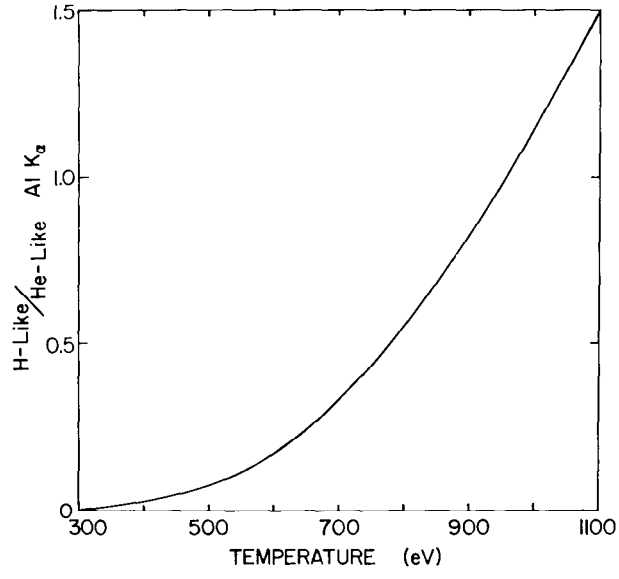

Fig. 15 — Ratio of intensities for the 1*s*-2*p* transitions in H- and He-like Al vs plasma temperature computed from the coronal equilibrium model

development [26]. However, it can be used to test for departures from ionization equilibrium even if the extent of departure cannot be precisely determined.

Line Profile Calculations

The discussion to this point has centered on the energies and intensities of lines observe with grating or crystal instruments. However, each line also has an intrinsic shape, sometimes expressed by the width (FWHM) and an asymmetry index. The line characteristics depends on conditions in the emission region. With sufficient resolution, physical (intrinsic) contributions to the line profile exceed source size or instrumental (extrinsic) contributions. Then line profile analysis can yield additional information on the plasma conditions.

Physical processes contributing to the widths include Doppler, Stark (pressure broadening) and Zeeman effects. The dependence of line widths on ion temperature and density and magnetic field for some carbon and iron lines is given in Fig. 16 [27]. The instrumental width for the NASA grating spectrograph (0.015 A) is also indicated in the figure.

Calculation of line profiles in high temperature and high density plasmas is an active area of research. Most line shape work has been done for low atomic number plasmas with more moderate properties than those produced at a laser focus. Calculations for heavier ions and higher densities involve extension of earlier work. Figure 17 shows theoretical profiles for the 1*s*-6*p* line in one-electron carbon [27]. Effects due to Doppler and Stark broadening, ion temperature and ion density are exhibited separately. A marked dependence on ion density, but not temperature, is evident.

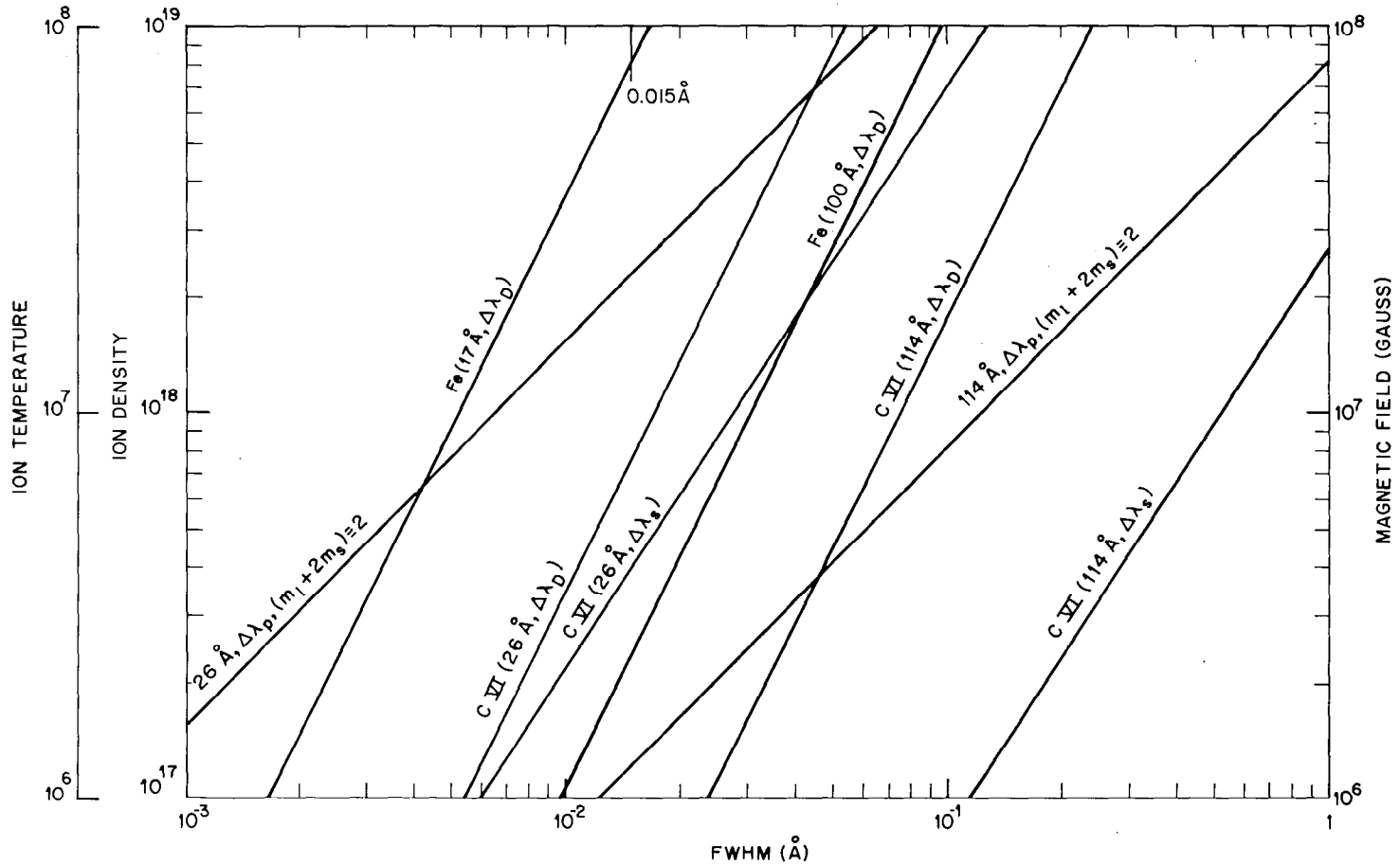

Fig. 16 — Calculated widths of C (26 A and 114 A) and Fe (17 and 106 A) lines due to Doppler, Stark and Zeeman effects

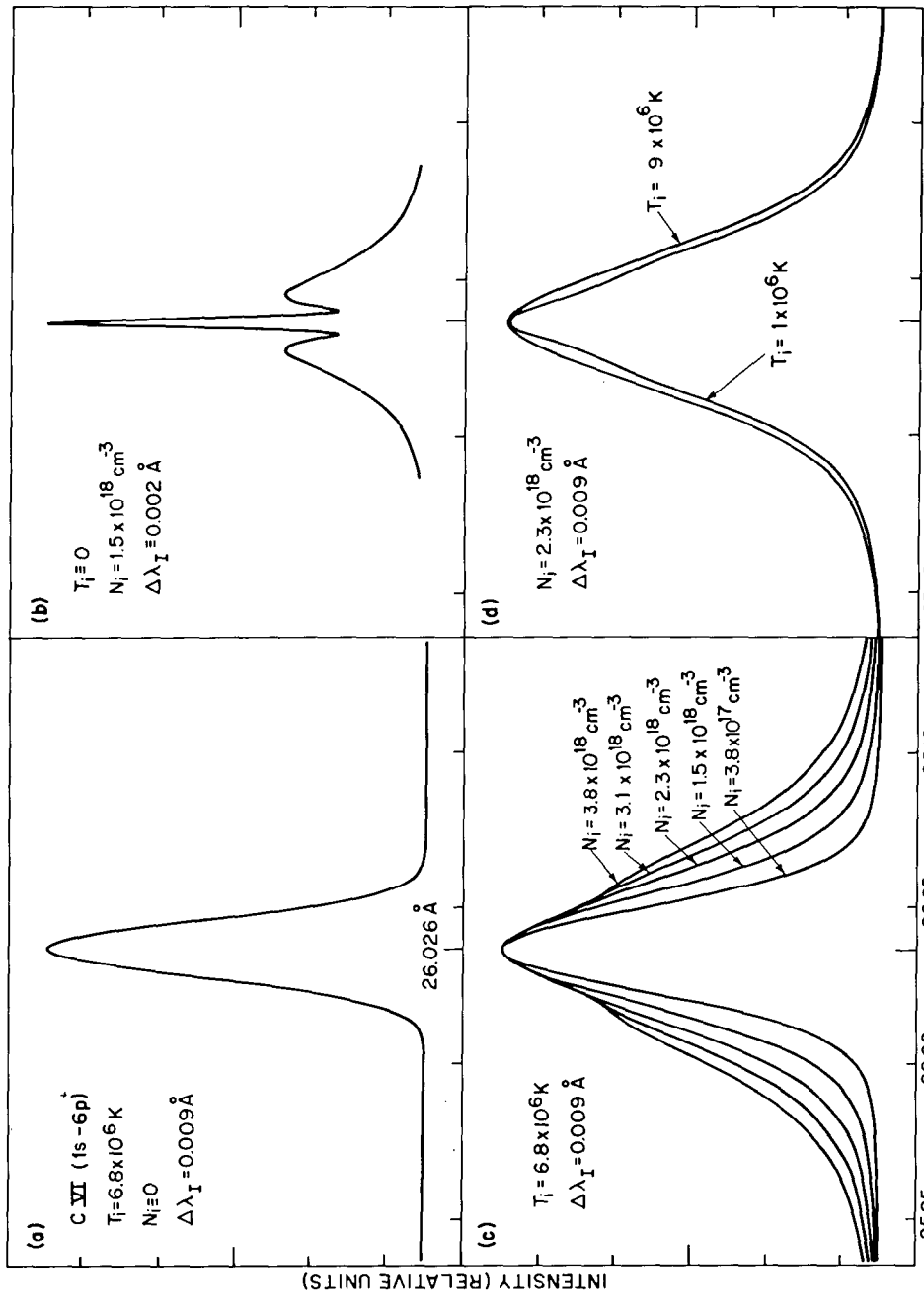

Fig. 17 — Computed profiles for the 1s-6p line in CVI for the conditions shown. These curves illustrate the effects of (a) Doppler broadening, (b) Stark broadening, (c) density variation and (d) ion temperature variation

Active Detector Response Functions

This and the next discussion are concerned with the analysis and use of data from continuous spectra, in contrast to the interpretation of line spectra given so far in this section. Intense continuum spectra can be measured with dispersive instruments. Then corrections for spectrograph (film recording) or spectrometer (active detector recording) can be applied to yield absolute spectra. The slope of such spectra is related to the electron temperature.

If the continuum is weak, or if one desires to avoid the relatively complex corrections for a dispersive spectrograph, then active detectors alone are used. They are usually preceded by windows which keep out light or the expanding plasma (and often serve as electrodes). Windows act as filters which limit the low-photon-energy response of detectors. Additional, separate filters are also commonly used to influence the spectral sensitivity of a detector. The high-energy response of detectors is limited by transparency of the active medium in the detector.

The response, or window, function of a detector is a curve which gives its sensitivity as a function of photon energy. It is given in units such as coulombs (out of the detector) per keV or Joule (of energy incident), or amps per watt on a time basis. The total signal obtained from an active detector (by a time-integrating under an oscilloscope trace) is proportional to the product of the absolute response function and spectrum. Cable and any other losses must be considered for absolute spectral determinations.

The shape of a response function depends primarily on absorption in the absorbers, entrance window and active medium. The scale factor (absolute magnitude) of the function often depends on additional factors, such as light-gathering efficiency and PM tube gain. Sometimes it is possible to compute both the shape and magnitude of a response function. For example, response functions for ionization chambers and Si p-i-n detectors can be accurately calculated if their composition and geometries are sufficiently well-known, and if care is taken to avoid problems such as recombination. In other cases, the shape of a response function can be computed satisfactorily and the scale factor must be determined experimentally for at least one photon energy. The use of NaI-scintillators with PM tubes is an example. In some cases, the entire response function must be determined empirically because, for example, the signal output does not vary linearly with energy deposited in the active region of the detector. This is true for some scintillator materials.

Response functions computed for Si p-i-n detectors behind two different Be windows are given in Fig. 18. The curves fall off slowly, according to the absorptivity of the 250 μm Si active region. The products of the response functions and spectral shape for a 1 keV plasma continuum are also given in Fig. 18. They illustrate the well-known net behavior of an active detector, namely that the overall window is limited on the high-energy side by the falling spectrum.

The response functions for absorber-scintillator-PM tube systems were computed and then put on an absolute basis by experimental calibration using radioactive x-ray sources. The sensitivity of the thermopile (microvolts per millijoule absorbed) was measured using low power laser pulses.

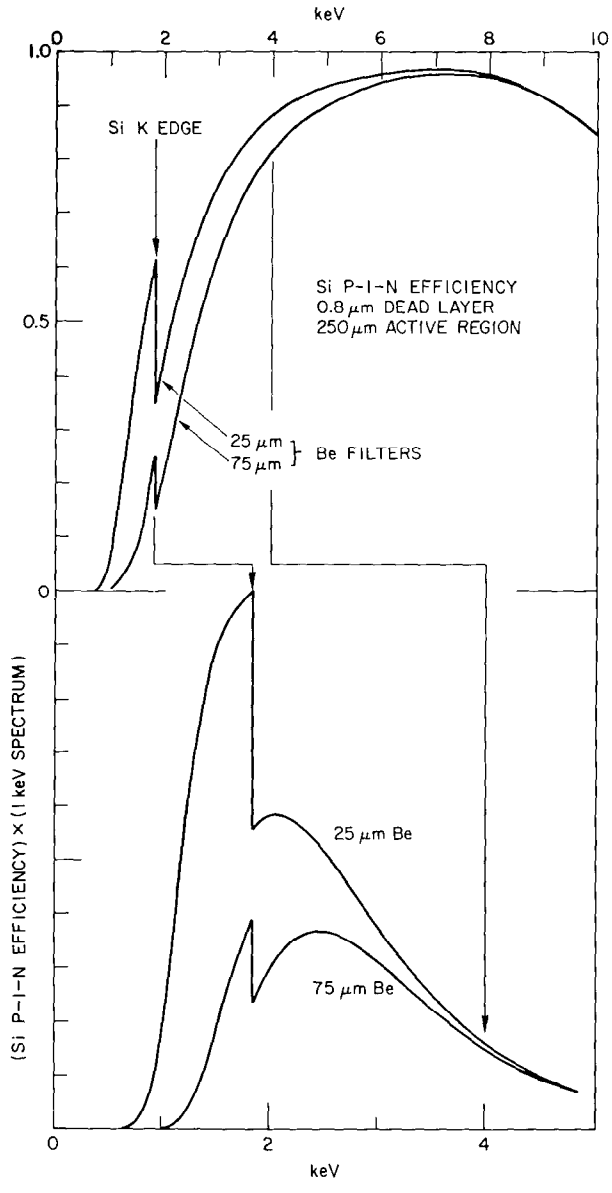

Fig. 18 — Response functions for 250 μm Si p-i-n detectors behind Be absorbers without (top) and with (bottom) a 1 keV spectrum

Temperature Determination for Continuum Data

A classical technique for determination of the effective plasma temperature involves the use of similar detectors behind different absorber foils to measure the intensity of the bremsstrahlung continuum [28]. Usually, different thicknesses of the same absorber material are used, as in Fig. 18. The ratio of signals from two such channels is uniquely related to plasma temperature, as shown in Fig. 19. Such a curve can be used for low atomic number plasmas ($\leqslant 6$) for which there are no lines in the photon energy region passed by the thinnest-absorber channel. The use of additional (> 2) channels permits the plasma temperature to be determined more accurately (if the continuum spectrum has a single slope) or permits determination of the curvature of a spectrum from a plasma which requires more than one effective temperature for its description.

Temporal Unfolding

The methods for x-ray data analysis discussed so far have involved line and continuum spectra. We now briefly consider the question of increasing the information available from time history measurements. The universal approach for obtaining information on a finer time scale is to improve the experimental time resolution. However, a complimentary mathematical effort aimed at unfolding the instrumental smearing function from a measured time history should also be made. The situation for temporal data is entirely analogous to that for spectral resolution. It is unquestionable that better experimental resolution is desirable, but the best available raw data can usually be improved substantially by unfolding.

In order to enhance a measured time history, the smearing function must be known. It can be measured for detectors with response times greater than about 100 psec. But for streak and sampling systems of interest in laser fusion, the smearing function can only be computed.

Once the smearing function is in hand, two routes can be taken to determine the true history free of instrumental effects. In the first, an assumed history can be folded through the instrumental function to obtain a curve to compare with the measured curve. The procedure can be iterated until a good comparison results. Then the assumed time history which gives the best match is taken as the actual temporal behavior. In the second approach any of several mathematical techniques can be used to go directly from the measured curve and the smearing function to the original time history. However, such methods are more complex than the first approach. They are also fraught with noise and truncation problems.

Since we are not developing fast (< 1 nsec) detectors in the NRL program, we are not using sophisticated methods for temporal unfolding. Only simple estimates for broadening introduced by the measuring equipment with time resolution ~ 1 nsec have been made. But it seems clear that more elaborate means to improve temporal information will be desirable to achieve x-ray time resolution < 10 psec.

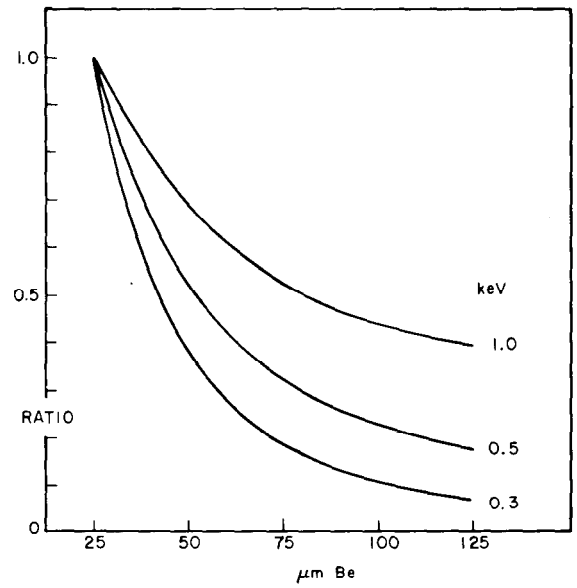

Fig. 19 — Ratios of p-i-n signals vs Be absorber thickness for the indicated plasma temperatures

Image Treatment

The information content of x-ray images (usually taken with a pinhole camera) can be improved by additional data treatment. In particular, two-dimensional densitometry of images allows quantitative comparison with theory. Figure 20 exhibits a pinhole camera image as taken and after contour densitometry. The density can be converted to intensity (photons/cm^2) in such an image since the most intense radiation which forms such an image usually spans a relatively narrow spectral region (1-2 keV wide). The efficiency of x-ray films is dependent on x-ray energy but it changes slowly enough with energy to permit use of a central energy in the spectrum for conversion of density to intensity. X-ray images can also be subjected to color-addition procedures which yield pictures in which each density (intensity) range has a different color. Such pictures are not necessary for quantitative analysis but they are useful for visual examination of an x-ray image.

D. SOFT X-RAY RESULTS

This section contains the results obtained with the equipment described in section B and the data analysis methods discussed in section C. A survey of the general characteristics of x-ray emission is given first. It includes various spectral, intensity, isotropy, time and source size information for targets ranging from CH_2 through uranium. Then, results with targets of increasing atomic number are described in more detail, beginning with grating and absorber-foil spectroscopy of CH_2 plasmas. Plasma characteristics obtained from a fluorine spectrum are summarized next. Laser-pulse-variation experiments (0.53 and 1.06 μm, < 1 to 60 J, 50-900 psec) with aluminum targets which yielded the dependence of x-ray spectra and electron temperature on pulse parameters are then described. Systematic measurements of K spectra (Na-Ti), L spectra (Cr-Zr) and M spectra (Sn-Er) are reviewed prior to a summary and discussion of x-ray and plasma diagnostic results which is given at the end of the section.

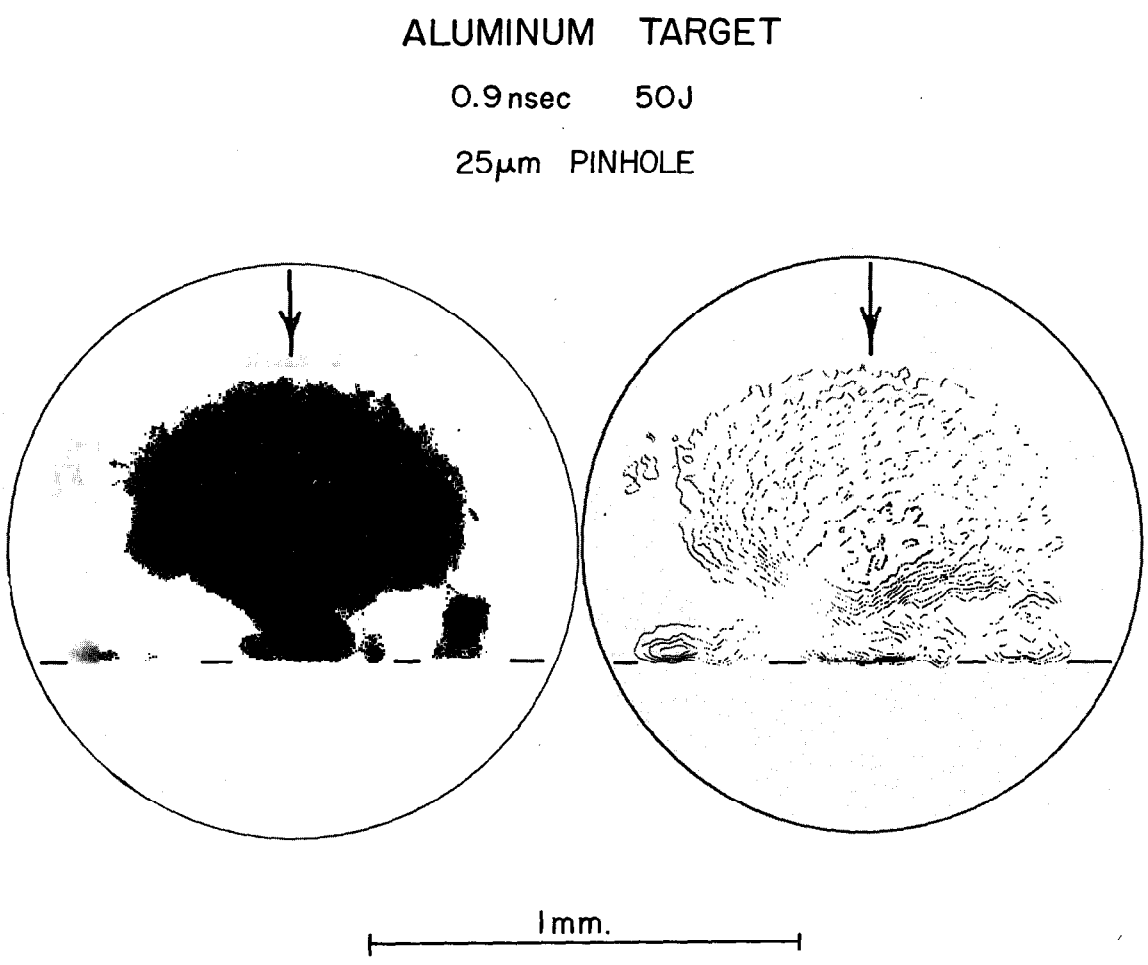

Fig. 20 — X-ray pinhole camera images as recorded (left) and after contour densitometering (right)

General X-Ray Characteristics

A long range aim of the soft x-ray measurements of laser plasmas is determination of the dependence of the x-ray characteristics on experimental conditions. The major variables include: pulse parameters (wavelength, shape, total energy, etc.), focusing conditions (focal length of lens, shape and size of the focal region, etc.) and target characteristics (composition, geometry, orientation, etc.). Most of the work to date involved determination of changes in spectra and intensities as a function of the laser power and target composition.

Spectra were obtained with the NASA grating instrument from targets containing elements from lithium through uranium. Figure 21 illustrates typical spectra obtained on one of the plates in the spectrograph. The CH_2 and fluorine spectra are discussed in detail later.

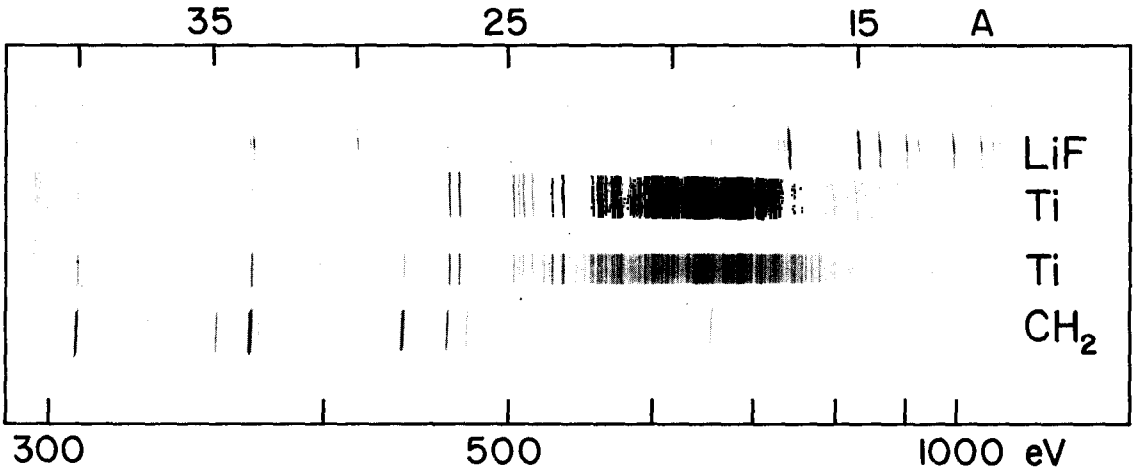

Fig. 21 — One plate from the NASA grating spectrograph showing, from top to bottom, a F spectrum from LiF, two Ti spectra and a carbon spectrum from CH_2

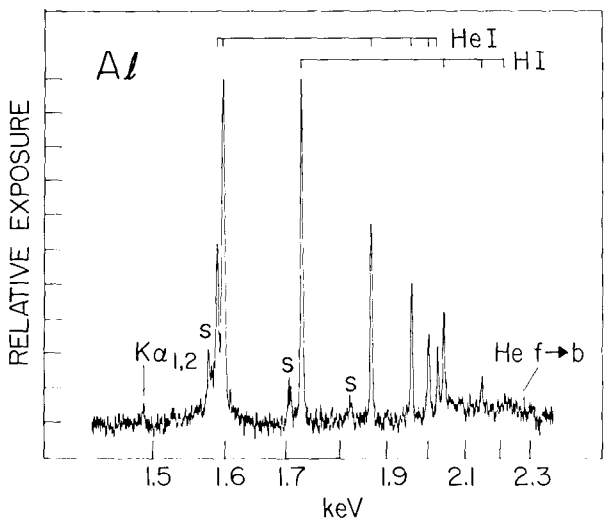

Fig. 22 — Al K x-ray spectrum from a plasma produced by a 1.8-J, 0.25-nsec laser pulse. Rydberg series from Al ions isoelectronic with H and He atoms, the He-like free-to-bound continuum and satellite lines S constitute the plasma spectrum. The $K\alpha_{1,2}$ lines are from target fluorescence.

X-ray spectra were measured with crystal instruments from elements in the range from sodium through uranium. Figures 22 through 24 show typical K, L, and M spectra from increasingly heavier elements excited with power densities on the order of 10^{14} W/cm^2 [29,30].

K x-ray spectra resulting from transitions to the 1*s* level have been obtained from elements in the range Na-Ti. Spectra from all these elements are similar. Figure 22 shows the Al spectrum. Classification of lines in spectra such as this presented no problem because of many laboratory and solar measurements of similar emission lines from elements in this range. As indicated in Fig. 22, lines from three ion species appear. An intense Rydberg series and free-to-bound continuum from He-like (2-electron) Al are evident, as

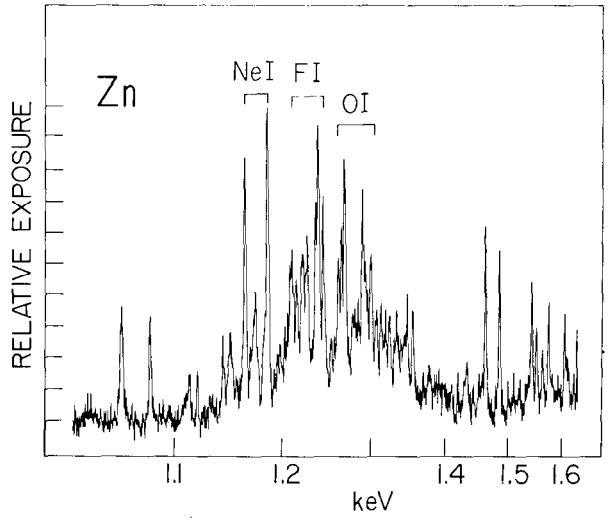

Fig. 23 — Zn L x-ray spectrum from a plasma generated by a 2.0-J, 0.9-nsec laser pulse. Groups of lines from $2p$-$3d$ transitions in Zn ions isoelectronic with O, F, and Ne atoms are indicated.

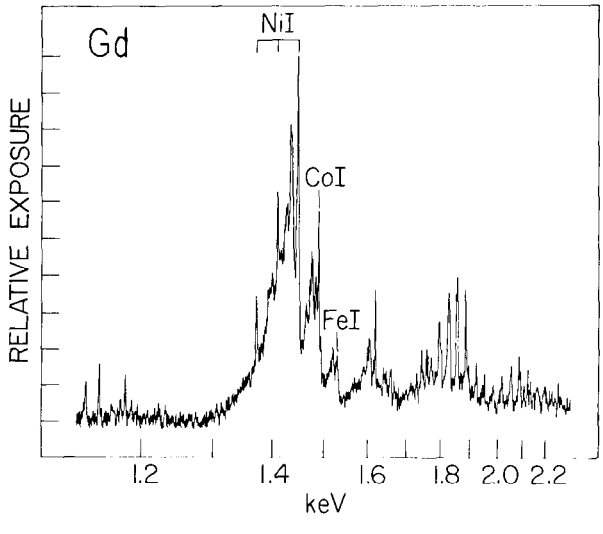

Fig. 24 — Gd M x-ray spectrum from a plasma produced by a 3.5-J, 0.9-nsec laser pulse. Lines from $3d$-$4f$ transitions in Gd ions isoelectronic with Fe, Co, and Ni are labeled.

is the Lyman series of H-like (1-electron) Al. Poorly resolved satellites from transitions in Li-like (3-electron) ions appear near the He $1s$-$2p$ resonance line, while satellites from He-like ions accompany the H $1s$-$2p$ (Lyman α) line.

L x-ray spectra from transitions to the $2s$ and $2p$ levels were measured from about half of the elements Cr through Zr. The spectrum of Zn given in Fig. 23 is typical of these spectra. It is more complex than the K spectrum in Fig. 22 due to the larger number of possible ionization stages and strong multiplet structure present for most transitions. Interpretation of the Zn spectrum is not complete, but it is possible to identify the major ionization stages. Again, laboratory and solar spectra from lighter elements were used to interpret our results. Transition energy calculations using self-consistent Dirac-Slater wave

functions were made to confirm identifications of the major lines in the Zn spectrum. As indicated in Fig. 23, transitions $2p$-$3d$ in Ne-like (10 electron), F-like (9-electron) and O-like (8-electron) Zn ions dominate the spectrum. Two pairs of lines from Ne-like ions are also strong, $2p$-$3s$ below 1.1 keV and $2p$-$4d$ near 1.47 keV.

M x-ray spectra due to transitions to the $3p$ and $3d$ levels from Sn through Er were also measured. Figure 24 shows the spectrum of Gd which is representative of the M spectra. Just as the K and L spectra are quite distinctive in appearance, the M spectra also have a characteristic pattern. But much less was known about this M radiation compared to the K and L spectra in the other figures. Spectral measurements (in the UV) for transitions to the $3p$, d levels had been made only up to Mo, 14 atomic numbers below Ba. Hence we had to rely on the SCF calculations to identify the ionization stages and transitions which produced the spectrum in Fig. 24. As shown, $3d$-$4f$ transitions occurred in Ni-like (28-electron), Co-like (27-electron) and Fe-like (26-electron) Gd ions. Four other transitions are important. The three strongest lines below 1.2 keV are due to $3d$-$4p$ transitions in Ni-like ions. Isoelectronic extrapolation of the lighter-atom UV data confirmed the $3d$-$4p$, f identifications for Ni-like Gd. The group of lines around 1.6 keV is due to $3p$-$4d$ electron jumps. Another group (1.7-1.9 keV) is from $4d$-$5p$, f transitions. And, finally, the radiation above 2.0 keV is due to $4d$-$6p$, f electron jumps.

N x-ray spectra from very high atomic number elements might also be expected. But, laser irradiation of U did not result in any resolved lines $>$ 800 eV. Only a faint continuum was visible on the film.

The general spectral results obtained in this work can be summarized by use of the Semi-Moseley diagram (square root of x-ray energy vs atomic number) shown in Fig. 25 [31]. The lines trace the energies of the lowest resonance transitions in K, L, and M spectra from He-like (2-electron), Ne-like (10-electron) and Ni-like (28-electron) ions, respectively. Points indicate elements for which spectra were measured in the NRL LMI program. The crosses on the L and M lines show the limits of those series prior to this work. Resonance K spectra from elements heavier than Ti had been measured before with a vacuum spark source but both the L and M sequences were substantially extended by use of laser data. The dotted line connects the extreme elements in each series for which spectra can be obtained in a single shot with 10^{14} W/cm^2 power density. The decrease in the dotted line with increasing atomic number is attributed to the additional energy and time which must be expended in stripping heavier elements. Curiously, the line appears asymptotic to an energy value nearly equal to the plasma electron temperature. Figure 25 indicates only one transition for each type of closed shell ion. Actually, complex spectra resulting from several transitions (each of which usually involves multiplet structure) in at least three ionization stages are usually observed, as in Figs. 22 through 24.

Measurements of spectra, or integrated intensities made with active detectors, are necessarily made in one (or at most a few) emission directions. The uniformity of x-ray emission was determined for Al, Cu and Gd targets using x-ray films [32]. Results for the first two of these elements are given in Fig. 26. The points near the density axis in Fig. 26 show that, for both Al and Cu targets, there is a tendency for the intensity to peak in the direction normal to the target. In the Al measurement, a small enhancement along the target plane is also visible. However, these departures from isotropy are relatively

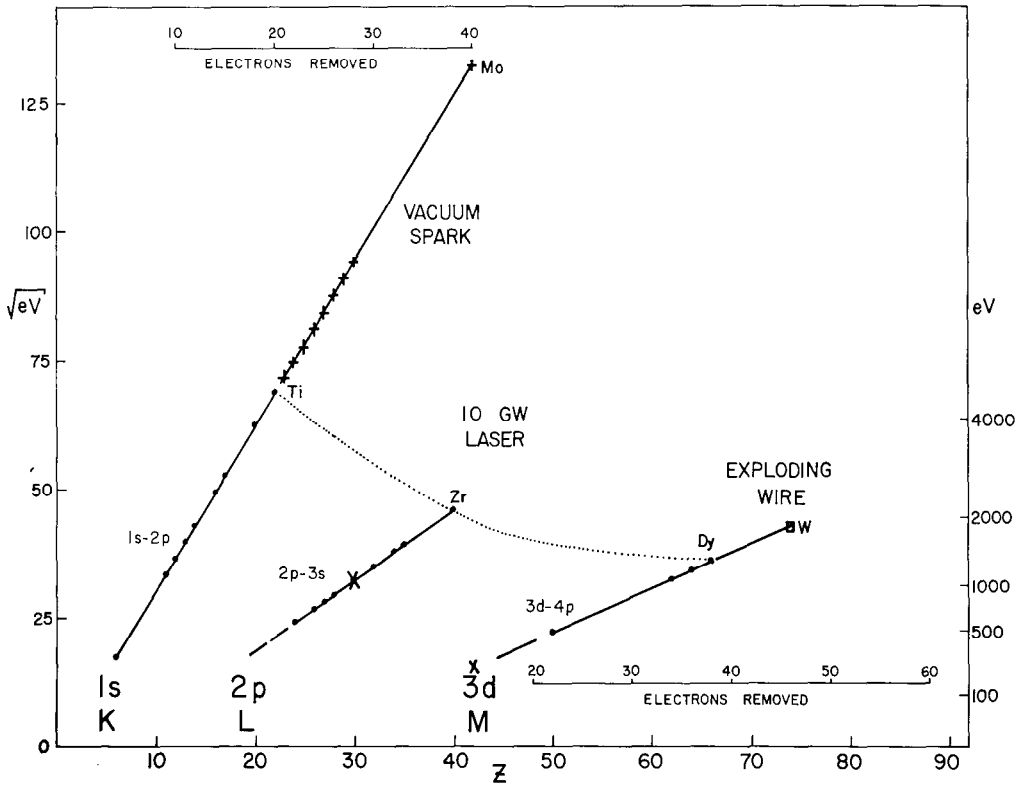

Fig. 25 — Semi-Moseley plot for first resonance lines in K, L, and M spectra from closed shell ions in high-temperature plasmas. Ionization stages are indicated for K and M series. The dotted line connects the heaviest element for which lines can be excited and measured with a crystal-film spectrograph using a 10 GW, 1 nsec laser pulse.

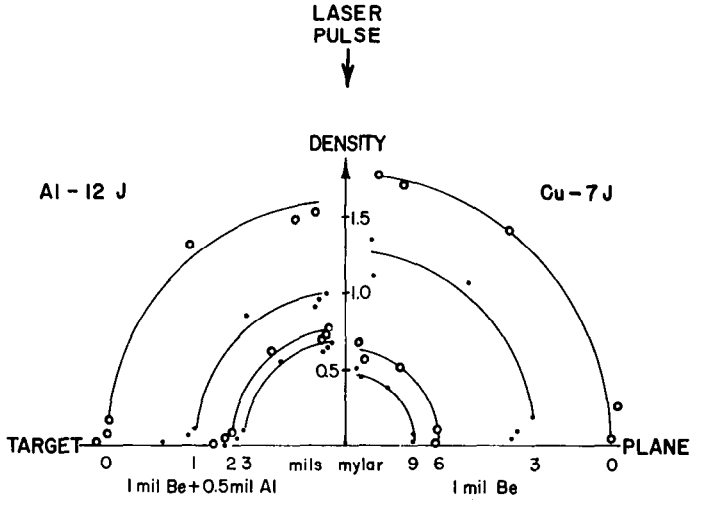

Fig. 26 — Angular distribution x-ray data from Al (left) and Cu (right) targets obtained through the windows and filters shown at the bottom with film packs such as shown in the center of Fig. 10. Film density is plotted as a function of direction relative to the target plane and the normally-incident laser beam.

small. That is, the x-ray emission can be taken as spatially uniform over the 2π solid angle away from the target. Measurements in the remaining 2π solid angle cannot be made with thick slab targets. However, because there is no preferred emission direction for soft x-rays from a plasma and because opacity effects are not evident, it can be assumed that an equal intensity will be emitted into the target. Of course, some of the energy will be deposited in the denser plasma and be radiated again or contribute to the plasma expansion energy. Measurements of the x-ray angular distribution using thin targets should show directly the magnitude of the x-ray intensity in the forward direction.

The spectra in Figs. 22 to 24 were corrected for film efficiency. Further corrections for crystal efficiency and Be window absorption were made. Then the spectra were integrated over photon energy and over solid angle to obtain the total x-ray line emission. The ratios of integrated x-ray line energy to the incident laser energy are 0.5% for Al, 9.0% for Zn and 1.5% for Gd (± 20% relative) [30].

Most of the total intensity measurements were done with active detectors, in particular the Ag thermopile behind a 25 μm Be window. Dependence of the x-ray intensity on atomic number Z was determined for 25-45 J, 900 psec pulses with targets CH_2 through Pb [33]. The result is given in Fig. 27 expressed as the efficiency for conversion of laser light into x-rays which will pass through a 25 μm Be window (800 eV cutoff) (again integrated over 4π solid angle). The strong dependence of integrated intensity on Z is easily rationalized: peaks occur when K, L, or M binding energies match the electron temperature T_e. The decline of each peak toward low Z is caused by inefficient production of radiation in an overheated plasma and by absorption of the relatively soft line radiation in the detector window. It is expected that the use of a thinner window or lower laser power would shift the peaks to lower Z. The falloff toward high Z results from the atomic electrons being too tightly bound to be efficiently excited at the existing plasma temperature. Increasing laser power and T_e should shift the peaks to higher Z. Variations in T_e with Z must exist since radiative cooling alternates in importance with increasing Z, being maximum at the peaks in Fig. 27. Also, more energy goes into ionization at high Z compared to low Z. But it is expected that variations in T_e are less important in determining the peak locations in Fig. 27 than the rapid variations in binding energies with changing Z. Additional measurements are needed to better define the shapes of the peaks and to test the expected variations with detector window thickness and laser power.

As the laser power and T_e are increased for fixed targets, the x-ray intensity will vary depending on the relation of binding energies to T_e. Figure 28 shows the dependence of intensity on laser power for elements at or near the peaks in Fig. 27 [33]. There are peaks for each element, with the peaks being sharper for higher spectral series. That is, the Al (K lines) peak is broad while the Gd (M lines) peak is sharp. Cu (L lines) is intermediate. A prepulse leads to substantially higher x-ray intensity. As shown for Cu, increases up to about 50% can result from use of the prepulse.

Variation in x-ray intensity with time could not be followed in detail without a streak camera. However, the pyroelectric detector trace shown in Fig. 29 contains useful information [6]. The main peak has a FWHM of nearly 1 nsec after removal of the detector-cable-scope system response time. Hence the bulk of the x-ray emission appears in a time nearly equal to the laser pulse width. The small shoulder (3-4 nsec) and the tail in Fig. 29 may be due to recombination radiation.

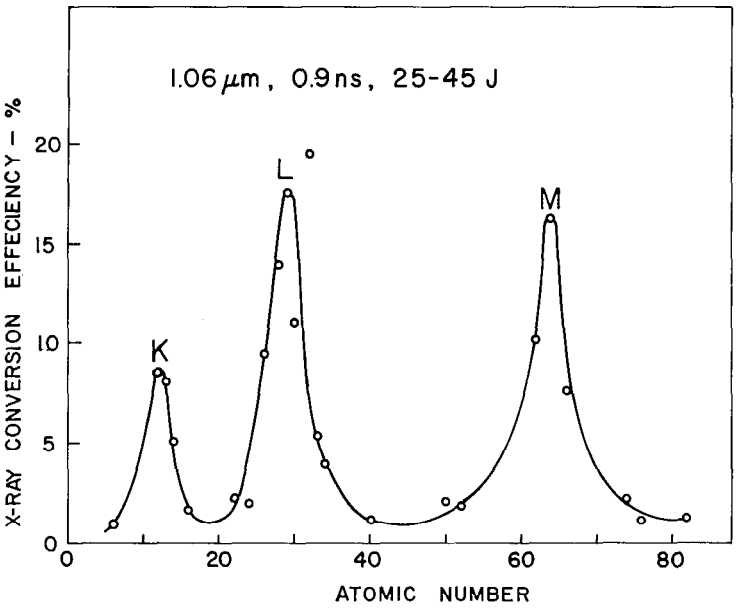

Fig. 27 — X-ray intensity from various elemental targets excited by pulses with the indicated characteristics as measured through a 25 μm window (800 eV cutoff) with the thermopile shown in Fig. 8. The measured intensities were integrated over 4π solid angle and divided by the incident pulse energy in order to be expressed as conversion efficiencies.

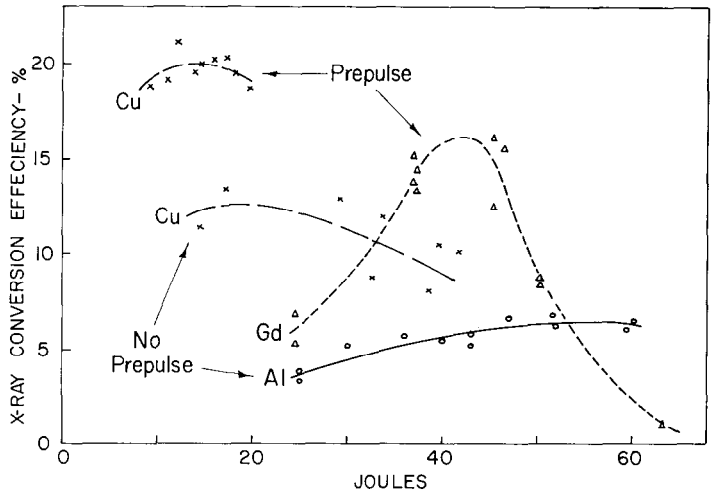

Fig. 28 — Power dependence of x-ray conversion efficiency for 0.9 nsec pulses on Al, Cu and Gd targets. The effect of a prepulse 5% as big as the main pulse and 0.75 nsec ahead of it is shown for the Cu target.

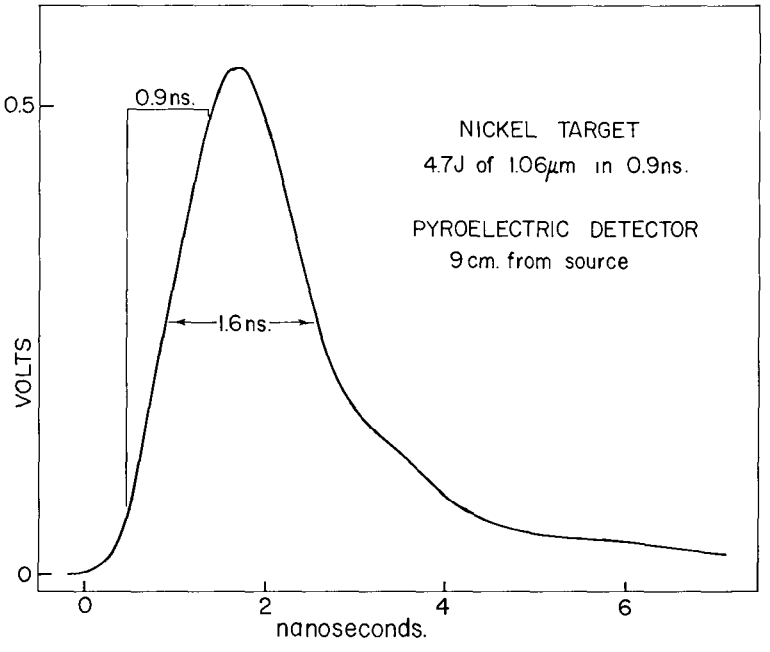

Fig. 29 — Oscilloscope record of the x-ray intensity for the indicated conditions as measured with the pyroelectric detector shown in Fig. 9

The size of the x-ray emitting region has been determined using screen, pinhole, and collimator devices. The early shadowgraphy experiments with a screen (Fig. 11) yielded low-resolution information [12]. These showed that the greatest x-ray intensity came from a region smaller than 50 μm in size (the wire dimension). However, it was not possible to determine the shape of the region of strong emission or the extent of the region of weak emission in that experiment.

High-resolution, low-sensitivity pinhole cameras gave information on the focal region. A pinhole picture was shown in Fig. 20. In that case, the x-ray emission arose from a region substantially in front of the target surface, in contrast to the photographs usually obtained. In some photographs from low-melting-point meterials, rays apparently caused by ejecta are visible in the pinhole photographs. The basic result of the pinhole photography is that the x-ray emission arises predominantly from the focal regions, that is, from a volume about equal to the cube of the focal spot diameter. Figure 30 shows an image of the region of most intense emission from a Zr target as measured with a 25 μm pinhole [34]. Use of higher laser powers extends the region of intense emission. To measure the region of weak emission, a bundle of collimator tubes (Fig. 12) was used with the result shown in Fig. 31. It is seen that for the lighter target, x-ray emission is visible from as far as 3 cm in front of the target. Differences in ion velocity and emission characteristics yield a smaller image for the Gd target.

The characteristics of x-ray emission arising from focused $<$ 10-60 J, $\sim$ 1 nsec laser pulses are easily summarized: (a) the spectra contain many lines from $<$ 1 to about 4 keV

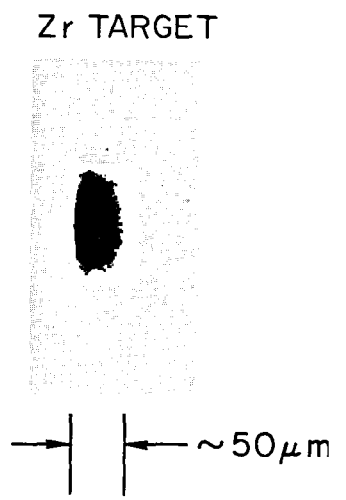

Fig. 30 — X-ray pinhole photograph taken with 1-3 keV radiation through a 25 μm pinhole and recorded on Kodak No-Screen x-ray film behind a 25 μm Be window. The plasma was created by a 900 psec, 10 J pulse focused with an f/14 lens from the right.

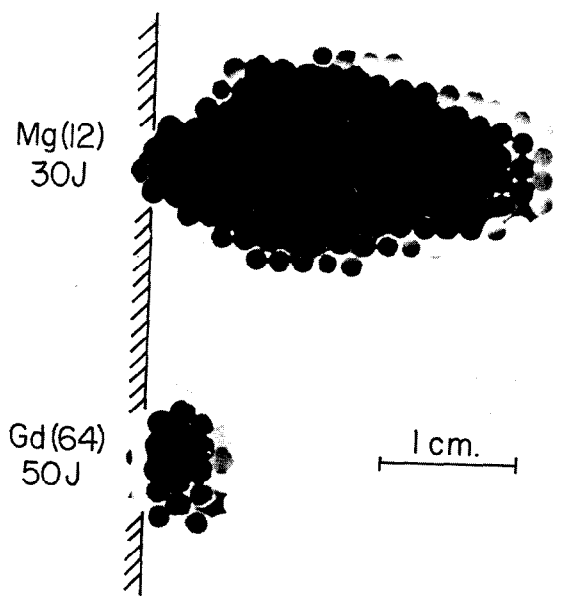

Fig. 31 — Collimator x-ray images obtained with the device shown in Fig. 12. The collimator was 2 cm from the plasma, with the tube axes parallel to the target plane. A 25 μm-window Be pack with No-Screen film was placed immediately after the collimator.

with K, L, and M spectra having characteristic and different appearances, (b) x-ray conversion efficiencies which range up to nearly 20% (based on a measurement of nearly isotropic emission) are strongly dependent on the target atomic number and less-strongly dependent on the laser power, (c) the emission time is about equal to the laser pulse time, and (d) the most intense emission comes from a region similar to the focal spot size (< 100 μm) but appreciable emission arises from a larger volume. Taken together, these data on the general x-ray characteristics show that laser plasmas emit x-rays at a rate exceeding 10^{13} W/cm^3 of the plasma.

CH_2 Spectra

Two soft x-ray experiments have been done with CH_2 to date: (a) a grazing-incidence grating measurement of the line spectrum in the 300 eV to 500 eV range generated by 30 J, 900 psec pulses and (b) measurement of the absolute continuum intensity in the few keV range excited by few joule, 50 psec pulses. The aim of the first experiment was plasma diagnostics, in particular determination of the electron density. The second set of measurements is a prelude to a later experiment at NRL with pulse conditions similar to those employed in an experiment at LASL. The results of the work to date at NRL are summarized here.

Figure 32 is a densitometer trace of the carbon K region of the spectrum (Fig. 21) obtained from CH_2 in the first measurement. Rydberg series for H- and He-like ions are visible, generally similar to the Al results given earlier in Fig. 22, except that here emission from one-electron ions is the most intense. An expanded densitometer recording of the 1*s*-6*p* and 1*s*-7*p* lines in one-electron carbon is given in Fig. 33 [27]. The calculated profiles in this figure were obtained by making a fit to the 1*s*-6*p* line and then using the parameters obtained to compute the 1*s*-7*p* line shape. The instrumental width was 0.015 A and the doppler broadening corresponding to an ion temperature of 7×10^6 K was used. The fit shown in Fig. 33 may be improved slightly but doing so will not affect the derived density significantly. The resulting ion density of $n_i = 2 \times 10^{18}$ cm^{-3} (which caused the dominant Stark broadening) is not sensitive to the ion temperature. This ion density corresponds to an electron density of 1.2×10^{19} cm^{-3}. Such a value is considerably less than the critical density of 10^{21} cm^{-3} because in the present time- and space-integrated measurement, emission was obtained from regions of the plasma with densities which varied over a wide range below 10^{21} cm^{-3}.

For the second CH_2 measurement, 3-6 J, 50 psec pulses were focused by a f/14 lens to power densities of around 2×10^{14} W/cm^2. The integrated continuum intensity was measured with a Si p-i-n detector and x-ray film behind 30 μm Be windows [35]. Hence, x-ray energies in the range from above 800 eV to several keV were recorded. Figure 18 shows the Be p-i-n window response functions for a temperature of 1 keV which is in the range found in other work for about 10^{14} W/cm^2 on target. Figure 34 compares the results with a calculation performed at Livermore for similar pulse conditions [36]. Only a single p-i-n detector was used in this preliminary measurement so that no temperature was obtained. But the temperature-dependent acceptance band of the p-i-n detector must be known to obtain an absolute intensity. Three values (1/2, 1 and 2 keV) were assumed, consistent with other measurements [37] and the theoretical curve. The results are plotted in Fig. 34 for two assumed temperatures. The film results are between 2 and 3 times lower

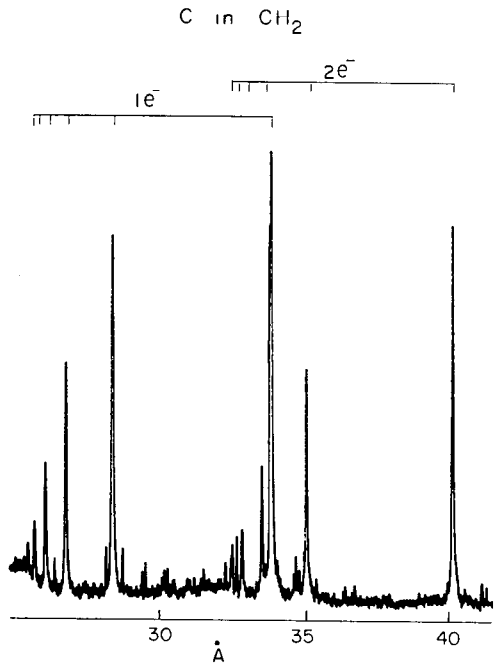

Fig. 32 — The Rydberg series from C V and C VI from CH_2 target excited with a 30 GW pulse

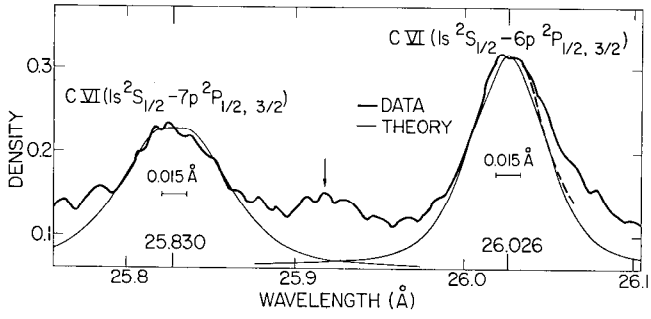

Fig. 33 — Measured densitometer trace and theoretical Holtsmark profiles for the 1*s*-6*p* and 1*s*-7*p* lines of C VI at 26.026 and 25.830 A, respectively. The dashed line defines the unshifted line shape. The vertical arrow indicates the presence of a weak impurity line. The instrumental FWHM is 0.015 A. Zero intensity of the theoretical profiles is the level of true background and continuum.

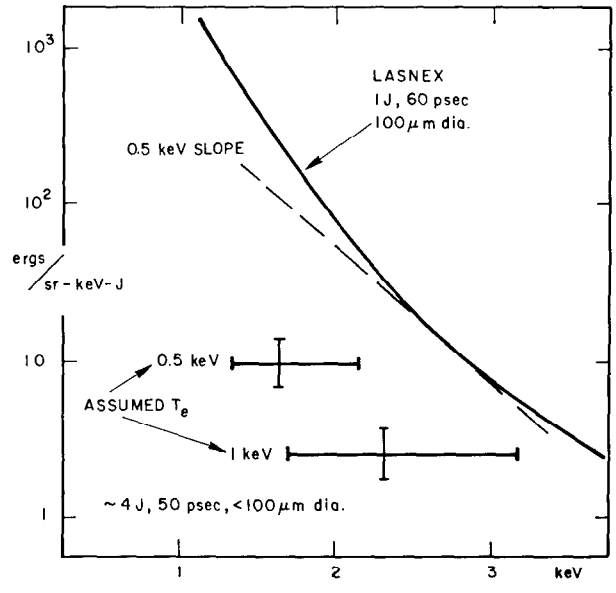

Fig. 34 — Computed and measured continuum spectra for 2×10^{14} W/cm^2 irradiation of CH_2 targets. The vertical bars indicate the variation for five shots and the horizontal bars give the width of the acceptance band of the p-i-n detectors for the temperatures assumed.

than the p-i-n results (they were gotten assuming a single photon energy, namely the peak of the response function). Figure 34 shows that the NRL results (normalized per Joule incident) are about one order of magnitude below the LASNEX calculations. This discrepancy at the 10^{14} W/cm^2 level is smaller than that found between LASNEX predictions and LASL measurements at the 10^{16} W/cm^2 level.

Fluorine Spectrum

A particularly well-resolved and useful fluorine spectrum was obtained with the grating spectrograph for 900 psec, 30 GW pulses (see Fig. 21) [38]. As can be seen from the densitometer trace in Fig. 35, the spectrum is qualitatively similar to the carbon spectrum in Fig. 32. Three types of plasma diagnostic information were extracted from the spectrum: (a) the intensity ratio of 1*s*-2*p* lines (labelled A) in the H- and He-like ions gave an estimate of the *electron temperature*, which was 400 eV in this instance, (b) the widths of lines (labelled B) near the series limits and the ratio of a He-like satellite to the 1*s*-2*p* He-like intercombination line (labelled C) both yielded an *electron density* of 5×10^{19} cm^{-3} and (c) the intensity ratio of the two longest wavelength satellites (labelled D) indicated that the plasma was only *approximately in ionization equilibrium.* The analysis of the fluorine spectrum is indicative of what plasma information can be extracted from high resolution spectra. However, work is not limited to the three factors enumerated above. As was done for the carbon spectrum, line profile analysis can yield a check on the electron density obtained. Also, the free-to-bound continuum above each series limit can yield the electron temperature if a spectrum is measured with a spectrograph of known efficiency (as a function of wavelength).

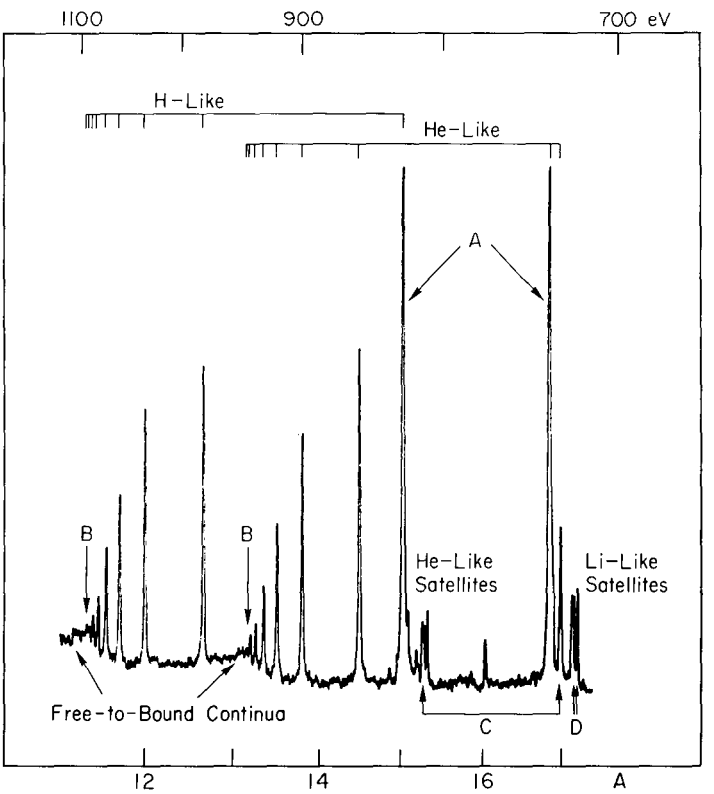

Fig. 35 — Fluorine K spectrum from a laser-produced LiF plasma showing H- and He-like Rydberg series and associated satellites. Features used for plasma diagnostics are labelled A-D and discussed in the text.

Aluminum (Pulse Variation)

Spectra from Al plasmas, such as that shown in Fig. 22, have been measured with crystal spectrographs over a wide range of pulse conditions [39,40,41]. The extremes of the excitation conditions were: $<$ 1-60 J, 50-900 psec and 0.53 μm and 1.06 μm incident laser light. Not all combinations of parameters could be tested. However, power variation was accomplished by changing the pulse energy and width independently. And, some results on wavelength variation were obtained.

Figure 36 shows the changes in Al K resonance spectrum as the incident energy in 900 psec pulses is varied. The increasing intensity of the H-like $1s$-$2p$ resonance line is evident.

Figure 37 shows changes in Al spectra as a function of pulse width for pulses with energies near 1.7 J. In this case, the intensity of the Lyman α line relative to the He $1s$-$2p$ resonance line first increases and then decreases as the laser power is increased (as the pulse width is decreased).

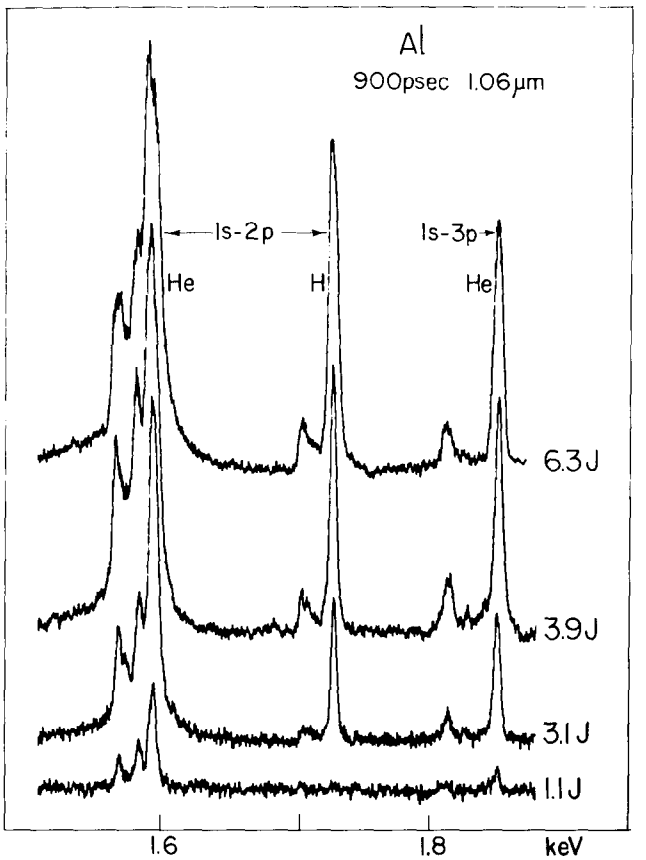

Fig. 36 — Al K resonance spectra obtained for constant pulse width and variable laser energy

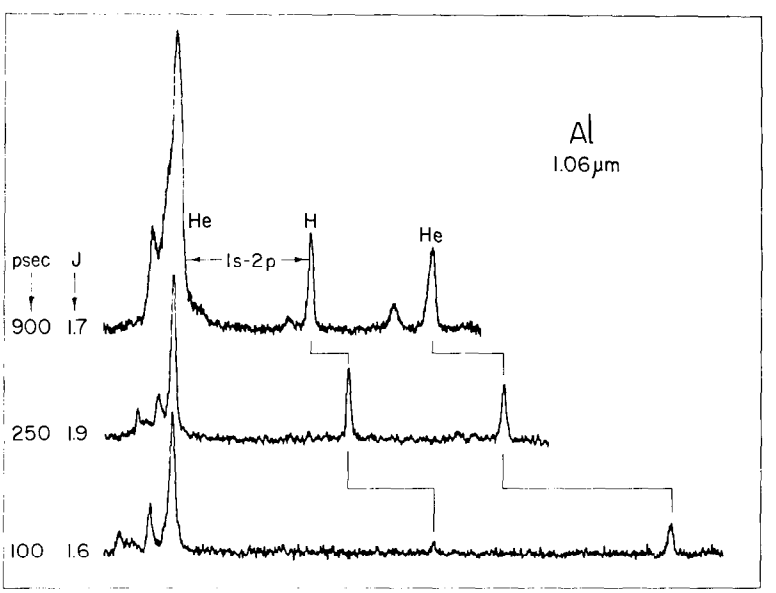

Fig. 37 — Al K resonance spectra obtained for nearly constant laser energy and variable pulse width

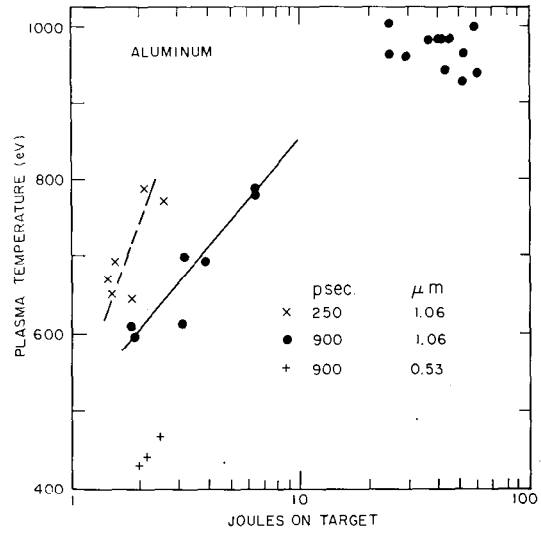

Fig. 38 — Plasma electron temperatures estimated from the H to He $1s$-$2p$ intensity ratio by use of Fig. 15 for various pulse conditions

Spectra such as those shown were corrected for the nonlinear film response using extrapolated film sensitivity curves. Then line intensity ratios were used with computed ratio vs electron-temperature curves such as that shown in Fig. 15 in order to obtain effective temperatures. Figure 38 gives the results for 250 and 900 psec pulses. Temperatures for 900 psec pulses increase with incident energy up to about 10-20 J. However, the temperature seems to saturate for pulses in the 20-70 J range. This saturation may be due to limitations in this method of estimating temperatures from time-integrated spectra. Or, it may be real and due to energy loss to surrounding material in the slab targets by electron thermal conduction. If the latter possibility is correct, then the use of limited-mass target sizes matched to the laser pulse conditions should yield Al plasma temperatures greater than 1 keV. For pulses of a few joules, the plasma temperatures produced with the 250 psec width are greater than those for the 900 psec width. But the trend does not continue for the very short pulses. As shown in Fig. 37, short pulses appear to produce a colder plasma. Again, this effect may be due to a breakdown in the conditions assumed in this method of determining an effective plasma temperature. For short pulses, a state of transient ionization may exist during the entire laser pulse. In that case, the conditions for coronal equilibrium would not be established. That is, the electron temperature may be high enough to excite H-like lines, but there is not enough time for 50 psec pulses to strip the Al ions to the H-like stage. As shown in Fig. 38, a few shots were obtained with frequency-doubled green light. These yielded plasmas with somewhat lower temperatures, as would be expected from simple models of laser heating of dense plasmas.

Questions concerning the applicability of the line-ratio method of temperature determination will be answered by comparison of the measured spectra with the results of numerical rate-equation calculations of spectra [42]. In the interim, the method provides a useful although approximate effective temperature with which to study the effects of laser-pulse-parameter variation over much of the experimentally accessible range.

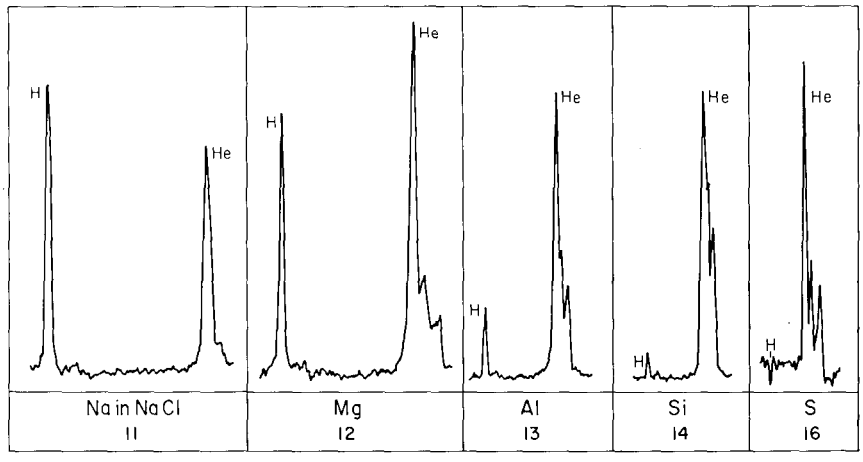

Fig. 39 — Densitometer traces of 1*s*-2*p* transitions in H-like and He-like ion species produced by 1.06 μm, 2 J, 0.9 nsec pulses. Vertical scales are arbitrary.

Sodium Through Titanium (K Spectra)

Three examples of K resonance spectra were already presented and discussed: C, F, and Al. Additional studies of the 1*s*-2*p* transitions in H- and He-like ions and their associated satellites have been performed and will be discussed here.

Figure 39 shows the result of an early set of low-power (2 J, 900 psec) low resolution measurements of 1*s*-2*p* transitions in Na-Si and S [43]. The intensity from H-like ions (i.e., the Lα line) is strongest for the lower Z elements which are most easily ionized. It remains to extract temperatures from the line ratios for each element in order to study the Z dependence of plasma temperature for constant pulse conditions. Elements for which radiative cooling is important (e.g., those near the peaks in Fig. 27) may have somewhat lower temperatures than those which do not radiate efficiently.

A higher-resolution study of the Lα region was made for Na, Mg and Al as shown in Fig. 40. Helium-like satellites (lines 1-5) of Lα (lines 6 and 7) are evident. These satellites should prove useful for plasma diagnostics [44].

Satellites of the He 1*s*-2*p* resonance and intercombination lines have been extensively used to determine electron temperatures and ionization equilibrium conditions in solar and laboratory plasmas [26]. Figures 41 and 42 give high resolution spectra of elements in the Na-Ti range [44]. This work represents the most complete study of these lines to date. As with Fig. 39, the overall intensity decreases with increasing Z. Several trends with Z are discussed in detail elsewhere [44]. Among them is the increasing intensity of the satellites such as peaks *k* and *j* relative to the resonance peak *w* in going from Na to Ti. Roughly, this occurs because it is more difficult to produce and excite He-like ions in higher Z atoms and inner-shell ionization of the predominant Li-like ions becomes relatively more important. Analysis of the satellite intensities in Figs. 41 and 42 showed that existing theory was inadequate. Recently new calculations of Auger rates in Li-like ions have been performed [26]. The new rates lead to relative satellite intensities which agree better with experiment for laser-produced plasmas.

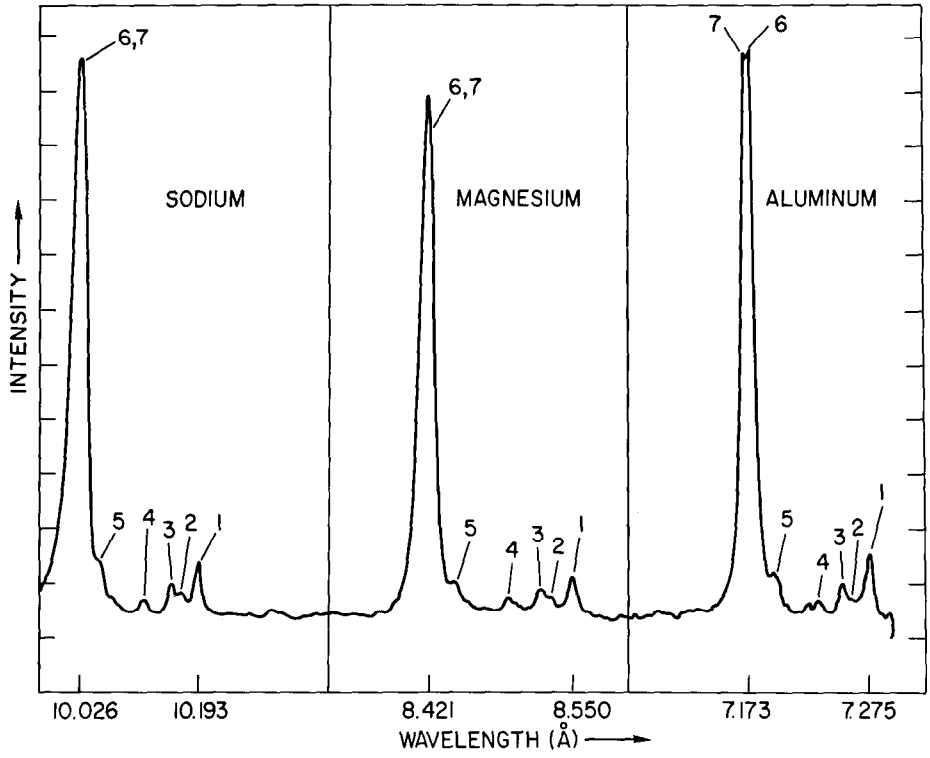

Fig. 40 — Satellite lines of the $1s^2S_{1/2}$—$2p^2P_{1/2,3/2}$ Lα lines. The numbers refer to the transitions tabulated in Ref. 44. Note the fine-structure splitting of the aluminum Lα line.

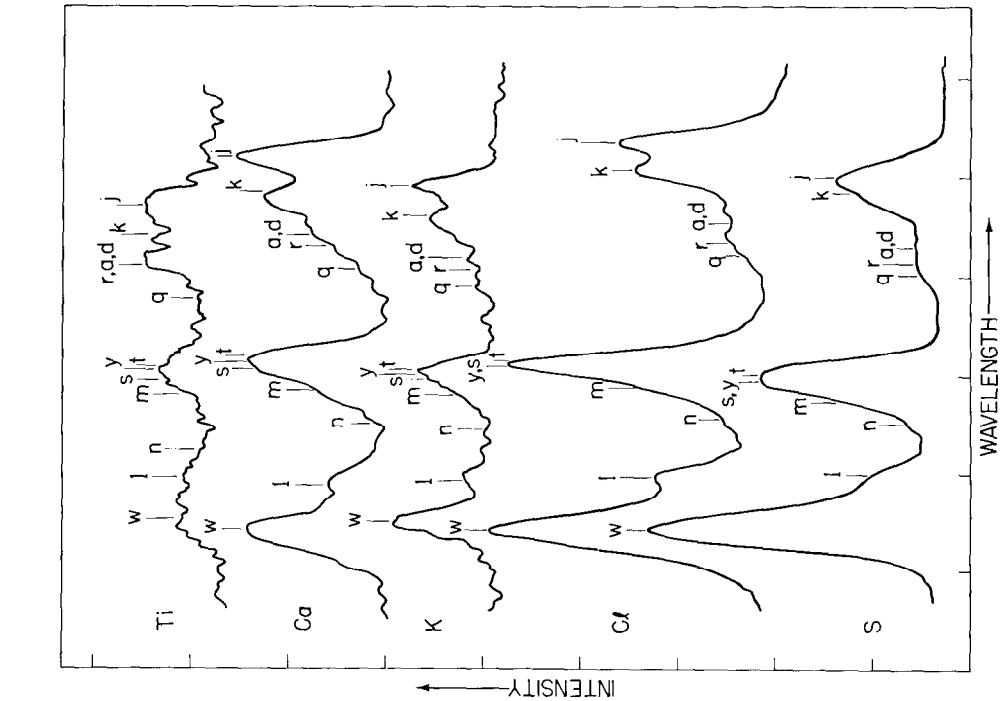

Fig. 42 — Satellite lines of the $1s^2\ {}^1S_0$—$1s2p\ {}^1P_1$ resonance line (labelled W) of the helium-like ions. The letters are conventional labels for these satellites (see Ref. 25).

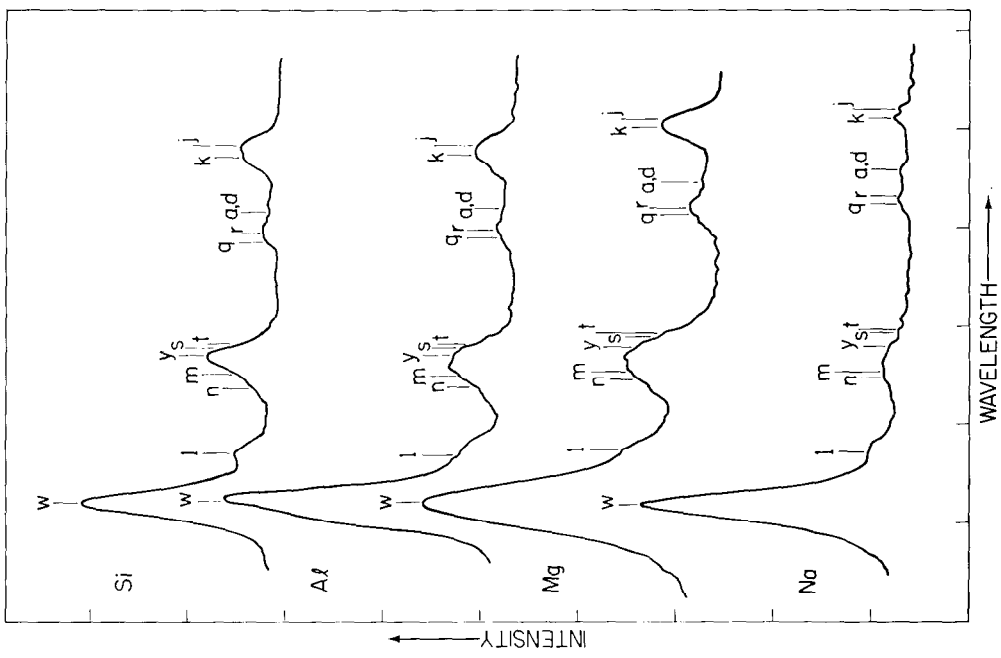

Fig. 41 — Satellite lines of the $1s^2\ {}^1S_0$—$1s2p\ {}^1P_1$ resonance line (labelled W) of the helium-like ions. The letters are conventional labels for these satellites (see Ref. 25).

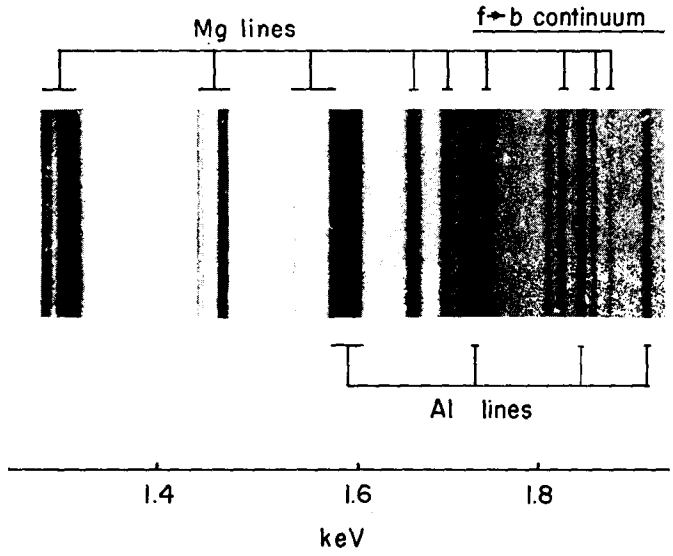

Fig. 43 — Spectrum obtained from laser excitation (~5 GW) of a target with 0.1 μm of Al evaporated on Mg

Most of the laser-plasma x-ray spectroscopy has been done with homogeneous pure-element or chemical-compound targets. However, experiments with layered targets have been started. These promise to yield temperatures and densities from separate materials at known initial depths in a target. A spectrum from a target with 1000 A of Al on Mg is shown in Fig. 43 [45].

The x-ray spectra discussed above are spatially as well as temporally integrated. Recent work at other laboratories with low Z targets, namely Be [46] and C [47], and grating instruments has yielded space-resolved spectra. That is, intensity was obtained for each spectral line as a function of distance from the target surface. Such work is valuable since it permits calculation of density at various points in front of the target. The first spatially-resolved x-ray spectrum for a heavier element (Mg) was obtained with a crystal spectrograph and is given in Fig. 44 [48]. The satellite lines appear to arise only in the high density region near the target surface while resonance lines produced by recombination come from substantial distances away from the target. To insure that differences in line extent are not merely due to differences in exposure, satellites and resonant lines of equal photographic density should be compared. This cannot be done for the data in Fig. 44, but the behavior observed here is indeed consistent with the results for lighter ions. This data is not sufficiently well resolved to yield a density-distance curve but it is a useful step toward that goal.

Chromium Through Zirconium (L Spectra)

K resonance spectra in one- and two-electron ions of lighter elements are highly useful for diagnostics of laser-generated plasmas, as already discussed. L spectra from intermediate elements are expected to be similarly useful, but their interpretation and use are not so well

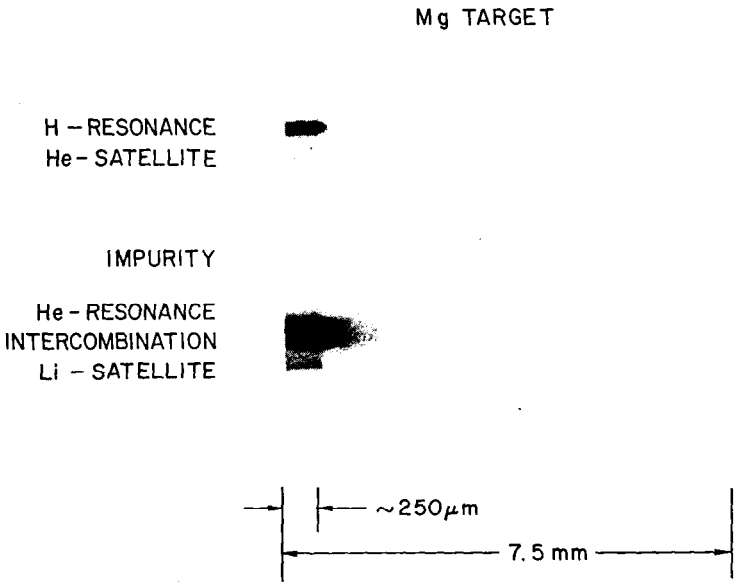

Fig. 44 — Spatially resolved Mg spectrum. The laser pulse was incident from the right.

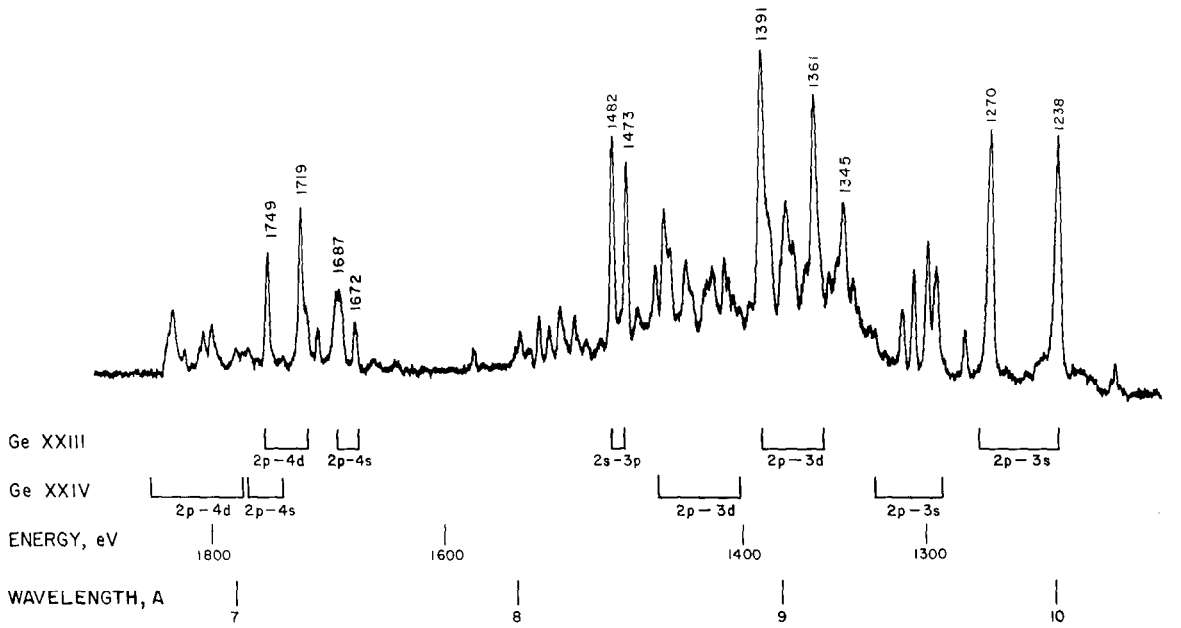

Fig. 45 — Laser-produced x-ray spectrum for Ge with 10 J on target. The energy regions for the indicated transitions in Ne-like Ge XXIII and F-like Ge XXIV were obtained by extrapolation from published UV measurements. Lines prominent in the Ne I isoelectronic sequence have x-ray energy values given above the spectrum.

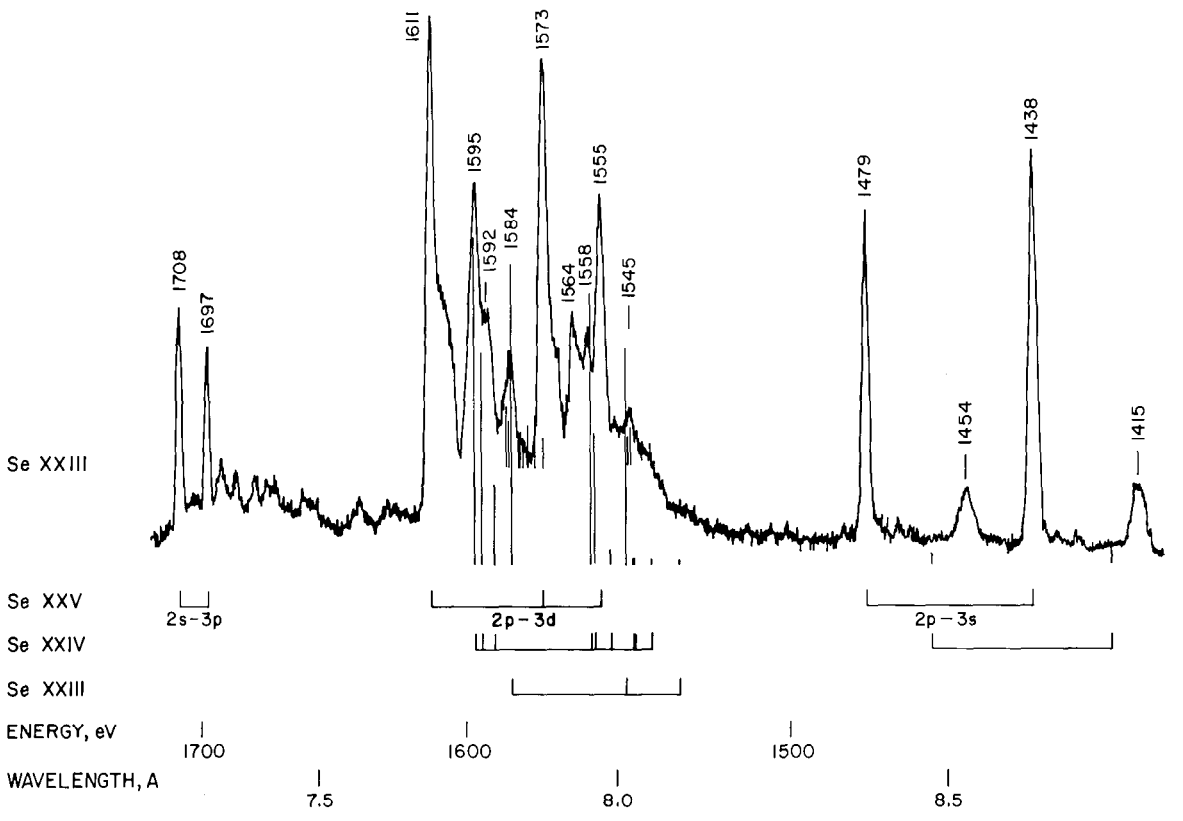

Fig. 46 — Laser-produced spectrum for Se. Transition energies and relative oscillator strengths for the Ne-like Se XXV and Na- and Mg-like satellites obtained by atomic structure calculations are indicated as vertical lines.

developed as for K spectra. Hence, resonance, inner-shell and satellite transitions to the L shell have been studied for elements in the Cr-Zr range [34]. One such spectrum for Zn was already shown in Fig. 23. Related spectra for Ge, Se and Zr are given in Figs. 45 through 47. We already observed that for constant pulse conditions, lower ionization stages become more important with increasing Z (see Fig. 39). The same effect prevails for L spectra. In the Ge spectrum, radiation from Ne-like (10 electron) ions is strong and there is a substantial contribution from the next higher ionization stage F-like (9 electron) Ge XXIV. In the Se spectrum, the Ne-like contribution is still strong but F-like emission is absent. However, Na-like (Se XXIV) satellite emission is evident. In the Zr spectrum, the satellite intensity is relatively strong. It produced long wavelength ramps for many of the lines. As shown in Figs. 46 and 47, multiplet calculations by Cowan were used in analysis of the spectra [21,22]. A Semi-Moseley plot for $2p$-$3s$, $2p$-$3d$ and other transitions in Ne-like ions is given in Fig. 48. This work extends by ten atomic numbers the ability to use L resonance spectra for plasma diagnostics. More importantly, it is a major step towards being able to use satellites of L spectra in a manner similar to the use of K satellites.

Fig. 47 — Laser-produced spectrum for Zr and atomic structure calculations

Fig. 48 — Semi-Moseley plot for Ne I isoelectronic sequence. The solid dots are published UV measurements while the crosses are laser-produced x-ray data.

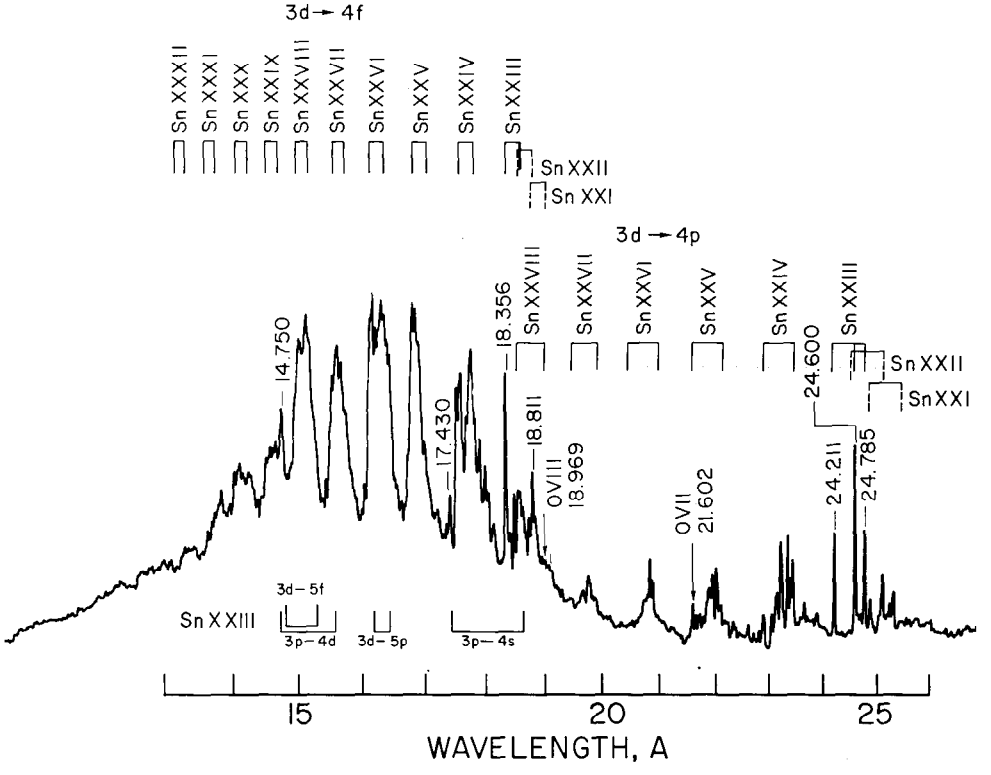

Fig. 49 — Laser-produced Sn spectrum in the 13 to 46 A region. The vertical lines above the spectrum correspond to wavelengths calculated by the SCF method for $3d^k$-$3d^{k-1}4p$ and $3d^k$-$3d^{k-1}4f$ transitions. The dotted vertical lines are values calculated for satellites containing 4*s* electrons. Below the spectrum are calculated line positions for other transitions in Sn XXIII.

Tin Through Erbium (M Spectra)

Although heavy elements are of little interest for laser fusion, we have found laser-generated plasmas highly useful to extend what was known about M resonance spectra. An example (Gd) was given in Fig. 24. Additional work with M spectra is shown in Figs. 49 through 51 for a Sn target [49]. The spectra were measured with the grating spectrograph in the 10-60 A range. Figure 49 shows the 13-26 A region which contains lines from ten ionization stages. This situation stands in contrast to the K and L spectra presented earlier because they evidenced only three or four ionization stages. The difference is due to the laser producing a plasma temperature relatively high compared to Sn M binding energies. Such a condition leads to ionization well into the M-shell. Details of the spectra in Fig. 49 are given in the following two figures. Again, the Cowan multiplet calculations were used to analyze the spectral details. Figure 52 is another Semi-Moseley plot, this one being for 3*d*-4*p* and 3*d*-4*f* transitions in Ni-like (28-electron) ions [50].

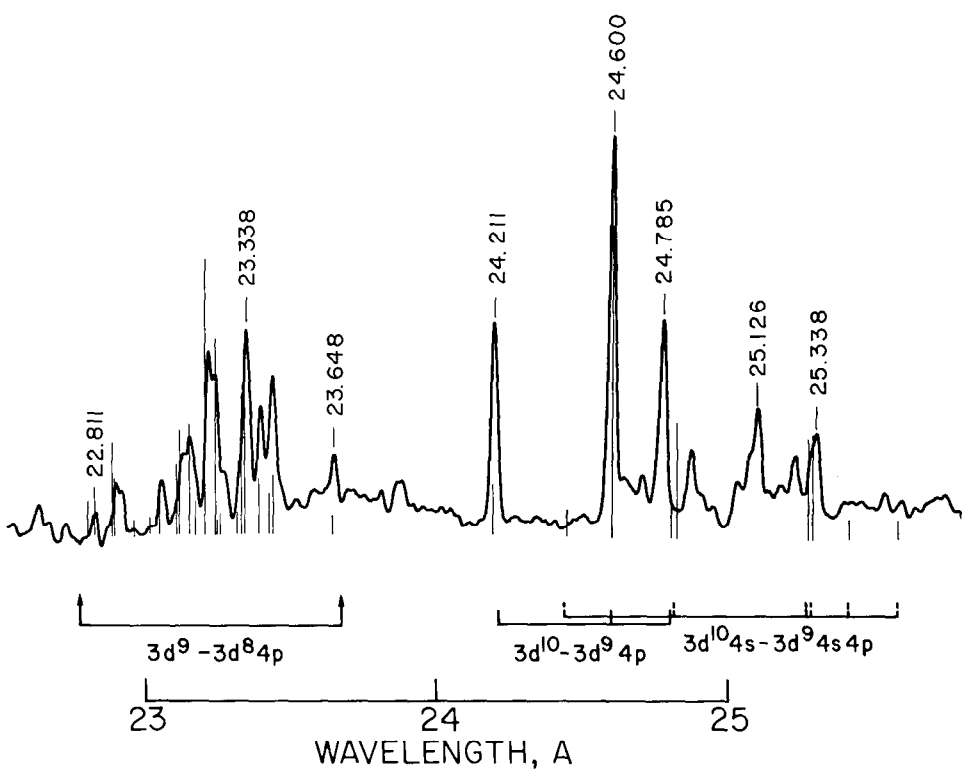

Fig. 50 — Comparison of observed spectrum with theoretically calculated line positions for the 3*d*-4*p* transition arrays

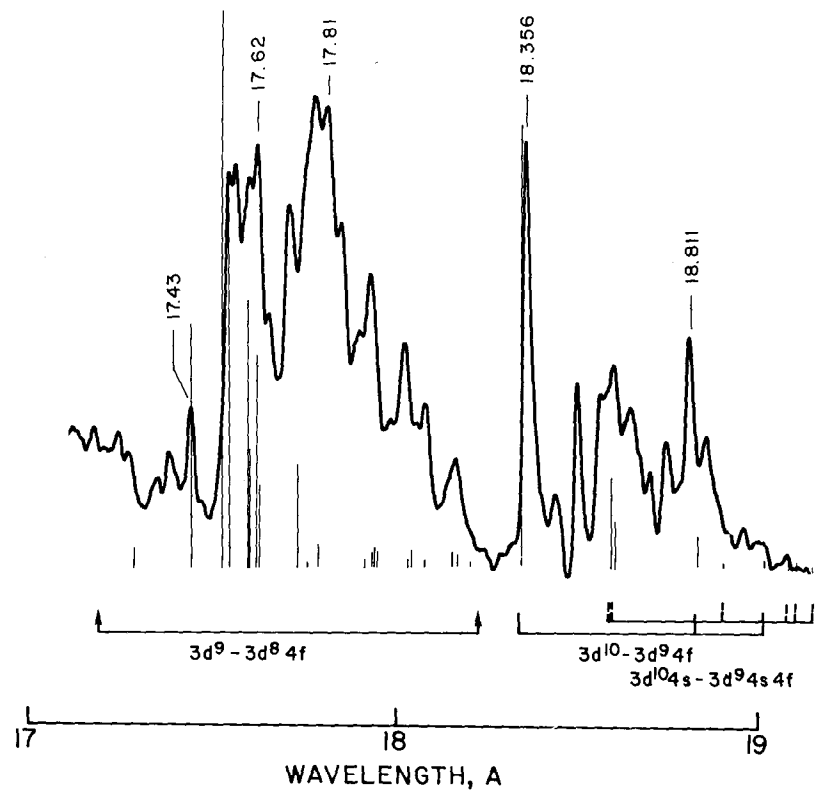

Fig. 51 — Comparison of observed spectrum with theoretically calculated line positions for the $3d$-$4f$ transition arrays

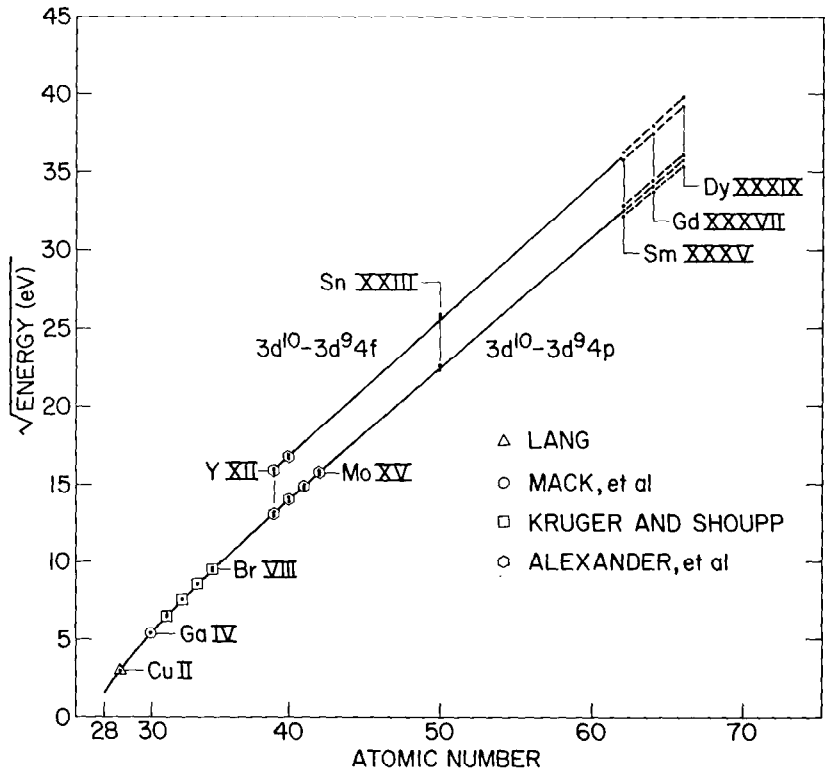

Fig. 52 — Semi-Moseley plot for Ni I isoelectronic sequence

Summary and Discussion

The characteristics of x-ray emission from plasmas produced at the focus of a sub-nanosecond, 1-60 GW laser were summarized at the bottom of page 94. In general terms, laser plasmas are unique x-ray sources since they give short, intense bursts of soft x-rays. Figure 53 compares the temporal and spectral characteristics of flash x-ray sources.

The major use at present for the x-rays emitted by laser-produced plasmas is the determination of plasma characteristics. General plasma-diagnostic results for the time and space-integrated measurements discussed above can be summarized as follows: plasmas created from slab targets by focusing 10 J, 1 nsec Nd laser pulses to 10^{14} W/cm^2 are: (a) electron temperatures are in the 500-1000 eV range, (b) average electron densities of 10^{19}-10^{20} cm^{-3} exist in the radiating region, (c) the thermal energy (3/2 nkT) is about 10^4 J/cm^3, (d) approximate ionization equilibrium exists, (e) radiative cooling which can be higher than 10^{13} W/cm^3 is important and (f) the radiating ions have velocities near 10^7 cm/sec (determined from doppler broadening). The precise values of these parameters vary with target and pulse conditions.

The second most important use of laser generated x-rays now is atomic spectroscopy. Of course, classification of spectra must precede their use for plasma diagnostics. However,

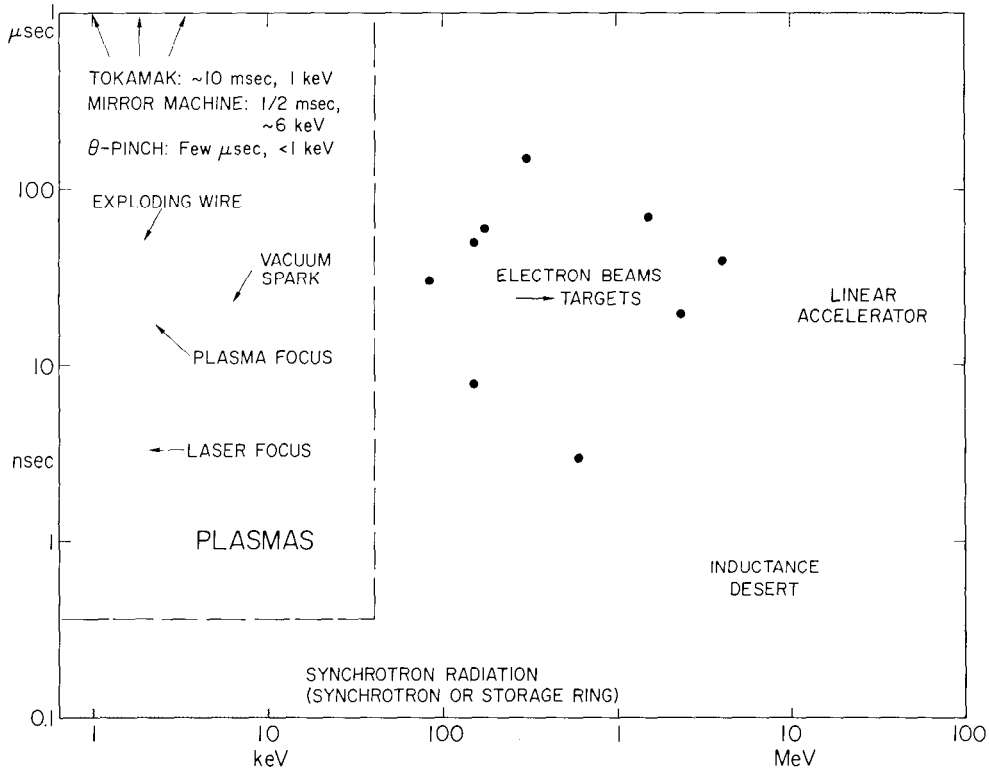

Fig. 53 — Comparison of pulse lengths and spectra for various types of flash x-ray sources. The repetition rate and available intensity vary widely for different sources.

the interpretation of spectra is a field unto itself. It is largely concerned with determination of energy levels and transition probabilities, both experimentally and theoretically. The study of L and M resonance spectra from heavier elements is most readily done using x-rays from laser-plasmas, and it lays the groundwork for future plasma diagnostics work with intermediate and high Z elements.

Other potential uses of laser-generated x-rays from heavier elements are evident and may be pursued in the future [30,51]. For example, the high speed and soft spectrum of laser-plasma x-ray emission make it attractive for radiography of another plasma. It should also be possible to do transient radiation effect studies, e.g., color center decay, using x-rays from laser-plasmas. Finally, dynamic material studies involving diffraction of laser-produced x-rays may be possible.

E. RELATED WORK

The soft x-ray results have contributed useful information towards understanding the coupling and distribution of laser energy in planar targets. However, they have additional ramifications concerning compression diagnostics, x-ray laser research and diagnosis of other plasmas. These are examined briefly in the remainder of this section.

X-ray Compression Diagnostics

The soft x-ray measurements of plasmas generated from slab targets have been useful in themselves, but in some sense they are merely a prelude to measurements of radiation from compressed targets [52]. There are three areas in which x-ray determination of the temperature and density in the core of a compressed pellet will be useful: (a) in the regime where attained compressions are insufficient to produce significant neutron yields, (for densities $\lesssim 10^2$ gm/cm^3), (b) as a complement to data from nuclear reaction products and (c) for study of laser compression of non-fusion spherical targets containing heavier elements.

Four aspects of the x-ray emission from spherical laser targets might be useful as compression diagnostics, namely the spectrum, total intensity, emission time history and source size and shape.

a. X-Ray Spectrum: Fine structure in UV spectra from plasmas has been used extensively to determine densities of low temperature plasmas. Such work is being extended to soft x-ray emission from laser-produced plasmas. Recent studies of spectra from planar targets have yielded spatially-resolved density values for Be and CH_2 targets. In these studies, the densities were sufficient to cause strong reabsorption of the centers of resonance lines. Even in the absence of resonance absorption, stark broadening of lines should yield useful density values.

b. Total X-Ray Intensity: The overall emitted energy (which is sensitive to x-ray generation and reabsorption processes) depends in part on density. Hence, intensity measurements combined with theory should yield density information. The intensity data can be gotten by using any of a wide variety of x-ray calorimeters and electronic detectors.

c. X-Ray Emission Time History: When the thermonuclear reaction begins in a pellet, the x-ray emission time history (with resolution of < 10 psec) would indicate if and when a compression high enough to result in significant nuclear reactions occurred.

d. X-Ray Source Size and Shape: X-ray images of a laser target can give the size and configuration of the target while it is hot enough to emit x-rays. Pinhole camera images of compressed pellets were obtained recently by KMS Industries, Inc.

Analysis of spectra may yield temperatures and densities without recourse to compression calculations. However, the intensity, temporal and spatial data should be compared to the results of numerical calculations in order to determine conditions reached in the pellet center.

Laser compression of matter promises to surpass densities attainable in the laboratory in static or explosive experiments by over two orders of magnitude. Figure 54 compares the densities and masses of "compressed" material in ion-collisions, ordinary laboratory high-pressure experiments and astrophysical plasmas with expected laser compression values. States of matter (internuclear distances) attained in laser compression, even though well past what can be done in the laboratory now for microgram samples, will still be far removed from those attainable in collisions or existing in stars. Many interesting compression studies of non-fusion targets are contemplated, e.g., the z-dependence of attainable densities.

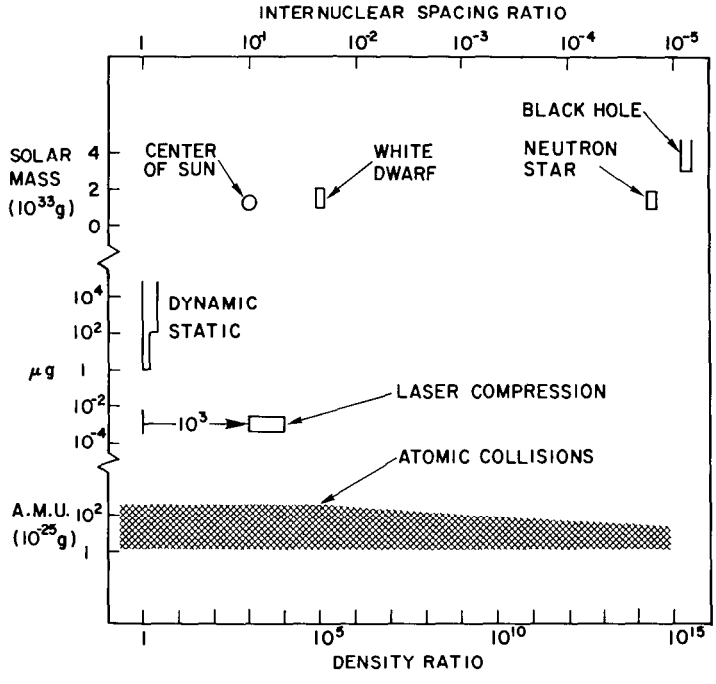

Fig. 54 — Internuclear spacing and density ratios for atomic collisions, laboratory high-pressure experiments and astronomical bodies

X-Ray Laser Research

Figure 55 shows that the ability to produce coherent electromagnetic radiation has not kept up in recent years with the earlier growth curve [53]. Now, however, there is intense interest, and even some optimism, concerning the possibility of producing a laser with wavelength shorter than a few hundred angstroms. This enthusiasm is due to the development of very high-power lasers in recent years and their use to produce plasmas. It is widely held that a laser-produced plasma will be the lasing medium for a high-photon energy laser. Hence, the plasma diagnostic information (temperature and densities) have substantial relevance to research aimed at production of a soft x-ray laser. Furthermore, it has been suggested by Mallozzi that x-rays from a laser-generated plasma may be useful to pump another medium by photoionization in order to produce an inverted population. Hence, the spectral, intensity, temporal, and source size information presented earlier is useful input to schemes involving the possibility of x-ray pumping of an x-ray laser.

Related X-Ray Work With Other Plasmas

Measurement and interpretation of soft x-ray data from laser-produced plasmas has benefited from and assisted work with other plasma x-ray sources. These include vacuum spark, exploding wire and plasma focus devices, which generate dense, high-temperature plasmas [54]. Diagnostic equipment and procedures developed for other work have proven highly useful in the present research. For example, the measurement of x-ray tubes spectra

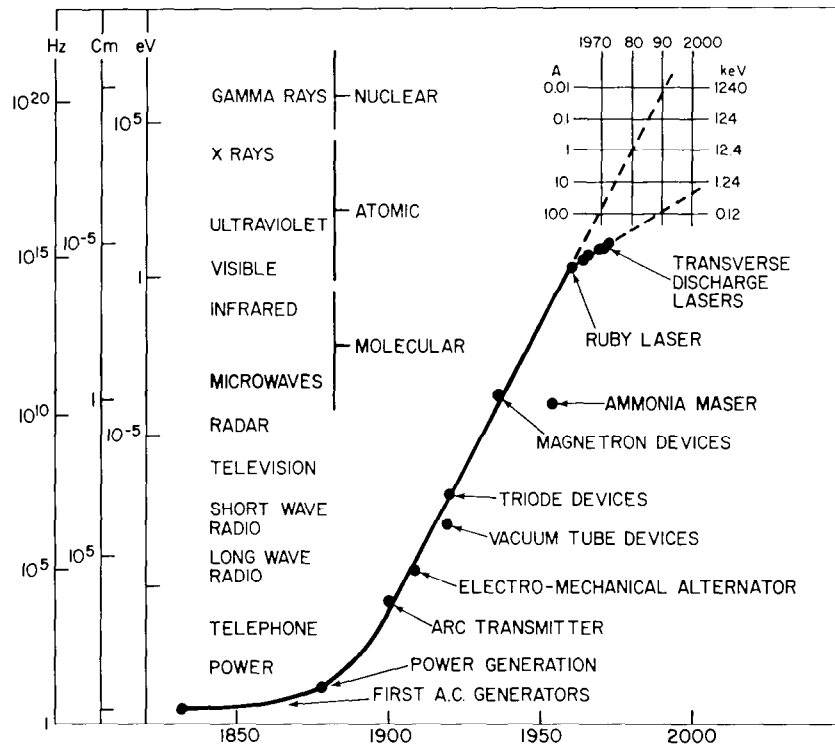

Fig. 55 — History of the capability to generate coherent electrical and electromagnetic waves

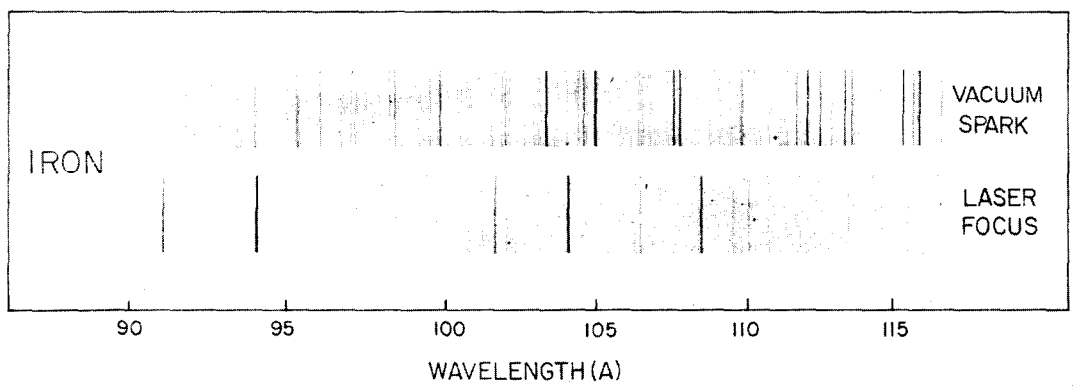

Fig. 56 — Comparison of Fe spectra near 100 A as excited in a vacuum spark or laser-produced plasma

(used for calibration) as well as crystal and film efficiencies, have been pursued at NRL for many years. On the other hand, laser-plasma spectra have proven very useful for interpretation of other laboratory and solar spectra. For example, Fig. 56 shows that spectra from laser-generated plasmas are much simpler than those from a vacuum spark [55]. It is also possible to control the ionization stages produced by a laser more easily (by varying the focal conditions). Hence, it is easier to analyze laser-produced spectra, and then to interpret spectra from other sources. In particular, spectra from laser-plasmas will prove useful for analysis of impurities in plasmas in other fusion machines. Even though there is a drastic density difference between laser-plasmas and those in Tokamaks, the similarities in temperatures can yield similar resonance spectra. We note finally that there is also useful interrelationship between laser and other plasma x-ray diagnostics and the measurements of x-rays from projectiles produced by high-energy accelerators [56].

REFERENCES

1. W.E. Behring, R.J. Ugiansky, and U. Feldman, Appl. Optics **12**, 258 (1973).
2. C.M. Dozier, R.R. Whitlock, and D.J. Nagel, unpublished.
3. L.S. Birks, Rev. Sci. Ins. **41**, 1129 (1970).
4. C.M. Dozier et al., unpublished.
5. T.N. Lee and D.J. Nagel, Bull. Am. Phys. Soc. **18**, 684 (1973).
6. D.J. Nagel and J.F. Holzrichter, unpublished.
7. R.K. Bardin et al., Bull. Am. Phys. Soc. **19** 557 (1974).
8. G.C. Vogel, A. Savage, and M.A. Duguay, Eighth Quantum Electronics Conference, San Francisco (1974).
9. R.A. Nuttleman et al., *Adv. in X-Ray Analysis*, Vol. 18, Plenum Press, New York (1975).
10. C.F. McConaghy and L.W. Coleman, Appl. Phys. Lett. **25**, 268 (1974).
11. C.M. Dozier et al., Conf on Adv. in X-ray Analysis, Denver (1974).
12. J.F. Holzrichter, C.M. Dozier, and J.M. McMahon, Appl. Phys. Lett. **23**, 687 (1973).
13. For crystal calibration, see for example; J. Vierling, J.V. Gilfrich and L.S. Birks, Appl. Spect. **23**, 342 (1969), and for film calibration see C.M. Dozier, J.V. Gilfrich, and L.S. Birks, Appl. Optics **6**, 2136 (1967).
14. D.B. Brown, M. Fatemi, and L.S. Birks, *Adv. in X-Ray Analysis*, Vol. **17**, Plenum Press, New York (1974) p. 436.
15. C.M. Dozier et al., unpublished.
16. L.S. Birks et al., J.O.S.A. **60**, 649 (1970).
17. W.J. Veigele, D.E. Stevenson, and E.M. Henry, J. Chem. Phys. **50**, 5404 (1969).
18. F. Herman and S. Skillman, *Atomic Structure Calculations*, Prentice Hall, Englewood Cliffs (1963).

19. C. Froese, Can. J. Phys. 41, 1895 (1963).
20. D. Liberman, J.T. Waber, and D.T. Cromer, Phys. Rev. 137, A27 (1965).
21. R.D. Cowan, Phys. Rev. 163, 54 (1967).
22. R.D. Cowan, J.O.S.A. 58, 808 (1968).
23. G.A. Doschek, Space Sci. Rev. 13, 765 (1972).
24. B.M. Klein et al., Bull Am. Phys. Soc. 18, 685 (1973).
25. A.H. Gabriel, Mon. Not. Royal. Astr. Soc. 160, 99 (1972).
26. C.P. Bhalla and A.H. Gabriel, Space Sci Rev., to be published.
27. G.A. Doschek et al., to be published.
28. R.C. Elton, NRL Report 6738 (1968).
29. D.J. Nagel et al., 5th European Conf. on Contr. Fusion and Pl. Phys., Moscow (1973).
30. D.J. Nagel et al., Phys. Rev. Lett. 33, 743 (1974).
31. D.J. Nagel, *Adv. in X-Ray Analysis*, Vol. 18, Plenum Press, New York (1975) p. 1-25.
32. R.R. Whitlock and D.J. Nagel, Bull. Am. Phys. Soc. 19, 557 (1974).
33. D.J. Nagel et al., Bull. Am. Phys. Soc. 19, 557 (1974).
34. P.G. Burkhalter, D.J. Nagel, and R.D. Cowan, to be published.
35. R.R. Whitlock and D.J. Nagel, unpublished.
36. H. Shay, Lawrence Livermore Lab., private communication.
37. T.P. Donaldson, R.J. Hutcheon, and M.H. Key, J. Phys. B. 6, 1525 (1973).
38. U. Feldman et al., Ap. J. 187, 417 (1974).
39. C.M. Dozier et al., Bull. Am. Phys. Soc. 16, 972 (1972).
40. B.M. Klein et al., 5th European Conf. on Contr. Fusion and Pl. Phys., Moscow (1973).
41. D.J. Nagel et al., unpublished.
42. J. Davis et al., 5th European Conf. on Contr. Fusion and Pl. Phys., Moscow (1973).
43. D.J. Nagel et al., Bull. Am. Phys. Soc. 16, 972 (1972).
44. U. Feldman et al., Ap. J. 192, 213 (1974).
45. R.R. Whitlock and D.J. Nagel, unpublished.
46. G. Tondello, to be published.
47. N.J. Peacock, to be published.
48. P.G. Burkhalter, unpublished.
49. P.G. Burkhalter, U. Feldman, and R.D. Cowan, J.O.S.A. 64, 1058 (1974).
50. P.G. Burkhalter, D.J. Nagel, and R.R. Whitlock, Phys. Rev. A. 9, 2331 (1974).

51. C.M. Dozier et al., *Adv. in X-Ray Analysis*, Vol. 17, Plenum Press, New York (1974) p. 423.

52. D.J. Nagel, Physica Fennica 9 (S1), 403 (1974).

53. D.J. Nagel, Physica Fennica 9 (S1), 381 (1974).

54. D.J. Nagel et al., Conf. on X-ray and UV Spectroscopy of Lab. and Astrophys. Plasmas, Harvard (1974).

55. U. Feldman et al., Ap. J. 183, L43 (1973).

56. D.J. Nagel, *Proc. 5th Int. Conf. on Atomic Collisions*, Plenum, New York, to be published.

VI. HARD X-RAY STUDIES

The role of super-thermal electrons in the laser-target interaction is critical to present laser fusion schemes because the generation of hot non-thermal electrons may hinder target compression by preheating the target or decoupling from the atmosphere [1,2]. The production of energetic electrons in the laser-target interaction may be studied through the subsequent bremsstrahlung radiation. Extensive measurements of the production of x-rays with energies greater than 15 keV have been carried out during FY-74. These measurements have been made for 1.06 μ laser pulses focused onto slab targets. A preliminary report of this work has been presented [3] and a more complete report has been published [4]. These studies are summarized below.

Hard x-rays are detected through a 1-mm thick aluminum absorber by a 4-mm thick NaI detector. In this way observations are restricted to x-ray energies greater than 15 keV. Also the output of such a detector is integrated over energy and time. Properties of these x-rays which have been investigated include:

1. Intensity dependence on:
   (a) Incident laser energy (1-100 J)
   (b) Laser pulse duration (0.9 ns, 0.25 ns)
   (c) Focal properties
   (d) Atomic number of the target (4-42)
2. Source dimension,
3. Angular distributions.

The emission of hard x-rays, measured as a function of incident laser energy from 1 to 100 Joules, is shown in Fig. 1a. These results were obtained for 0.9-nsec laser pulses without prepulse focused onto natural or deuterated polyethylene targets (focal spot dia. $\sim$ 100 μm). The NaI detector is calibrated in energy with radioactive sources. The total absolute x-ray emission in Fig. 1 is based on angular isotropy and an estimated 75% detection efficiency. The scatter of data points is typical of the shot-to-shot reproducibility. For the 74-cm focal length (f/14) lens hard x-ray production increases rapidly with incident energy and then increases linearly. The 11-cm focal length (f/1.9) lens gives substantially higher output due to a smaller focal spot diameter ($\sim$ 30 μm) as evidenced by the damage patterns on target.

Measurements of hard x-ray emission at 0.25 nsec with prepulse are shown in Fig. 1b. The 0.9-nsec curve in this figure is taken from Fig. 1a and is normalized to experimental measurements obtained at 0.9 nsec with prepulse and an improved quality f/14 focusing lens. Measurements at 0.25 nsec on aluminum targets with and without prepulse indicate that hard x-ray emission is insensitive to the presence of a prepulse (see Fig. 1b). A comparison of the curves in Fig. 1a and 1b indicates that the new focusing lens produced an increase of 2.5 in hard x-ray emission due to a reduced focal spot diameter. However, measurements for polyethylene at 0.9 nsec and 0.25 nsec in Fig. 1b show no

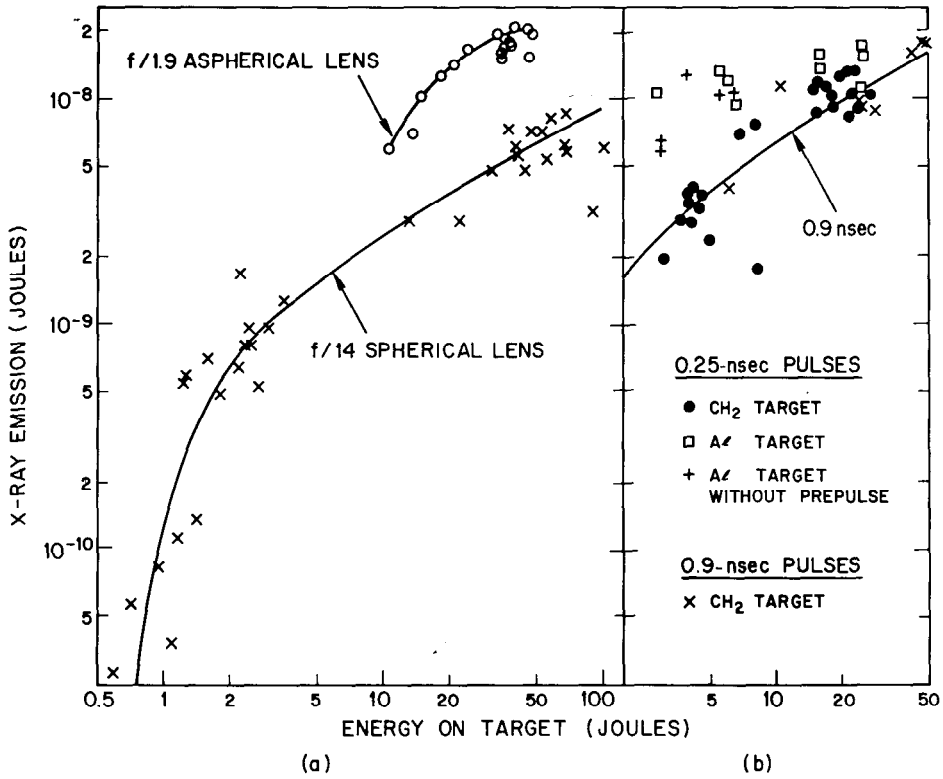

Fig. 1 — Hard x-ray emission measured with a 1-mm thick aluminum absorber and 4-mm thick NaI scintillator versus incident energy for (a) 0.9-nsec laser pulses incident on polyethylene targets and (b) 0.25-nsec laser pulses focused with an f/14 lens

significant increase in hard x-ray emission for an increase in laser power of 3.6. These results indicate that hard x-ray emission is sensitive to energy density in the target rather than power density.

Only an extremely small fraction of the incident laser energy is radiated away as hard x-rays. For example, from Fig. 1a, at 10 Joules incident energy only 3×10^{-10} of the incident energy is converted to hard x-rays. This result is consistent with similar measurements using thinner aluminum or thicker nickel absorbers [1]. Of the energy emitted as hard x-rays, only 10 MeV is actually detected. This corresponds, for example, to only 200 50-keV photons or 500 20-keV photons.

One of the more difficult measurements with a high power laser is to determine the optimum focus at high power because laser glass causes an intensity dependent divergence of the laser beam. The intensity of hard x-rays does provide a sensitive indication of the position of the target relative to laser focus at high power. Figure 2 compares a through-focus series of measurements for hard x-rays, soft x-rays as measured by a calorimeter, and the intensity of the back-reflected light. These results were obtained for 0.9-nsec pulses focused through a 74-cm lens onto a copper target. Incident energies ranged from

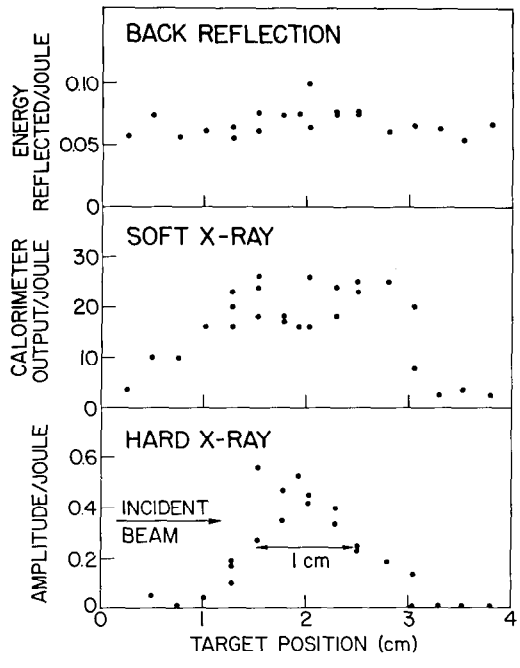

Fig. 2 — Comparison of a through-focus series of measurements for hard x-rays, soft x-rays, and back-reflected light for 1.06 μ, 0.9 nsec pulses focused through a 74-cm focal length lens onto a copper target

12 to 20 Joules for these measurements. Note that the hard x-ray signal is more sensitive to target focus than either the soft x-ray or back reflection. The focus corresponding to maximum hard x-ray output may not be the same as that determined by other methods, but it is close to that corresponding to minimum diameter damage spot on target. Also, a monitor of the hard x-rays provides a useful check on laser focusing from shot-to-shot over long periods of time.

The dependence of the total hard x-ray energy on the atomic number of the target is illustrated in Fig. 3. The datum for each target is averaged over several shots in the energy range from 8 to 11 Joules. The hard x-ray emission displays little variation with atomic number. This result contrasts with soft x-ray (1 to 3 keV) production which displays large variations with atomic number [6]. The smaller hard x-ray energies for CH_2, Si and S compared to Al, Cu, Mo, and Zr (in Fig. 3) suggest a metallic versus non-metallic dependence. This behavior is expected if the generation of super-thermal electrons is sensitive to laser produced magnetic fields [7,8].

Do these x-rays originate at the focus of the laser on target, or are they generated over a larger volume due to energetic ejected electrons? The experimental setup illustrated in Fig. 4 was used to study this question. The target is viewed at 90° by two NaI detectors through 2.5-mm slits in a Pb collimator. The collimator may be translated along the incident beam axis relative to the target. The slits are 2.5 cm from the target and the detectors are 36 cm from the target. The target is rotated on the support rod to provide a fresh surface for each shot. The results of scanning the hard x-ray intensity by translating the slits are shown in Fig. 5. When the slits are centered on the front surface of the target, hard x-rays are observed. When the slits are translated one slit width in either direction, the hard x-ray intensity drops to essentially zero. It is concluded that the hard x-rays must originate from a source near the target surface with a volume of dimensions much less than 2.5 mm.

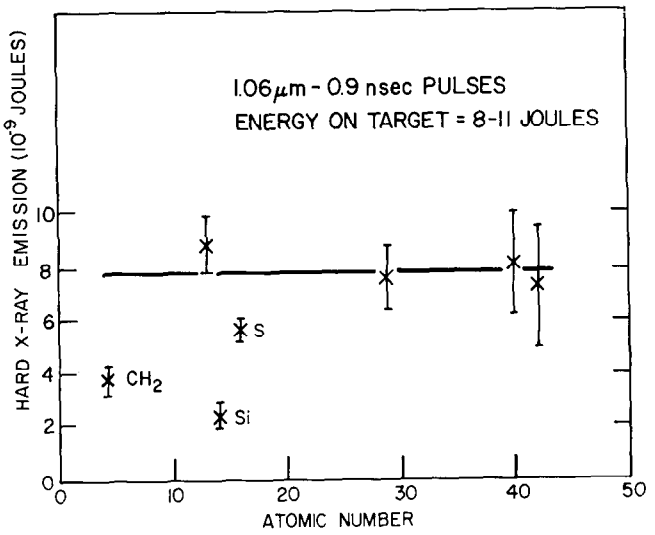

Fig. 3 — Hard x-ray emission measured with a 1-mm thick aluminum absorber and 4-mm thick NaI scintillator as a function of atomic number of the target

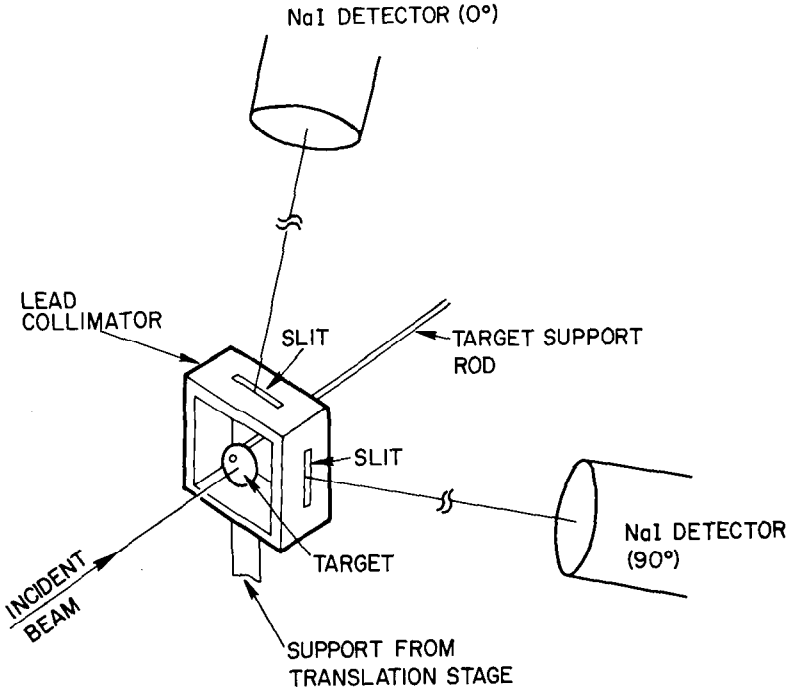

Fig. 4 — Experimental setup to study the dimensions of the source of hard x-rays in the laser target interaction

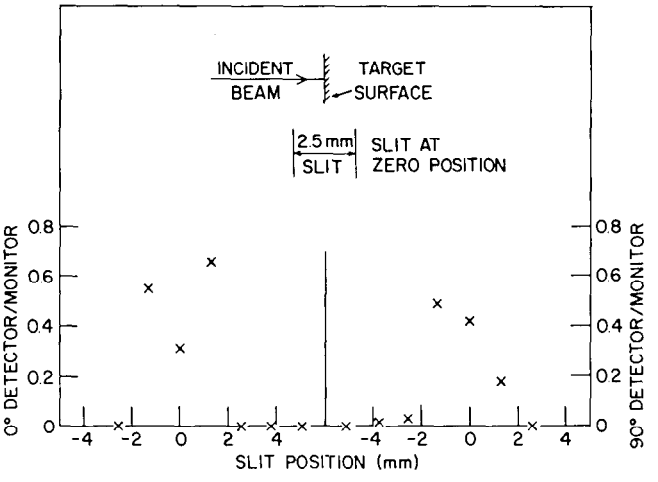

Fig. 5 — Hard x-ray emission measured by the NaI detectors in Fig. 4 as the slits are scanned in the direction of the incident laser beam

Angular distribution measurements of hard x-rays have been made on polyethylene targets for 0.9-ns and 0.25-ns laser pulses. Six NaI detectors, 5.1-cm dia. by 1.27-cm thick, are used to measure distributions in both the polar and azimuthal planes. The detectors are located 36 cm from the source and their relative efficiencies are determined with radioactive sources placed at the target position. The pulse from each detector is amplified and stored digitally in a transient recorder for later readout on oscilloscope or punch paper tape. X-ray absorption in the 0.76-mm thick target is negligible. Typical results for the azimuthal plane are shown in Fig. 6a. Results for the polar plane are shown in Fig. 6b. The errors in these measurements arise from two independent sources: (a) an uncertainty in the measurement of signal amplitude registered by the transient recorder, and (b) a statistical error in the number of photons detected. No significant deviations from isotropy are apparent in these measurements.

All of these results taken together suggest that energetic electrons are produced within the plasma volume and spontaneous magnetic fields play a role in confinement and perhaps acceleration so that energetic x-rays result from electron collisions within the plasma atmosphere.

Preliminary studies of the spectrum of energetic x-rays have been made during FY-74 using thin NaI detectors and different foil absorbers. Four detectors with absorbers corresponding to energy windows of 20, 40, 60 and 80 keV were used. Measurements were carried out on $(CH_2)_n$ slab targets for 0.25 nsec and 50 psec laser pulses of 3 to 7 Joules incident energy. No significant x-ray intensities were measured in the 40-, 60-, and 80-keV detectors. The results from the 20-keV detector are consistent with the data at 250 psec in Fig. 1b.

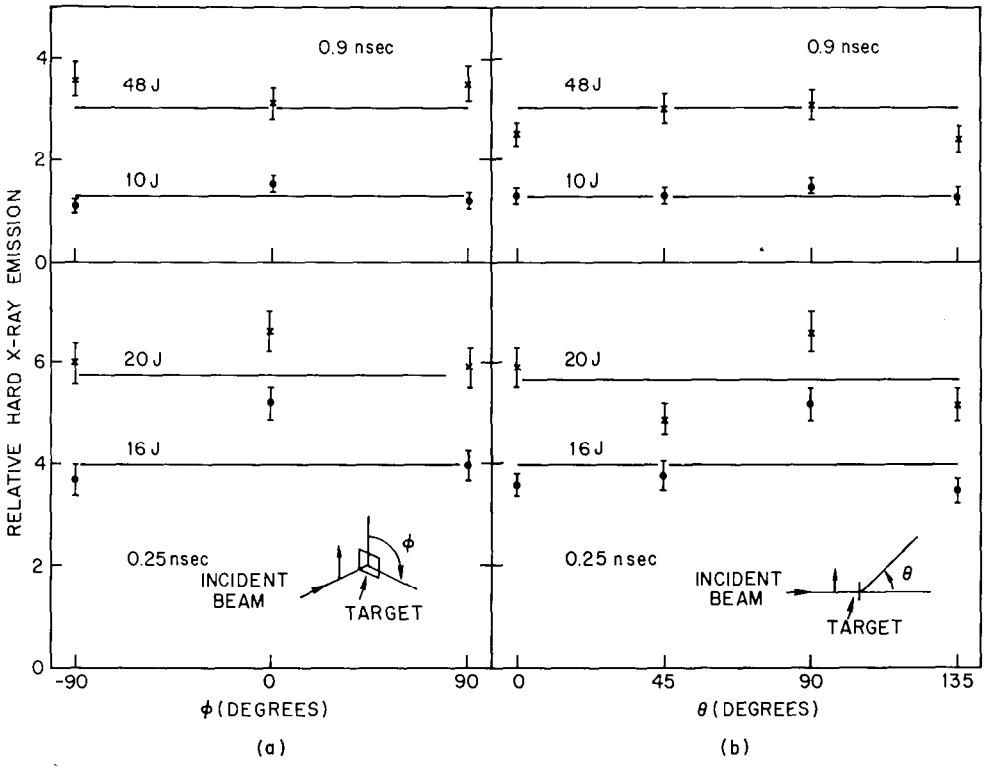

Fig. 6 — Angular distributions of the hard x-rays (a) in the plane perpendicular to the incident laser beam and (b) in the plane of the incident laser beam direction and the direction of polarization of the laser beam. The data are labelled with the incident energy and the lines represent the average of the six measurements.

REFERENCES

1. J. Nuckolls, L. Wood, A. Thiessen and G. Zimmerman, Nature (London) **239**, 139 (1972).
2. J.S. Clarke, H.N. Fisher and R.J. Mason, Phys. Rev. Lett. **30**, 89 (1973).
3. F.C. Young, D.H. Walker, and O.C. Barr, Bull. Am. Phys. Soc. Ser. II, **19**, 557 (1974).
4. F.C. Young, Phys. Rev. Lett. **33**, 747 (1974).
5. J.W. Shearer, S.W. Mead, J. Petruzzi, F. Rainer, J.E. Swain and C.E. Violet, Phys. Rev. **A6**, 764 (1972).
6. D.J. Nagel, P.G. Burkhalter, C.M. Dozier, B.M. Klein and R.R. Whitlock, Bull. Am. Phys. Soc. Ser. II, **19**, 557 (1974).
7. D.A. Tidman and J.A. Stamper, Appl. Phys. Lett. **22** 498 (1973).
8. N.K. Winsor and D.A. Tidman, Phys. Rev. Lett. **31**, 1044 (1973).

VII. THEORETICAL PLASMA STUDIES

A. A MODEL FOR THE PRODUCTION AND TRANSPORT OF ENERGETIC ELECTRONS IN A LASER PRODUCED PLASMA

The question of whether many energetic electrons are generated in a laser-produced plasma is of crucial importance for laser fusion. Let us say that the laser power flux P is incident on the target. If a fraction α is absorbed by the plasma, then the particle thermal flux at a density just greater than the absorbing density (generally the critical density) must be αP. Thus, given the fractional absorption, the principal constraint on the plasma is that energy flux be αP.

If the power flux is small, it is given by $K(\partial T/\partial x)$, where K is the thermal conductivity. In a laser-fusion plasma, since the absorption region is localized, $K(\partial T/\partial x)$ is quite large and can be bigger than the thermal flux of half a Maxwellian distribution, $1/2(nmV_e^3)$. In this case, it is generally assumed that the heat flux is limited to some fraction of $1/2(nmV_e^3)$. Although this result is certainly reasonable, it does not rest on any rigorous foundation. For instance if the distribution function has a nonthermal tail on one side which goes as V^{-n} where $3 < n < 4$, the first three moments are well behaved, but the energy flux is infinite and has no relation to the thermal velocity. In principle, at least, the heat flux may be much greater than $1/2(nmV_e^3)$ [1,2].

Once the laser light is absorbed and a fraction α is converted to particle heat flux, the question is what the distribution function looks like. The constraints are that the density is the critical density and the heat flux is αP. For instance two distribution functions which have the same density and heat flux are shown in Fig. 1. Of the two, that shown in Fig. 1b is much more harmful, since a much larger fraction of the heat flux is carried by highly energetic particles [3].

In order to study the heat flux and particle distribution, we have developed analytical theory and have performed a series of numerical simulations. Since most anomalous absorption mechanisms rely on converting the laser energy to electrostatic wave energy inside the plasma, we have modeled the absorption process by launching an electrostatic wave at one point in the plasma and propagating it toward regions of lower density. Since the dispersion relation is given by

$$\omega^2 = \omega_p^2(x) + 3k^2 V_e^2, \tag{1}$$

as the wave propagates outward it goes to lower phase velocity. When the phase velocity is sufficiently small, the wave Landau damps and gives its energy to the particles. The equations which describe the wave motion and particle distribution function are

$$\frac{d}{dx} P = \int dV \frac{\pi}{2} mV^2 \frac{\partial}{\partial V}\left(\frac{e}{m}\right)^2 \frac{|E(k)|^2}{k} R\left(V - \frac{\omega}{k}\right) \frac{\partial f}{\partial V} \tag{2}$$

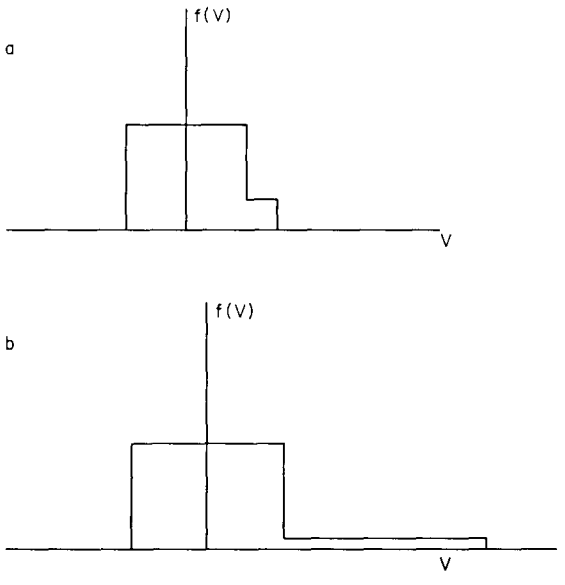

Fig. 1 — Two distribution functions which conduct energy either in the form of not very energetic particles, or highly energetic particles

$$V\frac{\partial f}{\partial x} = \sum_k \frac{\partial}{\partial V}\pi\left(\frac{e}{m}\right)^2 |E(k)|^2 \, R(\omega - kV)\frac{\partial f}{\partial V} \tag{3}$$

where a resonance function $R(\omega - kV)$ rather than a delta function $\delta(\omega - kV)$ is used, since the wave has nonzero trapping width.

These equations have been solved numerically and show that a nonthermal tail forms on the distribution function, which cuts off sharply at between five and seven thermal velocities. To further study the heat-conduction process, a series of five simulations were performed. The wave was launched with an antenna at one point in an inhomogeneous plasma. The particles are reflected from the low-density side, and on the high-density side, are in thermal contact with a heat source at the initial temperature. There is an initial heating of the plasma, and thereafter, the system reaches a steady-state temperature greater than the initial temperature. When the system has reached steady state, all energy put in by the antenna is conducted to the cooler core. To see how this energy flux is apportioned between energetic and thermal particles, we have measured the time average distribution function on the high-density side of the antenna. The distributions for the five different simulations are shown in Fig. 2. The time-averaged heat fluxes are $\alpha P/1/2(nmV_e^3)$ = 0.41, 0.56, 0.47, 0.16, and 0.25 for the five simulations. Thus we conclude that the energy is conducted by particles whose velocity is between about four and seven times the thermal velocity and that the flux limits generously imposed are reasonable [4,5].

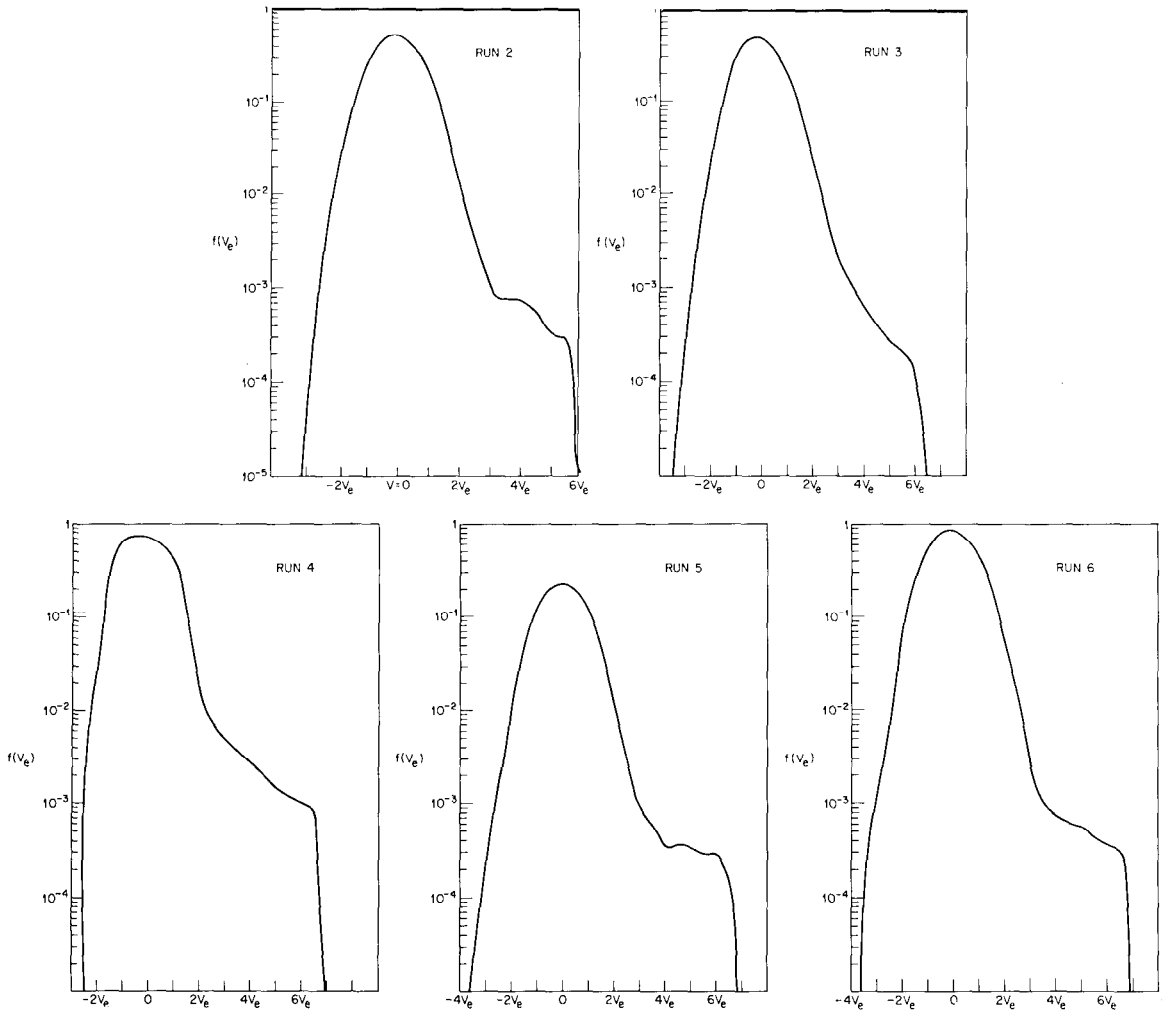

Fig. 2 — Computed steady-state distribution functions for electron heat transport

B. THE EFFECT OF TRAPPING ON REFLECTION OF LASER LIGHT DUE TO THE RAMAN BACKSCATTER INSTABILITY

One potentially dangerous anomalous effect in laser fusion is the Raman backscatter instability. In this process, the laser light, in the underdense plasma, decays into an electron plasma oscillation and a backscattered photon at frequency $\Omega - \omega_p$, where Ω is the angular frequency of the laser light. In an inhomogeneous plasma, this process can proceed only in a region of space where all three waves are in phase. Since the wave number of the plasma oscillation is a much more rapidly varying function of position than is the laser or scattered wave number, the resonant region size ℓ is defined by

$$\pi = \int_0^{\ell} dx \frac{dk_p}{dx} x. \tag{4}$$

Utilizing the dispersion relation for plasma waves is an electron fluid with thermal velocity V_e, we find

$$\ell^2 = \frac{12\pi\, k_p\, V_e^2\, L}{\omega_p^2 e}, \tag{5}$$

L being the density gradient scale length. One can then determine the inhomogeneous threshold by setting $\gamma^2 \tau_p \tau_s \approx 1$ where γ^2 is the backscatter instability growth rate $\gamma^2 = 1/16\ (\omega_p\ \Omega)(V_{os}/C)^2$ and τ_s is the time the scattered wave is in the system, $\tau_s = \ell/c$ and τ_p is the time the plasma wave is in the system, ℓ/V_{go}. Putting it all together, and assuming $k_p \approx 2\Omega/c$, we find for the threshold in the inhomogeneous system is

$$\frac{\pi}{4}\frac{\Omega L}{c}\left(\frac{V_{os}}{c}\right)^2 > 1. \tag{6}$$

In the underdense plasma, at say 1/10 the critical density, the density gradient scale lengths might be quite long from linear theory, Raman backscatter is a potentially dangerous process [6].

We have examined carefully the effect of electron trapping on this instability in an inhomogeneous system. Our results are that nonlinearities can substantially increase the threshold power (or alternatively increase the threshold length); for instance, in the calculations we show here, the threshold scale length is larger by a factor of between 5 and 25 for substantial reflection. However if the threshold power does exceed the nonlinear threshold, then theory shows that a substantial flux of energetic electrons is produced. For instance, if the scattering takes place at 1/7 the critical density, the maximum particle energy is of order 100 keV [7].

We have worked out the theory by considering a simple energy balance between the three waves involved in the scattering process. The pump wave (laser) and scattered wave exert a low-frequency pondermotive force which is in phase with the density fluctuation of the plasma wave, and therefore causes it to grow. Similarly the plasma wave and pump wave cause a current density in phase with the scattered wave, causing it to grow. One derives the linear theory by equating these energy inputs to the growth rate of wave energy. In the nonlinear regime however, the energy input to the plasma wave is dissipated by trapping electrons. Since an electron gains a tremendous amount of energy upon becoming trapped, the process slows down considerably in the nonlinear regime.

We have worked out the steady-state (in time) nonlinear theory for a plasma slab. The slab width may be assumed to correspond roughly to the phase coherence length ℓ in the inhomogeneous system. As boundary conditions, we assume that the laser light impinges on the slab from the left and that the plasma wave and reflected wave have zero amplitude at respectively the left and right hand edge of the slab. The coupled, spatially dependent, three-wave mode coupling equations are then solved in the linear and nonlinear regime. For the parameters shown in Fig. 3, the reflection coefficient is shown as a function of slab width where trapping is neglected and then where trapping is accounted for. Notice that trapping increases the slab width by approximately a

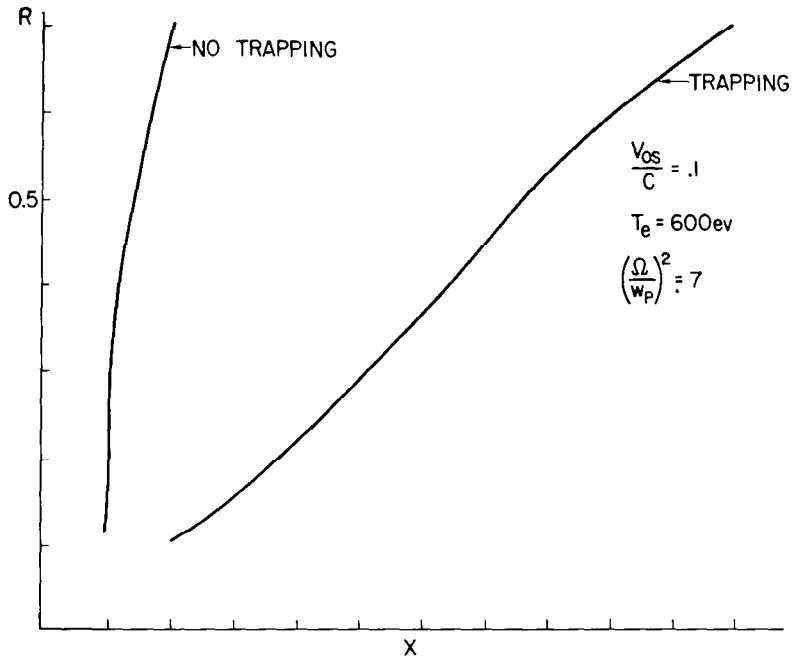

Fig. 3 — Comparison of reflection coefficient for Raman backscatter as a function of slab width with and without electron trapping

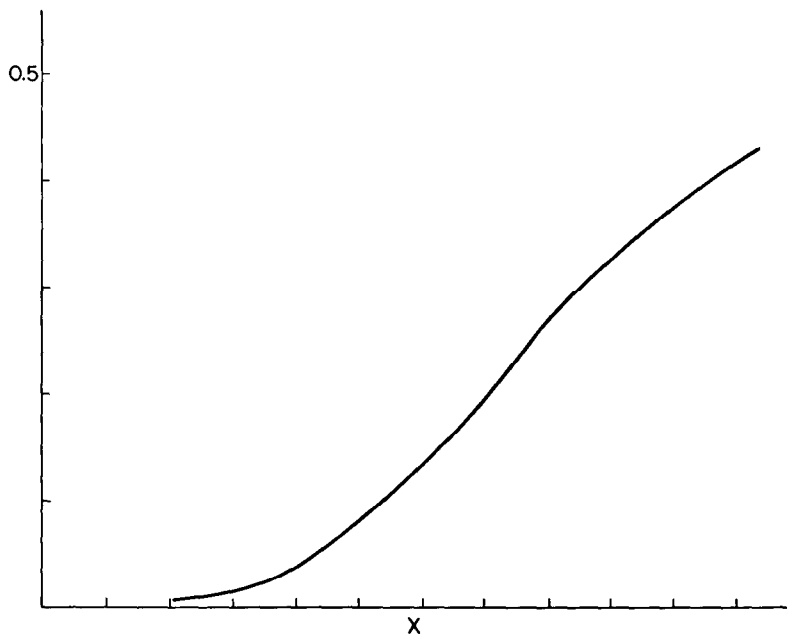

Fig. 4 — Energetic electron energy flux as a function of incident laser flux for parameters of Fig. 3

factor of five at given reflection coefficient. This means an increase in density gradient scale length of a factor of 25, since $L \sim \ell^2$. However if the scale length is above the nonlinear threshold, we find that a substantial fraction of the incident energy flux is converted into energetic particle flux. Figure 4 shows the particle energy flux divided by laser energy flux, again as a function of slab width. Thus, nonlinear effects increase the scale length for significant reflection, which is beneficial for laser fusion, but tend to create highly energetic electrons if above the nonlinear threshold, which is detrimental.

C. COMPTON SCATTERING IN THE OUTER REACHES OF A LASER FUSION PLASMA

In the outer reaches of a laser fusion plasma, where $\kappa\lambda_D \gtrsim 1$, κ being the wave number of the laser light, most parametric instabilities cannot occur. An important exception is the stimulated Compton scatter instability. Before the laser light can get to the critical density where it is absorbed, it must first pass through the underdense region. Thus, it is important to carefully examine any stimulated process which occurs in the far underdense region [8].

We have examined the stimulated Compton scatter instability with numerical simulations and also with analytic theory. We find that for an infinite homogeneous plasma, the system is well described by quasi-linear theory [9].

If ω is the difference between the frequencies of the incident and scattered modes, and if $\underline{k}$ is the difference in wave number, then the quasi-linear theory may be summarized by the expression for growth rate and heating rate,

$$\gamma \approx 1/10 \frac{\omega_{pe}^2}{\Omega} \left(\frac{V_{os}}{V_e}\right)^2 \tag{7}$$

and

$$\frac{dv_e^2}{dt} = \frac{1}{2} \sum_k \left(\frac{e}{m\Omega}\right)^4 \frac{\pi\omega^2}{V_e^2 |\underline{k}|} \frac{|E_o(\kappa) \cdot E_c(\kappa - k)|^2}{2\sqrt{3}\, V_e}. \tag{8}$$

Since the thermal velocity appears in the denominator of both Eq. (7) and Eq. (8), it is clear that as the plasma heats, the Compton scattering process slows down. Simulations clearly show this effect. In Fig. 5 is shown a graph of electron thermal velocity $V_{ex}^2 + V_{ey}^2$ as a function of time for a two-dimensional simulation of Comptron scatter at 1/50 the critical density. The initial plasma has $V_{os}/c = 0.3$ and $V_{os}/V_e = 3/2$. Notice the rapid initial heating, followed by a slower heating later in the run. The heating rates at all times are in approximate agreement with Eq. (8). It is also of interest that this heating is in the body of the distribution function and *not* in the tail. This is because the stimulated Compton scatter instability is an instability of a wave scattering off thermal particles in the distribution. In Fig. 6 is shown the measured electron distribution function at three different times. Clearly, the heating is in the body and not in a nonthermal tail. We are currently working to extend the theory to a study of the time independent, spatially dependent quasi-linear theory of the instability.

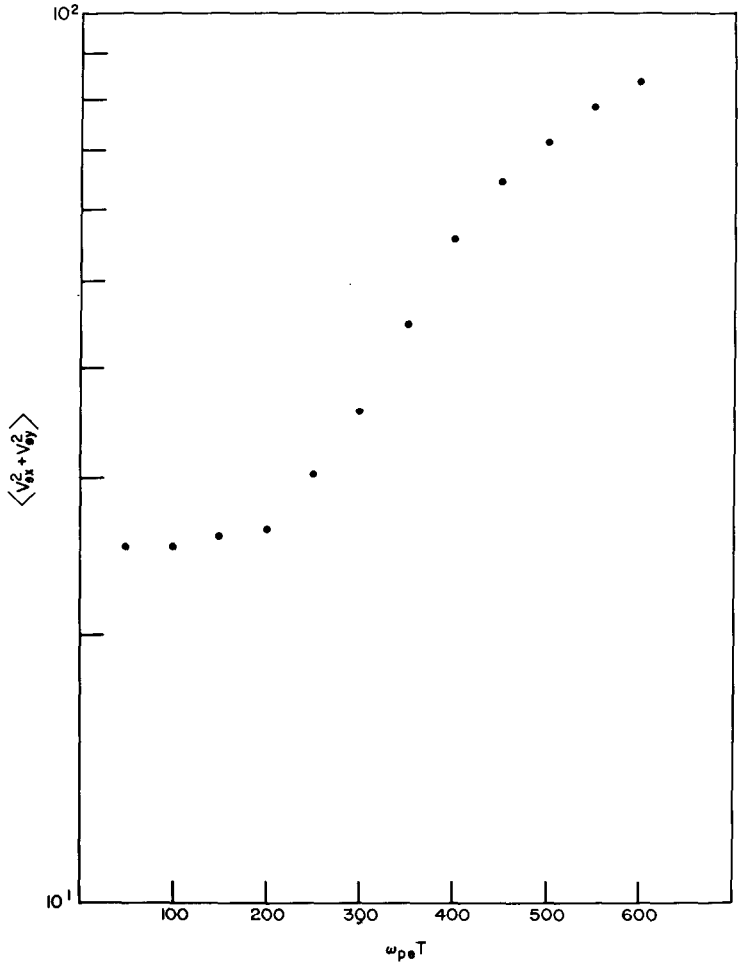

Fig. 5 — Electron temperature as a function of time in a simulation of the Compton scatter instability

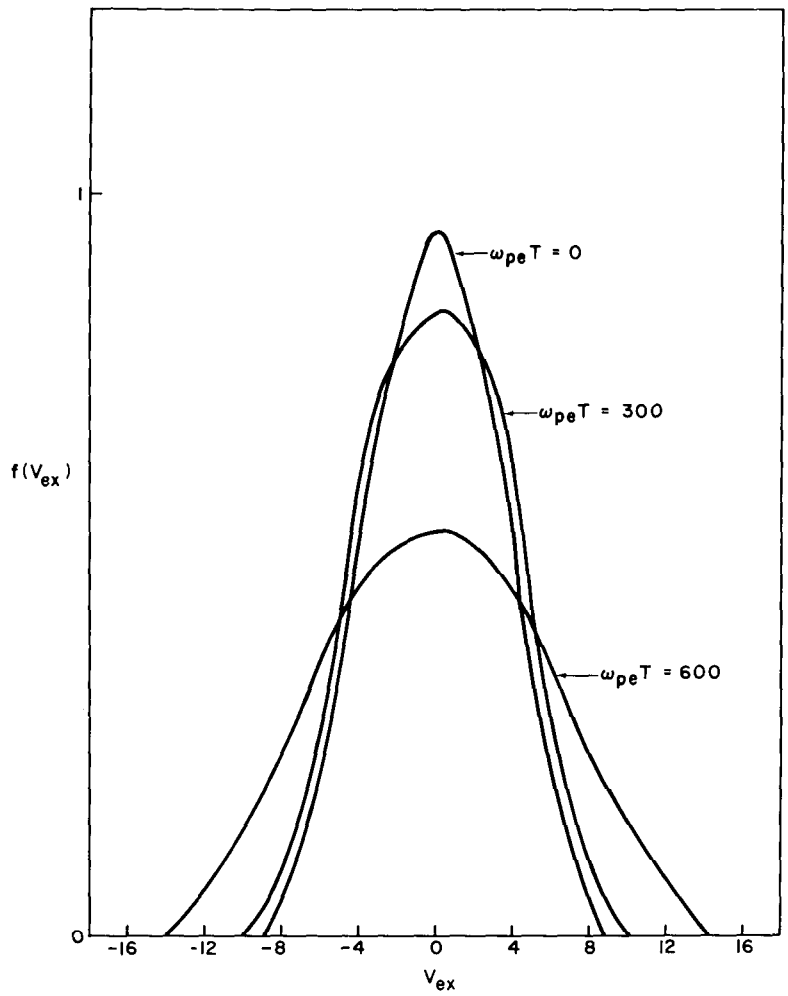

Fig. 6 — Electron distribution function at three different times, showing that the heating is in the body and not the tail

REFERENCES

1. R. Morse and C. Nielson, Phys. Fluids **16**, 909 (1973).
2. J.P. Christiansen, D. Ashly and K.V. Roberts, UKAEA Research Group Preprint CLM p. 374.
3. J. Thompson, R. Faehl, and W. Kruer, Phys. Rev. Lett. **31**, 918 (1973).
4. H. Klein and W. Manheimer, Phys. Rev. Lett. **33**, 953 (1974).
5. W. Manheimer and H. Klein, Phys. Fluids, to be published.
6. D. Forshend, J. Kendel, and E. Lindman, Phys. Rev. Lett. **30**, 739 (1973).
7. W. Manheimer and H. Klein, Phys. Fluids, Oct. 1974.
8. A.V. Vinogradov, B. Y. Fel'dovich, and I.I. Sobel'man JETP Lett. **17**, 195 (1973).
9. E. Ott, W. Manheimer, and H. Klein, Phys. Fluids, Oct. 1974.

VIII. TWO DIMENSIONAL COMPUTER MODELLING OF LASER HEATED PLASMAS*

INTRODUCTION

In this section we describe a detailed two-dimensional computer model for the interaction of a focused laser pulse with targets of various atomic weights and present results from it. The work was sponsored by DNA. The model is based on a coupled system of hydromagnetic equations with cylindrical symmetry [1-4] (including self generated field effects), rate equations [5], radiation transport [6] (including frequency diffusion[7]), and radiation pressure effects [8-10]. The work is principally motivated by the prospect of using a high atomic weight target as a means for efficient conversion of laser energy into an x-ray pulse via production of a high density, non-LTE, kilovolt plasma [11-14]. Results from the code include information on the time-dependent emission spectrum, together with the total x-ray conversion efficiency, as a function of the laser pulse parameters and initial target conditions. The model however is also applicable to studies of other situations such as those involving laser plasmas produced for thermonuclear experiments or ion sources.

The physical model is illustrated schematically in Fig. 1. Incident laser radiation of frequency ω_L enters the target and is reflected at the critical depth where $\omega_L \simeq \omega_e$. Absorption occurs along the incident and reflected radiation path with maximum absorption near the critical depth.

To date we have considered subnanosecond neodymium glass laser pulses with intensities $> 10^{14}$ watts/cm^2 through the focal spot, which can give rise to target plasma temperatures above 1 keV. Thermal energy spreads from the laser focal region via electron thermal conduction, fluid expansion, and transport of line and continuum x-ray emission from highly charged ion states. Magnetic fields in the megagauss range are generated internally in the plasma, and tend to inhibit thermal conduction in the r and z directions, perpendicular to $\underline{B}$, in regions where $\Omega_e \tau_e > 1$.

The equations on which the model is based divide into three groups and are summarized in the following sections on fluid equations, rate equations, and radiation transport equations. It should be noted that for many cases the atomic collision processes proceed at rates that are not fast enough to establish LTE or even a less restrictive coronal equilibrium situation, i.e., the phenomenon must be treated as a nonequilibrium reactive flow problem.

Our code differs from the Livermore code [15], LASNEX, in the detail with which the x-ray emission and propagation is described. LASNEX contains a coronal equilibrium approximation for the atomic states instead of solving the rate equations. It also contains a diffusion approximation for spatial radiation transport and neglects frequency diffusion. On the other hand, we have not yet developed a model for suprathermal electron generation [16,17] which has recently been included in LASNEX. Thus we expect our code to predict more accurately than LASNEX the x-ray emission originating in thermal electrons and ions, but not to give the high energy tail of hard x-rays which is included in LASNEX.

*The work in this chapter was fully supported by the Defense Nuclear Agency.

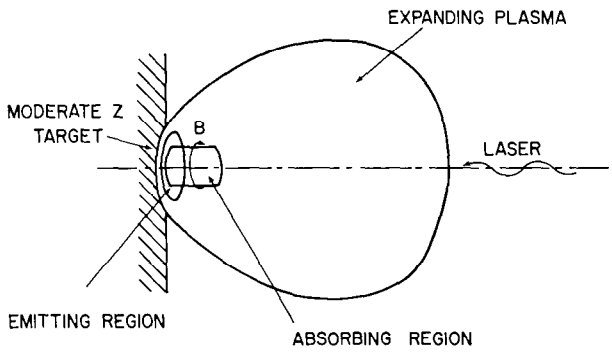

Fig. 1 — Schematic of the numerical experiment

Several other 2D codes have been described by other authors. The Sandia model [18] contains magnetic source terms, but does not include the complete effects of magnetic field on the transport coefficients as listed in Braginskii [1], or detailed atomic physics. Compared with the algorithm in use at Los Alamos [19], our code should be better able to resolve shock structure (by use of FCT [20]), but less able to follow large changes in system size amenable to their almost-Lagrangian method. Our code, in contrast to Chase, LeBlanc and Wilson [4], uses physically correct energy and magnetic field equations. None of these latter codes is concerned with x-ray emission.

A. FLUID EQUATIONS

In the fluid equations used we assume that the electrons and ions may have different temperatures. They are (in c.g.s. units)

$$\frac{\partial N}{\partial t} + \underline{\nabla} \cdot (N\underline{V}) = 0, \tag{1}$$

$$NM\left(\frac{\partial}{\partial t} + \underline{V} \cdot \underline{\nabla}\right) \underline{V} + \underline{\nabla} \cdot \left\{P\,\underline{\underline{I}} + \underline{\underline{I}}\frac{B^2}{8\pi} - \frac{\underline{\underline{BB}}}{4\pi}\right\} + \underline{\nabla} \cdot \underline{\underline{P}}_R = 0, \tag{2}$$

$$\frac{\partial \mathcal{E}}{\partial t} + \underline{\nabla} \cdot (\mathcal{E}\underline{V}) = -P\underline{\nabla} \cdot \underline{V} + \underline{J} \cdot \underline{\underline{r}} \cdot \underline{J} + P_L - R_e - \underline{\nabla} \cdot \underline{Q}_e, \tag{3}$$

$$\left(\frac{\partial}{\partial t} + \underline{V} \cdot \underline{\nabla}\right)\left(\frac{3}{2}NkT_i\right) + \frac{5}{2}NkT_i\,\underline{\nabla} \cdot \underline{V} = \nu_{ei}\frac{3}{2}Nk(T_e - T_i), \tag{4}$$

$$\frac{\partial \underline{B}}{\partial t} = \underline{\nabla} \times \left\{ \underline{V} \times \underline{B} - \frac{c^2}{4\pi} \underline{\underline{r}} \cdot (\underline{\nabla} \times \underline{B}) \right\} - \frac{ck}{eN_e} \underline{\nabla} N_e \times \underline{\nabla} T_e - \frac{c}{4\pi e} \underline{\nabla} \times \left[\frac{1}{N_e} (\underline{\nabla} \times \underline{B}) \times \underline{B} \right] . \tag{5}$$

where $\underline{V} = \hat{e}_r V_r + \hat{e}_z V_z$, $\underline{B} = \hat{e}_\theta B$, and no fluid quantities depend on θ. In these equations N is the total ion number density, $N = \Sigma N_\mu$, $N_e = ZN \equiv \Sigma Z_\mu N_\mu$; P_L is the laser energy deposition power density, $P = Nk(T_i + ZT_e)$ the total pressure, $\mathcal{E}$ the thermal plus ionization energy density, and R_e the rate of change of $\mathcal{E}$ due to radiation losses. The absorption part of the radiation pressure term is included in the present version of the code, i.e., $\underline{\nabla} \cdot \underline{\underline{P}}_R \cong \hat{i}_z (\vec{P}_L - \overleftarrow{P}_L)/c$, which is the momentum transfer due to absorption of the incident and reflected laser radiation.

The heat flux $\underline{Q}_e$, as given by Braginskii, consists of two parts:

$$\underline{Q}_e = \underline{q}_u + \underline{q}_T \tag{6}$$

with

$$\begin{aligned} \underline{q}_T &= -\underline{\underline{K}} \cdot \underline{\nabla} k T_e \\ \underline{q}_u &= \underline{\underline{\beta}} \cdot \underline{u} \end{aligned} \tag{7}$$

where $\underline{u}$ is the electron current velocity,

$$\underline{u} = \frac{c}{4\pi e N_e} \underline{\nabla} \times \underline{B}, \tag{8}$$

and the components of the thermal conductivity $\underline{\underline{K}}$ and $\underline{\underline{\beta}}$ are given by ($\underline{b} = \underline{B}/B$),

$$\underline{\underline{K}} \cdot \underline{\nabla} T_e = K_\parallel \underline{b}\,\underline{b} \cdot \underline{\nabla} T_e + K_\perp \underline{b} \times \underline{b} \times \underline{\nabla} T_e + K_\wedge \underline{b} \times \underline{\nabla} T_e \tag{9}$$

$$\begin{cases} K_\parallel = \gamma_o \dfrac{ZNkT_e\tau}{m} \equiv K_o , \\ K_\perp = \dfrac{ZNkT_e\tau}{m} \dfrac{(\gamma_1' x_o^2 + \gamma_o')}{(x_o^4 + \delta_1 x_o^2 + \delta_o)} \\ K_\wedge = \dfrac{ZNkT_e\tau}{m} \dfrac{x_o(\gamma_1'' x_o^2 + \gamma_o'')}{(x_o^4 + \delta_1 x_o^2 + \delta_o)} \end{cases} \tag{10}$$

$$\begin{cases} \beta_{\parallel} = N_e T_e \beta_o \\ \beta_{\perp} = \dfrac{N_e T_e (\beta_1' x_o^2 + \beta_o')}{(x_o^4 + \delta_1 x_o^2 + \delta_o)} \\ \beta_{\wedge} = \dfrac{N_e T_e x_o (\beta_1'' x_o^2 + \beta_o'')}{(x_o^4 + \delta_1 x_o^2 + \delta_o)} \end{cases} \tag{11}$$

where $x_o = \Omega_e \tau$, and the coefficients γ_o, γ_o', γ_1', γ_1'', δ_o, δ_1, β_o, β_1', β_1'', β_o', β_o'' are listed in Braginskii [1] for plasmas of various atomic charges. Also, the resistivity $\underline{\underline{r}}$ is,

$$\underline{\underline{r}} = \underline{b}\,\underline{b}\;\sigma_{\parallel}^{-1} + (\underline{\underline{I}} - \underline{b}\,\underline{b})\sigma_{\perp}^{-1} \tag{12}$$

with

$$\begin{aligned} \sigma_{\perp} &= \frac{Ze^2 N\tau}{m}\,, \text{ for } x_o \gg 1 \\ \sigma_{\perp} &= \sigma_{\parallel}\,, \text{ for } x_o \ll 1, \end{aligned} \tag{13}$$

and independently of x_o,

$$\sigma_{\parallel} = \frac{1.96\ Ze^2 N\tau}{m} \equiv \sigma_o\,. \tag{14}$$

The electron collision time in these equations is,

$$\tau = \frac{1.72\ 10^{23}(kT_e)^{3/2}}{Z^2\ N\ \ell n\Lambda}, \tag{15}$$

where kT_e is in ergs and N in cm^{-3}, and $\ell n\Lambda$ is the Coulomb logarithm [1].

The above equations are solved numerically on an Eulerian grid. The mass and momentum equations are solved explicitly using the FCT algorithm [20]. The energy and the magnetic field equations are time-split: the convective terms are solved using explicit FCT, whereas the diffusion and the source terms are solved through the use of an implicit scheme. The radiation terms and the internal energy terms, which vary on the atomic-states time-scale, are integrated on this faster time scale simultaneously with the rate equations. The time scale for changes in ion state population is determined at each point of the grid for each time step and rate equation integrations are performed consistently with this data.

B. LASER ENERGY DEPOSITION

Laser energy deposition by inverse bremsstrahlung is treated by an analytic path-integrated method which is energy conservative. The incident wave, on reaching the critical depth, is then split up into an evanescent and a reflected wave, both of which then further deposit energy in the target. The evanescent wave is important in that it extends the region near the critical depth over which the laser deposition power density P_L is large.

In the results reported here the classical absorption coefficient (corrected by Johnston and Dawson [21]) was used,

$$K = \frac{16\pi\, Z\, N_e^2\, e^6\, \ell n\Lambda}{3c(\omega/2\pi)^2(2\pi mkT_e)^{3/2}\left(1-\dfrac{\omega_p^2}{\omega^2}\right)^{1/2}} \tag{16}$$

where $\nu = \omega/2\pi$ is the laser radiation frequency in cps and $\omega_p^2 = 4\pi N_e e^2/m$. Absorption and reflection processes deriving from radiation-driven instabilities can also be simply incorporated into the code. However, the results reported here are classical.

C. RATE EQUATIONS

The above equations contain the energy density $\mathcal{E}$ and average charge $Z(N_e = Z\,N)$, which are two quantities determined as weighted sums over partial densities N_μ for ions in state μ:

$$Z = \frac{1}{N}\sum_\mu Z_\mu\, N_\mu \tag{17}$$

$$\mathcal{E} = \frac{3}{2}\,(NkT_i + N_e kT_e) + \sum_\mu E_\mu\, N_\mu \tag{18}$$

where for ion ground states,

$$E_{\mu=z} = \sum_{z'=0}^{z} \chi_{g,z'}\,. \tag{19}$$

In these equations E_μ is the total energy used to create state μ, $\chi_{g,z'}$ is the ground state ionization potential of an ion of effective charge z', and $E_i \equiv \Sigma E_\mu N_\mu$ is the internal energy of the ions. In order to obtain the above quantities, as well as R_e (the rate of change of $\mathcal{E}$ due to radiation processes), we must solve a system of rate equations for what are deemed the most important atomic processes (the plasma is in a region where neither LTE nor the coronal approximations to the rate equations are generally valid).

The atomic model used includes the dominant collisional and radiative processes as well as an appropriate treatment of self-absorption effects. Since our present interest is in the generation of x-rays with energies of from about 0.3 to 1 keV, only the ground states of all but the last two ionization stages are included in the calculation. Laser pulses with energies sufficient to rapidly burn through the L-shell electrons and excite K-shell line radiation are considered. For the hydrogen- and helium-like ions, the principal level structure is added by including several members of the np ($n \leqslant 5$) series. These levels are assumed coupled to their respective ground states by allowed dipole transitions only. Finally, the free electrons are given a Maxwellian distribution for calculation of the transition rates for collision processes.

The following processes are included in the rate equations:

(i) Excitation of an ion of charge z from the ground state q to an excited state p by electron impact at a rate W^{CE}.

$$e + N_z(q) \rightarrow e + N_z(p). \tag{20}$$

(ii) Ionization of the ion from level p and its inverse, three-body recombination,

$$e + N_z(p) \rightleftarrows N_{z+1} + e + e. \tag{21}$$

Their rate coefficients are given the symbols W^{CI} and W^{CR}.

(iii) Spontaneous radiative decay from level p to the ground state q,

$$N_{z-1}(p) \rightarrow N_{z-1}(q) + h\nu. \tag{22}$$

The spontaneous decay rate is given by the Einstein coefficient A_{qp}.

(iv) Radiative recombination of an electron and ion of charge z to form an ion of charge $z-1$ in level p.

$$N_z + e \rightarrow N_{z-1}(p) + h\nu. \tag{23}$$

The rate coefficient is denoted by W^{RR}. As an example the processes coupling the various energy levels and charge states of aluminum are shown in Fig. 2. For the lower stages of ionization only ground state configurations are included.

The rate at which the population density N_μ of the μ^{th} ion state evolves is given by a set of equations of the form

$$\frac{\partial N_\mu}{\partial t} + \underline{\nabla} \cdot (N_\mu \underline{V}) = \sum_{\nu=1}^{n} W_{\mu\nu} N_\nu \quad (\mu=1, \ldots n). \tag{24}$$

$W_{\mu\nu}$ are the rates mentioned above for transition from the ν^{th} into the μ^{th} level, and

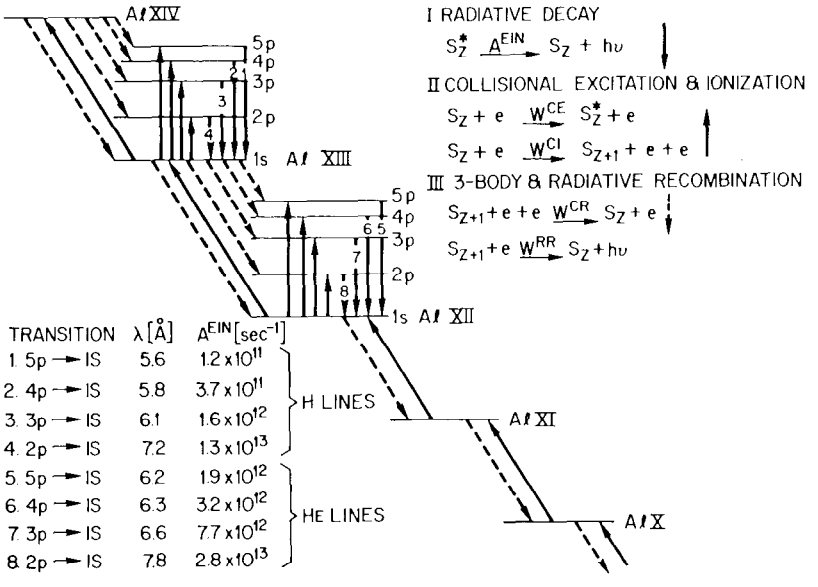

Fig. 2 — Atomic system present in the code. The system shown is aluminum and includes 14 ground states as well as the 8 most important K-shell excited states. The excited states are not coupled together as can be seen from the arrows, which indicate the processes taken into account in the description of the system.

$$W_{\mu\mu} = -\sum_{\nu \neq \mu} W_{\mu\nu} \tag{25}$$

is the sum of rates of all transitions out of the μ^{th} level. Weighted sums of Eqs. (22) yield the equations of motion for N_e, E_i, and Eq. (1).

Atomic Parameters

In this section we give some specific rate coefficients. A review of the experimental results [22] for some of the lighter atomic ions suggested a first-generation atomic model based only on the processes discussed in the previous section. This model is designed to describe only the main features of the emitted H- and He-like spectra. Forbidden collisional and radiative decay processes cascading from higher levels, dielectronic recombination (which populates doubly excited states and produces satellite lines and continua which are unresolvable from the associated resonance lines), inner shell excitation, and direct double excitation all contribute to the population of given levels and can be included in later models as necessary. Heavy particle collisional excitation is also neglected since kT_i is never large compared with ion excitation energies. It is only important in the case of collisional coupling between fine structure levels, i.e., in redistributing the angular momentum.

The analytical expressions used for the various rate coefficients were adopted on the criterion that they generate data in reasonable agreement with available measured and/or predicted values. Wherever possible experimental data was used for such atomic parameters as line strengths, oscillator functions, and energy level data.

Since accurate cross-section data are not available for highly stripped ions, it was necessary to employ approximate expressions. The ionization rate coefficient used for ionization from the ith level of an ion of charge Z_i, was obtained by integrating Seaton's [23,24] electron-ion excitation cross section over a Maxwellian velocity distribution. The result is

$$W^{CI}/N_e = 4.5 \times 10^{-24} \, (kT_e)^{1/2} \sum_i \xi_i \chi_i^2 \, e^{-\chi_i/kT_e} \tag{26}$$

where ξ_i is the number of equivalent electrons in the ith shell and χ_i is the ionization energy of the electron in the ith shell.

The calculation of recombination rates is more difficult than that of ionization rates, and there is less experimental evidence against which to check the theory. We have considered two recombination processes: radiative and three-body recombination. A convenient formula for the rate coefficient for radiative recombination into all levels of hydrogenic ions has been given by Seaton [23]

$$W^{RR}/N_e = 5.2 \times 10^{-14} \, Z_i \lambda^{1/2} \, [0.43 + 0.5 \, \ell n \lambda + 0.47 \, \lambda^{-1/3}] \tag{27}$$

where Z_i is the effective charge of the ion into which recombination takes place and $\lambda = \chi_i/kT_e$. This result is used also for nonhydrogenic systems because of its simplicity. For a more precise estimate, alternate methods must be employed.

In the case of three-body recombination, the excess energy released in the process is carried off by the free electron. Also, because of the three-body interaction, the rate will scale as the square of the free electron density. The rate coefficient per ion can be obtained by detailed balance, viz.

$$\frac{W^{CR}}{N_e} = \left(\frac{h^2}{2\pi m k T_e}\right)^{3/2} e^{\chi_i/kT_e} \, W^{CI}. \tag{28}$$

The excitation rate coefficient responsible for populating the bound levels is evaluated from the SCI [25] method. It is most conveniently expressed in terms of the oscillator strength f_{ij}, i.e.,

$$W_{ji}^{CE} = 16 \, N_e \left(\frac{2\pi}{3mkT_e}\right)^{1/2} \frac{I_H^2}{E_{ij}} \, e^{-E_{ij}/kT_e} \, f_{ij} \, \bar{g} \, \pi a_o^2 \tag{29}$$

where I_H is the ionization energy of hydrogen, E_{ij} the excitation energy, and $\bar{g}$ is a thermally averaged Gaunt factor.

Self-Absorption Effects

Total radiation losses can be estimated by summing the local radiation power loss densities over the plasma volume. However, at the high densities encountered in laser-generated plasmas, self-absorption of line radiation must be considered in calculating the actual radiation loss rates. In such cases the total loss rate can be smaller than the rates predicted by assuming the plasma to be optically thin.

When there is self-absorption, the RHS of the equations for the excited state ion densities are modified to include photoexcitation and stimulated emission processes. For example the rate coefficient for photoexcitation is

$$B_{q\leftarrow p} \int_o^\infty d\nu\ \rho_\nu\ \psi_\nu \tag{30}$$

where

$$\psi_\nu = \frac{1}{\sqrt{\pi}\Delta\nu_o} \exp\left[-\left(\frac{\nu - \nu_o}{\Delta\nu}\right)^2\right]$$

is the doppler spectral function, B_{qp} is the Einstein absorption coefficient, $\Delta\nu_D$ is the e^{-1} width of the doppler broadened absorption profile for the line centered at the frequency ν_o, and ρ_ν is the radiation spectral energy density. This density has to be calculated by integrating, over all solid angles $\underline{\Omega}$, the specific intensities $I_\nu(r,\underline{\Omega})$ obtained by solving the equation of radiative transfer through the plasma. We have transported a single frequency group and replaced $\int d\nu\ \rho_\nu\ \psi_\nu$ by

$$\psi_{\nu=\nu_o} \int d\nu\ \rho_\nu \equiv \frac{\rho}{\sqrt{\pi}\Delta\nu_o} \quad \text{where } \rho(r) = \frac{1}{c}\int d\underline{\Omega}\ I_{\nu_o}\ (r,\underline{\Omega}).$$

With the above processes included in Eq. (24) the rate at which the excited state population density $N(p)$ changes due to radiative processes is given by

$$\left(\frac{dN(p)}{dt}\right) = -\left(A_{qp} + B_{qp}\frac{\rho}{\sqrt{\pi}\Delta\nu_o}\right) N(p) + B_{pq}\frac{\rho}{\sqrt{\pi}\Delta\nu_D} N(q) + (\text{collision terms}) \tag{31}$$

where $B_{qp}/B_{pq} = (g_q/g_p)$ and g_p is the degeneracy factor of state p.

D. RADIATION

Emitted radiation — contained in the R_e term of Eq. (3) — is made up of bremsstrahlung, recombination, and line emission (the contribution of cyclotron radiation to the total radiation is negligible). It is emitted over a wide spectrum of frequencies in both continuum and line emission, and over all angles. The spectrum is complicated in that many stages

of ionization will be passed through as the plasma temperature changes. Each of these stages will have excited levels capable of excitation and radiative decay.

The term R_e can be written

$$R_e = \sum_{\nu} (\tilde{j}_\nu - k_\nu J_\nu) \tag{32}$$

where J_ν is the sum over specific intensities, $J_\nu = \int d\underline{\Omega}\, I_\nu(\underline{\Omega})$, j_ν the emission coefficient $\tilde{j}_\nu = \int d\underline{\Omega}\, j_\nu(\underline{\Omega})$, k_ν the absorption coefficient, and $\underline{\Omega}$ is the direction of propagation. The emission has three contributions

$$\tilde{j}_\nu = \tilde{j}_\nu^b + \tilde{j}_\nu^{rr} + \tilde{j}_\nu^{\ell} \tag{33}$$

where the bremsstrahlung losses are represented by

$$\sum_{\nu} \tilde{j}_\nu^b = 1.2 \cdot 10^{-19} (kT_e)^{1/2} N_e \sum_{\mu} Z_\mu^2 N_\mu, \tag{34}$$

the radiative recombination losses by

$$\sum_{\nu} \tilde{j}_\nu^{rr} = \sum_{\nu,\mu} N_\mu W_{\nu\mu}^{RR} (E_\mu - E_\nu), \tag{35}$$

and line emission by

$$\sum_{\nu} \tilde{j}_\nu^{\ell} = \sum_{\mu,\nu} A_{\mu\nu} N_\nu (E_\nu - E_\mu). \tag{36}$$

where E_μ is the energy of state μ.

For some frequencies, the medium opacity may become larger than (or of order) one, and reabsorption of the emitted radiation becomes important. In this case the distribution of radiation intensity within the plasma must be computed as a part of the already complex reactive flow problem. We solve for I_ν using the transport equation,

$$\underline{\Omega} \cdot \underline{\nabla} I_\nu = j_\nu - k_\nu I_\nu. \tag{37}$$

In this equation, $\partial I_\nu / \partial t$ has been neglected on the left hand side, i.e., it is assumed that a quasi-steady distribution for $I_\nu(\underline{x}, \underline{\Omega})$ is reached on a time scale short compared with the time scales involved.

Equation (37) is solved for the eight directions which are defined by connecting a cell center to each adjacent cell center in the 2D finite-difference grid. This method performs transport from each cell to its immediate neighbors and ensures that radiation

travels in straight lines in the computational plane. This scheme is explicit and requires at most two time steps to connect any two cells. It is described in detail elsewhere [6].

The radiation intensities are computed for the main spectral lines of H- and He-like aluminum and for the remainder of the lines plus continuum. The continuum is transported in order to deposit this energy along with line X-radiation in the dense cool plasma behind the critical density region. In this way, both electron thermal conduction and X-radiation absorption contribute to the heating of plasma in the over-dense region. Radiation transport is performed for discrete lines and not for arbitrary energy groups for two reasons: First, spectra of moderate Z target elements present very well defined dominant lines. Second, one of the purposes of this simulation study lies in comparing numerical with experimental results (e.g. spectral lines).

The total absorption coefficient is

$$k_\nu = k_\nu^{bb} + k_\nu^{bf} + k_\nu^{ff} \tag{38}$$

for photons that are absorbed due to bound-bound, bound-free, or free-free transitions. In our case the free-free absorption line is small. The coefficient for bound-bound absorption, which determines the strength by which line radiation is trapped within the hot plasma, is expressible in terms of the Einstein A coefficient for the bound-bound transition.

$$k_{\nu(q,p)}^{bb} = \frac{1}{8\pi} \frac{g_p}{g_q} A_{qp} \lambda^2 N_q \left[1 - \frac{g_q}{g_p} \frac{N_p}{N_q}\right] \frac{1}{\sqrt{\pi}\Delta\nu_D} \tag{39}$$

where λ is the transition wavelength: $\lambda = hc/(E_p - E_q)$. The bound-free coefficients allow for emission or ejection of inner shell electrons in the cooler-regions of the plasma containing low-lying ionization stages by means of the following approximate formula [26]:

$$k_\nu^{bf} = 2.10^{-19} \sum_{\mu=1}^{n_L} N_\mu \tag{40}$$

where n_L is the number of ion states having electrons which can be ejected by a photon of energy $h\nu$ and where we have ignored the frequency dependence since the major contribution occurs at the absorption edges. Bound-bound absorption is dominant in the hot plasma region while bound-free absorption dominates in the overdense plasma, where $k^{bf} \cong 300\ \text{cm}^{-1}$.

The radiation intensity is coupled to the non-equilibrium reactive flow in two ways. In the case of bound-free absorption, the energy goes directly into the electron thermal energy in the dense plasma. From bound-bound absorption, photon energy goes into ion internal energy, i.e., into the formation of ion excited states.

In Fig. 3 we have illustrated the model for frequency diffusion included in the present code. Frequency diffusion is an important escape mechanism for that radiation which is trapped by the plasma. Photons are emitted with a distribution function centered around ν_o where ν_o is the line transition frequency. If we suppose that the plasma is thick for

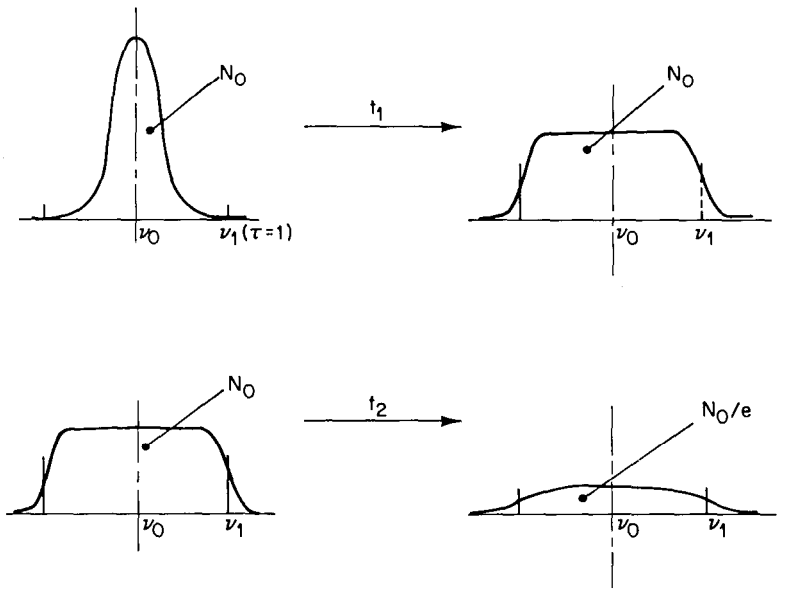

AT TIME t, FRACTION OF ESCAPED PHOTONS IS

$$f = \frac{N_0 - N}{N} = 1 - e^{-(t-t_1)/t_2}$$

$$\text{WITH} \begin{cases} t_1 = (\tau_0 - 1)/k_0 C \\ t_2 = 2\tau_0 \ln \tau_0 / k_0 C \end{cases}$$

Fig. 3 — Frequency diffusion model and its characteristic times

this frequency, we see that somewhere in the wing there is a frequency ν_1 for which the plasma becomes optically thin. Due to scattering, the photon distribution spreads to ν_1 in a characteristic time t_1 without any loss of energy and then photons escape from the wings of the distribution in a characteristic time t_2. These times t_1 and t_2 have been computed by Julienne and Davis [7] and can be shown to be less than 10^{-12} sec for the conditions we are interested in. So this mechanism provides an efficient way for the photons to escape, once they are trapped, and the escaped fraction must be computed as a function of time since it depends on the plasma parameters which change with time. Our treatment of radiation trapping and escape then includes time-dependent energy groups for the main radiation lines.

A frequency diffusion model in the transport equation is accomplished in our code by the local replacement of j_ν by $(1 - f)j_\nu$ for the main lines where f is the escaped fraction as defined in Fig. 3. The remainder fj_ν is added to the continuum source function at that same location. Thus frequency diffusion allows partitioning of the source terms among frequency groups. In this way a portion of K_α line radiation is transported freely within the hot emitted plasma and absorbed in the dense plasma of the target or emitted out the front of the heated plasma.

2-D SIMULATION

Al 20 J τ_L = 250 ps r_f = 100 μ

ENERGY BALANCE

	NO RAD TRANSPORT		WITH RAD TRANSPORT	
	t = 200	500 ps	t = 200	500 ps
THERMAL ENERGY	58.8	45.0	55.4	46.0
CONVECTED ENERGY	20.0	20.0	16.6	15.0
ION INTERNAL EN.	13.2	15.0	25.0	30.0
TOTAL X RAY EN.	8.0	20.0	3.0	9.0

Fig. 4 — Partitioning of the incident laser energy into various final forms, with and without radiation transport, at two different times

E. DISCUSSION

In the sample results displayed in Figs. 4 to 19 a gaussian laser pulse of half width 250 ps is incident on an initially cool plasma ($T \sim 8$ eV). The peak of the laser pulse occurs at $t = 100$ ps. The target plasma has an exponential density ramp in which the ion density goes from $N_i = 1.5 \cdot 10^{21}$ to $1.5 \cdot 10^{17}$ in a distance of 1600 μ and a constant density region of thickness 200 μ exists at both ends of this exponential ramp. This initial plasma can be viewed as having been set up by a laser prepulse, although in principle if we choose to make the density variation very steep then the resulting dynamics is similar to what would be the case if the pulse were incident on a solid target with no prepulse. The target plasma is Al in the examples shown.

A number of comparison runs have been made with radiation transport included and excluded. Figure 4 shows an energy balance for a 20 J run as function of time and of radiation transport. We see that at short times most of the energy is still found in a thermal form and that this fraction decreases as a function of time, with or without radiation transport. The convected energy is the energy flowing out of the grid. One of the differences between radiation transport and no radiation transport shows in the ion internal and total x-ray energy. When radiation transport is included, a larger fraction of the energy is found in the ion energy states. Counter-balancing this, the x-ray energy is much smaller. Besides the fact that the energy is returned to the ion states instead of being emitted, the x-ray energy is smaller because a large fraction of the free-streaming radiation is now reabsorbed in the back region. As a result of the redistribution by radiation transport, the computations show that approximately 65% of the unabsorbed radiation is convected into thermal energy in the back region.

The calculation of a line emission spectrum is an important test of our model with experiment. The shape of the spectrum depends in varying degrees on the modeling of the laser absorption, heat conduction, rate equations, and radiation transport. As an important feature of our present model, only the K_α lines, which have the largest opacities, are coupled back to the ions. However, while self-absorption of the other K-lines

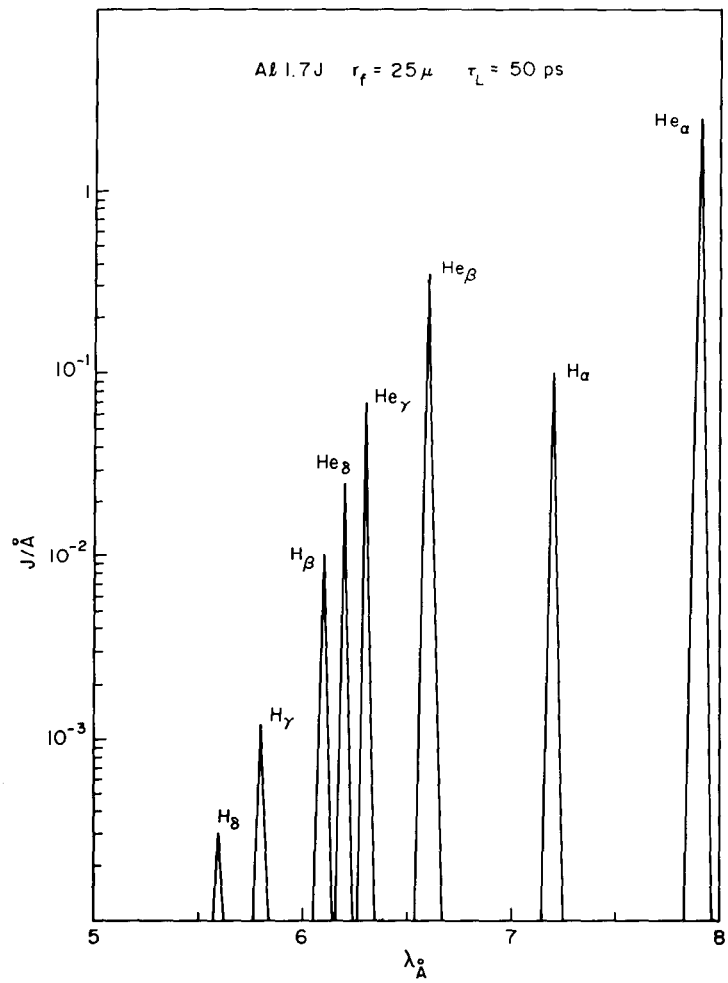

Fig. 5 — Time-integrated atomic spectrum obtained numerically for an aluminum target. The laser pulse characteristics are 1.7 J, 25 μ focal spot radius, 50 ps FHWM.

is a smaller effect, it will have to be treated in later versions of the model. A typical emission spectrum is shown in Fig. 5. The laser parameters that were used are given on the figure and correspond to the measured values of a recent NRL experiment. The total energies radiated in the K_α and K_β lines of H- and He-like aluminum were computed to be $(K_\alpha)_H = 2.49 \times 10^4$ ergs, $(K_\beta)_H = 2.11 \times 10^3$ ergs, $(K_\alpha)_{He} = 6.00 \times 10^5$ ergs and $(K_\beta)_{He} = 6.89 \times 10^4$ ergs.

In Figs. 6-9 some plots of n_e, T_e, T_i, P_L, and the line emission power density L_R are shown as a function of z along the laser beam axis for $r = 0$. Some general features are apparent from these plots. First considering the temperature profiles, we note that T_e/T_i at the critical depth ranges from ~ 5 to ~ 8 as the laser energy increases from 20 to 200 J. The electron temperature falls off more slowly than T_i in the underdense

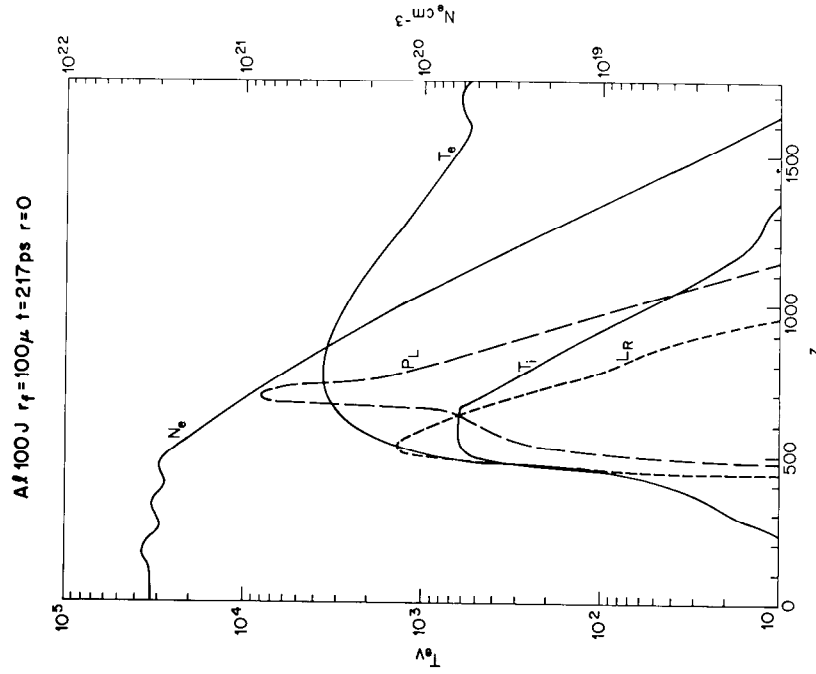

Fig. 7 — Same data as Fig. 6 for a 100 J laser pulse at t = 217 ps

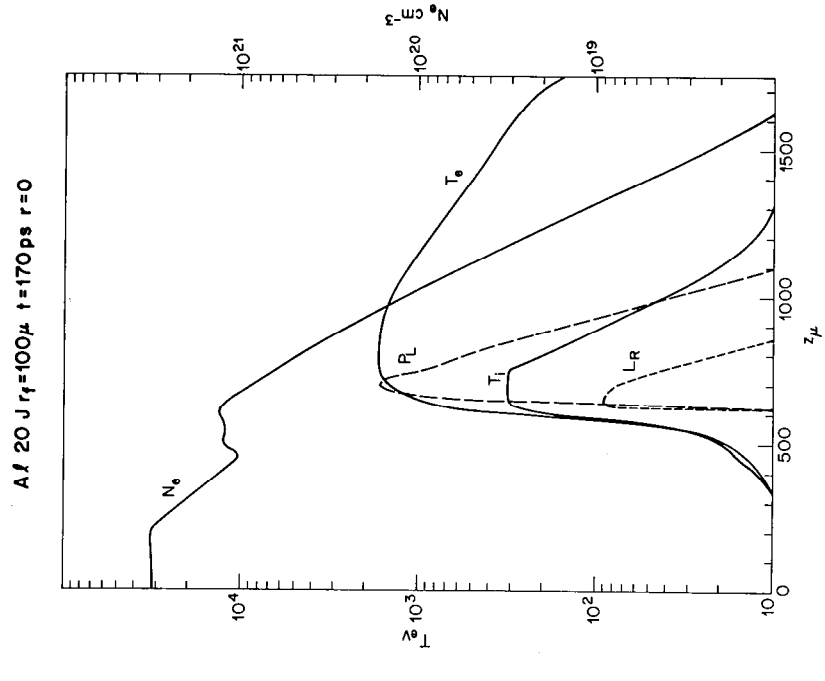

Fig. 6 — Electron density, electron and ion temperature, absorbed laser power and line radiation power as a function of distance on the axis for a 20 J, 100 μ, 250 ps laser pulse at t = 170 ps (70 ps after the peak of the laser pulse)

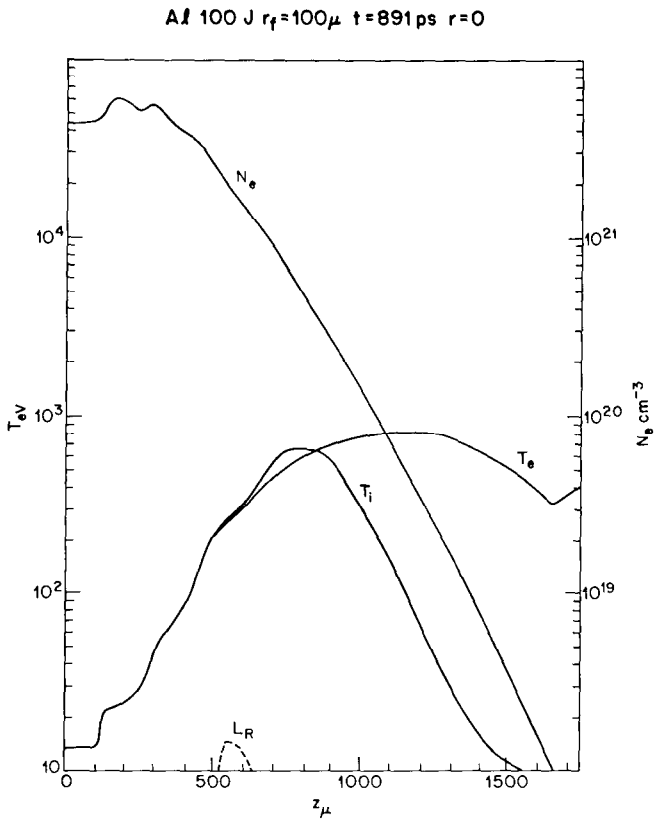

Fig. 8 — Same as Fig. 7, at t = 891 ps. The absorbed laser power is negligible at that time.

region due to the high electron thermal conductivity, and of course, in this region T_i greatly lags T_e. Maximum temperatures range from $T_e \sim 1.7$ keV to 5 keV.

The line emission has a maximum that occurs where $T_e \cong 1$ keV so that it is displaced into the overdense region beyond the maximum in P_L which occurs at the critical depth. This displacement increases with laser energy. Energy is deposited in the overdense region by direct deposition from the evanescent wave, thermal conduction, and radiation transport, and then radiates more efficiently from this region. The evanescent wave appears to penetrate more deeply as T_e increases (see the 200 J case).

The increase in electron density $N_e = ZN$ above the initial density (this is most pronounced in the late time case Fig. 8) is principally due to an increase in Z and is not ion density compression.

Fluid velocities are small in the examples shown. This is a consequence of the slow fall-off in density of the initial target as can be verified by estimating the fluid velocity from $V \sim \tau_L v_s^2/\ell$ where v_s is the sound speed and ℓ the initial gradient scale. A steeper initial gradient gives rise to higher fluid velocities. Radiation pressure was also observed to have a large effect on the fluid velocity while the pulse was on.

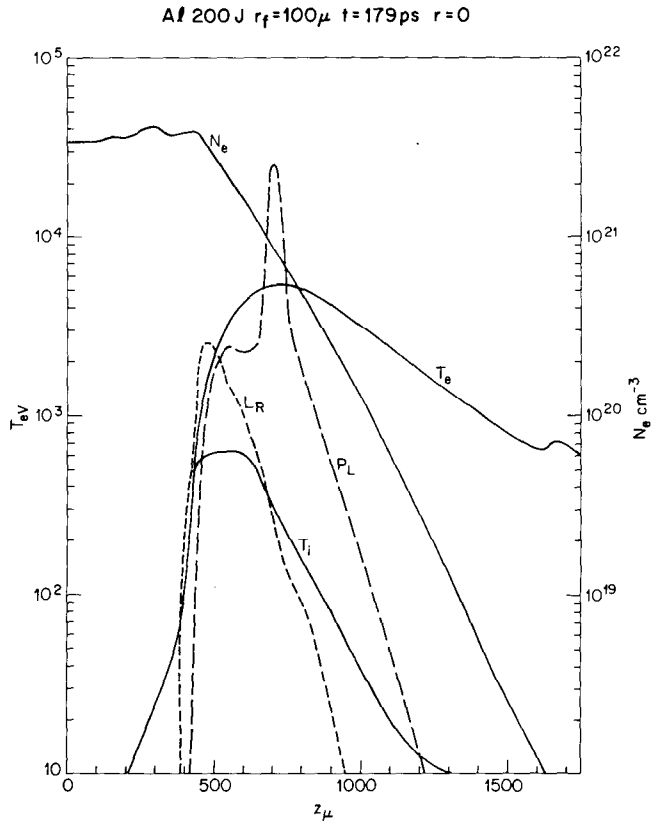

Fig. 9 — Same data and time as Fig. 6, but for 200 J laser pulse

An off-axis plot of the same parameters is shown in Fig. 10 and shows similar features. The radial dependence of T_e, P_L, and L_R is shown more clearly in Figs. 11, 12, and 13. In Figs. 11 and 12 it is interesting to note that $T_e(r)$ has a maximum for fixed z that occurs *off axis*. This can be understood as due to the magnetic field which is zero at $r = 0$ but has a maximum off axis. The reduced thermal conductivity in the high B region leads to a slower transport of deposited laser energy out of that region. This is supported by Fig. 13 in which the maximum in T_e returns to $r = 0$ if B fields are suppressed in the code. In Fig. 11 we also note that the emission L_R has a maximum displaced off axis.

Figure 14 is an illustration of a diagnostic which has been developed in order to compare experimental results with our code results. These pinhole photographs can be obtained for both main line radiation and total radiation. They are time-resolved and because of their sensitivity to both density and temperature profiles, they provide one of the most accurate comparisons between numerical and experimental results.

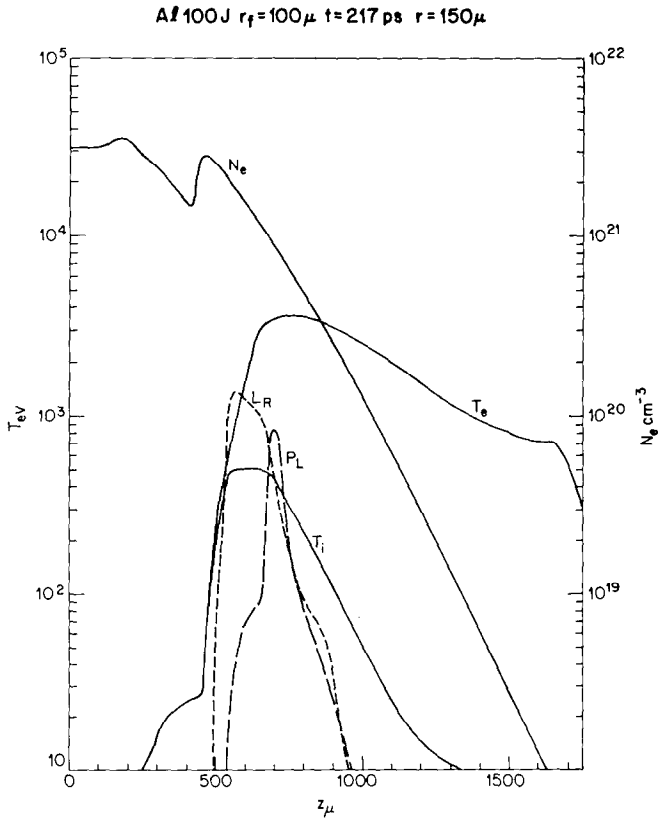

Fig. 10 — Same case as Fig. 7 viewed off-axis at r = 150 μ

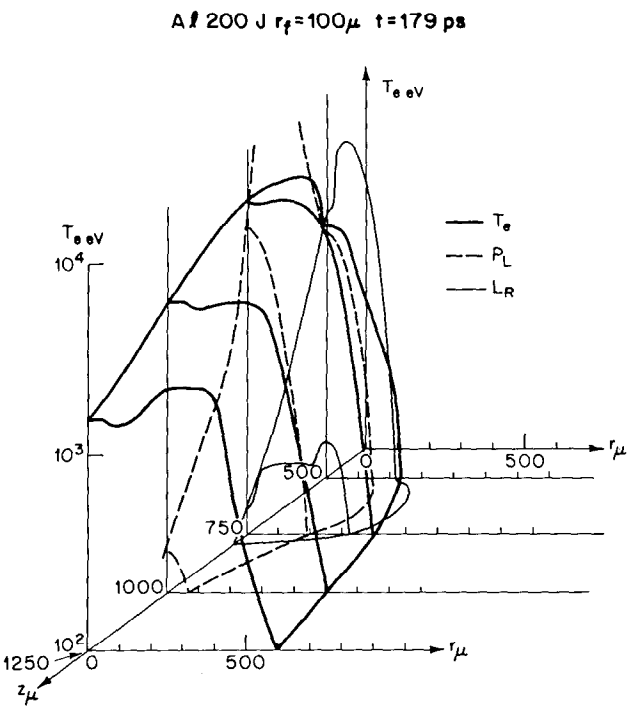

Fig. 11 — Electron temperature, absorbed laser power and line radiation power as a function of both distance along the axis and radius for case shown in Fig. 9

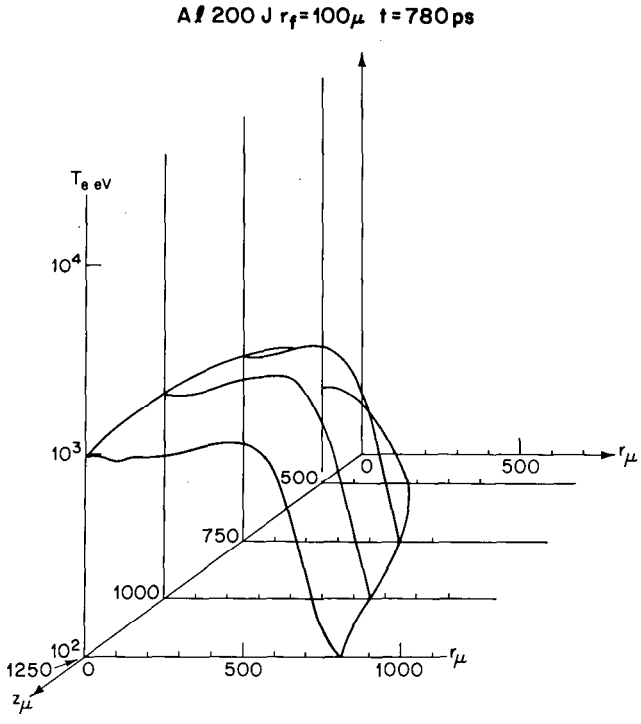

Fig. 12 — Electron temperature for the case of Fig. 9 at t = 780 ps

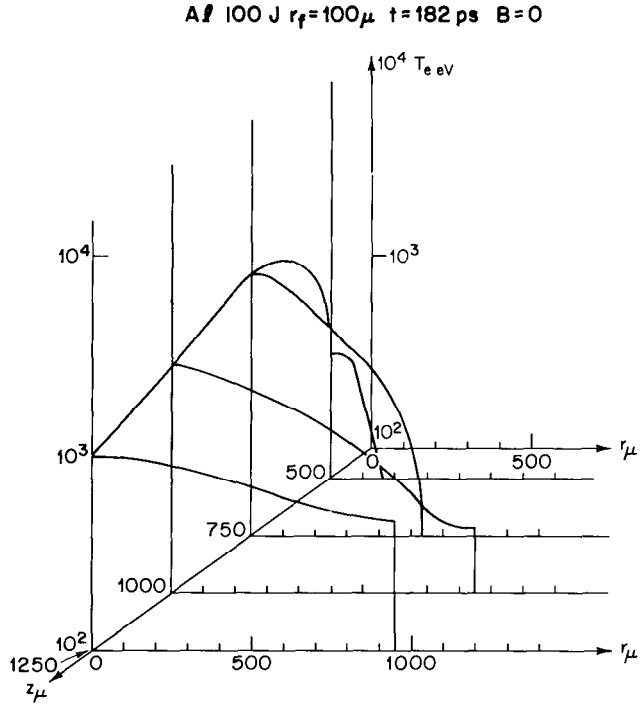

Fig. 13 — Electron temperature as a function of r and z for 100 J incident energy without any self-generated B field at t = 182 ps. Without any B field the temperature is more uniform in the radial direction.

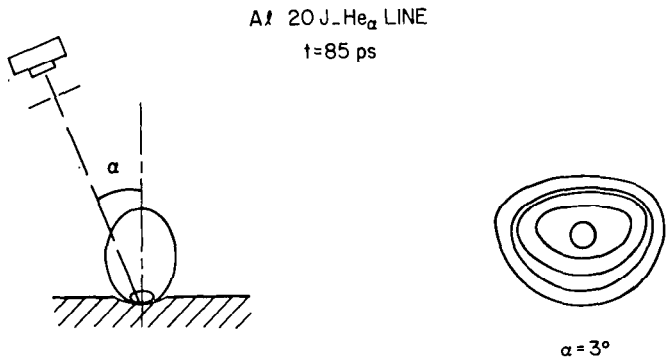

Fig. 14 — Time-resolved pinhole photograph for the He_α line at t = 85 ps. The lines shown in the photograph are contours of equal intensities.

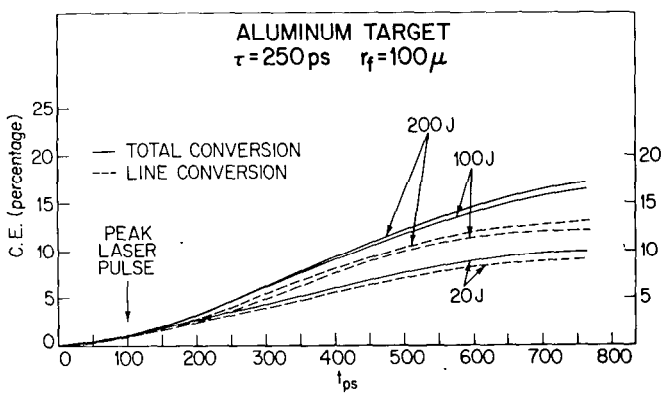

Fig. 15 — Conversion efficiencies of incident laser energy into x-ray energy as a function of laser energy and time. This is also a plot of conversion efficiencies as a function of laser intensities for a fixed focal spot radius (100 μ).

The x-ray conversion efficiency into escaping photons is plotted as a function of time and laser energy in Fig. 15. The maximum emission is delayed by about 275 ps from the maximum in the laser pulse. This delay is also a consequence of the fact that the maximum emission occurs from plasma for which $T_e \cong 1$ keV. The focal spot first overshoots this optimum temperature and only later spreads the energy sufficiently that a large emitting region of 1 keV plasma is present. The total x-ray conversion efficiency is observed to increase with laser energy and can reach values of about 20% for E_J = 200 J.

Figures 16-19 represent a series of computer runs aimed at understanding how to scale our results for the conversion efficiency to large pulses. The total energy incident in the laser pulse can be written as $W_L \cong \pi r_f^2 I_o \tau_L$ where I_o is the axial intensity, r_f the focal spot radius, and τ_L the laser pulse duration. In the limit that $W_L \to \infty$ and $r_f \to \infty$ with I_o and τ_L remaining constant, we expect the dynamics of the plasma to become one-dimensional. In this limit the conversion efficiency satisfies

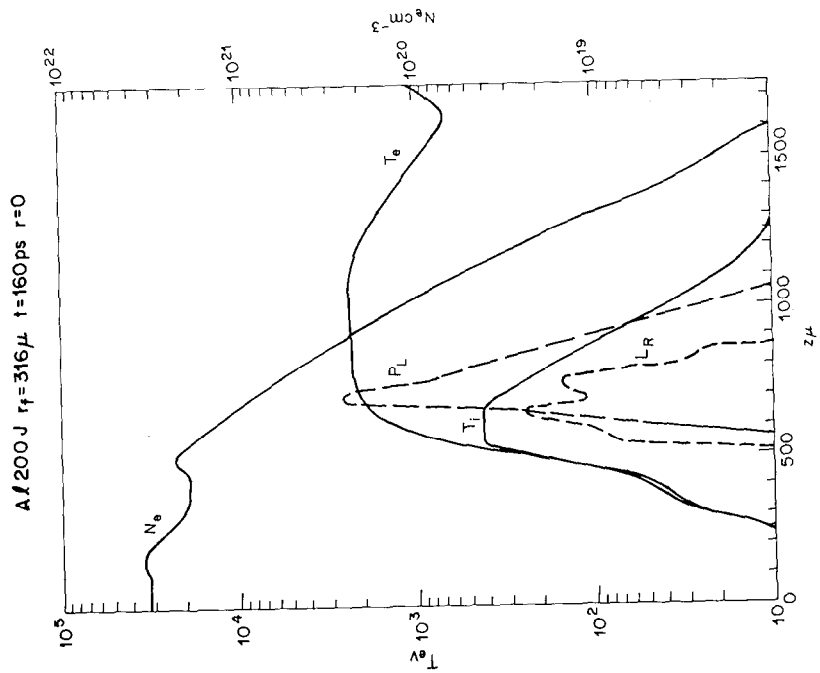

Fig. 17 — Same data as Fig. 16, for focal spot area multiplied by 10

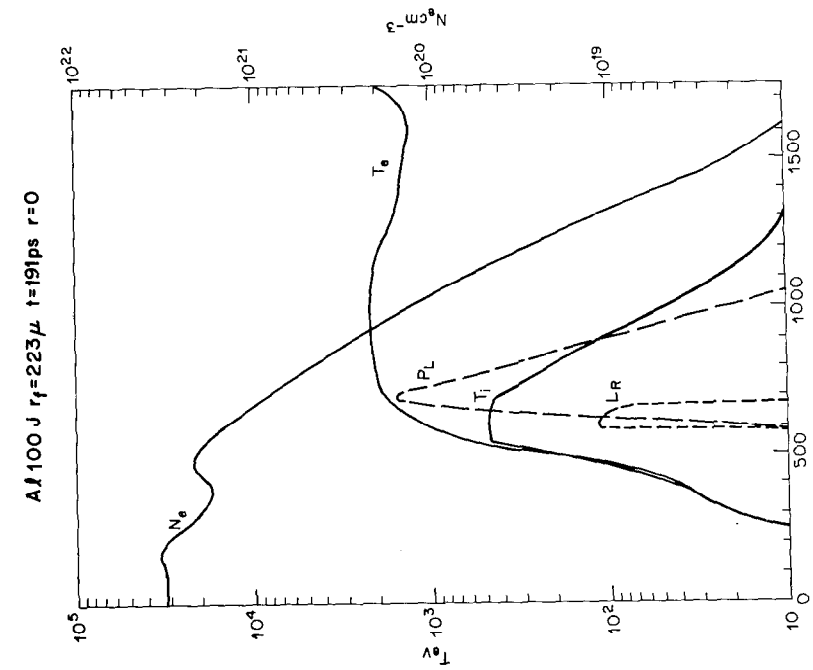

Fig. 16 — Typical quantities as a function of z for the same intensity of laser pulse as in Fig. 6, but the focal spot area has been increased by a factor of 5

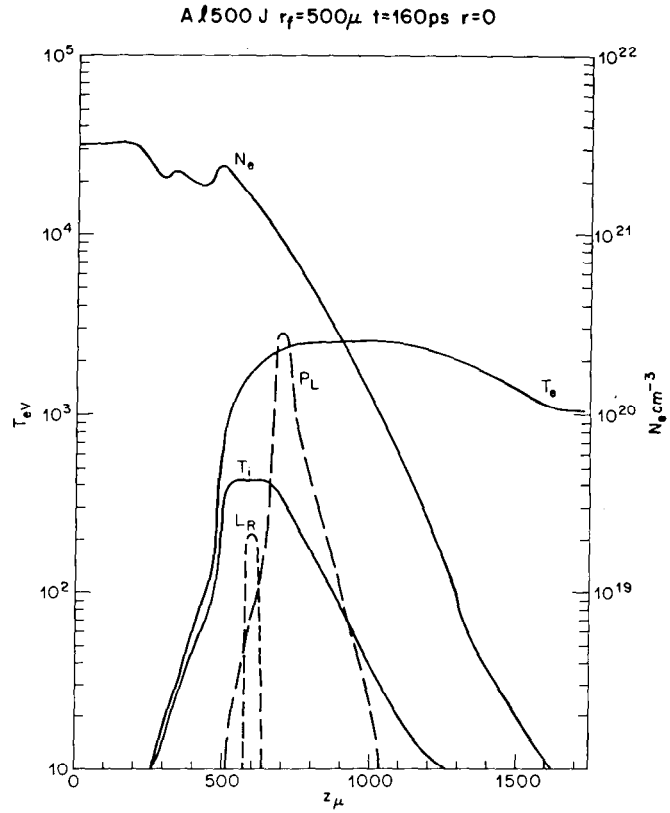

Fig. 18 — Same data as Fig. 16, for focal spot area multiplied by 25

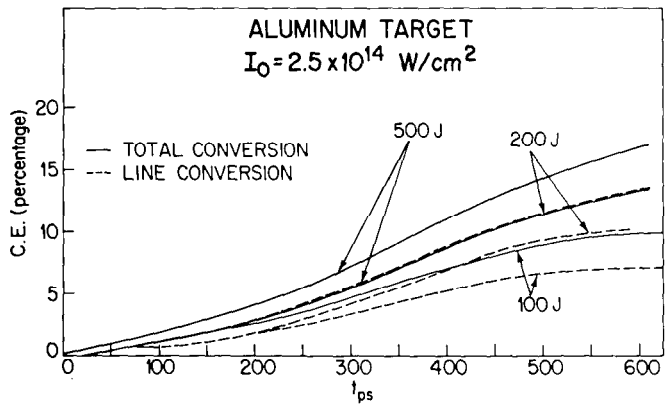

Fig. 19 — Conversion efficiencies of incident laser energy into x-ray energy for cases shown in Figs. 16-18. For the same intensity, this figure shows the variation of conversion efficiencies with focal spot size (two-dimensional effects).

$$CE^{\text{Total}}\Big|_{r_f \to \infty} = \frac{\pi r_f^2 \int I_\nu \, d\nu dt}{(\pi r_f^2 I_o \, \tau_L)} = \frac{\int_{\nu_M}^{\infty} d\nu \int_o^{\infty} dt \, I_\nu}{I_o \, \tau_L} ,$$

i.e., it becomes a function of I_o and τ_L only. If we are given this function then the conversion efficiency for very large pulses can be simply predicted as the value of CE corresponding to $I_o \tau_L = W_L / \pi r_f^2$ for the pulse in question. For a given I_o and τ_L there will of course be a minimum energy W_L^{Min} above which the system is essentially $1D$ and the above scaling applies. For $W_L < W_L^{\text{Min}}$ the dynamics is two dimensional and the scaling does not apply.

In Figs. 16, 17, and 18 we have plotted 3 profiles of several target plasma parameters for the pulses in which W_L = 100 J, r_f = 223 μ; W_L = 200 J, r_f = 316 μ; and W_L = 500 J, r_f = 500 μ, i.e., these three pulses have a constant axial intensity ($I_o = 2.5 \times 10^{14}$ W/cm^2) and pulse width τ_L = 250 ps. As expected the maximum electron temperatures reached in these 3 cases are approximately the same (they range from 2.15 keV to 2.5 keV). Further, the conversion efficiencies are shown in Fig. 19.

REFERENCES

1. S.E. Braginskii, in *Reviews of Plasma Physics*, edited by M.A. Leontovich (Consultants Bureau, New York, 1965), p. 205.
2. J.A. Stamper, K. Papadopoulos, S.O. Dean, E.A. McLean, and J.M. Dawson, Phys. Rev. Lett. 26, 1012 (1972).
3. N.K. Winsor and D.A. Tidman, Phys. Rev. Lett. 31, 1044 (1973).
4. J.B. Chase, J.L. LeBlanc, and J.R. Wilson, Phys. Fluids 16, 1142 (1973).
5. K. Whitney and J. Davis, J. Applied Phys., to be published, Dec. 1974.
6. D. Colombant and N.K. Winsor to be published.
7. P.S. Julienne and J. Davis, *Radiation Escape from an Optically Thick Plasma*, Naval Research Laboratory Memo Report 2556 (1973).
8. J.D. Lindl and P.K. Kaw, Phys. Fluids 14, 371 (1971).
9. J.W. Shearer and J.L. Eddleman, Phys. Fluids 16, 1753 (1973).
10. J.A. Stamper and D.A. Tidman, Phys. Fluids 16, 2024 (1973).
11. See, e.g., Bull. Amer. Phys. Soc. 18, 684 (1973), abstracts HN5-HN14. See also J.A. Stamper, O.C. Barr, J. Davis, G.A. Doschek, C.M. Dozier, U. Feldman, B.M. Klein, W.M. Manheimer, E.A. McLean, J.M. McMahon, D.J. Nagel, D.A. Tidman, R.R. Whitlock, K. Whitney, N. Winsor, and F.C. Young, *Laser-Matter Interaction Studies at NRL*, to appear in Proceedings of the Third Workshop on "Laser Interactions and Related Plasma Phenomena," Rensselaer Polytechnic Institute (1973).

12. P.J. Mallozzi, H.M. Epstein, R.G. Jung, D.C. Applebaum, B.P. Fairand, and W.L. Gallagher, in "Fundamental and Applied Laser Physics: Proceedings of the Esfahan Symposium," ed. by M.S. Feld, A. Javan, and N.A. Kurnit (Wiley, New York, 1973).

13. P.J. Mallozzi, H.M. Epstein, R.G. Jung, D.C. Applebaum, B.P. Fairand, W.J. Gallagher, R.L. Uecker, and M.C. Muckerheide, J. Appl. Phys. 45, 1891 (1974).

14. D. Colombant and G.F. Tonon, J. Appl. Phys. 44, 3524 (1973).

15. See the Semi-Annual Report of the Laser Fusion Program, Lawrence Livermore Lab., Jan.-June 1973 p. 177 (UCRL-50021-73-1).

16. H.D. Shay, D. Bailey, S. Bodner, J. Katz, W. Kruer, J. Nuckolls, W. Slivinsky, E. Valeo, and G. Zimmerman, *Suprathermal Electron Distributions in Laser-Produced Plasmas*, paper at the 7th European Conference on Plasma Production by High Power Lasers, Garching, April 22, 1974.

17. J.P. Freidberg, R.W. Mitchell, R.L. Morse, and L.I. Rudsinski, Phys. Rev. Lett. 28, 795 (1972).

18. M.M. Wilson, Bull. Am. Phys. Soc. II 18, 1317 (1973).

19. A.A. Amsden and C.W. Hirt, LASL Report LA-5100 (Los Alamos, 1972), unpublished.

20. J.P. Boris and D.L. Book, J. Comput. Phys. 11, 38 (1973).

21. T.W. Johnston and J. Dawson, Phys. Fluids 16, 722 (1973).

22. D.J. Nagel, P.G. Burkhalter, C.M. Dozier, J.F. Holzrichter, B.M. Klein, J.M. McMahon, J.A. Stamper, and R.R. Whitlock, Phys. Rev. Lett., 33, 743 (1974).

23. M.J. Seaton in "Atomic and Molecular Processes," (D.R. Bates), Academic Press, New York and London, 1962.

24. M.J. Seaton, M.N.R.A.S. 119, 81 (1959).

25. J. Davis, J.Q.S.R.T. 14, 549 (1974).

26. E. Daltabuit and D.P. Cox, Astrophys. J. 177, 885 (1972).

IX. MODEL STUDIES

In addition to the 2-D MHD reactive flow code already discussed in Chapter VIII in detail, two additional models are in the development phase and are near completion. They will be able to treat spherical and cylindrical targets with an expanded atomic physics model coupled with a 1-D fluid, radial expansion model. An additional feature is the inclusion of a radiative transport scheme capable of exhibiting such characteristics as line inversion as well as frequency diffusion in an integrated fashion. An earlier version of one of these models is referred to as the hot-spot model and will now be described.

A. INTRODUCTION

When laser energy is deposited quickly ($\ll 1$ ns) in a cold plasma, a substantial conversion of this energy to K-line x-rays is possible in low-Z target plasmas [1]. Thus, while the absorption of laser radiation rapidly heats the electron gas and, in turn, the plasma, radiative losses can produce a comparable cooling of the plasma. The cooling rate by K-line emission depends on the degree of plasma heating and on the plasma Z.

In general, to treat the evolution of laser-heated plasmas, one must employ a fluid dynamic description that is based on equations of motion for the following fluid quantities [2-4]: $\{N_\mu\}$, the ion population densities; $\vec{B}$, the spontaneously generated magnetic field [5]; $\vec{v}$, the fluid velocity; T_e, the electron temperature; and T_i, the ion temperature. In this paper, however, a simpler model will be developed that describes specifically K-line emission from a small-volume element of *stationary* laser-heated plasma. The dynamic variables of this theory are $\{N_\mu\}$, T_e, and T_i; $\vec{v}$ and $\vec{B}$ are assumed to remain zero. The model is designed to provide first-order comparisons of the capability of different Z plasmas to convert laser energy to K-radiation. Its validity rests on the assumption that, when a cold plasma absorbs laser radiation in less than a quarter nanosecond at intensity levels between 10^{11} and 10^{16} W/cm^2, only a weak, at first neglectable, magnetohydrodynamic plasma motion will be generated over 1 to 2 ns time intervals. The justification for this assumption is that the buildup time for the B-field and fluid-motion energies is roughly a nanosecond, as estimated from the same temperature gradient used to compute conduction losses [1]. On the other hand, the plasma in our model is cooled by heat conduction and K-line emission in less than a nanosecond.

After the model is proposed in Sections B and C, a comparison of its predictions with experiment will be made in Section D. The remainder of the paper will then be devoted to a discussion of the problem of maximizing laser-energy conversion to K-line x-rays in carbon, fluorine, and aluminum plasmas. These plasmas produce K-radiation in different frequency intervals, and the ability to maximize x-ray output in a given frequency interval may be important if, for example, laser-heated plasmas are to find use as x-ray sources for the pumping of vacuum UV lasers.

B. THE MODEL

In developing our model, we envision the physical situation sketched in Fig. 1. We imagine that a sphere of uniform and stationary plasma is located in the focus of a laser beam, where it absorbs a prescribed amount of laser radiation. The sphere radius r is chosen equal to the radius of the focal spot. Since light absorption is resonant when the laser frequency ω_L equals the plasma frequency, the ion density N_i within the sphere is determined by the condition that $N_i = N_e^c/Z$, where Z is the nuclear charge of the ions and N_e^c is the critical electron number density: $4\pi e^2 N_e^c/m = \omega_L^2$. This choice of N_i ensures that the sphere remains strongly absorbing, yet translucent to the light throughout the course of the plasma heating.

Heating of the plasma will be studied by deposition of a small quantity of laser energy E_o into the volume ΔV of the sphere in a given time interval Δt. The deposition rate S_e will be taken to be Gaussian:

$$S_e = \frac{E_o}{\Delta V} \frac{1}{\sqrt{\pi}\Delta t} e^{-\left(\frac{t-t_o}{\Delta t}\right)^2} \tag{1}$$

for mathematical convenience. The exact shape of the heating pulse will depend on the shape of the laser pulse and on changes of the plasma absorption coefficient during the course of the plasma heating. The absorption length λ_{abs} for absorption by inverse bremsstrahlung is [6],

$$\lambda_{abs} = \frac{8.3 \times 10^9 \; T_e^{3/2} \left(1 - \frac{N_e}{N_e^c}\right)^{1/2}}{(N_e^2/N_i) \; \ell n\Lambda (N_e/N_e^c)}$$

where $\ell n\Lambda$ is the Coulomb logarithm. For a singly ionized Al plasma, for example, at a temperature of 3×10^4 °K ($\sim$ 3eV) and an electron density of roughly 7×10^{19} cm^{-3} ($N_e^c = 10^{21}$ electrons/cm^{-3} is the critical density for 1.06 μ neodymium laser radiation), λ_{abs} is on the order of 100 μ. When the electron temperature increases to 10^7 °K and the electron density and Coulomb logarithm increase correspondingly an order of magnitude, λ_{abs} largely maintains its value. The only large changes in λ_{abs} occur because of time lags in the changes of N_e that are brought about by changes in T_e. However, as T_e increases, collisional ionization rates of low-lying ionization stages approach values of 10^{12} sec^{-1}, so that lag times are only on the order of picoseconds. Thus, the heating and laser pulses should not differ significantly. Moreover, the laser radiation will penetrate spheres smaller than 100 μ in diameter. In this model, however, we will be concerned only with the energy actually deposited within the sphere in a given Δt in order to compute efficiencies with which it is converted to x-rays.

E_o, Δt, and r are free parameters whose values are chosen in accordance with the physics of the model. For example, since we are assuming that the plasma densities and temperatures are uniform within ΔV, r should be chosen as small as possible. A good lens can focus the laser beam to a 46-μ spot; accordingly, we have taken $r = 23$ μ ($\Delta V = 5 \times 10^{-8}$ cm^3). Then, since an ideal electron gas with a density of 10^{21} electrons cm^3 and

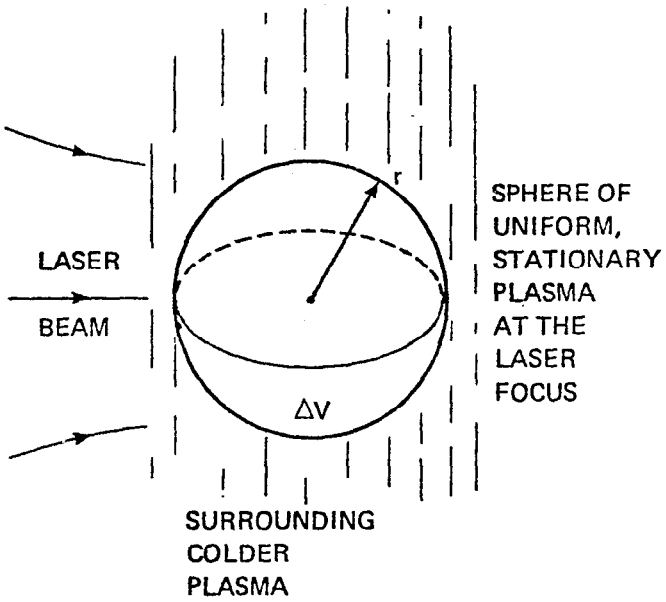

Fig. 1 — Hot-spot model geometry

a temperature of 1 keV has an energy density of 2×10^5 J/cm^3, the net absorption of only 10^{-2} Joules is sufficient to heat the plasma in a sphere of 5×10^{-8} cm^3 to keV temperatures. Moreover, since this energy is conducted outside the sphere to a larger volume of plasma, the surrounding plasma will not be heated as strongly as the sphere, where direct energy deposition is assumed. Thus, in the theory to follow, E_o will have values ranging around 10^{-2} J and will be restricted to values less than 1 or 2 J. Finally, in order to protect our assumption that there be negligible MHD motion generated in the course of the plasma heating and cooling, the laser energy will be deposited quickly, generally $\Delta t \leqslant 1/10$ ns, and the plasma internal dynamics will be studied only over 1 or 2 ns periods. (Δt = 1/4 ns will be used to compare theory to experiment in one case.)

If light is absorbed in ΔV predominantly through the process of inverse bremsstrahlung, one can assume that the laser energy is deposited directly as thermal energy into the electron gas. The electrons then share their energy with the ions through collisions that heat, excite, and ionize the ions. When the electron gas is heated to temperatures between 100 and 1000 eV, low Z ions ($Z \leqslant 13$) can be stripped to their two K-shell electrons. The excitation and subsequent radiative decay of these hydrogen-like and helium-like ionization stages will be modeled in some detail in this paper to allow computation of the K-line emission spectrum that has been observed in laser heated carbon, fluorine, and aluminum plasmas. Examples of experimental C [7], F [8], and Al [9] K-line spectra are shown in Figs. 2 through 4. The prominent lines they contain are emitted by $np-1s$ ($n \geqslant 2$) transitions in H- and He-like ions.

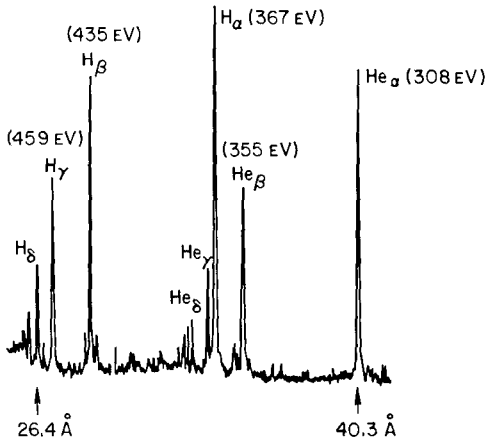

Fig. 2 — Experimental carbon K-line spectrum (C in CH_2)

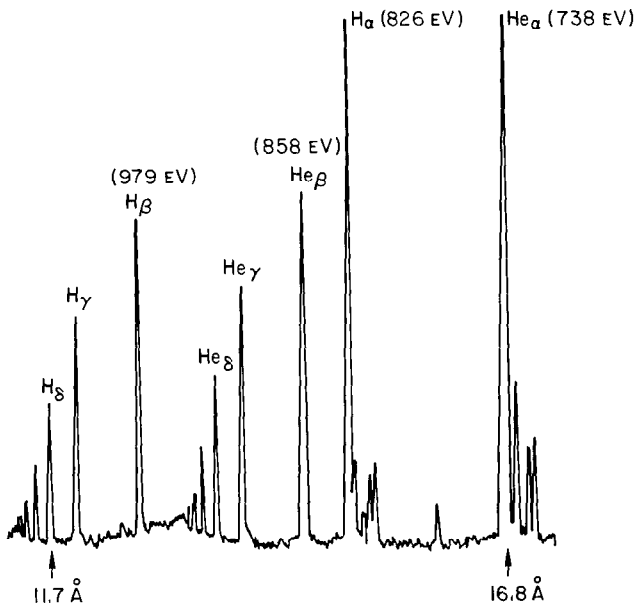

Fig. 3 — Experimental fluorine K-line spectrum (F in LiF)

Guided by the spectra in Figs. 2-4, we have set up a description of laser-heated plasma x-ray generation based on the energy level diagram of Fig. 5. The topmost state is the state of total ionization, which is alternatively CVII, FX, or Al XIV. Only four H-like and four He-like p-states are used; no other excited states are presently included in our model. The p-states emit most of the radiation recorded in Figs. 2-4. They are excited from the ground state above them by collisional and radiative recombination and from the ground state below by collisional excitation. Thus, line emission is generated in both the ionizing (or heating) and deionizing (or cooling) stages of the plasma's time evolution. Neighboring ground states are connected to each other by collisional ionization and radiative and collisional recombination processes.

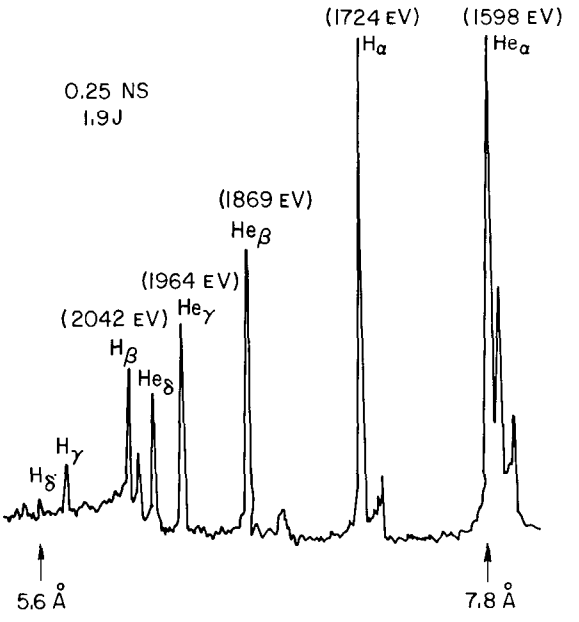

Fig. 4 — Experimental aluminum K-line spectrum

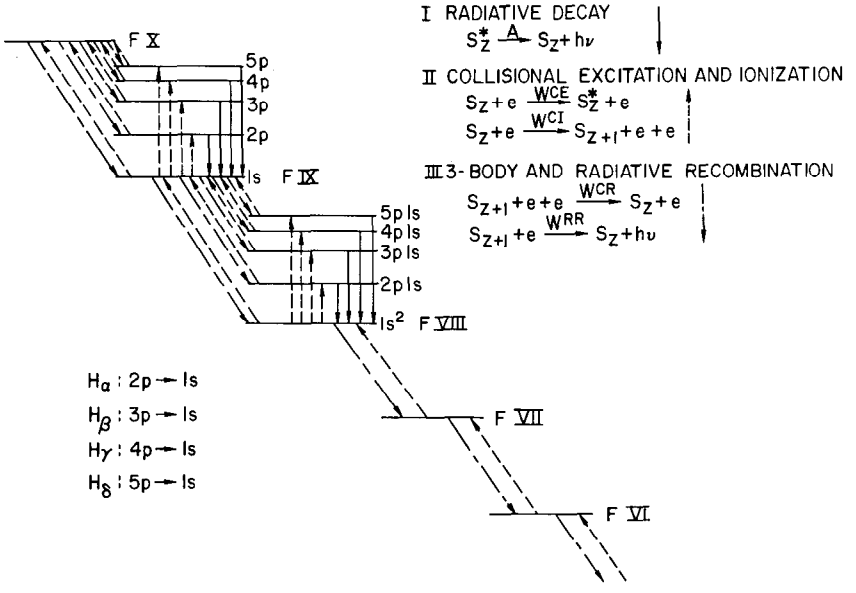

Fig. 5 — Fluorine energy level diagram showing the transitions used in the rate equation theory

C. EQUATIONS OF MOTION AND RATE COEFFICIENTS

The equations of motion of our model describe a small-volume energy flow that is representable diagrammatically, as shown in Fig. 6. Generation of internal ion energy and x-radiation is described by a set of rate equations for the ion population densities. They are based on the energy diagram of Fig. 5 and have the form:

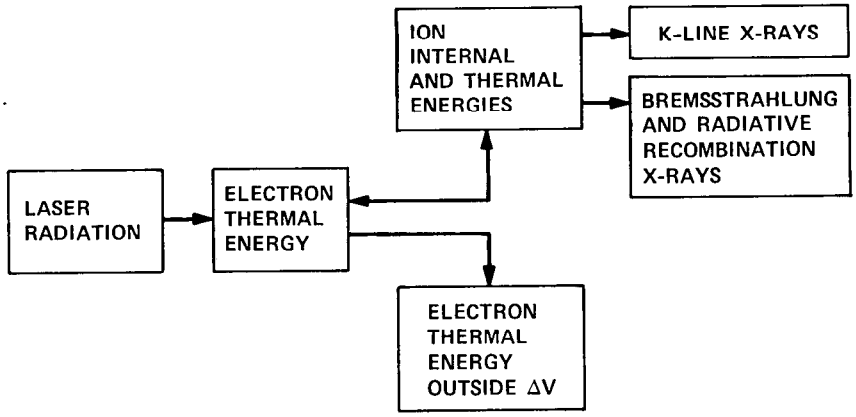

Fig. 6 — Energy flow diagram of the hot-spot model

$$\partial_t N_\mu = \sum_\nu W_{\mu\nu} N_\nu (\mu = 1, \text{---}, s) \tag{2}$$

where s is the number of energy levels in Fig. 5. The rates $W_{\mu\nu}$ for $\mu \neq \nu$ correspond to transitions from the νth to the μth energy level, and

$$W_{\mu\mu} = -\sum_\nu W_{\nu\mu}.$$

$$N_i = \sum_\mu N_\mu$$

is a constant of the motion. The rates depend on the energy density of the electron gas through the electron temperature and on the electron density,

$$N_e = \sum_\mu Z_\mu N_\mu \tag{3}$$

where $\{Z_\mu\}$ are the ionic charges.

On multiplying the equation for N_μ by E_μ, the energy of the μth ionic level, and summing over μ, one obtains an equation of motion for the plasma internal energy,

$$E_i = \sum_\mu E_\mu N_\mu:$$

$$\partial_t E_i = Q_i - R_i \tag{4}$$

where Q_i is the net rate of energy transfer from the electrons to the ions via collisional excitation and ionization less collisional recombination processes. R_i is the rate of energy loss from the ions by line and radiative recombination emission processes:

$$R_i = \sum_{\mu\nu} \left\{ N_\mu W^{RR}_{\nu\mu}(E_\mu - E_\nu) + N_\mu A^{Ein}_{\nu\mu}(E_\mu - E_\nu) \right\} . \tag{4a}$$

To obtain a complete description of the energy flow in ΔV, one must supplement the equation for E_i with equations of motion for the electron and ion thermal energies. When there is no hydrodynamic motion and therefore no generation of motional energy, these equations can be written as follows [10]:

$$\partial_t \left(\frac{3}{2} N_e k T_e \right) = S_e - \nabla \cdot \vec{q}_e - \frac{3m_e}{m_i} \frac{N_e k}{\tau_e} (T_e - T_i) - Q_i - R_b \tag{5}$$

$$\partial_t \left(\frac{3}{2} N_i k T_i \right) = \frac{3m_e}{m_i} \frac{N_e k}{\tau_e} \left(T_e - T_i \right) \tag{6}$$

where τ_e is the electron-electron $\pi/2$ collision time. The first term on the right-hand side of Eq. (5) is the laser heating term; the second, involving the heat-flow vector $\vec{q}_e$, represents thermal conduction losses; the third term describes the exchange of thermal energy between the electrons and ions; Q_i is described in Eq. (4); and R_b represents energy losses due to the emission of bremsstrahlung radiation [11]:

$$R_b = 1.2 \times 10^{-19} \sqrt{kT_e}\, N_e \sum_\mu Z_\mu^2 N_\mu . \tag{7}$$

Equations (2), (5), and (6) can be solved only when an estimate for $\nabla \cdot \vec{q}_e$ in terms of N_e and T_e can be made. Since the plasma is assumed to be uniform within ΔV, Eq. (5) can be averaged over the sphere and $\nabla \vec{q}_e$ replaced by

$$\frac{1}{\Delta V} \int_{\Delta V} dV\, \nabla \vec{q}_e = \frac{3}{r} \vec{q}_e \cdot n \tag{8}$$

where $\hat{n}$ is a unit vector normal to the sphere's surface. A phenomenological estimate for $\vec{q}_e \cdot \hat{n}$, the conduction loss rate across a unit area of the sphere's surface, can be made by setting

$$\vec{q}_e \cdot \hat{n} = - \kappa_e \hat{n} \cdot \nabla T_e \simeq \kappa_e \frac{T_e}{\ell_e} \tag{9}$$

where

$$\ell_e = \begin{cases} 10^{-2} \text{ cm} & t \leqslant 10^{-10} \\ 10^3 \sqrt{t} \text{ cm} & t \geqslant 10^{-10} \end{cases} \tag{10}$$

With this choice of ℓ_e, the temperature gradient scale, the conduction losses are not allowed to exceed physically realizable values for $t \leqslant 10^{-10}$ [12]. The formulas that were used in this paper, expressing κ_e, the electron thermal conductivity, and τ_e in terms of N_e, N_i, and T_e, are found in Braginskii [10]. Thus, the addition of Eqs. (4) and (5):

$$\partial_t \left\{ \frac{3}{2} N_e k T_e + E_i \right\} = S_e - \frac{3\kappa_e T_e}{r\ell_e} - \frac{3m_e}{m_i} \frac{N_e k}{\tau_e} (T_e - T_i) - R_i - R_b \tag{11}$$

yields an equation that together with Eqs. (2) and (6) provides a closed set of equations of motion for N_μ, T_e, and T_i.

As shown in Fig. 5, rate coefficients for five different rate processes must be known as functions of T_e in order to model the atomic physics of the carbon, fluorine, and aluminum plasmas. The values of the Einstein A coefficients for spontaneous radiative decay were taken from Weise [13] when available, or, in the case of the high-lying ($4p \rightarrow 1s$ and $5p \rightarrow 1s$) He-like transitions, they were found by extrapolation of $2p \rightarrow 1s$ and $3p \rightarrow 1s$ tabulated values. All of the rates for the collisional processes were calculated by standard techniques.

The formula used to compute the ionization coefficients $S^Z \equiv W^{CI}/N_e$ was obtained by integrating Seaton's [14] electron-ion impact ionization cross-section [15] over a Maxwellian electron velocity distribution. On neglect of processes such as autoionization and inner-shell excitation, one can approximate S^Z's dependence on T_e by the expression,

$$S^Z \cong 4.5 \times 10^{-24} (kT_e)^{1/2} \xi_i X_i^{-2} e^{-(X_i/kT_e)} \tag{12}$$

where ξ_i is the number of equivalent valence electrons in the ith shell and X_i is the ionization energy of an electron in the ith shell. For the reverse process of collisional recombination, the rate coefficient $\beta^Z \equiv W^{CR}/N_e^2$ was obtained by detailed balance:

$$\beta^Z = \sqrt{\left(\frac{h^2}{2\pi m k T_e} \right)^3} e^{X_i/kT_e} S^Z. \tag{13}$$

The formula used to calculate the radiative recombination coefficient $\alpha^Z \equiv W^{RR}/N_e$ was also derived by Seaton [16]. By retaining the first three terms in the asymptotic expansion of the Kramers-Gaunt factor, he found that

$$\alpha^Z = 5.2 \times 10^{-14} Z \lambda^{1/2} (0.43 + 1/2 \ln\lambda + 0.47\lambda^{-1/3}) \tag{14}$$

where $\lambda = X_i^{(Z-1)}/kT_e$. This formula is valid for the case of an electron and nucleus recombining to form a hydrogenic ion; nevertheless, we have used it for all ion recombinations because no other simple formula is available.

Finally, the electron impact excitation coefficients, $X_{ij} \equiv W^{CE}/N_e$, for excitation from level i to level j, were evaluated using a prescription similar to Burgess' semiclassical method [17], but modified in the threshold region and extended to cover a larger range of electron temperatures [18]:

$$X_{ij} = 16\left(\frac{2\pi}{3m_e}\right)^{1/2} \frac{I_H}{(kT_e)^{1/2}} \frac{I_H}{\Delta E} e^{-\Delta E/kT_e} f\langle g\rangle \pi a_o^2 \tag{15}$$

where I_H is the ionization energy of hydrogen, ΔE is the energy separation between levels i and j, f is the absorption oscillator strength of the transition, and $\langle g\rangle$ is an average Gaunt factor given by

$$\langle g\rangle = \int_{\Delta E} dEg(E)e^{-E/kT_e} \Big/ \int_{\Delta E} dEe^{-E/kT_e}. \tag{16}$$

The evaluation of $\langle g\rangle$ for multicharged ions can very considerably from Allen's values [19] for both resonance and nonresonance transitions. However, the temperature dependence of $\langle g\rangle$ obtained from Eq. (16) is in good agreement with values obtained by considerably more detailed computational methods [20].

Because stimulated absorption and emission processes are not included in Eq. (2), our rate theory treats the plasma sphere as if it were optically thin to the x-radiation it emits. This feature of the model limits its numerical validity to the establishment of upper bounds for cooling by x-ray emission. Estimates we have made indicate, in fact, that, at ion densities corresponding to the neodymium critical density, a 46-μ sphere of carbon plasma is effectively thick to its helium-like K_α radiation, a 46-μ fluorine is effectively grey, and 46-μ aluminum plasma is effectively thin. Thus, the K-line emission cooling rates calculated in this paper for carbon and fluorine are too large. Nevertheless, by first treating the plasmas as if each were optically thin, one can make useful initial comparisons between different Z-target materials that depend primarily on the locations of their K-line spectra.

D. COMPARISON WITH EXPERIMENT

The spectrum in Fig. 4 was obtained in an experiment where 1.9-J, 0.25-ns pulse of neodymium laser radiation was focused to a 50-μ spot on a slab of solid aluminum in vacuo [9]. The average intensity at the focus of this pulse was 4×10^{14} W/cm^2. In the experiment, the conversion of incident laser energy to K-line x-ray energy was at least 0.6 percent, measured under the assumption that the emission was isotropic. The measured ratio of energies in the hydrogen-like $K\alpha$ to helium-like $K\alpha$ lines was 0.6.

We would like to compare the results of this experiment to the predictions of the hot-spot model as represented by Eqs.(1) through (16). Before making this comparison, however, we must digress momentarily to justify it.

One of the main questions that can be answered by solving Eqs. (2), (6) and (11) is what are the laser-energy converting capabilities of a *given* quantity of plasma. Because hydrodynamic motion is neglected, once energy is deposited into ΔV and the plasma is heated, only radiative and thermal conduction energy losses compete to cool the plasma. If this competition is properly described by Eqs. (1) through (16), the deposition of a

comparable amount of laser energy into ΔV with an intensity comparable to that used in the above experiment should produce comparable amounts of K-line x-rays assuming the experiment produced a plasma roughly equivalent to the plasma sphere described in the hot-spot model.

One can argue that this assumption is correct on the basis of the model for plasma generation from a solid target proposed by Kidder [21]. In this model, the absorbed light generates a Chapman-Jouguet deflagration, which drives a shock wave into the solid and a blowoff rarefaction into the vacuum. The rarefaction is self-regulated, so that the density in the blowoff plasma is maintained at or near the critical density until the time when the optical thickness of the rarefaction equals one. According to Kidder's analysis, at 4×10^{14} W/cm^3, blowoff from an aluminum target becomes opaque to the incident laser radiation only after 0.8 ns. Moreover, if the blowoff occurs at a velocity of $\sim 3 \times 10^7$ cm/sec (the sound speed, $\sqrt{(Z+1)\,kT_e/m_i}$, of a 2-keV aluminum plasma) 75 μ of the blowoff plasma would be generated in a 1/4-ns period. Thus, in the rest frame of the blowoff, a Chapman-Jouguet deflagration generates a plasma in the above experiment whose size and density resemble closely the plasma modeled by Eqs. (1) through (16).

In an attempt, therefore, to compare the above experiment with theory, Eqs. (2), (6), and (11) were solved numerically under the following conditions. One and a half Joules of laser energy were deposited into the electron gas in 0.25 ns. The plasma within ΔV was taken to be initially in equilibrium at a temperature of 10^6 °K (86 ev). Thus, the initial thermal energy stored by the electrons within ΔV at a density near 10^{21} cm^{-3} J. Since electron and ion energy densities in a plasma are comparable, only milli-Joules of energy was stored initially in ΔV. The addition of 1.5 J of laser energy is therefore a major perturbation of the plasma. Consequently, one can assume that the calculation did not depend too sensitively on the chosen equilibrium initial conditions.

Results of the numerical integration of Eqs. (2), (6), and (11) are shown in Figs. 7 through 11. The electron temperature was driven to a maximum value of 2 keV in 0.3 ns, falling with equal rapidity to values below 0.5 keV. The fact that Al XIII ions outnumber Al XII ions for only about 0.5 ns (Fig. 8) accounts for the fact that the He-like lines are more prominent than the H-like lines of the computed x-ray spectrum of Fig. 9. The emission rates for the two sets of lines, which are plotted in Figs. 10 and 11, peak slightly before (for He-like) or at (for H-like) the time when the electrons are at their peak temperature and the collisional excitation rates are largest. The double peaking of some of these rates is indicative of the fact that we have allowed for the population of the Al XIII and Al XII excited states from above by collisional and radiative recombination. Thus, as the plasma cools and Al XIV and Al XIII ground states are depopulated, excited states are formed and line emission continues. The fall of the power curves of the H-like and He-like lines are correlated, for this reason, to the fall of the Al XIV and Al XIII population curves respectively.

The computed spectrum in Fig. 9 looks qualitatively very much like the experimental spectrum of Fig. 4, which is a film densitometer tracing. The quantitative agreement between the K-line outputs in the computer and laboratory experiments was also good. In the computer experiment, 1.5 J of laser energy was converted to 7×10^{-3} J of K-line x-rays, a 0.5-percent conversion efficiency. Moreover, the computed ratio of (total)

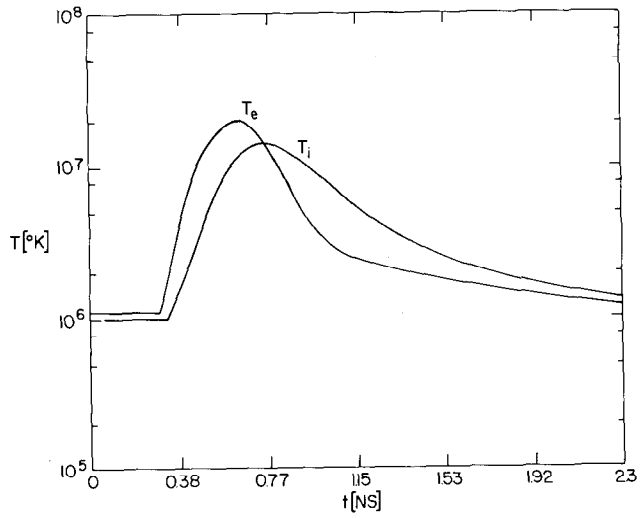

Fig. 7 — Electron and ion temperatures versus time

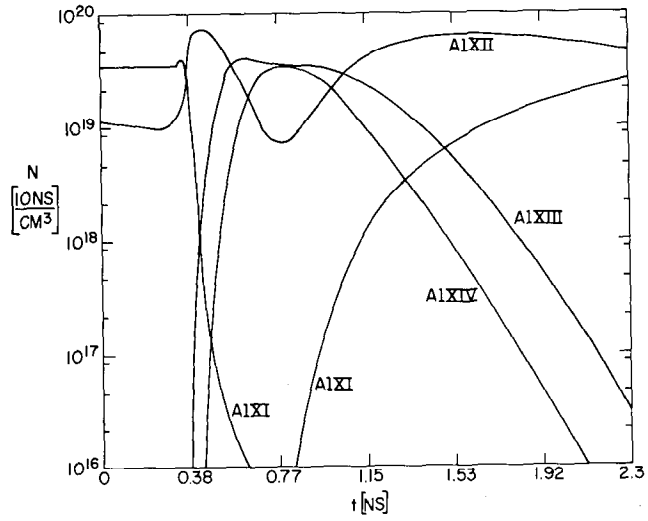

Fig. 8 — Ion population densities versus time

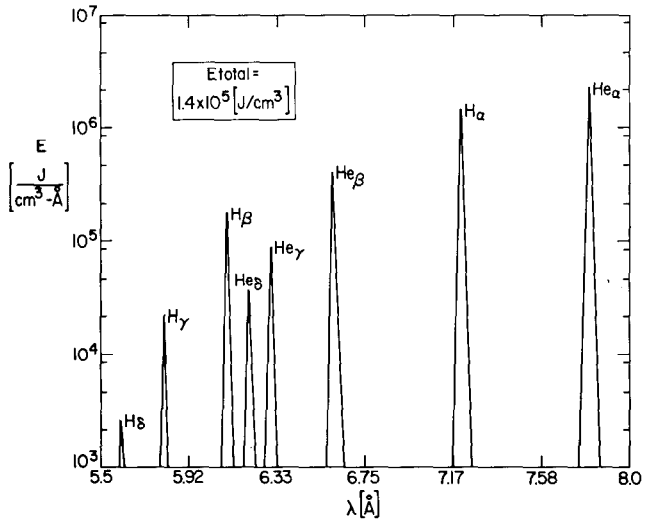

Fig. 9 — Computed time integrated K-line spectrum

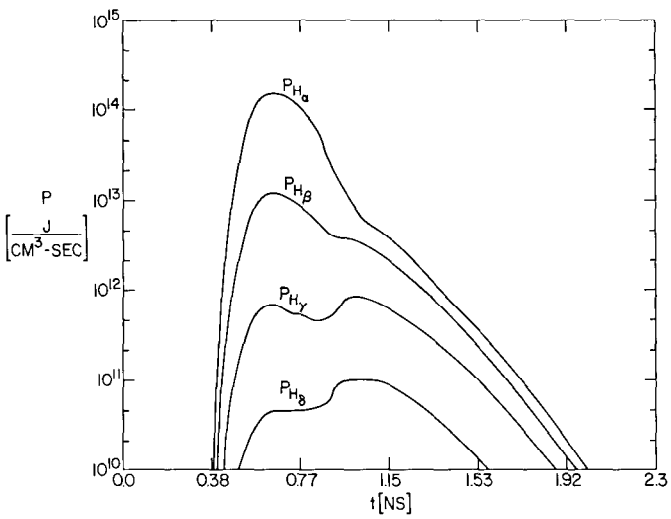

Fig. 10 — Power output from the H-like ion lines versus time

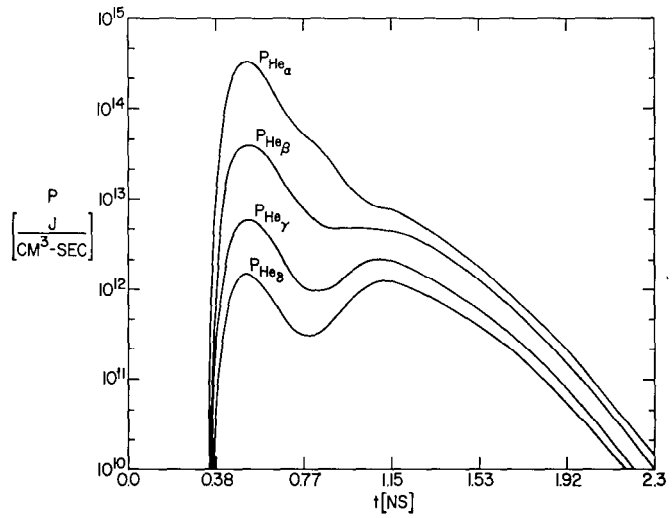

Fig. 11 — Power output from the He-like ion lines versus time

emitted hydrogen-like K_α to helium-like K_α radiation was 0.55. When a similar calculation was performed using a coronal model, in which the ion densities were determined from the requirement that they be in equilibrium with the electron gas rather than from a solution to rate equations, agreement between experiment and the hot-spot model was much worse [22].

E. COMPUTATION OF CONVERSION EFFICIENCIES

The good agreement between the predictions of the hot-spot model and experiment in the above case supports the model's further use to compute variations of the laser-light-to-x-ray conversion efficiency when the laser energy, pulse width, or conduction loss rate is changed. This conversion efficiency can also depend on the length of time (for short times < 1 ns) over which one integrates the x-ray production. For good x-ray conversion, one would like the short-time conversion efficiency to be large.

For this reason, we chose to compare the C, F, and Al plasmas using 25 ps laser pulses. The energy deposited was varied, corresponding to an equivalent variation in the average intensity of light incident on the sphere. The plasmas were initially chosen to be in equilibrium at a low plasma temperature of 10^4 °K in order to insure again that our results are independent of initial conditions for a broad range of laser energies. Maximum energy deposition occurred at t_o = 75 ps; the conversion efficiency (C.E.) to K-line x-rays was computed over the first nanosecond of plasma-time evolution. Figure 7 shows this is sufficient time for the K-line emission to go to completion. In effect, therefore, the plasma was heated by laser-energy deposition during the first 0.1 ns and cooled over the last 0.9 ns. For each plasma history, a K-line conversion efficiency was calculated. These results are plotted for carbon, fluorine, and aluminum plasmas in Fig. 12 [23].

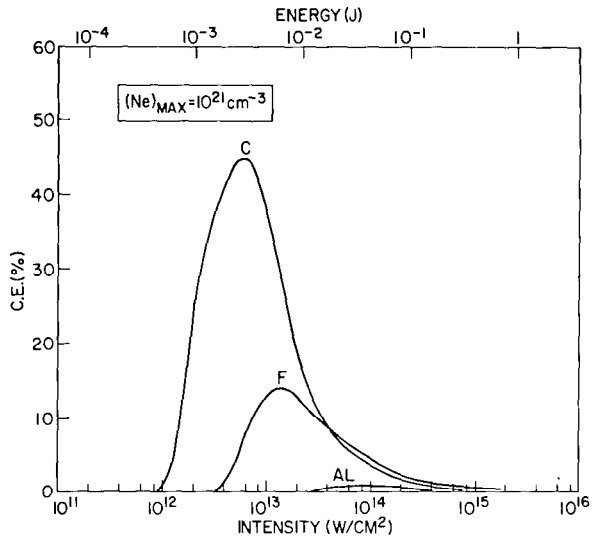

Fig. 12 — K-line conversion efficiencies in carbon, fluorine, and aluminum plasmas as a function of laser intensity

The striking differences between the conversion efficiencies of the three plasmas are due to several causes. To begin with, the energies of the K-line photons increase as Z^2. Therefore, for increasing Z, one must heat the plasma to progressively higher temperatures in order to excite K-line emission. For example, near coronal equilibrium, peak emission of the He-like K-lines occurs roughly at electron temperatures of 70, 250, and 900 eV respectively for C, F, and Al plasmas. For this reason, the peaks in the C.E. curves shift to higher intensity as the plasma Z is increased. However, since the conduction loss rate goes as $T_e^{5/2}$ [24], conduction losses also increase as the plasma becomes hotter. This is one reason why the C.E. peaks get smaller as Z increases. Another reason for the peak decrease is that, in our model, there are more emitters per cubic centimeter in the plasma with the smaller Z. For example, the requirement that $N_e = 10^{21}$ cm^{-3}, the neodymium critical density, when the plasma is fully ionized, sets the ion density at 1.67×10^{20}, 1.11×10^{20}, and 7.69×10^{19} respectively for the C, F, and Al plasmas.

The C.E. curve for carbon peaks sharply in our theory, since we do not account for the laser energy once it is conducted from the sphere. All of the computed conversion takes place within ΔV. In Fig. 13, curves showing the radiative energy input and output of the carbon sphere, which illustrate this point, are plotted. As the deposited energy is increased, the electrons are driven to higher temperatures, which in turn increases the plasma radiation loss rate. However, past the intensity for peak conversion, the plasma is overheated. The electrons get too hot, too fast, stripping the ions of their bound electrons and causing a decrease in the emission of x-rays on the ionizing side of the plasma's time evolution. It is clear that once the plasma is strongly overheated and totally ionized, it can no longer emit line or radiative recombination radiation. It cools only by thermal conduction, or more weakly by bremsstrahlung emission (which occurs at slower rates than line and radiative recombination emission). This statement explains why the total

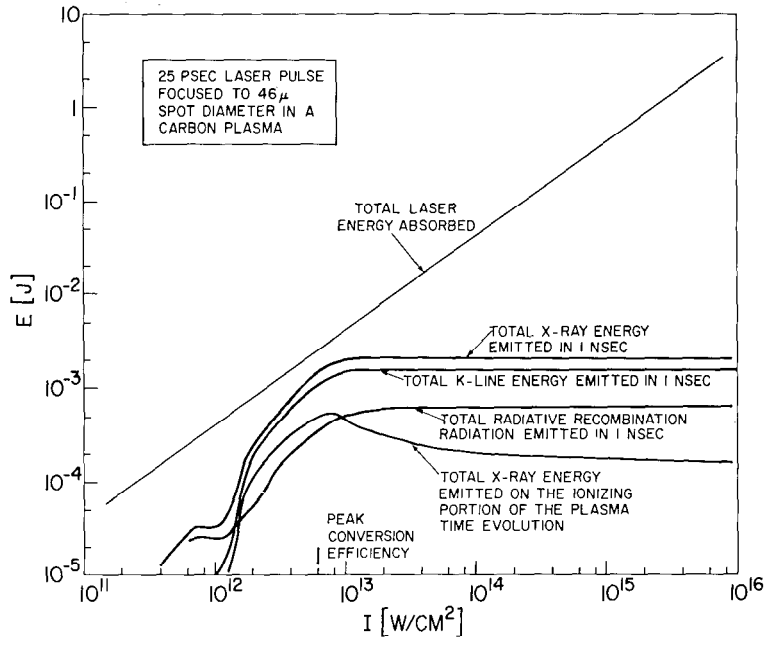

Fig. 13 — Total energies emitted and absorbed from a carbon plasma as a function of laser intensity

x-ray output saturates and why additional laser energy, in excess of 1 or 2 mJ, cannot be converted to 1 ns to x-rays within the carbon sphere. It is lost by conduction instead.

In order to convert more laser energy to x-rays within the sphere, one would be led to try to (a) speed up the line emission losses, (b) slow down the conduction losses, or (c) deposit the energy more slowly to avoid overheating the plasma. Once excited, the p-states radiate in 1/10 to 10 ps, that is, in times generally shorter than the laser-energy deposition time. Therefore, to increase line emission, one must increase the excitation rates of the p-states by heating a higher density plasma [1]. One can either heat denser plasmas by using light with a frequency higher than neodymium laser radiation or deposit excess amounts of neodymium laser radiation into a plasma with a density gradient such that, by thermal energy conduction, denser regions of plasma would be heated beyond the depository site. An example of the effect of increasing the p-state excitation rates is shown in Fig. 14 for a fluorine plasma at a density corresponding to the absorption of frequency-doubled neodymium laser radiation. At this density, a 46-μ sphere of fluorine plasma has a comparable optical thickness to its K-lines as the 46-μ sphere of carbon plasma has at the neodymium critical density.

Two conversion-efficiency curves are shown in Fig. 14. They give the efficiency of converting 0.53 μ laser energy to K-lines and to radiative recombination radiation which is emitted when H-like and He-like ground states are formed. Conversion to K-line peaks at 47 percent, in contrast to the 14-percent fluorine peak of Fig. 12. Thus, increasing the ion density fourfold, increased the peak K-line conversion by almost the same amount.

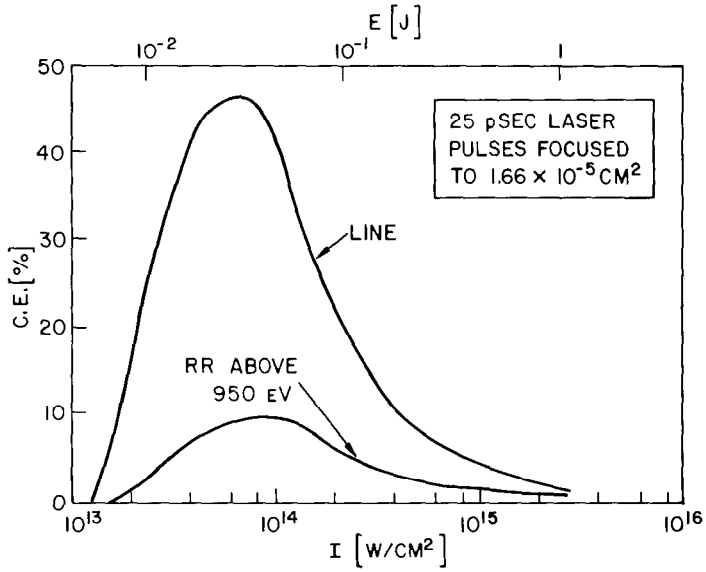

Fig. 14 — Conversion efficiencies in a fluorine plasma with an ion density corresponding to the critical density for 0.53μ radiation

The conduction-loss rate in our model can be controlled by decreasing the temperature gradient at the surface of the sphere — that is, by heating more plasma with laser energy. Figure 15 shows the effect on the C.E. curve of a fluorine plasma of changing the minimum value of ℓ_e from 10^{-2} to 2×10^{-2}, to 10^{-1}. As expected, the peak of the curve rises as ℓ_e increases. Note however that the peak is not shifted or broadened. For a fixed pulse width, good conversion is obtained for a well-defined range of pulse energies, corresponding to optimally heated plasmas.

Finally, in an effort to convert more laser energy in ΔV to K-lines, one might deposit the greater energy at a slower rate. In Fig. 16, conversion efficiency curves for fluorine, obtained by using 10-ps and 100-ps laser pulses, are compared to the fluorine curve of Fig. 12. The dashed line in Fig. 16 represents the conversion one gets in 0.6 ns using 25-ps pulses. It merges with the curve showing conversion in one or more nanoseconds of 25-ps pulses. One sees from these two curves that most of the conversion to K-line x-radiation occurs in the first 0.6 ns. Because the C.E. curves are plotted against laser intensity rather than energy, peak conversion using 100-ps pulses, for example, is displaced from peak conversion for 25-ps pulses. Both peaks occur at the same input energy and are therefore displaced in intensity by a factor of four. The range of energies over which one gets good conversion is also the same; therefore, as expected, one gets less overheating in ΔV and better conversion by lengthening the laser pulse so that the heating rate more closely equals the K-line emission cooling rate. Similar statements hold in comparing the 10-ps and 25-ps C.E. curves. Consequently, one would expect that, as the density of the increased, the pulse width used for *optimal* heating would have to decrease. In this way, one would adjust the heating rate to the increased K-line cooling rate.

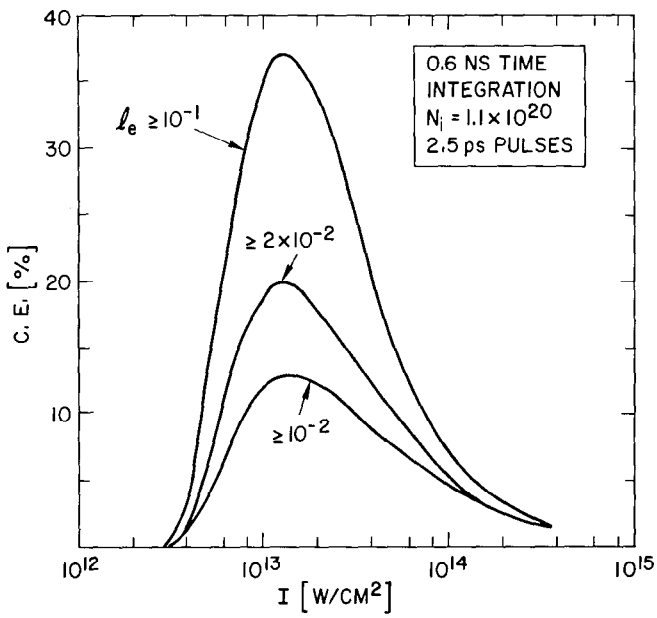

Fig. 15 — Conversion efficiencies in a fluorine plasma for different rates of heat conduction loss from the sphere

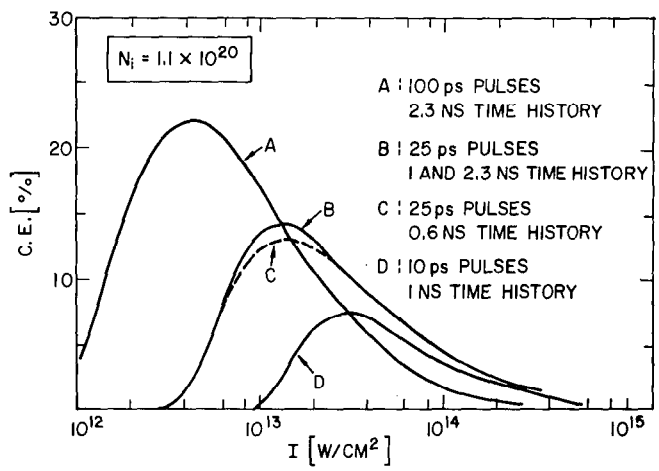

Fig. 16 — Conversion efficiencies in a fluorine plasma for different laser pulse widths

F. SUMMARY AND CONCLUSIONS

We have developed a simple, but illustrative, model describing K-line emission from laser-heated plasmas. The development proceeded along two lines. On the one hand, we established a correspondence between the physical situation described by our model and a particular set of experiments in which a blowoff plasma is generated and heated by the same (subnanosecond) laser pulse. The pulse, which is incident on a solid target, sets up a Chapman-Jouguet deflagration that expels hot plasma into a vacuum at the critical density of the laser frequency. We used the results of an experiment involving an aluminum target as a fiducial point for our model. The reasonable agreement between the predictions of the model with the experimental results indicated that our phenomenological description of the conduction losses from the sphere was adequate. On the other hand, having established contact with experiment, we used our model to make some parameter studies of the K-line conversion efficiency.

In all cases, for a fixed set of conditions, we found there was a well-defined peaking of the K-line conversion efficiency as a function of laser intensity (i.e., as a function of the plasma heating rate). Two important ideas regarding the peak location and the peak height emerged from the results of our parameter studies [25].

The location of the peak depends on the location of the K-lines, i.e., on their photon energy. As the plasma Z is increased, more energy must be deposited to heat the plasma sufficiently to excite the He-like and H-like p-states. For the same reason, the peak shifts to higher energies as the plasma density increases. However, for a given Z and given density, peak location depends on the degree and not the rate of plasma heating. For 10, 25, and 100 ps pulses, the plasma heating rate in C, F, and Al plasmas is faster than its cooling rate. In these cases, the conversion efficiencies peak at the same value of energy deposited rather than at the same value of light intensity. In other words, light energy/area and not light energy/area-time is important in determining peak location for short pulses.

Peak height depends on the competition between radiative and conduction losses. A decrease in the temperature gradient at the sphere's surface brought corresponding increases in peak height. However, the peak width remained the same, showing that the rise in the C.E. curves was associated with the achievement of high enough electron temperatures to excite the K-lines, whereas the fall in the curves was associated with overheating of the electrons, which caused total ionization of the plasma. Because conduction losses increase with T_e, peak height decreased with plasma Z for a given critical density. However, as the electron density is increased the conduction-loss rates decrease through κ_e as N_e^{-2}. Moreover, the p-states are pumped more effectively so that the radiative cooling rate increases. These two effects cause the peak height to increase with plasma density. Our estimates for C, F, and Al seem to indicate, in fact, that the peak heights of these three plasmas are comparable under conditions where they trap their K-radiation with comparable strength. Large K-line conversion is attainable in C, F, and Al plasmas only when the plasma is optically thick to this radiation. Before it escapes, therefore, it may be quenched or frequency redistributed.

REFERENCES

1. K.G. Whitney and J. Davis, Appl. Phys. Lett. 24, 509 (1974).
2. J.B. Chase, J.M. LeBlanc, and J.R. Wilson, Phys. of Fluids 16, 1142 (1973).
3. K.G. Whitney, N.K. Winsor, J. Davis, and D.A. Tidman, Bull. Am. Phys. Soc. II 18, 1317 (1973).
4. N.K. Winsor and D.A. Tidman, Phys. Rev. Lett. 31, 1044 (1973).
5. J.A. Stamper, K. Papadopoulos, R.N. Sudan, S.O. Dean, E.A. McLean, and J.M. Dawson, Phys. Rev. Lett. 26, 1012 (1971).
6. T.W. Johnston and J.M. Dawson, Phys. of Fluids 16, 722 (1973).
7. G.A. Doschek, U. Feldman, and D.J. Nagel, unpublished.
8. U. Feldman, G.A. Doschek, D.J. Nagel, W.E. Behring, and R.D. Cowan, Astrophys. J. 187, 417 (1974).
9. D.J. Nagel, P.G. Burkhalter, C.M. Dozier, J.F. Holzrichter, B.M. Klein, J.M. McMahon, J.A. Stamper, and R.R. Whitlock, Phys. Rev. Lett., to be published.
10. S.I. Braginskii, "Reviews of Plasma Physics," ed. by M.A. Leontovich (Consultants Bureau, New York, 1965, p. 205).
11. L. Spitzer, Jr., "Physics of Fully Ionized Gases," Interscience, New York (1962).
12. A more elaborate computation of ℓ_e would have to account for its dependence on temperature and density, see: J.M. Dawson, Phys. of Fluids 7, 981 (1964). For the convenience of estimating ΔT_e simply under time changing conditions, we have chosen an average value for ℓ_e.
13. W. Wiese, M. Smith, and B. Miles, "Atomic Transition Probabilities," NBS-22, Vol. II (1969).
14. M. Seaton, "Atomic and Molecular Processes," ed. by D. Bates, Academic Press (1962).
15. M. Seaton, Phys. Soc. 79, 1105 (1962).
16. M. Seaton, MNRAS 119, 81 (1959).
17. A. Burgess, Culham Conference on Atomic Collisions, AERE Rept. 4818, 63 (1964).
18. J. Davis, JQSRT, 14, 549 (1974).
19. C.W. Allen, "Astrophysical Quantities," Althone Press (London), 1965.
20. J. Davis and E. Oran, J. Appl. Phys. 45, 2480 (1974).
21. R.E. Kidder, Nucl. Fusion 8, 3 (1968); "Proceedings of the International School of Physics 'Enrico Fermi,' Course 48," ed. by P. Caldirola and H. Knoepfel, New York academic Press, 1971, p. 306.
22. J.A. Stamper, O.C. Barr, J. Davis, G.A. Doschek, C.M. Dozier, U. Feldman, B.M. Klein, W.M. Manheimer, E.A. McLean, J.M. McMahon, D.J. Nagel, D.A. Tidman, R.R. Whitlock, K. Whitney, N.K. Winsor, and F.C. Young, in the Third Workshop on "Laser Interactions and Related Plasma Phenomena," at Rensselaer Polytechnic Institute, Troy, N.Y., August 13-17 (1973).

23. The large peak conversion efficiencies computed here are for K-shell line radiation. Comparable conversion efficiencies for L-shell radiation from Fe and Cu plasmas using 1 ns neodymium laser pulses has been reported by P.J. Mallozzi, H.M. Epstein, R.G. Jung, D.C. Applebaum, B.P. Fairand, W.J. Gallagher, R.L. Uecker, and M.C. Muckerheide, J. Appl. Phys. 45, 1891 (1974).

24. Under the assumption of a constant ℓ_e.

25. The peak width will depend on the amount of plasma included in the calculation. Our model deals with the converting capabilities of a given volume of plasma under the (violatable) assumption that it constitutes the bulk of the plasma heated by E_o. X-ray production from energy conducted outside the plasma sphere is not computed.

X. LASER RADIATION FORCE

The forces exerted by laser radiation play a varied role in laser-produced plasmas. Radiative forces have been shown to contribute to such phenomena as plasma acceleration [1], self-focusing of laser radiation [2], parametric instabilities [3,4], and magnetic field generation [5,6]. These effects may be important in laser-fusion applications [7,8]. A discussion is given here of physical mechanisms involved in the radiative force, and the limitations in a particular theory (ponderomotive force) are pointed out. The discussion is concerned mainly with laser radiation (transverse waves), but much of the reasoning also applies to plasma (longitudinal) waves.

Radiative forces act primarily on the electrons, due to their small mass. Part of this force is transmitted via an irrotational electric field and collisions to the ions, so that this part of the force acts effectively on the neutral plasma. However, for typical focal-region geometries, the radiation-induced electric field has a large solenoidal component which drives currents and generates magnetic fields. The solenoidal nature is dependent on the net field momentum carried by the laser beam and on the different directions of the electron density and laser intensity gradients. Both effects are ignored in the ponderomotive theory of radiative forces. A general description of radiative forces must include both the plasma force and the electric field.

The radiative force involves a time-averaged momentum transfer in the electron fluid. One contribution, a direct transfer of field momentum (e.g., due to absorption), could occur with initially homogeneous fields. However, with the resulting inhomogeneous fields, there is another contribution which does not depend on a net field momentum. This contribution involves a momentum transfer within the electron system and is due to the electron quiver motion in the inhomogeneous fields. The quiver force is analogous to the force on the electron fluid resulting from a thermal pressure gradient. From these considerations, one can see why [6] the effective radiation pressure (time-averaged momentum flux associated with the laser radiation) in a laser-produced plasma is the sum of a field and quiver pressure.

Field momentum and energy, being quadratic in the fields, are transported at the group velocity. Purely sinusoidal fields, i.e., a single Fourier component, do not allow the definition of group velocity and thus cannot account implicitly for the transport of field energy and momentum. Thus, the finite bandwidth of laser radiation must be included if a microscopic theory is to account for field momentum.

Field momentum is implicitly accounted for when the wave spectrum is given, and it can be expressed in terms of the group velocity $\underline{v}_g$. It is also possible to explicitly account for a net field momentum density $\underline{g}$ in the form of the radiation pressure $\underline{\underline{P}}^r$

$$\underline{\underline{P}}^r = P_o^r \underline{\underline{I}} + \underline{v}_g \underline{g} \tag{1}$$

where there is a scalar radiation pressure P_o^r and a directed part $\underline{v}_g\underline{g}$. Field momentum produces an anisotropy in $\underline{\underline{P}}^r$ which is essential to the nature of the radiation-induced forces and fields.

The radiative force considered here is a time-averaged, nonrelativistic force density on the electrons due to high-frequency electromagnetic fields having a weak spatial inhomogeneity. Two types of descriptions are discussed: that derived from the radiative force on a single electron, and the radiative force on the electron fluid.

The term "pondermotive force" is used here to denote the radiative force density derived by considering the force on a single electron due to fields having a purely sinusoidal time variation [3,4,9]. The amplitudes of the fields are assumed to be arbitrary functions of space, so that the theory could apply to both macroscopic and microscopic phenomena. However, one should note how time averaging the product of fields places restrictions on the spatial description [10].

The force on a single electron can be expressed [11] as $-(e^2/2m\omega^2)\nabla\langle(\delta\underline{E})^2\rangle$. The ponderomotive force, or radiative force density, can thus be written as

$$\underline{f}_o^r = -\frac{1-\epsilon}{8\pi}\nabla\langle(\delta\underline{E})^2\rangle . \tag{2}$$

The time-averaged force density or the electron fluid due to high-frequency electromagnetic fields can be derived by taking the first velocity moment of the electron kinetic equation [5,6]. This force density will be referred to simply as the radiative force in order to distinguish it from the ponderomotive force. It can be expressed as [5,6],

$$\underline{f}^r = -\nabla\cdot\underline{\underline{P}}^r - \frac{\partial \underline{g}}{\partial t} \tag{3}$$

where $\underline{\underline{P}}^r$ is an effective radiation pressure or time-averaged momentum flux associated with the high-frequency fields and where $\underline{g} = \langle\delta\underline{E}\times\delta\underline{B}\rangle/4\pi c$ is the field momentum density.

The ponderomotive formulation has implicit in it several restrictions. It ignores field momentum, since field momentum cannot be represented explicitly in a scalar radiation pressure, and it cannot be represented implicitly by purely sinusoidal variations (i.e., there is no wave spectrum). Note that the force per particle is conservative (derivable from a potential) and hence cannot represent dissipative effects such as absorption by collisions or plasma turbulence. Field momentum is transferred to the electrons during the absorption of directed laser energy. Recall that the rate per unit volume at which field momentum is transferred to the plasma is given by $\langle\delta\rho\,\delta\underline{E} + c^{-1}\,\delta\underline{J}\times\delta\underline{B}\rangle$ where, for laser-produced plasmas, the coupling is due almost entirely to the oscillating current $\delta\underline{J}$ associated with electron quiver motion. Ignoring field momentum is thus equivalent to setting $\langle\delta\underline{J}\times\delta\underline{B}\rangle$ equal to zero.

Since the ponderomotive force is derived from a single particle theory, it refers, in effect, to a homogeneous, neutral plasma. If one calculates the force on a single particle and then multiplies this result by the particle number density, the resulting force density does not correctly include the effects of density variations. In effect, it refers to the force

density in a homogeneous ($\nabla n = \underline{0}$) plasma. Similarly, one cannot correctly account for charge-density effects in the force density by multiplying the unit charge in the single particle force equation by number density.

The ponderomotive description is valid for purely sinusoidal fields in a neutral, homogeneous, nonabsorbing plasma. In fact [10], applying these restrictions to Eq. (3) yields Eq. (2).

The electric field in a plasma is commonly evaluated from a generalized Ohm's law which is dependent on various forces acting on the electron fluid [12]. This is reasonable since, due to the small electron inertia, various forces acting on the electron fluid tend to be balanced by the electrical force. For example, a thermal pressure gradient produces a contribution $-(1/ne)\nabla P_e$ to the electric field which primarily drives the thermally generated magnetic fields [13,14]. When the radiative force density is included in the electron equation of motion [5,6], then it appears as a contribution $\underline{E}^r = \underline{f}^r/ne$ to the slowly varying electric field.

Little thought is usually given to this electric field since, in many circumstances, it is primarily of an irrotational nature, so that it merely represents an electrostatic transmission of the radiative force from the electrons to the ions. The effective radiation force is then on the neutral plasma. However, for the case of highly focused laser radiation, the solenoidal component of $\underline{E}^r$ is large so that, in addition to the force on the neutral plasma, electric currents are produced and magnetic fields are generated [5,6].

The contributions to $\nabla \times \underline{E}^r$ can be seen by considering $\underline{E}^r = -(1/ne)\nabla \cdot \underline{\underline{P}}^r$ where $\underline{\underline{P}}^r$ has the form given in Eq. (1) with P_o^r equal to $(1-\epsilon)\langle(\delta \underline{E})^2\rangle/8\pi$

$$ne\underline{E}^r = \nabla P_o^r + (\underline{v}_g \cdot \nabla)\,\underline{g} + (\nabla \cdot \underline{v}_g)\,\underline{g}. \tag{4}$$

One can see from Eq. (4) that there are two major contributions to $\nabla \times \underline{E}^r$. For simplicity, these are considered separately. One is due to density variations and would exist even when the field momentum $\underline{g}$ vanishes so that $\underline{\underline{P}}^r$ is isotropic.

Setting $\underline{g} = \underline{0}$ gives

$$\nabla \times \underline{E}^r = (8\pi en^*n)^{-1}\,\nabla\langle(\delta \underline{E})^2\rangle \times \nabla n. \tag{5}$$

Since the gradient of $\langle(\delta \underline{E})^2\rangle$ or laser intensity has, due to absorption, a large component in the direction of the laser beam, and since ∇n is not so constrained, it is seen that the density effect will generally make a large contribution.

Next assume the density is constant and consider the effect of field momentum. Setting $\nabla n = \underline{0}$ shows that this is a direct result of the anisotropy of $\underline{\underline{P}}^r$, depending on the structure of $\underline{\underline{P}}^r$ and not on the relative variation of different quantities in $\underline{\underline{P}}^r$. For example, one term is proportional to $\nabla(\nabla \cdot \underline{v}_g) \times \underline{g}$ and thus depends on the variation of a single quantity.

Since ∇n and $\underline{g}$ are both assumed to be zero in the ponderomotive description, the ponderomotive theory cannot account for solenoidal contributions to $\underline{E}^r$.

REFERENCES

1. H. Hora, Phys. Fluids 12, 182 (1969). See also H. Hora, *Laser Interaction and Related Plasma Phenomena*, (H. Schwarz and H. Hora, Eds.) Plenum, New York; Vol. 1, p. 383 (1971) and Vol. 2, p. 341 (1972).
2. J.W. Shearer and J.L. Eddleman, Phys. Fluids **16**, 1753 (1973).
3. Francis P. Chen, chapter in *Laser Interaction and Related Plasma Phenomena*, Vol. 3 (H. Schwarz and H. Hora, Eds.) Plenum, New York (1973). See also Chen's University of California Report, PPG-160, Aug. 1973.
4. W.M. Manheimer and E. Ott, to be published in Phys. Fluids (June or July 1974).
5. J.A. Stamper and D.A. Tidman, Physics of Fluids **16**, 2024 (1973).
6. J.A. Stamper et al., chapter in *Laser Interaction and Related Plasma Phenomena*, Vol. 3 (H. Schwarz and H. Hora, Eds.) Plenum, New York (1973).
7. J. Nuckolls, L. Wood, A. Thiessen and G. Zimmerman, Nature **239**, 133 (1972).
8. J.S. Clarke, H.M. Fisher and R.J. Mason, Phys. Rev. Lett. **30**, 89 (1973).
9. G. Schmidt, *Physics of High Temperature Plasmas* (Academic Press, New York 1966), p. 47ff.
10. J.A. Stamper, submitted to Phys. Fluids; see also NRL Memorandum Report 2775.
11. Most observable quantities are time averages (designated by $\langle\ \rangle$) of quantities (designated by a prefix δ) oscillating at the frequency of the laser radiation.
12. S.I. Braginskii, *Reviews of Plasma Physics*, ed. by Acad. M.A. Leontovich, Vol. 1, p. 267ff (1965).
13. J.B. Chase, J.L. LeBlanc and J.R. Wilson, Phys. Fluids **16**, 1142 (1973).
14. J.A. Stamper, NRL Report 7411, June 1972, p. 2,3.

XI. PUBLICATIONS AND REPORTS

"A Large Aperture High Extinction Ratio Faraday Rotator Isolator," O.C. Barr, J.M. McMahon, IEEE Jour. Quant. Elect., Nov. 1973, p. 1124.

"Analysis of Discrete Pulse Forming Networks Driving Nonlinear Flashlamps Loads," O.C. Barr, NRL Memorandum Report 2808, June 1974.

"Optical Isolation and the Design of Large Aperture, High Extinction Ratio Faraday Rotators for High Power Glass Lasers," O.C. Barr, NRL Memorandum Report 2817, June 1974.

"Design of Fanned and Wedged Stacked Plate Polarizers for High Power Lasers," O.C. Barr and J.M. McMahon, NRL Memorandum Report 2830, July 1974.

"Laser-Produced Rare Earth X-Ray Spectra," P.G. Burkhalter, D.J. Nagel and R.R. Whitlock, Phys. Rev. A 9, 2331 (1974).

"Transitions in Highly Ionized Sn Spectra from a Laser-Produced Plasma," P.G. Burkhalter, U. Feldman and R.D. Cowan, J. Opt. Soc. Am. 64, 1058-1062 (1974).

"The Influence of High Density Plasmas on Series Merging," J. Davis, NRL Memorandum Report 2655, October 1973.

"Effective Gaunt Factors for Electron Impact Excitation of Multiply Charged Nitrogen and Oxygen Ions," J. Davis, J. Quant. Spectrosc. Radia. and Transfer 14, 549 (1974).

"Electron Impact Cross Sections and Rates for One- and Two-Electron Aluminum Ions," J. Davis, and E. Oran, J. Appl. Phys. 45, 2480 (1974).

OI Isoelectronic Sequence: Transitions $2p^4$-$2p^3 2s$, by G.A. Doschek et al., J.O.S.A. 63, 1463 (1973).

"X-Ray Emission from Laser-Produced Plasmas," C.M. Dozier, P.G. Burkhalter, B.M. Klein, D.J. Nagel and R.R. Whitlock in *Advances in X-Ray Analysis*, Vol. 17 (Plenum Press, N.Y., 1974), p. 423.

"X-Ray Point Source Projection Photography with a Laser-Produced Plasma," J.F. Holzrichter, C.M. Dozier and J.M. McMahon, Appl. Phys. Lett. 23, 687-689 (1973).

"Variation of the Temperature of Laser-Produced Plasmas with Laser-Pulse and Target Parameters, by B.M. Klein et al., Proc. European Conf. on Contr. Fusion and Plasma Physics, Moscow (1973).

"The Effect of Sidescatter Instabilities on the Propagation of an Intense Laser Beam in Inhomogeneous Plasma," H. Klein, W. Manheimer and E. Ott, Phys. Rev. Lett 31, 1187 (1973).

"The Effect of Trapping on the Saturation of the Raman Backscatter Instability," H.H. Klein, E. Ott and W. Manheimer, accepted for Physics of Fluids.

"Parametric Decay of Intense Radiation into a Whistler Wave," H.H. Klein, W.M. Manheimer and E. Ott, accepted for Phys. Fluids.

"The Effects of Plasma Inhomogeneity on the Production of Energetic Electrons," H.H. Klein and W. Manheimer, submitted to Physical Review Letters.

"Compression and Shaping of Pulses from High Power Solid State Lasers," R.H. Lehmberg, PROC-IEEE Electron Devices Meeting (Nov. 1973).

"Two Photon Resonantly Enhanced Self Defocusing in Cs Vapor at 1.06 μ," R.H. Lehmberg, J. Reintjes and R.C. Eckardt, accepted for publication in Appl. Physics Letters.

"Stripline Pockels Cell Assembly," J.P. Letellier, NRL Memorandum Report 2716, Jan. 1974.

"Passively Mode-Locked Nd:YAG Laser Stability Study," J.P. Letellier, NRL Memorandum Report 2684, Nov. 1973.

"Parametric Instabilities Induced by the Coupling of High and Low Frequency Plasma Modes," W. Manheimer and E. Ott, Phys. Fluids, July 1974. This was in last RPI report.

"A Connection Between the Linear and Nonlinear Theory of Anomalous Reflection from a Plasma Slab," W. Manheimer, Phys. Fluids, Sept. 1974.

"The Coherent Production of Energetic Electrons in Anomalous Reflection and Absorption of Intense Laser Light," W. Manheimer and H. Klein, accepted for Physics of Fluids.

"A Glass Disc Laser Amplifier," J.M. McMahon, J.L. Emmett, J.F. Holzrichter and J.B. Trenholme, IEEE J. QE, Oct. 1973, p. 992.

"A Glass Laser System Designed for Target Irradiation," J.M. McMahon, and O.C. Barr, Proc. SPIT (Aug. 1973).

"A Helically Pumped Disc Laser Amplifier," J.M. McMahon, O.C. Barr, Proc. IEDM (Nov. 1973).

"Suppression of Parasitic Oscillation in Laser Rod Amplifiers," J.M. McMahon, R.P. Burns, and T.H. DeRieux, Proc. ASTM-NBS Sym. on Damage in Laser Materials, May 1974.

"X-Ray and UV Emission of Laser Produced Plasmas," by D.J. Nagel et al., Proc. Eur. Conf. on Controlled Fusion and Plasma Phys., Moscow 1973.

"X-Ray Diagnostics of Laser-Compressed Plasmas," D.J. Nagel, Physica Fennica, 9(S1), 403-405 (1974).

"Power Dependence of Laser-Plasma X-Ray Emission," D.J. Nagel, P.G. Burkhalter, C.M. Dozier, B.M. Klein, and R.R. Whitlock, Bull. Am. Phys. Soc. **19**, 557 (1974).

"Transitions of Fe XVIII and Fe XIX Observed in Laser-Produced Plasmas," U. Feldman, G.A. Doschek, D.J. Nagel, W.E. Behring, and L. Cohen, Astrophys. J. **183**, L430 (1973).

"Laser-Plasma Spectra of Highly Ionized Fluorine," U. Feldman, G.A. Doschek, D.J. Nagel, W.E. Behring, and R.D. Cowan, Astrophys. J. **187**, 417 (1974).

"Satellite Line Spectra from Laser-Produced Plasmas," by U. Feldman, G.A. Doschek, D.J. Nagel, R.D. Cowan, and R.R. Whitlock, Astrophys. J., **192**, 213 (1974).

"X-Ray Emission from Laser-Produced Plasmas," D.J. Nagel, P.G. Burkhalter, C.M. Dozier, J.F. Holzrichter, B.M. Klein, J.M. McMahon, J.A.Stamper and R.R. Whitlock, Phys. Rev. Lett. **33**, 743 (1974).

"Time-Resolved Laser-Plasma Backscatter Studies," B.H. Ripin, J.M. McMahon, E.A. McLean, W.M. Manheimer and J.A. Stamper, Phys. Rev. Lett. 33, 634 (1974).

"Picosecond Diagnostics of Laser Light Scattered from Laser-Produced Plasmas," B.H. Ripin and J.A. Stamper, Proceedings of the Electro-Optical Systems Design Conference, 1974 West (to be published).

Laser-Matter Interaction Studies at NRL, John Stamper, et al., Proc. of Third Workshop on "Laser Interactions and Related Plasma Phenomena," at Renssalaer Polytechnic Institute, Troy, N.Y. Aug. 1973.

"Magnetic Field Generation due to Radiation Pressure in a Laser-Produced Plasma," J.A. Stamper and D.A. Tidman, Phys. of Fluids **16** (1973).

"Role of Magnetic Fields in Suprathermal Particle Generation by Laser-Produced Plasmas," D.A. Tidman and J.A. Stamper, Appl. Phys. Lett. **22**, 498 (1973).

"Field-Generating Thermal Instability in Laser-Heated Plasmas," D.A. Tidman and R.A. Shanny, NRL Memorandum Report 2667, Oct. 1973.

"Conversion Efficiencies of Laser to X-Ray Energy in C, F, Al Plasmas," K. Whitney and J. Davis, Appl. Phys. Lett. **24**, 509 (1974).

"K-Shell Line Radiation from Laser-Produced Aluminum Plasmas," K. Whitney, J. Davis, and E. Oran, NRL Memorandum Report 2644, June 1973.

"Laser Target Model," N.K. Winsor and D.A. Tidman, Phys. Rev. Lett. **31**, 1044 (1973).

"Measurements of Energetic X-Rays from Laser-Produced Plasmas," F.C. Young, Phys. Rev. Lett. **33**, 747 (1974).